JUSTUS-LIEBIG-
UNIVERSITÄT
GIESSEN

NF-κB p65 proximity labeling reveals multi-level crosstalk with lysosomal transcription factors TFE3, TFEB, and zinc finger protein GLIS2

Dissertation for the acquisition of the academic degree
Doctor rerum naturalium
(Dr. rer. nat.)

Submitted by
Lisa Leib
Gießen, 2024

Prepared at the
Faculty 08 of Biology and Chemistry
in collaboration with the
Rudolf Buchheim Institute of Pharmacology
Justus Liebig University Gießen

submitted on: 19.02.2024
submitted by: **Lisa Leib**

First supervisor: Apl. Prof. Dr. Peter Friedhoff
Institute of Biochemistry
Faculty of Biology and Chemistry
Justus Liebig University Gießen

Second supervisor: Prof. Dr. Michael Kracht
Rudolf Buchheim Institute of Pharmacology
Faculty of Medicine
Justus Liebig University Gießen

Table of contents

Abbreviations

Ab	antibody
AD	activation domain or acidic domain
AGS3	activator of G-protein signaling 3
AnkR	tandem ankyrin repeat domain
AP-1	activator protein 1
APEX	engineered ascorbate peroxidase
ARE	adenosine and uridine (AU)-rich elements
as	anti-sense sequence
ATP	adenosine triphosphate
bHLH-LZ	basic helix-loop-helix-leucine zipper domain
bHLH-zip	basic helix-loop-helix-leucine zipper
BMDM	bone-marrow-derived macrophages
bp	base pairs
BPL	endogenous biotin protein ligases
C	cytosolic fraction
Ca^{2+}	calcium cation
CAPTURE	CRISPR affinity purification *in situ* of regulatory elements
CBP	CREB-binding protein
cDNA	complementary DNA
CFB	complement factor B
CFD	complement factor D
ChIP-seq	chromatin immunoprecipitation sequence analysis
CLASP	Cas9 locus-associated proteome
CLEAR	coordinated lysosomal expression and regulation
Co-IP	co-immunoprecipitation
CRISPR	clustered regularly interspaced short palindromic repeats
CRISPR-ChAP-MS	CRISPR-based chromatin affinity purification with mass spectrometry
CSF	colony-stimulating factors
C_T	cycle threshold
CtBP1	C-terminal binding protein 1
ctr	control
DAMPs	damage-associated molecular patterns
DBD	DNA-binding domain
dCas9	deactivated Cas9
DCs	dendritic cells
DD	death domain
ddH_2O	double-distilled water
DEGs	differentially expressed genes
DK	double knockdown
DMEM	Dulbecco's Modified Eagle Medium
DMSO	dimethylsulfoxide
DNA	deoxyribonucleic acid
dNTP	deoxyribonucleotide triphosphate
E/I	glutamate 39 to isoleucine
EMSA	electrophoretic mobility shift assay
enChIP	engineered DNA-binding molecule-mediated chromatin immunoprecipitation
ER	endoplasmic reticulum
EV	empty vector
E values	expression values
exp 1/2	experiment 1 and 2
FACS	fluorescence-activated cell sorting
FB	FLAG-tag and biotin-acceptor-site
FBS	fetal bovine serum

FISH	fluorescence *in situ* hybridization
FL/DD	phenylalanine 213 and leucine 215 to aspartic acid
FLCN	folliculin
FNIP1	folliculin-interacting protein 1
FNIP2	folliculin interacting protein 2
FRET	Förster resonance energy transfer
FSC	forward scatter
fwd	forward primer sequence
GAPs	GTPase-activating proteins
GDP	guanosine diphosphate
GEFs	guanine nucleotide exchange factors
GFP	green fluorescent protein
GLIS	GLI-similar Krüppel-like zinc finger proteins
GLISBS	GLIS binding sites
Gln	glutamine-rich domain
GOIs	genes of interest
gt	goat
GTP	guanosine triphosphate
GTPases	hydrolase enzymes, that hydrolyze GTP to GDP
H^+	hydrogen cation
H3K27ac	DNA packaging histone H3 acetylation of lysine residue 27
H3K4me1	DNA packaging histone H3 monomethylation at lysine residue 4
HA-tag	Human influenza hemagglutinin (HA)-tag
HBSS	Hank's Balanced Salt Solution
HCI	high-confidence interactors
HDAC	histone deacetylase
HP	HiPerFect transfection reagent
HPGDS	hematopoietic prostaglandin D synthase
HRP	horseradish peroxidase
i4C	intrinsic 4C
IF	immunofluorescence
IFN	interferons
IKK	IκB kinase complex
IL	interleukins
IL-1R	IL-1 receptors
IL-1R1	IL-1 receptor type 1
IL-1Ra	IL-1 receptor antagonist
IL-1RAcP	IL-1R accessory protein
IL-1α	interleukin-1α
IN	input
IRAKs	IL-1 receptor-associated kinases
IRFs	interferon regulatory factors
ISG	interferon-stimulated genes
IκB	NF-κB inhibitor
JNK	c-Jun N-terminal kinase
K48, K63	lysine residue 48 or 63
kb	kilobases
kDa	kilodalton
LB	Luria-Bertani
LC-MS/MS	liquid chromatography with tandem mass spectrometry
LFC	$\log_2$ fold change
lncRNA	long noncoding RNA
LPS	lipopolysaccharide
LSDs	lysosomal storage disorders
LZ	leucine zipper domain
MAPK	mitogen-activated protein kinase

MCOLN1	mucolipin 1
mESCs	mouse embryonic stem cells
MiT/TFE	microphthalmia/transcription factor E
MITF	microphthalmia-associated transcriptionfactor
MLIV	mucolipidosis type IV
mRNA	messenger RNA
ms	mouse
MS	mass spectrometry
mTb	miniTurbo
mTORC1	mammalian target of rapamycin complex 1
MyD88	myeloid differentiation primary response 88
N1	nuclear fraction
N2	chromatin-bound proteins
NAFLD	nonalcoholic fatty liver disease
NBio/CBio	N/C-terminal BioTAP-tag
NDH	neonatal diabetes and congenital hypothyroidism
NEAA	non-essential amino acids
NEMO	NF-κB essential modulator
NF-κB	nuclear factor binding near the kappa light chain in B cells
NICD	Notch intracellular domain
NK(T)	natural killer (T) cells
NLS	nuclear localization sequence
nt	nucleotides
OD	optical density
p	p value
PAMPs	pathogen-associated molecular patterns
PBS	phosphate-buffered saline
PCR	polymerase chain reaction
PD	pulldown
PDA	pancreatic ductal adenocarcinoma
PERK	PKR-like ER kinase
PG	prostaglandin
pH	power of hydrogen
PLA	proximity ligation assay
PMSF	phenylmethylsulfonyl fluoride
Pol II	RNA-polymerase II
PP2A	protein phosphatase 2A
PPIs	protein-protein interactions
Pro	proline-rich domain
PRRs	pattern recognition receptors
PtdIns(3,5)P2	phosphatidylinositol 3,5-bisphosphate
PTMs	posttranslational modifications
PVDF	polyvinylidene fluoride
RA	rheumatoid arthritis
rb	rabbit
rev	reverse primer sequence
RHD	Rel homology domain
RNA	ribonucleic acid
RNAi	RNA interference
ROI	region of interest
RT	room temperature
RT-qPCR	quantitative reverse transcription PCR
rtTA	reverse tetracycline-controlled transactivator
S211, S122, etc.	serine residue 211, 122, 142 or 321
SD	standard deviation
se	sense sequence

Ser	serine-rich region
sgRNAs	single guide RNAs
siLuci	non-targeting siRNA directed against the luciferase mRNA
siRNA	small inhibitory RNA
SN	supernatant
SSC	sideward scatter
STAT	signal transducer and activator of transcription
TAB	TGF-β-activated protein kinase binding proteins
TAD	transactivation domain
TAE	Tris-Acetate EDTA
TAK-1	TGF-β-activated protein kinase 1
TBP	TATA-binding protein
TBS	Tris buffered saline
TF	transcription factor
TFE3	transcription factor E3
TFEB	transcription factor EB
TFEC	transcription factor EC
TFIIB	transcription factor IIB
TGF	transforming growth factors
TIR	Toll interleukin-1 receptor
TLRs	Toll-like receptors
TNF	tumor necrosis factors
TPC	two-pore channel
TRAF6	TNF associated factor 6
TRPML	mucolipin family of transient receptor potential channels
TSC	tuberous sclerosis complex
TTP	tristetraprolin
C3	complement component 3
ULK1	Unc-51-like kinase 1
UPR	unfolded protein response
v-ATPase	vacuolar-type ATPase
W	wash
w/o	without
wt	wild type
wt(bio)	biotin-omitted wild type sample
wt(dox)	doxycycline-omitted wild type sample
Y2H	yeast two-hybrid
ZFP36	zinc finger protein 36
3′UTR	3′ untranslated region (3′UTR)
Δ	single knockout
Δ30TFEB	constitutive nuclear mutant of TFEB
Δp65	p65-deficient cells
ΔΔ	double knockout
A	ampere
V	volts
%	percentage
× g	times gravity
rpm	rounds per minute
°C	degree Celsius
h, min, s	hours, minutes, seconds
g	gram
mol	molar (M)
U	units (the enzyme unit)
l	liter

Summary

The IL-1α-NF-κB signaling pathway represents a prime example of an inducible transcription factor system and plays a central role in the immune response and cancer. Despite an in-depth understanding of cytosolic signal transduction, little is known about the molecular networks that coordinate gene-specific, spatial and temporal activation of NF-κB-regulated immune genes in the nucleus. In this work, the hypothesis that the NF-κB-dependent function of a cell is modulated by dynamic interaction networks and continuous communication with other subcellular systems was investigated. To this end, two innovative biotin-based pulldown technologies (CAPTURE and MiniTurboID) were used to determine the specific NF-κB interactome in relation to individual inflammatory promoters or the NF-κB subunit p65. While CAPTURE-based purification of individual chromatin loci was experimentally established but ultimately did not lead to the identification of specific factors, MiniTurboID proximity labeling enabled the mapping of the transient and dynamic NF-κB p65 protein interactome. For proximity labeling, p65-deficient cells were reconstituted with a doxycycline-inducible p65-miniTurbo fusion protein or with p65 mutants (E/I or FL/DD), and the biotin-tagged interactors were subsequently identified by affinity proteomics using LC-MS/MS. A comprehensive bioinformatic analysis revealed more than 300 high confidence interactors (HCIs). Most HCIs are of nuclear origin, involved in the regulation of transcription or chromatin processes and require intact p65 dimerization but no DNA binding. A siRNA screen of the top 38 HCIs revealed a regulatory role of TFE3, TFEB and GLIS2 in the inducible expression of three prototypical IL-1α-regulated NF-κB target genes. TFE3 and TFEB are considered master transcription factors regulating the expression of lysosomal CLEAR (coordinated lysosomal expression and regulation) genes, while GLIS2 is a member of the Krüppel-like zinc finger protein subfamily. Prototypic CLEAR genes were expressed independently of p65. In contrast, transcriptome-wide analysis of p65-, TFE3-, TFEB-, TFE3/TFEB- or GLIS2-deficient cells revealed 44 IL-1α-regulated genes that require p65, TFE3 and TFEB for their expression and 83 genes that are cooperatively regulated by p65 and GLIS2. In addition, more than two-thirds of the p65/RELA motifs found among p65 ChIP-seq peaks were closely associated with TFE3 and GLIS2 motifs. Protein interaction maps derived from these data revealed a novel p65-TFE3-TFEB genetic network enriched with multiple components of interleukin signaling pathways and a TNF-centric subnetwork regulated by p65 and GLIS2. In summary, the combined analysis of selected NF-κB p65 interactors at the level of loss-of-function screens, genome-wide mRNA expression and chromatin recruitment revealed a multi-step crosstalk of lysosomal and NF-κB signaling pathways and additionally provided novel insights into critical functions of GLIS2 affecting components of both signaling axes.

Zusammenfassung

Der IL-1α-NF-κB-Signalweg ist ein Paradebeispiel für ein induzierbares Transkriptionsfaktorsystem und spielt eine zentrale Rolle bei der Immunantwort und Krebs. Trotz eines vertieften Verständnisses der zytosolischen Signalweiterleitung ist bisher wenig über die molekularen Netzwerke bekannt, welche die genspezifische, räumliche und zeitliche Aktivierung von NF-κB-regulierten Immungenen im Zellkern koordinieren. In dieser Arbeit wurde die Hypothese untersucht, dass die NF-κB-abhängige Funktion einer Zelle durch dynamische Interaktionsnetzwerke und die kontinuierliche Kommunikation mit anderen subzellulären Systemen moduliert wird. Zu diesem Zweck wurden zwei innovative Biotin-basierte Pulldown-Technologien (CAPTURE und MiniTurboID) eingesetzt, um das spezifische NF-κB Interaktom in Bezug auf einzelne Entzündungspromotoren oder die NF-κB-Untereinheit p65 zu bestimmen. Während die CAPTURE-basierte Reinigung einzelner Chromatin-Loci zwar experimentell etabliert wurde, aber letztlich nicht zu der Identifikation spezifischer Faktoren führte, ermöglichte das MiniTurboID *proximity-labeling* die Kartierung des transienten und dynamischen NF-κB p65 Proteininteraktoms. Für das *proximity-labeling* wurden p65-defiziente Zellen mit einem Doxycyclin-induzierbaren p65-miniTurbo-Fusionsprotein oder mit p65-Mutanten (E/I oder FL/DD) rekonstituiert, und die Biotin-markierten Interaktoren anschließend durch Affinitätsproteomik mittels LC-MS/MS identifiziert. Eine umfangreiche bioinformatische Analyse ergab mehr als 300 hoch-spezifische Interaktoren (*high confidence interactors*, HCI). Die meisten HCI sind nuklearer Herkunft, an der Regulierung der Transkription oder von Chromatinprozessen beteiligt und erfordern die intakte p65-Dimerisierung, aber keine DNA-Bindung. Ein siRNA-Screening der top 38 HCIs zeigte eine regulatorische Rolle von TFE3, TFEB und GLIS2 bei der induzierbaren Expression von drei prototypischen IL-1α-regulierten NF-κB-Zielgenen auf. TFE3 und TFEB gelten als *Master*-Transkriptionsfaktoren, welche die Expression von lysosomalen CLEAR-Genen (*coordinated lysosomal expression and regulation*) regulieren, während GLIS2 ein Mitglied der Krüppel-ähnlichen Zinkfingerprotein-Unterfamilie ist. Prototypische CLEAR-Gene wurden unabhängig von p65 exprimiert. Dagegen ergab die transkriptomweite Analyse von p65-, TFE3-, TFEB-, TFE3/TFEB- oder GLIS2-defizienten Zellen 44 IL-1α-regulierte Gene, welche p65, TFE3 und TFEB für ihre Expression benötigen, und 83 Gene, die kooperativ durch p65 und GLIS2 reguliert werden. Darüber hinaus waren mehr als zwei Drittel der p65/RELA-Motive, welche unter p65-ChIP-seq-Peaks gefunden wurden, eng mit TFE3- und GLIS2-Motiven assoziiert. Aus diesen Daten abgeleitete Proteininteraktionskarten zeigten ein neuartiges genetisches p65-TFE3-TFEB-Netzwerk, das mit multiplen Komponenten von Interleukin-Signalwegen angereichert ist, sowie ein TNF-zentriertes Subnetzwerk, das durch p65 und GLIS2 reguliert wird. Zusammenfassend zeigte die kombinierte Analyse ausgewählter NF-κB-p65-Interaktoren auf der Ebene von *loss-of-function* Screens, genomweiter mRNA-Expression und Chromatin-Rekrutierung einen mehrstufigen *Crosstalk* von lysosomalen und NF-κB Signalwegen sowie neue Einblicke in kritische Funktionen von GLIS2 mit Auswirkungen auf Komponenten beider Signalachsen.

1 Introduction

1.1 The immune response in human

The immune system protects humans and other mammals from a plethora of pathogens or irritants by recognizing and eliminating them through different mechanisms. Host defense mechanisms are divided into two domains, the innate and adaptive parts of the immune system. As the innate immune response is non-specific and immediately effective, it represents the host's first line of defense. The innate immune response is the evolutionarily conserved part of the immune system and thereby capable of recognizing molecular patterns exposed by many microbes and toxins. The rapid innate immunity is predominantly mediated by tissue-resident macrophages, dendritic cells (DCs), and circulating neutrophil granulocytes [1, 2]. Epithelial cells, e.g., of the lung or intestine, also contribute to the innate immune response by forming an effective first barrier against microbes, but also by producing a large number of immunoregulatory mediators [3, 4]. Adaptive immunity, on the other hand, is highly specific but has a delayed onset. The adaptive immune response is mediated by T- and B-lymphocytes and represents the acquired part of the immune system. It relies on gene elements that rearrange somatically to form antigen-binding molecules that enable recognition of unique foreign structures. After initial contact with an antigen, long-lived memory cells remain in the host for several decades and trigger an effective immune response upon renewed contact with the pathogen or irritant [1, 2].

The process by which the immune system responds to infection or tissue injury is called inflammation. Inflammatory inducers can be of exogenous (pathogenic bacteria, viruses, toxins, allergens) or endogenous (tissue signals released by dead, damaged or stressed cells) nature. At the molecular level, these inducers carry pathogen-associated molecular patterns (PAMPs) or damage-associated molecular patterns (DAMPs) on their surface, which are recognized by pattern recognition receptors (PRRs) such as membrane-associated Toll-like receptors (TLRs) expressed by macrophages or DCs [5–7]. During inflammation, local tissue cells, resident macrophages, and DCs release chemokines to attract circulating leukocytes to the site of infection by chemotaxis and diapedesis. Macrophages and DCs also contribute to antigen clearance by phagocytosis and serve as antigen-presenting cells for T- or B-lymphocytes after leukocyte infiltration. The recruited leukocytes themselves express cytokines that further mediate inflammation. In the acute phase of inflammation, abundant neutrophil granulocytes are the most prominent cells as they destroy their antigen by releasing reactive oxygen species or granules containing lysozyme, matrix metalloproteinases, and myeloperoxidase. The adaptive immunity becomes more important in the late phase of inflammation, when infiltrated T- and B-lymphocytes mediate complex defense mechanisms, including secretion of cytokines, costimulation of lymphocytes, and production of antibodies and immune complexes. In addition to lymphocytes, circulating thrombocytes also participate in inflammation by aggregating and forming thrombi or releasing chemokines and other inflammatory mediators [8].

1.2 Cytokines as mediators of the immune response

The complex mechanisms underlying innate and adaptive immune responses are largely conveyed by small mediator proteins named cytokines. Cytokines comprise subgroups of interleukins (IL), tumor necrosis factors (TNF), chemokines, interferons (IFN), colony-stimulating factors (CSF), and transforming growth factors (TGF). Their functions are diverse and range from activating intracellular signaling cascades, chemotactic effects, and stimulating leukocyte migration to supporting viral defense or mediating proliferation and functional maturation of immune cells [9–13]. Besides immune cells, many other body cells, including endothelial cells, fibroblasts, epithelial cells and various stromal cells are capable of secreting cytokines. Released cytokines act through their respective receptors on a variety of target cell types or on the same cell from which they were released. This leads to a local signal amplification that is required for the effective inflammatory response [14, 15]. Two classes of cytokines usually act in concert to activate, coordinate, and terminate this response. While pro-inflammatory cytokines such as IL-1β, IL-1α, TNF-α, IL-6, and IL-8 promote inflammation, anti-inflammatory cytokines such as IL-10, TGF-β, and IL-4 counteract this activation [16]. In the producing cell, cytokine expression is tightly controlled at the levels of cellular signaling, post-translational modifications, transcription factor binding, and feedback loops, as well as mRNA stability and secretion [13]. Numerous inflammatory diseases such as rheumatoid arthritis (RA), Crohn's disease, and atherosclerosis are characterized by unbalanced levels of pro- and anti-inflammatory cytokines [17–19]. Although many antibody-based and small-molecule drugs targeting cytokines or their receptors are now significantly improving patients' lives, they generally do not yet result in complete remission. A comprehensive understanding of the molecular mechanism underlying inflammatory cytokine secretion, signaling, and gene expression is therefore an essential requirement for the development of curative therapeutic strategies in the future [20].

1.3 The pro-inflammatory cytokine interleukin-1α

Interleukin-1α (IL-1α) is a key pro-inflammatory cytokine primarily engaged in innate immunity and inflammation. The cytokine belongs to the IL-1 family of proteins, which consists of 11 members with pro-inflammatory and anti-inflammatory functions. Members of the IL-1 family are expressed by epithelial, endothelial, platelet, fibroblast, and immune cells (e.g., macrophages and neutrophil granulocytes) and are found as precursors in the cytoplasmic compartment. An exception is the IL-1 receptor antagonist (IL-1Ra), which has a signal peptide sequence that causes its continuous secretion into the extracellular milieu. IL-1β, the best studied member, is secreted in its bioactive form after processing by the inflammasome, whereas IL-1α is released as a bioactive mediator in response to necrotic cell death [21–23].

All members of the IL-1 family bind to IL-1 receptors (IL-1R). The IL-1R family includes 10 receptors, designated by the numbers 1 through 10 [24]. IL-1R-mediated intracellular signal transduction strongly resembles that of TLRs, as receptors of both families contain a cytoplasmic Toll interleukin-1 receptor

(TIR) domain. IL-1α, IL-1β, and IL-1Ra bind to the IL-1 receptor type 1 (IL-1R1). Receptor binding of IL-1α or IL-1β allows association of IL-1R3 (formerly called IL-1R accessory protein, IL-1RAcP) and formation of a trimeric complex. As a result, conformational changes occur that lead to dimerization between the two TIR domains in the cytoplasm. Dimerization creates docking sites for multiple adaptor proteins and protein kinases, leading to activation of signaling cascades and ultimately to activation of transcription factors that belong to the Nuclear Factor binding near the kappa light chain in B cells (NF-κB) and Activator protein 1 (AP-1) families [22, 25]. Unlike IL-1α or IL-1β, receptor binding of IL-1Ra does not lead to a conformational change and prevents inflammatory signal transduction. Anakinra, the recombinant form of this anti-inflammatory cytokine, is therefore used to treat a broad spectrum of inflammatory diseases, including RA and cardiovascular diseases [21, 26, 27].

1.4 The IL-1α-NF-κB signaling pathway

IL-1α-induced cytoplasmic signal transduction is characterized by rapid assembly of adaptor proteins that form an initial signaling module at the receptor (Figure 1). These proteins are Myeloid differentiation primary response 88 (MyD88), IL-1 Receptor-associated kinases (IRAKs) 1/2/3/4, and TNF associated factor 6 (TRAF6). (Auto-) phosphorylation of IRAK4 leads to phosphorylation of IRAK1 and IRAK2 and subsequently to recruitment and oligomerization of TRAF6. The E3 ubiquitin ligase TRAF6, together with the E2 ligase complex and E3 ubiquitin ligases PELI1/2 attach K63-linked poly-ubiquitin chains to TGF-β-activated protein kinase binding proteins (TAB) 2/3. Both are components of the two TGF-β-activated protein kinase 1 (TAK1) kinase complexes TAB1-TAK1-TAB2 and TAB1-TAK1-TAB3. After conformational changes, TAK1 (also known as MAP3K7) is activated and phosphorylates mitogen-activated protein kinase kinases (MAPK kinases). MAPK kinases eventually initiate activation of c-Jun N-terminal kinase (JNK), p38 MAPK, and the canonical NF-κB pathway [28–30].

In the canonical NF-κB pathway, TAK1 activation leads to phosphorylation and K63-linked poly-ubiquitination of the IκB kinase complex (IKK) (Figure 1). The IKK complex consists of a trimer comprising the catalytic subunits IKKα and IKKβ and the regulatory subunit NF-κB essential modulator NEMO (also named IKKγ). In turn, this complex phosphorylates inhibitory proteins of the IκB family, of which IκBα is the prototypical family member. Phosphorylation of IκB proteins initiates their poly-ubiquitination and proteasomal degradation. As a consequence, NF-κB dimers trapped in the cytosol are released and migrate to the nucleus. While IKKα plays only a supportive role, IKKβ and NEMO are essential subunits for phosphorylation-dependent proteasomal degradation of IκBα [31–33].

In resting cells, inhibitory proteins of the IκB family are responsible for the retention of the transcription factor NF-κB in the cytoplasm. These proteins include IκBα, IκBβ, IκBε, BCL-3, IκBz, IκBNS, and the C-terminal domains of the precursor proteins p105 (IκBγ) and p100 (IκBδ). All family members contain multiple ankyrin repeat domains (AnkRs) that form helices that allow them to associate with NF-κB transcription factor dimers. IκBα binding of the canonical NF-κB transcription factor dimer p50/p65 covers the nuclear localization sequence (NLS) of subunit p65, but not p50 [34, 35].

Under stimulatory conditions, as activation of the IL-1 receptor complex by IL-1α, phosphorylation of IκBα by the IKK complex promotes its recognition by an E3 ligase complex that mediates its K48-linked poly-ubiquitination and subsequent degradation by the proteasome (Figure 1). NF-κB dimers are thereby liberated and translocate to the nucleus, where they bind several hundred target genes by recognizing specific DNA sequences termed κB sites found in the promoter regions of genes encoding a variety of inflammatory mediators, including chemokines, inhibitory proteins, and proteins contributing in the regulation of inflammatory mRNA stability [36, 37].

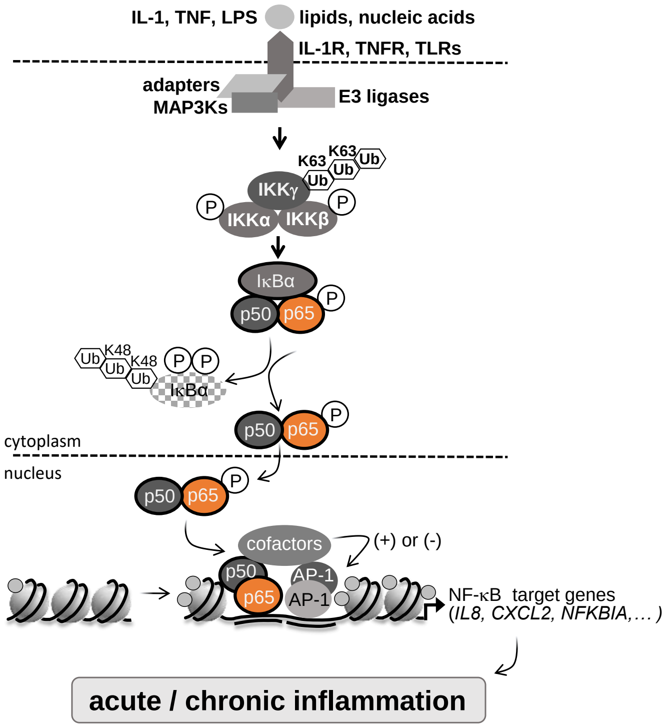

Figure 1: Levels of canonical NF-κB activation in acute and chronic inflammation.
Schematic illustrating the major signaling components of the NF-κB pathway. IL-1α and other triggers promote the rapid assembly of an initial signaling platform of adaptor proteins, MAP3Ks, and E3 ubiquitin ligases. This in turn activates the trimeric IKK complex, leading to rapid phosphorylation and ubiquitin-dependent degradation of the cytosolic inhibitor protein IκBα. This releases the canonical NF-κB transcription factor heterodimer of p50/p65, which associates with specific DNA elements within accessible chromatin after their nuclear translocation. This often occurs together with AP-1 transcription factors and other cofactors. NF-κB target genes include secreted cytokines (*CXCL8, CXCL2*) but also inhibitory proteins (*NFKBIA*) that regulate NF-κB activity via negative feedback loops. (The schematic was adapted from [38, 39].)

1.5 The NF-κB family of transcription factors

The transcription factor NF-κB, discovered more than 35 years ago, has emerged as a master regulator of genes controlling inflammation, cell cycle, and apoptosis. Activation of NF-κB has become a hallmark of inflammation and cancer and therefore a potential therapeutic target for several related diseases [40, 41]. The ubiquitously expressed transcription factor consists of several subunits belonging to the Rel protein family based on a common Rel homology domain (RHD). The Rel family includes five members: p65, RelB, c-Rel, p50, and p52, encoded by *RELA*, *RELB*, *REL*, *NFKB1*, and *NFKB2*, respectively [34, 42] (Figure 2). Homo- and heterodimerization between Rel family members results in the formation of at least 13 NF-κB dimer complexes. The paradigmatic NF-κB dimers are heterodimers of p50/p65 and p52/RelB [35]. The p50/p65 dimer is a target of the canonical NF-κB pathway, whereas the p52/RelB dimer is activated in response to the alternative pathway. Different receptors and IKK subunits shape signal transduction in both pathways [32]. While the canonical NF-κB pathway is rapidly induced by many cytokine receptors, PRRs, as well as T-cell receptors and B-cell receptors, signal transduction via the alternative pathway exhibits slower sustained kinetics and is triggered only by a select group of TNF receptors [33, 41]. Canonical NF-κB dimers exert broad functions in all types of immune responses, whereas the alternative NF-κB pathway may have evolved to play a supplementary role to canonical signaling, especially in the adaptive immune system [33].

The N-terminal region of NF-κB subunits contains the RHD, which is critical for DNA binding, dimerization, and assembly of inhibitory proteins [33, 34] (Figure 2). The N-terminal portion of the RHD mediates specific DNA binding to the NF-κB consensus sequence, termed κB, found in promoters and enhancers of NF-κB target genes, while the C-terminal portion of the RHD is required for dimerization and interaction with IκBs [35, 43]. The C-terminus of the NF-κB subunits p65, RelB, and c-Rel contains a strong transcriptional activation domain (TAD). The NF-κB subunits p50 and p52 lack this domain because they are formed by posttranslational cleavage of the N-terminal domains of the precursor proteins p105 and p100 [35]. NF-κB dimers thus activate the expression of their target genes but are also repressive when they lack the TADs. An important regulatory mechanism involves the selective binding of different NF-κB dimers to their κB target sequences (5′ GGGPuNNPyPyCC-3′), which can slightly differ in their base sequence [43]. In addition, various posttranslational modifications (PTMs) such as phosphorylation, ubiquitination, and acetylation control NF-κB activity and enable communication with other cellular signaling networks [43–45].

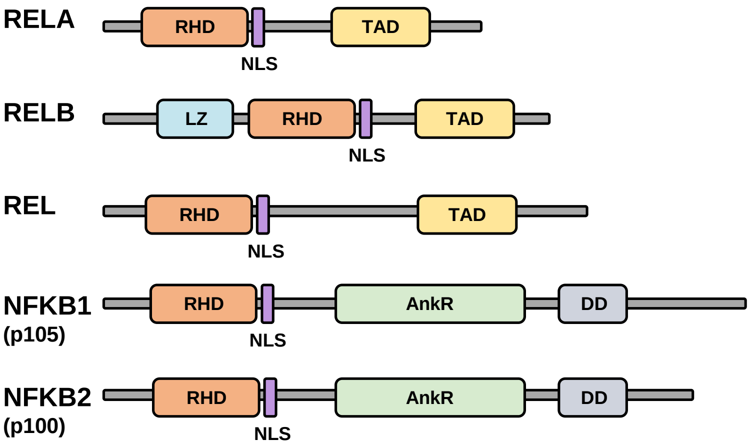

Figure 2: The domain structures of members of the NF-κB family.
The Rel homology domain (RHD) is characteristic of all five members of the NF-κB family. The NF-κB subunits p50 and p52 are the result of N-terminal cleavage of the precursor proteins p105 and p100. Domains that typify

each protein include the RHD, the nuclear localization sequence (NLS), the leucine zipper domain (LZ), the transactivation domain (TAD), the tandem ankyrin repeat domain (AnkR), and the death domain (DD). (The schematic was adapted from [35].)

NF-κB regulates the expression of several inflammatory genes encoding cytokines, chemokines, immune receptors, and cell adhesion molecules. NF-κB-regulated expression of these genes is also tightly regulated at many levels other than PTMs. The resynthesis of IκBα after induced degradation represents another important control mechanism, as this autoregulatory feedback loop is essential for shutting down NF-κB-dependent gene expression [46]. NF-κB p65 itself was reported to be regulated by intranuclear sequestration and subsequent proteasomal degradation in a PDLIM2-dependent fashion [47]. Recently, our research group demonstrated that the noncoding genome is involved in IL-1α-induced spatiotemporal reorganization of NF-κB target regions by mediating DNA interactions, histone acetylation, and coactivator recruitment [48, 49]. Another study demonstrated how a proximal long noncoding RNA (lncRNA), named UMLILO, facilitated epigenetic priming across several chemokine promoters [50]. Further investigations revealed that TADs enable the interaction of NF-κB with factors of the transcription machinery, including TATA-binding protein (TBP), general transcription factor IIB (TFIIB) [51], and coactivator p300 [52]. In addition, NF-κB-mediated transcription is assisted by other transcription factors, including members of the STAT and AP-1 (signal transducer and activator of transcription) families, as well as IRFs (interferon regulatory factors) and coactivators [41]. However, the full scope of this (co)regulatory NF-κB network has yet to be explored. In this regard, the C-terminal region of the NF-κB subunit p65, which according to the structure revealed by alphafold is largely unstructured, could serve as a higly flexible platform for many more protein-protein interactions (PPIs) than previously assumed [53].

1.6 Lysosomes

Since Christian De Duve's discovery in 1955, the lysosome has been recognized as a cellular degradation and catabolic organelle [54]. This organelle comprises more than 120 integral and peripheral membrane proteins, including transporters, ion channels, and over 60 soluble acid hydrolases such as glycosidases, proteases, lipases, nucleases, phosphatases, and sulfatases [55–59]. These enzymes act together in the lysosomal lumen to breakdown major macromolecules, including lipids, proteins, carbohydrates and nucleic acids [60]. The transportation of extracellular and intracellular macromolecules to lysosomes for degradation occurs through endocytosis and autophagy. Lysosomes also participate in secretion through a process called lysosomal exocytosis [61]. Lysosomal dysfunction, resulting from mutations in genes encoding lysosomal proteins, is the cause for more than 50 lysosomal storage disorders (LSDs) described thus far [56, 62]. The longstanding and preconceived notion that lysosomes are merely a cellular recycling system has been drastically overturned by their functional characterization. Nowadays, lysosomes are known to be multifaceted signaling hubs that interact with different cell organelles (e.g., the ER and mitochondria) and are involved in a variety of other cellular processes, including nutrient sensing, gene regulation, immune responses, plasma membrane repair, and tumorgenesis [56, 60, 63].

1.7 Nutrient sensing and calcium signaling at the lysosome

A key function of the lysosome is to process nutrient information to maintain cellular energy homeostasis. This is mediated by the mTOR kinase as part of the mammalian target of rapamycin complex 1 (mTORC1) complex. When nutrients are available, mTORC1 drives anabolic processes such as protein and lipid synthesis and promotes cell growth. During nutrient deficiency, it inhibits the cell's catabolic processes such as autophagy through phosphorylation of Unc-51-like kinase 1 (ULK1), an enzyme that is important in the early stages of autophagosome biogenesis [64–66]. A cruicial step in the activation of mTORC1 is its recruitment to the outer lysosomal surface. This process involves the amino acid-dependent activation of heterodimeric Rag GTPases and their interaction with multiprotein complex Ragulator [60, 67]. Ragulator exerts guanine nucleotide exchange activity towards the Rag GTPases in an amino acid- and v-ATPase-dependent manner [68]. In addition to guanine nucleotide exchange factors (GEFs), GTPase-activating proteins (GAPs) like folliculin (FLCN) likewise tether Rags to the lysosomal surface [69, 70]. Rag GTPases, in turn, recruit mTORC1 but also other nutrient-dependent proteins to the lysosome, including the mTORC1 regulatory complexes tuberous sclerosis complex (TSC) and FLCN-folliculin-interacting protein 1 (FNIP1), but also transcription factor EB (TFEB), the transcriptional master regulator of lysosome biogenesis and autophagy [60, 71].

Lysosomes play another critical role in maintaining global Ca^{2+} homeostasis as they are important intracellular calcium storage organelles. The release of Ca^{2+} is essential for numerous cellular processes, including the fusion of lysosomes with endosomes, autophagosomes, or the plasma membrane. Additionally, it mediates the formation of contact sites with the endoplasmic reticulum (ER), which in turn promotes Ca^{2+} influx into the lysosome. The v-ATPase utilizes ATP energy to enable Ca^{2+} replenishment of lysosomes through the H^+/Ca^{2+} exchanger. This influences the pH and thus the activity of hydrolases in the lysosome lumen [60, 72, 73]. The proteins of the two-pore channel (TPC) and the mucolipin family of transient receptor potential (TRPML) channels are involved in the lysosomal release of calcium. The most prominent lysosomal Ca^{2+} channel is TRPML1, also known as mucolipin 1 (MCOLN1). Mutations in this gene cause mucolipidosis type IV (MLIV) an autosomal recessive neurodegenerative disease [74, 75]. The proper release of lysosomal calcium through TRPML1 is essential for the activation of mTORC1 [76]. Activation of TRPML1-mediated Ca^{2+} release can be triggered by several factors, such as starvation, reactive oxygen species, or the phosphoinositide, phosphatidylinositol 3,5-bisphosphate (PtdIns(3,5)P2). Furthermore, TRPML1 regulates TFEB phosphorylation and cellular distribution, whereas, in turn, TFEB regulates the expression of *MCOLN1*, the gene encoding TRPML1 [60, 77].

1.8 Lysosomal adaptation and the CLEAR gene network

Lysosomal biogenesis and degradation were long considered an unglamorous housekeeping function of the cell. It is now known that cells adjust the number and activity of lysosomes in response to various forms of cellular stress, such as starvation, ER stress, mitochondrial stress, or pathogenic infections, through transcriptional regulation [78] (Figure 3). The first observation that lysosomal genes were regulated was made after mammalian fibroblasts were challenged with high levels of sucrose to study the effects of sucrose-induced vacuolation [79]. Then, pioneering findings by the Ballabio group showed coordinated transcriptional activation of a wide array of lysosomal genes, including several subunits of v-ATPase, lysosomal transmembrane proteins, and lysosomal hydrolases, following overexpression of TFEB, which was accompanied by enhanced lysosome degradation activity [80]. In addition, a promoter analysis they conducted identified a 10-base pair motif (GTCACGTGAC) located within 200 bp of the transcription initiation site of lysosomal genes [80]. This motif harbors an E-box sequence (CACGTG) that is recognized by the MiT/TFE factors. They named this motif coordinated lysosomal expression and regulation (CLEAR) element [78, 81]. Genome-wide chromatin immunoprecipitation sequencing (ChIP-seq) analysis revealed enrichment of lysosomal genes and direct binding of TFEB to CLEAR elements, thus leading Ballabio's group to define the CLEAR network of direct TFEB target genes [82]. The combination of these ChIP-seq data with microarray also indicated the involvement of TFEB in the expression of genes related to autophagy. Macro-autophagy (here referred to as autophagy) is a self-degradation process that is important for maintaining energy homeostasis of cells at various stages of development or during nutrient stress. During this process, misfolded or aggregated proteins and damaged organelles such as mitochondria, peroxisomes, or the ER, as well as intracellular pathogens, are engulfed by the autophagosome, an intermediate double-membrane vesicle. After fusion with the lysosome to form the autolysosome, these large structures are enzymatically degraded by the lysosome [83]. Another study by the Ballabio group demonstrated the ability of TFEB to coregulate and coordinate both, autophagy and lysosomal biogenesis, which are two major cellular degradation processes [84]. Additional research indicated the involvement of TFEB in mitophagy, lipophagy, endocytosis, and lysosomal exocytosis [81]. A more recent study showed that transcription factor E3 (TFE3) likewise binds CLEAR elements and regulates the expression of lysosomal and autophagy genes and demonstrated that its ability to increase the number of lysosomes was independent of the presence of TFEB [85]. Together, TFE3 and TFEB emerged as master regulators that coordinate lysosomal biogenesis and autophagy in response to many different environmental cues [78].

1.9 Activation of TFE3 and TFEB in response to cellular stress

The activation state of TFE3 and TFEB is mainly controlled by posttranslational modifications at several amino acid residues that affect their subcellular localization in response to cellular stress. In this context, several upstream kinases and phosphatases have been identified, including mTORC1, MAPK1, ERK, Akt, PKB, PKC, GSK3β, and MAP4K3. Inhibition of these kinases promotes activation of TFEB under stimulated conditions. In contrast, the phosphatases calcineurin and PP2A dephosphorylate TFEB, thereby activating the transcription factor under stimulated conditions [56, 81].

Important phosphorylation sites under nutrient deprivation are serine 211 (S211), serine 122 (S122), and serine 142 (S142) of TFEB and serine 321 (S321) of TFE3 [78, 81]. When cells are fully fed and amino acid levels are high, the GEF, Ragulator, alters the nucleotide status of heteromeric Rag GTPases at the lysosome, causing Rags to interact with TFE3 and TFEB and promote their recruitment to the lysosomal surface [85, 86]. At the lysosome, activated mTORC1 phosphorylates TFE3/TFEB at multiple residues, with phosphorylation sites S211 of TFEB and S321 of TFE3 serving as binding sites for chaperone 14-3-3. Interaction with 14-3-3 leads to sequestration of transcription factors in the cytosol [78, 85, 87–89] (Figure 3). Conversely, under starvation conditions, Rag heterodimers undergo nucleotide changes leading to the release of mTORC1 and TFE3/TFEB, resulting in a decrease in mTORC1-mediated phosphorylation and 14-3-3 binding [85, 86]. In parallel, MCOLN1-mediated Ca^{2+} release at the lysosome activates calcineurin phosphatase, leading to dephosphorylation and nuclear translocation of TFEB under starvation conditions [77, 78].

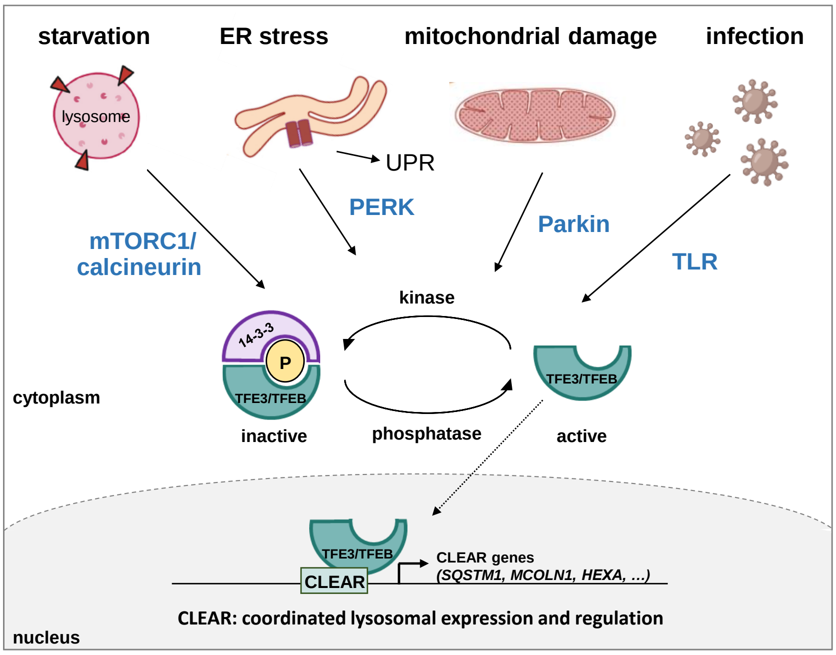

Figure 3: Activation of TFE3 and TFEB in response to different cellular stresses.
Various cellular stress pathways lead to the activation of TFE3 and TFEB. Under physiological conditions, mTORC1 phosphorylates TFE3 and TFEB at the lysosomal surface. This promotes the association of chaperone 14-3-3 and their sequestration in the cytosol. Starvation leads to inactivation of mTORC1 and concomitant activation of the phosphatase calcineurin. As a result, TFE3 and TFEB are dephosphorylated and translocate to the nucleus. TFE3/TFEB activation is also observed in response to ER stress (mediated by the kinase PERK), mitochondrial damage (via Parkin), and pathogen infection (via TLR signaling). (The schematic was adapted from [78].)

To date, several mTORC1-independent or partially independent mechanisms have been identified for the activation of TFE3 and TFEB following different cellular stress conditions (Figure 3). First, ER stress, characterized by the accumulation of misfolded proteins in the ER lumen, activates the unfolded protein response (UPR) and thus the kinase PERK, a key mediator of the UPR, which has been shown to transmit the ER stress-induced translocation of TFE3 [90]. Second, chemical induction of mitophagy, the process by which damaged mitochondria are degraded by autophagy, causes Parkin-dependent translocation of TFE3 and TFEB to the nucleus [91]. Third, treatment with lipopolysaccharide (LPS, TLR4 ligand) induces translocation of TFE3 and TFEB in an mTORC1-independent fashion [92, 93]. Nuclear migration of TFE3 and/or TFEB induced by ER stress, mitophagy, or LPS is (partially) independent of mTORC1 and could be attributed, although not solely, to phosphorylation changes of serine residues of TFE3 (S321) or TFEB (S211/S142), which also occur after nutrient deprivation [78, 81, 90–92].

1.10 The family of MiT/TFE transcription factors

TFE3 and TFEB, together with microphthalmia-associated transcriptionfactor (MITF) and transcription factor EC (TFEC) comprise the microphthalmia/transcription factor E (MiT/TFE) subfamily of basic helix-loop-helix-leucine zipper (bHLH-zip) transcription factors [94]. MITF, the first member of the MiT/TFE family, was cloned in 1993, and mutations in this gene were found to cause various defects in mice, particularly loss of eye pigmentation, decreased eye size, failure of secondary bone resorption, and decreased numbers of mast cells [95, 96]. MITF is a transcription factor specific to the melanocytic lineage that regulates melanocyte differentiation, proliferation, and pigment-specific transcription, thus making it a known driver of malignant melanoma [97]. All members of the MiT/TFE family are conserved in vertebrates and share common structural features (Figure 4). MiT/TFE proteins share a basic helix-loop-helix-leucine zipper domain (bHLH-LZ) that is important for PPIs and required for homo- and heterodimerization, which in turn is necessary for DNA recognition and transcriptional activation. They have an identical basic region required for DNA binding and an activation domain (AD) for transcription activation [63, 81, 94, 98]. Unlike other bHLH-zip proteins, MiT/TFE proteins form heterodimers exclusively with other members of the MiT/TFE subfamily, but not with any other bHLH-zip protein [94]. Moreover, MiT/TFE family members recognize the palindromic, canonical E-box motif CACGTG but also the M-box sequence TCATGTG that other bHLH-zip transcription factors do not recognize [81, 94, 99]. While the bHLH-LZ domain is largely conserved among all members of the MiT/TFE family, the regulatory regions outside the domain differ widely [96]. TFEC, the most divergent member, was originally assumed to lack the activation domain and to repress transcription in complex with TFE3 [100]. However, recent studies suggest that TFEC also functions as a transcriptional activator, and alignment of the amino acid sequences of human MiT/TFE family members suggests that TFEC does indeed possess the activation domain [96].

The expression patterns of MiT/TFE members vary widely across different cell types. MITF is mainly expressed in melanocytes, osteoclasts, mast cells, macrophages, natural killer (NK) cells, B-cells, and the heart. TFEC expression is strongly restricted to myeloid cells, especially macrophages and its physiological function has not been well studied [96]. TFE3 and TFEB are most broadly expressed across cell types [81]. TFE3 and TFEB share common features in terms of their domain structure, phosphorylation-dependent activation, and redundant binding to gene promoters (see above). A series of studies in mice with mutations in the TFE3 and TFEB gene locus reveal redundant roles in T-cell activation and function [81, 101] and cooperative behavior in the regulation of energy homeostasis, particularly glucose and lipid metabolism in the liver [102]. Various tissue-specific loss-of-function experiments show that TFEB is involved in cellular functions, including mitochondrial biogenesis in muscle and adipose tissue, DC function, myelination of glia cells, and intestinal epithelial barrier restoration [60]. Mice systemically lacking TFEB are embryonic-lethal [103], whereas TFE3 knockout mice are viable and do not exhibit a visible phenotype [81]. TFE3 knockout mice show that TFE3 plays an important role in osteoclast differentiation [104], embryonic stem cell (ESC) differentiation [105], and degranulation of mast cells [81, 106]. Although many individual and overlapping physiological functions of transcription factor TFE3 and TFEB have been uncovered, less is known about the genetic landscape regulated by each factor under different conditions of cellular stress or homeostasis and whether this genetic control is cooperative, complementary, or redundant.

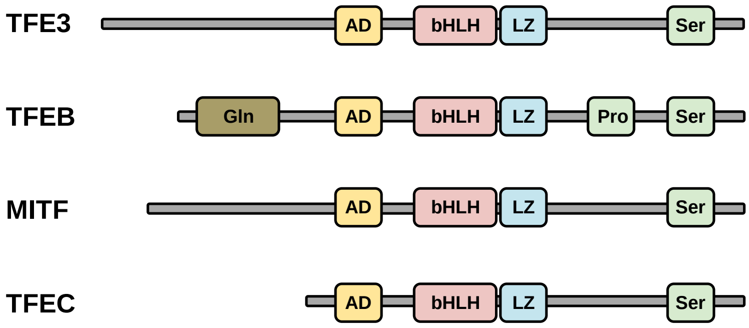

Figure 4: The protein domain structures of MiT/TFE family members.
In mammals, all four members of the MiT/TFE family share a basic helix-loop-helix and leucine zipper domain (bHLH-LZ) that is required for dimerization and DNA binding. They have an activation domain (or acidic domain, AD) for transcriptional activation and a serine-rich region (Ser) at their C-terminus. TFEB has additional glutamine-rich (Gln) and proline-rich (Pro) domains. (The schematic was adapted from [81, 96].)

1.11 Emerging roles of TFE3 and TFEB in the immune system

In recent years, emphasis has also been placed on investigating the role of TFE3 and TFEB in the immune defense, mainly owing to their function as master regulators of lysosome biogenesis and autophagy [107]. So far, the majority of evidence linking TFE3 and TFEB to the immune system is based on the multifaceted role of the lysosome-autophagy system in innate and adaptive immune functions. In innate immunity, the lysosome-autophagy system is activated by pathogens in macrophages and other immune cells, responds to PRRs, and engulfs and clears intracellular pathogens directly. In addition, the system controls the immune response by eliminating active inflammasomes and promotes NKT cell activation, cytokine secretion, and phagocytosis [81, 108–111]. In adaptive immunity, autophagy is involved in antigen processing and presentation and influences T-cell differentiation and homeostasis, the development and survival of B-cells, as well as plasma cell survival. In addition, pathogen infection activates many cellular stress signaling pathways, including the ER stress-triggered UPR, which leads to activation of TFE3 and TFEB [81, 111–113]. Only recently, two studies indicated a direct role of TFE3 and TFEB at the transcriptional level. In one study, the MiT/TFE ortholog, HLH-30, was shown to increase survival of the worm *Caenorhabditis elegans* following bacterial infection with *Staphylococcus aureus*. This was attributed to the upregulation of cytoprotective and antimicrobial genes by HLH-30 [114]. A more recent study demonstrated that TFE3 and TFEB control transcription of several immune mediators (e.g., *Il1b*, *Il6*, *Tnf*, *Ccl5*) in mouse RAW cells and bone-marrow-derived macrophages (BMDMs) after they were treated with LPS [92]. It was then shown that LPS-induced TFEB activation is dependent on Activator of G-protein signaling 3 (AGS3) [115]. However, it remained unclear whether this was dependent on the mTORC1 pathway or independent, as both studies came to opposite conclusions. In addition, TFEB exerts a direct or indirect function in the interferon-independent activation of interferon-stimulated gene (ISG) expression, which is essential for the host response to viral infection [116, 117]. Finally, there is also evidence for an indirect interplay with the NF-κB system, as NF-κB regulates the expression of some autophagy regulators (*BCL2*, *BECN1*, *BNIP3*, and *SQSTM1*), leading to enhanced or suppressed autophagy [118]. Furthermore, NF-κB is activated via TLR signaling that occurs at the endolysosome. Endocytosis is an entry site for pathogens and microbial nucleic acids can be recognized by three TLR receptors (TLR3, TLR7/8, and TLR9), which transmit these signals from the endolysosomal lumen to the cytosol to then activate NF-κB or interferon regulatory factors (IRFs) that in turn stimulate the production of inflammatory cytokines and/or interferons [60]. The understanding of the interplay between the NF-κB system and the lysosomal transcription factor system is still limited and further research needs to be done to comprehensively uncover how these systems communicate or modulate each other.

1.12 GLI-similar zinc finger protein GLIS2

GLIS2, together with GLIS3 and GLIS1, form a subfamily of Krüppel-like zinc finger proteins. All three proteins play key roles in embryonic development and other physiological processes. Mutations in the human GLIS3 gene are associated with neonatal diabetes and congenital hypothyroidism (also called NDH syndrome) [119, 120]. GLIS1 downregulation by siRNA in 4-cell bovine embryos caused defective embryonal development after the 16-cell stage [121]. GLIS1-3 are differentially involved in the reprogramming of somatic cells into induced pluripotent stem cells [122]. GLIS2 is perhaps most recognized for its importance in maintaining normal renal functions, as it is expressed at high levels in adult kidneys and plays a role in various human kidney diseases [123, 124]. By recruiting different groups of coactivators and corepressors, GLIS proteins can activate and repress the transcription of genes. While GLIS3 and GLIS1 mainly activate transcription, GLIS2 activates and represses transcription [119, 123, 125, 126]. GLIS2 interacts with C-terminal binding protein 1 (CtBP1) and repression by GLIS2 is likely based on the recruitment of CtBP1 and histone deacetylase 3 (HDAC3), which together form an transcriptional silencing complex [127]. GLIS2 has been shown to be an essential component of the Hedgehog signaling pathway, which is critical for embryonic kidney development by repressing the expression of several genes, including *GLI1*, *SNAI1*, and *WNT4* [128]. GLIS2 encodes a 55.8-kDa protein that, like GLIS3 and GLIS1, has a DNA binding domain (DBD) consisting of five tandem Cys(2)-His(2) zinc finger motifs [123] (Figure 5). GLIS proteins bind to guanine-rich DNA elements called GLIS binding sites (GLISBS) in the regulatory region of their target genes [119]. In addition, GLIS proteins might form homo- or heterodimers with different members of Krüppel-like zinc finger transcription factor subfamilies, as such mutual interactions have been reported for members of the ZIC and GLI subfamilies [129]. GLIS2 interacts with β-catenin and p120 catenin, both of which are involved in transcriptional regulation and cell adhesion [130]. GLIS2 also interacts with several E3 ubiquitin ligases and E3 SUMO ligases that alter its ubiquitination and sumoylation state, thereby affecting GLIS2 half-life, activity, and function [119]. Loss of GLIS2 function leads to a cystic kidney disease called nephronophthisis, which is characterized by cyst formation, renal atrophy, inflammation, and fibrosis [131]. Gene expression analysis showed that kidneys from GLIS2-deficient mice have increased expression of several genes associated with inflammation, fibrosis, and apoptosis [124, 131]. Apart from the structural knowledge and functions of GLIS2 mentioned above, the role that GLIS2 fulfills in many physiological systems, such as the immune system, is still unexplored.

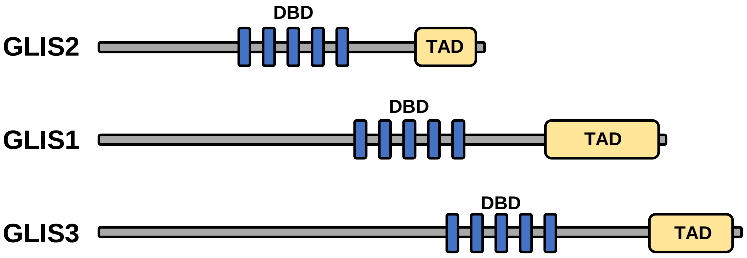

Figure 5: The domain structures of GLI-similar zinc finger proteins.
All members of the human Krüppel-like zinc finger transcription factor subfamily, consisting of GLIS1-3, possess a characteristic DNA binding domain (DBD) that encompasses five tandem Cys(2)-His(2) zinc finger motifs plus a transactivation domain (TAD) at their C-terminus. (The schematic was adapted from [119].)

1.13 Purification strategies for locus-specific interactome analysis

In recent years, the development of approaches combining CRISPR-Cas9 and proximity labeling with mass spectrometry (MS) has massively revolutionized the capabilities of protein interactome analysis across various species [132, 133]. Some of these new methods enable to capture the entire proteome that accumulates at a given chromatin locus and is thereby shaping its molecular function. These approaches use a catalytically inactive form of Cas9 (dCas9) that is affinity-tagged and can be directed to the locus of interest by a specific 20-nucleotide guide RNA [134]. The first reported method using the CRISPR system for locus-specific purification was engineered DNA binding molecule-mediated chromatin immunoprecipitation (enChIP) using antibodies directed against the 3xFLAG-tag that was fused to dCas9, which in turn was targeted to the human *IRF1* locus [135]. CRISPR-based chromatin affinity purification with mass spectrometry (CRISPR-ChAP-MS) that was developed shortly after, follows a similar principle but uses protein A as an affinity-tag and was targeted to the promoter region of the *GAL1* gene in yeast [136]. In the *in vitro* approach named Cas9 locus-associated proteome (CLASP), the 3xFLAG-tagged dCas9 molecule is added to a mixture of sheared chromatin from cross-linked cells; however, subsequent affinity purification and MS identification is performed as in all other procedures [137]. CRISPR affinity purification *in situ* of regulatory elements (CAPTURE) appears to be the most advanced approach, as it is based on biotinylation of a dCas9 tagged with FLAG and a biotin-acceptor-site (FB). This approach not only features high binding specificity, as demonstrated by the human β-globin locus, but also replaces antibody-based purification with high-affinity streptavidin-biotin purification [138].

With the development of proximity labeling approaches, the repertoire of methods enabling protein interactome analyses has become even broader. Proximity labeling followed by MS analysis can detect transient, low-affinity interactions that occur in living cells and are often lost in the harsh purification steps of normal affinity purification or immunopurification of tagged or endogenous proteins [139]. Proximity labeling involves the fusion of a bait protein with an enzyme that catalyzes the biotinylation of proteins in the vicinity of the bait protein. The main enzymes currently used for proximity labeling are engineered variants of biotin ligase (BioID/BirA, BioID2, TurboID, miniTurbo) and ascorbate peroxidase (APEX, APEX2) [133]. Biotin-labeled proteins are isolated from cell extracts using streptavidin beads and subjected to MS [140]. Combinations of CRISPR affinity purification and proximity labeling further expand the spectrum of locus-specific chromatin isolation methods. The first reported method of this kind is called CasID and is based on the fusion of dCas9 and BirA [141]. Later, other approaches named C-BERST, GloPro, and CAPLOCUS were published, all based on a similar principle but using the advanced enzyme APEX2 [142–145]. One drawback is that most of the expressed dCas9 fusion proteins do not bind to the target locus or even associate with non-specific target sites, contributing to extremely high noise [134]. However, despite its usage for single locus application, proximity labeling has also emerged as a powerful tool for determining the interaction network of a transcription factor [146]. As transcription factors usually bind specific DNA elements and thus strongly influence the environment of their target chromatin in cooperation with numerous other proteins, this approach likewise can provide valuable insight into local chromatin composition.

1.14 Aim of the Thesis

Research in the last decades has led to a comprehensive understanding of the cytoplasmic part of the IL-1α-induced NF-κB signaling pathway, whereas comparatively little is known about how exactly the signals are transduced within the nucleus at the chromatin. This entire nuclear network of cooperative and competitive transcription factors, coregulators, epigenetic modifiers, and regulatory chromatin elements needs to be defined to understand the link between gene regulation and the specificity and complexity of the immune response.

In this context, our research group has previously identified hundreds of new IL-1α-inducible active enhancers in epithelial and liver cells. Inhibitor and RNAi-based loss-of-function experiments revealed that the TAK1-IKK2-p65 NF-κB pathway controls histone H3K27 acetylation and the recruitment of p300/CBP and several AP-1 proteins to these enhancers as well as to IL-1 target gene promoters, such as *CXCL8* or *CXCL2* [48]. CRISPR-Cas-mediated deletion of two strongly induced enhancers flanking the chemokine locus on chromosome 4 suppressed the chromatin recruitment of the NF-κB subunit p65 and the transcription of four chemokine genes within this locus. The application of "intrinsic 4C" (i4C) enabled the capturing of multiple IL-1α-induced spatial chromatin interactions within 1 h of treatment [49].

The earlier findings indicate a well-coordinated multistep model for cytokine-regulated gene activation. This leads to questions about the number and types of proteins in the nucleus that work together to enable this intricate genetic control. Furthermore, there is a need to explore whether signals from other known cellular pathways are also integrated into the network and to what extent this integration takes place.

Hence, the aim of this work was to establish two biotin-based pulldown techniques to define the core nuclear network responsible for regulating the expression of IL-1α-NF-κB target genes: CAPTURE, a dCas9-sgRNA-based single locus purification approach, was used to uncover the specific proteome involved in the assembly at inflammatory gene promoters. MiniTurboID proximity labeling, wherein a bait protein is tagged with biotin-ligase miniTurbo, was used to explore the interactome of NF-κB p65, a key transcription factor subunit in inflammation. The application of CAPTURE and MiniTurboID is anticipated to allow identification of novel inflammatory regulators. A second goal was to validate these protein-protein interactions (PPIs) and explore the functional roles of these newly discovered factors to unraveling their contributions within the intricate networks of immune responses.

2 Material

2.1 Cell lines

Cell line	Source / Generated by	Parental / Engineered
HEK293FT	Human embryonic kidney cells (Thermo Fisher Scientific, R7000)	Parental
HeLa	Human epithelial cervix carcinoma cells (ATCC)	Parental
HeLa-pX459-RELA-sg1 (Δp65)	Generated by M. Poppe (Kracht lab)	CRISPR-Cas9 engineered
HeLa-FB-dCas9-BirA-V5 clone L4-7	Generated by J.J. and L.L.	Engineered, for this study
HeLa-dCas9-CBio	Generated by J.J. and L.L.	CRISPR-Cas9 engineered, for this study
HeLa-dCas9-CBio-sgGal4	Generated by J.J. and L.L.	CRISPR-Cas9 engineered, for this study
HeLa-dCas9-CBio-sgGUSB	Generated by J.J. and L.L.	CRISPR-Cas9 engineered, for this study
HeLa-dCas9-CBio-sgCXCL3	Generated by J.J. and L.L.	CRISPR-Cas9 engineered, for this study
HeLa-dCas9-CBio-sgCXCL1/2/3/8	Generated by J.J. and L.L.	CRISPR-Cas9 engineered, for this study
HeLa dCas9-CBio-10 sg's IL-1	Generated by J.J. and L.L.	CRISPR-Cas9 engineered, for this study
HeLa-LCV2-EV	Generated by L.L.	CRISPR-Cas9 engineered, for this study
HeLa-LCV2-RELA-sg1 (Δp65)	Generated by L.L.	CRISPR-Cas9 engineered, for this study
HeLa-LCV2-TFE3-sg1	Generated by L.L.	CRISPR-Cas9 engineered, for this study
HeLa-LCV2-TFE3-sg1+2	Generated by L.L.	CRISPR-Cas9 engineered, for this study
HeLa-LCV2-TFE3-sg4	Generated by L.L.	CRISPR-Cas9 engineered, for this study
HeLa-LCV2-TFE3-sg5 (ΔTFE3)	Generated by L.L.	CRISPR-Cas9 engineered, for this study
HeLa-LCV2-TFE3-sg1+5	Generated by L.L.	CRISPR-Cas9 engineered, for this study
HeLa-LCV2-TFE3-sg4+5	Generated by L.L.	CRISPR-Cas9 engineered, for this study
HeLa-LCV2-TFE3-sg6	Generated by L.L.	CRISPR-Cas9 engineered, for this study
HeLa-LCV2-TFEB-sg1	Generated by L.L.	CRISPR-Cas9 engineered, for this study
HeLa-LCV2-TFEB-sg1+3 (ΔTFEB)	Generated by L.L.	CRISPR-Cas9 engineered, for this study
HeLa-LCV2-TFE3-sg1-TFEB-sg1	Generated by L.L.	CRISPR-Cas9 engineered, for this study
HeLa-LCV2-TFE3-sg4-TFEB-sg1+3	Generated by L.L.	CRISPR-Cas9 engineered, for this study
HeLa-LCV2-TFE3-sg5-TFEB-sg1+3 (ΔΔTFE3/TFEB)	Generated by L.L.	CRISPR-Cas9 engineered, for this study
HeLa-LCV2-TFE3-sg6-TFEB-sg1+3	Generated by L.L.	CRISPR-Cas9 engineered, for this study
HeLa-LCV2-TFE3-sg1+5-TFEB-sg1+3	Generated by L.L.	CRISPR-Cas9 engineered, for this study
HeLa-LCV2-GLIS2-sg1	Generated by L.L.	CRISPR-Cas9 engineered, for this study

HeLa-LCV2-GLIS2-sg1+2	Generated by L.L.	CRISPR-Cas9 engineered, for this study
HeLa-LCV2-GLIS2-sg2	Generated by L.L.	CRISPR-Cas9 engineered, for this study
HeLa-LCV2-GLIS2-sg3	Generated by L.L.	CRISPR-Cas9 engineered, for this study
HeLa-LCV2-GLIS2-sg4	Generated by L.L.	CRISPR-Cas9 engineered, for this study
HeLa-LCV2-GLIS2-sg5	Generated by L.L.	CRISPR-Cas9 engineered, for this study
HeLa-LCV2-GLIS2-sg4+5	Generated by L.L.	CRISPR-Cas9 engineered, for this study
HeLa-LCV2-GLIS2-sg6	Generated by L.L.	CRISPR-Cas9 engineered, for this study
HeLa-LCV2-GLIS2-sg1+3	Generated by L.L.	CRISPR-Cas9 engineered, for this study
HeLa-LCV2-GLIS2-pool-sg1-6	Generated by L.L.	CRISPR-Cas9 engineered, for this study

2.2 Bacterial strains

Strain name	**Source**	**Genotype**
One Shot TOP10 Chemically Competent *E. coli*	Thermo Fisher Scientific	F-mcrA Δ(mrr-hsdRMS-mcrBC) Φ80LacZΔM15 Δ LacX74 recA1 araD139 Δ(ara-leu) 7697 galU galK rpsL (Str^R) endA1 nupG
XL-1 Blue Chemically Competent *E. coli*	Thermo Fisher Scientific	F′ Tn10(Tetr) proA +B + laclqΔ(lacZ)M15I recA1 gyrA96 (Nalr) tbi-1bsdR17 (r-k m-k) glnV44 relA1 lac
NEB® Stable Competent *E. coli* (High Efficiency)	New England Biolabs (C3040H)	F' proA+B+ lacIq Δ(lacZ)M15 zzf::Tn10 (Tet^R)/Δ(ara-leu) 7697 araD139 fhuA ΔlacX74 galK16 galE15 e14- Φ80dlacZΔM15 recA1 relA1 endA1 nupG rpsL (Str^R) rph spoT1 Δ(mrr-hsdRMS-mcrBC)
DH5α *E. coli* containing plasmids from Addgene	Addgene (#38120, #38119, #44445)	F$^-$ φ80lacZΔM15 Δ(lacZYA-argF)U169 recA1 endA1 hsdR17(r_K^-, m_K^+) phoA supE44 λ$^-$thi-1 gyrA96 relA1

2.3 Plastics and other disposable materials

The plastic and disposable materials were purchased from the following companies: Biosphere, Eppendorf, Ansell, Greiner, Neolab, Nerbe plus, Nunc, Omnilab, Brand, Carl Roth, Braun, Argos, VWR, GE Healthcare, Thermo Fisher Scientific, and Sarstedt.

2.4 Chemicals

Unless otherwise stated, the chemicals used in this study were purchased from the following companies: Baker, Biomol, Fluka, Invitrogen, Merck, Pharmacia, Promega, Carl Roth, Roche, Serva, Sigma-Aldrich, and Invitrogen/Thermo Fisher Scientific.

2.5 Medium, agar, and stimulants

Medium	Composition
Full Dulbecco's Modified Eagle Medium (DMEM) medium	10% Fetal bovine serum (FBS) 20 µg/ml Streptomycin 20 U/ml Penicillin 2 mM L-Glutamine
Tetracycline-free DMEM medium	10% Tetracycline-free FBS 100 µg/ml Streptomycin 100 U/ml Penicillin 2 mM L-Glutamine
DMEM (++++) medium for culturing HEK293FT	500 µl DMEM-medium with 10% FBS were supplemented with: 5 ml L-Glutamine (200 mM) 5 ml Non-essential amino acids (NEAA, 100X) 5 ml Sodium pyruvate (100 mM) 500 µg/ml Geneticin was added 1 h after splitting
Freezing medium	DMEM-medium was supplemented with: 40% FBS 10% Dimethylsulfoxide (DMSO)
LB medium	25 g LB-Bouillon, Miller (Luria-Bertani) from Becton Dickinson was solved in 1 l ddH2O and autoclaved Ampicillin (100 µg/ml) or Kanamycin (50 µg/ml) was added before culturing
LB agar plates	37 g Standard nutrient agar 1 l distilled water and autoclaved Ampicillin (100 µg/ml) or Kanamycin (50 µg/ml) was added before plating
TSS buffer	10% Polyethylene glycol 6000 5% DMSO 50 mM Magnesium sulfate heptahydrate LB medium was added to 25 ml

Recombinant IL-1α derived from *E. coli* (self-production, Kracht lab) and Hanks' Balanced Salt Solution (HBSS, PAN Biotech, #P04-32505) were used as stimulants to trigger the cellular response to inflammation or starvation.

2.6 Solutions and buffers

Buffers for SDS-PAGE and Western blot

Buffer	Composition
Special lysis buffer	10 mM Tris pH 7.05 30 mM $Na_4P_2O_7$ 50 mM NaCl 1% Triton X-100 2 mM Na_3VO_3 50 mM NaF 20 mM ß-Glycerophosphate Freshly added to 1 ml lysis buffer: 1 µl Pepstatin (1 µg/ml) 0.5 µl Leupeptin (10 µg/ml) 2.5 µl Phenylmethylsulfonyl fluoride (PMSF, 1 mM) 1 µl Microcystin (1 µM)
4X stock solution 1	40 mM HEPES 40 mM KCl 6 mM $MgCl_2$

	1.2 mM Na_3VO_4 80 mM ß-Glycerophosphate pH 7.9 with KOH
4X stock solution 2	80 mM HEPES 1.68 M NaCl 6 mM $MgCl_2$ 0.8 mM EDTA 1.2 mM Na_3VO_4 80 mM ß-Glycerophosphate pH 7.9 with KOH
Buffer A	For 1 ml Buffer A: 250 µl 4X Stock solution 1 10 µl E64 (10µM) 5 µl DTT (5mM) 0.5 µl Leupeptin (2.5 µg/ml) 1 µl Pepstatin (1 µM) 1.5 µl PMSF (0.3 mM) 1 µl Microcystin (1 µM) 731 µl Nuclease-free water (1 µl NP-40 (0.1%) and 730 µl Nuclease-free water)
Buffer B	For 1 ml Buffer B: 250 µl 4X Stock solution 2 10 µl E64 (10µM) 5 µl DTT (5mM) 0.5 µl Leupeptin (2.5 µg/ml) 1 µl Pepstatin (1 µM) 1.5 µl PMSF (0.3 mM) 1 µl Microcystin (1 µM) 250 µl Glycerol (25%) 481 µl Nuclease-free water
Fractional lysis buffer I	20 mM HEPES pH 8.0 10 mM KCl 1 mM $MgCl_2$ 0.1% Triton X-100 20% Glycerol 50 mM NaF 1 µM Microcystin 1 mM Na_3VO_4 1X Roche protease inhibitor cocktail
Fractional lysis buffer II	20 mM HEPES 2 mM EDTA 400 mM NaCl 0.1% Triton X-100 20% Glycerol 50 mM NaF 1 µM Microcystin 1 mM Na_3VO_4 1X Roche protease inhibitor cocktail
Fractional lysis buffer III	20 mM Tris pH 7.5 2 mM EDTA 150 mM NaCl 1% SDS 1% NP-40 50 mM NaF 1 µM Microcystin 1 mM Na_3VO_4 1X Roche protease inhibitor cocktail
Stacking gel buffer	1 M Tris pH 6.8
Separating gel buffer	1 M Tris pH 8.8
1X Laemmli buffer	25 mM Tris

	192 mM Glycine 0.1% SDS
Western blot buffer	25 mM Tris 192 mM Glycine 20% Methanol
Ponceau S	0.1% Ponceau S in 5% Acetic acid
Tris buffered saline (TBS) buffer	10 mM Tris 150 mM NaCl (pH 7.4) 0.05% Tween-20 for TBS-T

Buffers for Agarose Gel Electrophoresis

Buffer	**Composition**
TAE buffer	40 mM Tris 1 mM EDTA 0.11% Acetic acid
Methylene blue staining solution	0.2% Methylene blue in ddH$_2$O

Buffers for Chromatin-Immunoprecipitation (ChIP)

Buffer	**Composition**
PBS with PMSF	137 mM NaCl 2.7 mM KCl 4.3 mM Na2 HPO4 1.4 mM KH2PO4 PBS with 1 mM PMSF
Lysis buffer	1% SDS 10 mM EDTA 50 mM Tris/HCl pH 8.1 1 mM PMSF 1.5X Roche protease inhibitor cocktail
Dilution buffer	0,01% SDS 1.1% Triton X-100 1.2 mM EDTA 167 mM NaCl 16.7 mM Tris/HCl pH 8.1
Low salt buffer	0.1% SDS 1% Triton-X-100 2 mM EDTA 20 mM Tris/HCl pH 8.1 150 mM NaCl
High salt buffer	0.1% SDS 1% Triton-X-100 2 mM EDTA 20 mM Tris/HCl pH 8.1 500 mM NaCl
LiCl buffer	0.25 M LiCl 1% NP40 1% Sodium deoxycholate 1 mM EDTA 10 mM Tris/HCl pH 8.1
TE buffer	10 mM Tris/HCl pH 8.0 1 mM EDTA

Buffers for CAPTURE-ChIP

Buffer	Composition
Radioimmunoprecipitation (RIPA) 0 nuclear extraction buffer	10 mM Tris/HCl pH 7.4 1 mM EDTA pH 8.0 0.1% SDS 1% Triton X-100 0.1% Sodium deoxycholate Stored at 4°C for up to 6 months Freshly added: 1 mM DTT, 1 mM PMSF, 1.5X Roche protease inhibitor cocktail
Nuclear lysis buffer*	50 mM Tris/HCl pH 8.1 1 mM EDTA pH 8.0 0.5% SDS Stored at room temperature for up to 6 months Freshly added: 1 mM DTT, 1 mM PMSF, 1.5X Roche protease inhibitor cocktail
Radioimmunoprecipitation (RIPA) 0.3 buffer	10 mM Tris/HCl pH 7.4 1 mM EDTA pH 8.0 0.3 M NaCl 0.1% SDS 1% Triton X-100 0.1% Sodium deoxycholate Stored at 4°C for up to 6 months Freshly added: 1 mM DTT, 1 mM PMSF, 1.5X Roche protease inhibitor cocktail
High salt wash buffer	50 mM HEPES pH 7.5 1 mM EDTA pH 8.0 0.5 M NaCl 1% Triton X-100 0.1% Sodium deoxycholate Stored at 4°C for up to 6 months
LiCl wash buffer	10 mM Tris/HCl pH 8.1 1 mM EDTA pH 8.0 250 mM LiCl 0.5% NP-40 0.5% Sodium deoxycholate Stored at 4°C for up to 6 months
TE buffer	10 mM Tris/HCl pH 7.5 1 mM EDTA pH 8.0 Stored at room temperature for up to 6 months
SDS elution buffer	50 mM Tris/HCl pH 8.1 10 mM EDTA pH 8.0 1% SDS Stored at room temperature for up to 6 months

*buffer was also used for CAPTURE-Proteomics

Buffers for CAPTURE-Proteomics

Buffer	Composition
Cell lysis buffer	25 mM Tris/HCl pH 7.4 85 mM KCl 0.1% Triton X-100 Stored at 4°C for up to 6 months Freshly added: 1 mM DTT, 1 mM PMSF, 1.5X Roche protease inhibitor cocktail
SDS nuclear lysis buffer	50 mM Tris/HCl pH 7.4 10 mM EDTA pH 8.0 4% SDS

	Stored at room temperature for up to 1 month
Urea buffer	10 mM Tris/HCl pH 7.4 1 mM EDTA pH 8.0 8 M Urea Stored at room temperature for up to 1 month
IP binding buffer without NaCl	20 mM Tris/HCl pH 7.5 1 mM EDTA pH 8.0 0.1% NP-40 10% Glycerol Stored at 4°C for up to 1 month
IP binding buffer with NaCl	20 mM Tris/HCl pH 7.5 150 mM NaCl 1 mM EDTA pH 8.0 0.1% NP-40 10% Glycerol Stored at 4°C for up to 1 month
Radioimmunoprecipitation (RIPA) buffer	50 mM Tris/HCl pH 7.4 1% NP-40 0.25% Sodium deoxycholate 150 mM NaCl 0.1% SDS 2 mM EDTA pH 8.0 Stored at 4°C for up to 6 months

Buffers for MiniTurboID

Buffer	**Composition**
Lysis buffer	50 mM Tris/HCl pH 7.5 500 mM NaCl 2% SDS Freshly added: 1mM DTT, 1X Roche protease inhibitor cocktail
Washing buffer I	2% SDS
Washing buffer II	50 mM HEPES/HCl pH 7.5 1mM EDTA pH 8.0 500 mM NaCl 0.1% Sodium deoxycholate 1% Triton X-100
Washing buffer III	10 mM Tris/HCl pH 7.5 1 mM EDTA pH 8.0 250 mM LiCl 0.5% Sodium deoxycholate 0.5% NP-40
Washing buffer IV	50 mM Tris/HCl pH 7.5 50 mM NaCl 0.1% NP-40
Washing buffer V	50 mM Tris/HCl pH 7.5

Buffers for silver staining

Buffer	**Composition**
Fixative solution	12.5% TCA
Incubation solution	500 mmol/l Anhydrous sodium acetate 20 mmol/l Sodium thiosulfate 2% Glutaraldehyde
Staining solution	6 mmol/l Silver nitrate 0.05% Formaldehyde
Developer solution	235 mmol/l Sodium carbonate

	0.01% Formaldehyde
Stop solution	5% Acetic acid

Buffers for Immunofluorescence with RNA-Fluorescence *in situ* Hybridization

All buffers used for immuno-RNA-FISH are listed below. The components for RNA-FISH derived from the Affymetrix FISH Kit QuantiGene® ViewRNA ISH Cell Assay Kit (Thermo Fisher Scientific, #QVC0001). The according components are marked by asterisks (*).

Buffer / Component	**Composition**
Blocking solution	0.005% Saponin 10% Donkey serum in HBSS
Wash-/ incubation solution	0.005% Saponin in HBSS
PBS-T	1X PBS with 1:1000 dilution of Tween-20 (self-production)
10X PBS*	Phosphate-buffered saline
Wash buffer*	For 50 ml: 150 µl Wash Buffer component 1 250 µl Wash Buffer component 2 49.6 ml ddH$_2$O
Wash buffer component 1*	Aqueous solution containing detergent
Wash buffer component 2*	Aqueous solution
Detergent solution QC*	Aqueous buffered solution
Probe set diluent QF*	Aqueous solution containing formamide and detergent
Amplifier diluent QF*	Aqueous solution containing formamide and detergent
Label probe diluent QF*	Aqueous solution containing detergent
PreAmplifier mix*	DNA in aqueous buffered solution containing PreAmplifier
Amplifier mix*	DNA in aqueous buffered solution containing Amplifier
Label probe mix*	Fluorescent dye-labeled oligonucleotides in aqueous buffered solution

For detection of *NFKBIA* transcripts, the type 6 (magenta) specific branched probe set against *NFKBIA* (Affymetrix, #VA6-17971) was used (1:100 dilution) according to the manufacturer’s protocol.

Buffers for Immuno-Proximity Ligation Assay with Nuclear Poration

All buffers used for the immuno-PLA are listed below. The components for PLA derived from the Duolink® in Situ PLA® Kit (Sigma-Aldrich, #DUO92007, #DUO92006, #DUO92002 # DUO82046, and #DUO82048). The according components are marked by asterisks (*).

Buffer / Component	**Composition**
Tris buffer	0.1 M Tris/HCl pH 7.4
Permeabilization buffer	0.005% Saponin 0.1% Triton X-100 in DPBS
Freeze protection buffer	40% Glycerol in DPBS

Wash buffer A*	Wash solutions were prepared according to the manufacturer's protocol and then sterile filtered
Wash buffer B*	
1X blocking solution*	Reagent for blocking the sample
1X antibody diluent*	For dilution of PLA probes and primary antibodies
5X PLA probe anti-goat MINUS*	Donkey anti-goat secondary antibody conjugated to oligonucleotide MINUS
5X PLA probe anti-rabbit PLUS*	Donkey anti-rabbit secondary antibody conjugated to oligonucleotide PLUS
5X ligase solution*	Oligonucleotides that hybridize to the PLA probes and all components needed for ligation except the Ligase
1X ligase*	Ligase enzyme 1 unit/µl
5X amplification orange*	All components needed for Rolling Circle Amplification (RCA) except the Polymerase, plus oligonucleotide probes labeled with a fluorophore that hybridize to the RCA product
1X polymerase*	Polymerase enzyme 10 units/µl

2.7 Expression vectors

Plasmids for cloning the blasticidin-resistance cassette into pEF1a-BirA-V5

Plasmid	Source
pEF1a-BirA-V5-neo	Liu et al., Cell, 2017 (Addgene #100548)
plenti-dCAS9(D10A, N863A)-VP64_2A_Blast	Konermann et al., Nature, 2014 (Addgene #61425)

Plasmids for CAPTURE 1.0 and CAPTURE 2.0

Plasmid	Source
pEF1a-FB-dCas9-puro	Liu et al., Cell, 2017 (Addgene #100547)
pEF1a-BirA-V5-blasti	Cloned by L.L. and J.J., for this study
CAPTURE2_pLVX-EF1a-dCas9-CBio-IRES-zsGreen1	Liu et al., Genome Biol., 2020 (Addgene #138418)
pSLQ1651-sgRNA(F+E)-sgGal4	Liu et al., Cell, 2017 (Addgene #100549)
pSLQ1651-sg6GUSB_prom	Cloned by L.L. and J.J., for this study
pSLQ1651-sg3IL8_prom	Cloned by L.L. and J.J., for this study
pSLQ1651-sg3CXCL3_prom	Cloned by L.L. and J.J., for this study
pSLQ1651-sg3CXCL2_prom	Cloned by L.L. and J.J., for this study
pSLQ1651-sg2CXCL1_prom	Cloned by L.L. and J.J., for this study
pSLQ1651-sg3NFKBIA_prom	Cloned by L.L. and J.J., for this study
pSLQ1651-sg3IL6_prom	Cloned by L.L. and J.J., for this study
pSLQ1651-sg2FOSB_prom	Cloned by L.L. and J.J., for this study
pSLQ1651-sg2ZFP36_prom	Cloned by L.L. and J.J., for this study
pSLQ1651-sg1CCL2_prom	Cloned by L.L. and J.J., for this study
pSLQ1651-sg2CCL20_prom	Cloned by L.L. and J.J., for this study

Plasmids for generating different pTet-on-Puro-HA-miniTurbo expression vectors

Plasmid	Source
pTet-on-Puro-Myc-BirA(EV)	Cloned by U. Tenekeci (Kracht lab, Gießen)
linker-HA-miniTurbo in pUC57-Bsal-Free	Designed by M.L. Schmitz, ordered from General Biosystems
pEF-Puro-hu p65 WT-HA	Schmitz lab (Riedlinger et al., Faseb Journal 2019)
pEF-Puro-hu p65 E/I-HA	Schmitz lab (Riedlinger et al., Faseb Journal 2019)
pEF-Puro-hu p65 FL/DD-HA	Schmitz lab (Riedlinger et al., Faseb Journal 2019)

Plasmids for MiniTurboID

Plasmid	Source
HA(EV)	Kracht lab
pTet-on-Puro-HA-miniTurbo(EV)	Cloned by L.L. and J.J., for this study
pTet-on-Puro-p65(wt)-HA-miniTurbo	Cloned by L.L. and J.J., for this study
pTet-on-Puro-p65(E/I)-HA-miniTurbo	Cloned by L.L. and J.J., for this study
pTet-on-Puro-p65(FL/DD)-HA-miniTurbo	Cloned by L.L. and J.J., for this study

Plasmids for Lentivirus production and the Generation of CRISPR-mediated gene knockouts

Plasmid	Source
pLKO.1 GFP	Braun lab, Bad Nauheim
psPAX2	Addgene #12260
pMD2.G	Addgene #12259
Lenti-CrisprV2 (LCV2) Empty vector (EV)	Addgene #52961
LCV2_RELA_sg1	Cloned by L.L., for this study
LCV2_TFE3_sg1	Cloned by L.L., for this study
LCV2_TFE3_sg2	Cloned by L.L., for this study
LCV2_TFE3_sg4	Cloned by L.L., for this study
LCV2_TFE3_sg5	Cloned by L.L., for this study
LCV2_TFE3_sg6	Cloned by L.L., for this study
LCV2_TFEB_sg1	Cloned by L.L., for this study
LCV2_TFEB_sg3	Cloned by L.L., for this study
LCV2_GLIS2_sg1	Cloned by L.L., for this study
LCV2_ GLIS2_sg2	Cloned by L.L., for this study
LCV2_ GLIS2_sg3	Cloned by L.L., for this study
LCV2_ GLIS2_sg4	Cloned by L.L., for this study
LCV2_ GLIS2_sg5	Cloned by L.L., for this study
LCV2_ GLIS2_sg6	Cloned by L.L., for this study

Plasmids for protein overexpression experiments

Plasmid	Source
pcDNA 3.1(EV)	Kracht lab
pEGFP-C1(EV)	Kracht lab
pEGFP-C1-p65	Kracht lab
pEGFP-N1-TFE3	Addgene #38120
pEGFP-N1-TFEB	Addgene #38119
pEGFP-N1-Δ30TFEB	Addgene #44445

2.8 siRNAs

For each target gene a package of 4 preselected siRNAs was purchased from Qiagen (see Art. Nr. below). These siRNAs were pooled and transfected using the Hi-PerFect transfection reagent (Qiagen, #301705).

siRNA package	Source	Art. Nr.
ATXN1L	Qiagen	GS342371
CEBPD	Qiagen	GS1052
CRTC2	Qiagen	GS200186
EBF1	Qiagen	GS1879
FOSL1	Qiagen	GS8061
FOXC1	Qiagen	GS2296
FOXC2	Qiagen	GS2303
GATA6	Qiagen	GS2627
GLIS2	Qiagen	GS84662
HMG20B	Qiagen	GS10362
HOMEZ	Qiagen	GS57594
ISL1	Qiagen	GS3670
MAFG	Qiagen	GS4097
MAMLD1	Qiagen	GS10046
MSX1	Qiagen	GS4487
N4BP3	Qiagen	GS23138
NFYC	Qiagen	GS4802
PBX2	Qiagen	GS5089
PHC1	Qiagen	GS1911
PHLDA2	Qiagen	GS7262
RAD54L2	Qiagen	GS23132
RAP1A	Qiagen	GS5906
RAP1B	Qiagen	GS5908
RELA	Qiagen	GS5970
RUNX2	Qiagen	GS860
S100A8	Qiagen	GS6279

S100A9	Qiagen	GS6280
SIX5	Qiagen	GS147912
SKI	Qiagen	GS6497
SKIL	Qiagen	GS6498
SS18	Qiagen	GS6760
TBX1	Qiagen	GS6899
TFE3	Qiagen	GS7030
TNIP1	Qiagen	GS10318
ZBTB34	Qiagen	GS403341
ZBTB5	Qiagen	GS9925
ZIC2	Qiagen	GS7546
ZMIZ1	Qiagen	GS57178
ZMIZ2	Qiagen	GS83637
TFEB	Qiagen	GS7942

The control siRNA targeting the 5′-to-3′ sequence CGUACGCGGAAUACUUCGA of the luciferase gene was ordered from Eurofins.

2.9 TaqMan probes

The quantitative Polymerase Chain Reaction (qPCR) was performed using the 2X TaqMan® Fast Universal PCR Master Mix (Applied Biosystems, #4352042) and the TaqMan®Gene Expression Assays (Applied Biosystems) listed below. All probes were labeled with FAM-MGB. Unless otherwise stated, the Reference Sequence denoted in the tabular column refers to one of potentially multiple full-length mRNA transcript variants that are covered by the probe.

Probe	Product size [bp]	RefSeq.	Assay-ID
ACTB	171	NM_001101.3	Hs99999903_m1
GUSB	81	NM_000181.3	Hs99999908_m1
GAPDH	93	NM_001256799.2	Hs02758991_g1
IL8	101	NM_000584.3	Hs00174103_m1
CXCL3	99	NM_002090.2	Hs00171061_m1
CXCL2	68	NM_002089.3	Hs00236966_m1
CXCL1	70	NM_001511.3	Hs00236937_m1
NFKBIA	68	NM_020529.2	Hs00153283_m1
IL6	95	NM_000600.4	Hs00174131_m1
FOSB	106	NM_001114171.1	Hs00171851_m1
CCL2	101	NM_002982.3	Hs00234140_m1
CCL20	81	NM_004591.2	Hs00171125_m1
TNFAIP3	63	NM_001270507.1	Hs00234713_m1
CSF2	85	NM_000758.3	Hs00929873_m1

ATXN1L	71	NM_001137675.3	Hs01370353_g1
CEBPD	107	NM_005195.3	Hs00270931_s1
CRTC2	68	NM_181715.2	Hs01064500_m1
EBF1	100	NM_001290360.2	Hs01092694_m1
FOSL1	72	NM_001300855.1	Hs04187686_g1
FOXC1	61	NM_001453.2	Hs00559473_s1
FOXC2	102	NM_005251.2	Hs00270951_s1
GATA6	91	NM_005257.5	Hs00232018_m1
GLIS2	141	NM_001318918.1	Hs00261493_m1
HMG20B	69	NM_006339.2	Hs00173091_m1
HOMEZ	131	NM_020834.2	Hs00603839_m1
ISL1	57	NM_002202.2	Hs00158126_m1
MAFG	84	NM_002359.3	Hs00361648_g1
MAMLD1	72	NM_001177465.2	Hs00193976_m1
MSX1	144	NM_002448.3	Hs00427183_m1
N4BP3	67	NM_015111.1	Hs01585915_g1
NFYC	78	NM_001142587.1	Hs00360259_g1
PBX2	198	NM_002586.4	Hs00855025_s1
PHC1	148	NM_004426.2	Hs01863307_s1
PHLDA2	121	NM_003311.3	Hs00169368_m1
RAD54L2	93	NM_001322253.1	Hs00379387_m1
RAP1A	71	NM_001010935.2	Hs01092205_g1
RAP1B	97	NM_001010942.2	Hs04275955_g1
RELA	96	NM_001145138.1	Hs01042019_g1
RUNX2	86	NM_001015051.3	Hs01047973_m1
S100A8	107	NM_001319196.1	Hs00374264_g1
S100A9	83	NM_002965.3	Hs00610058_m1
SIX5	103	NM_175875.4	Hs01650774_m1
SKI	81	NM_003036.3	Hs01057032_m1
SKIL	92	NM_001145097.2	Hs01045418_m1
SS18	124	NM_001007559.2	Hs01075912_m1
TBX1	50	NM_005992.1	Hs00962558_g1
TFE3	125	NM_001282142.1	Hs00232406_m1
TNIP1	77	NM_001252385.1	Hs00374581_m1
ZBTB34	68	NM_001099270.1	Hs00291772_s1
ZBTB5	81	NM_014872.2	Hs04996213_m1
ZIC2	72	NM_007129.3	Hs00600845_m1
ZMIZ1	65	NM_020338.3	Hs01119362_m1
ZMIZ2	137	NM_001300959.1	Hs00230211_m1
TFEB	78	NM_001167827.2	Hs00292981_m1

SQSTM1	55	NM_001142298.1	Hs00177654_m1
MAP1LC3B	108	AK310224.1	Hs00917682_m1
MCOLN1	86	NM_020533.2	Hs01100653_m1
LAMP1	72	NM_005561.3	Hs00931461_m1
ATP6V0D1	70	NM_004691.4	Hs00371517_m1
HEXA	72	NM_000520.5	Hs00942659_m1

2.10 Oligonucleotides and primers

The oligonucleotides and primers of this study were synthesized by Eurofins Genomics at a synthesis scale of 0.01 µmol and purified using the Salt-Free technology, except for the specific forward primers of CAPTURE single guide RNAs (sgRNAs) (0.05 µmol) which were purified using High Purity Salt-Free (HPSF). All the sequences are written in a 5′-to-3′ direction.

Primers for cloning sgRNAs into pSLQ1651-sgRNA(F+E)

Primer	**Sequence**
sg6_GUSB_prom_fwd_2	GGAGAACCACCTTGTTGGAGACCTCGCCCTTATCGGCTGTTTAAGAGCTATGCTGGAAACAGCA
sg3_IL8_prom_fwd	GGAGAACCACCTTGTTGGGTCATACTCCGTATTTGATAGTTTAAGAGCTATGCTGGAAACAGCA
sg3_CXCL3_prom_fwd	GGAGAACCACCTTGTTGGAGAGTGCACGGGGGTTACTCGTTTAAGAGCTATGCTGGAAACAGCA
sg3_CXCL2_prom_fwd	GGAGAACCACCTTGTTGGAACCCAGTGCAGTGCGTCGTGTTTAAGAGCTATGCTGGAAACAGCA
sg2_CXCL1_prom_fwd	GGAGAACCACCTTGTTGGAGCGTTGTGTCTCGGATTTGGTTTAAGAGCTATGCTGGAAACAGCA
sg3_NFKBIA_prom_fwd	GGAGAACCACCTTGTTGGCCCATCAGGTCGGCGTCCTTGTTTAAGAGCTATGCTGGAAACAGCA
sg3_IL6_prom_fwd	GGAGAACCACCTTGTTGGGTTCTACAACAGCCGCTCACGTTTAAGAGCTATGCTGGAAACAGCA
sg2_FOSB_prom_fwd	GGAGAACCACCTTGTTGGAGTGCGGGACTCGATTTGGCGTTTAAGAGCTATGCTGGAAACAGCA
sg2_ZFP36_prom_fwd	GGAGAACCACCTTGTTGGCGCGTGCGACACAGACGGATGTTTAAGAGCTATGCTGGAAACAGCA
sg1_CCL2_prom_fwd	GGAGAACCACCTTGTTGGCTCTGCCCGCTTTCAATAAGGTTTAAGAGCTATGCTGGAAACAGCA
sg2_CCL20_prom_fwd	GGAGAACCACCTTGTTGGGGGTGTAACAATAGGAGTTCGTTTAAGAGCTATGCTGGAAACAGCA
Universal_rev	CTAGTACTCGAGAAAAAAAGCACCGACTCGGTGCCAC

The specific forward (fwd) primers for cloning sgRNAs into pSLQ1651-sgRNA(F+E) were designed by adding “GGAGAACCACCTTGTTGG” to the start of the sgRNA sequence and “GTTTAAGAGCTATGCTGGAAACAGCA” to the end of the sgRNA sequence. The forward and universal reverse (rev) primer sequences were taken from Liu et al., Current Protocols in Molecular Biology 2018 [147].

Oligonucleotides for cloning sgRNAs into Lenti-CrisprV2

Oligonucleotide	Sequence
RELA_sg1_se	CACCGGCTTCCGCTACAAGTGCGA
RELA_sg1_as	AAACTCGCACTTGTAGCGGAAGCC
TFE3_sg1_ se	CACCGACAGCACGAACACGGCTCGA
TFE3_sg1_ as	AAACTCGAGCCGTGTTCGTGCTGTC
TFE3_sg2_ se	CACCGCTCATGCGGCCGAACCAGCT
TFE3_sg2_ as	AAACAGCTGGTTCGGCCGCATGAGC
TFE3_sg4_ se	CACCGGCGTCGGGAACAGGCCGCCG
TFE3_sg4_ as	AAACCGGCGGCCTGTTCCCGACGCC
TFE3_sg5_ se	CACCGGAGAGGCAGGTGCAGGACTG
TFE3_sg5_ as	AAACCAGTCCTGCACCTGCCTCTCC
TFE3_sg6_ se	CACCGTGCTGCAGGTGGTAGCGCGT
TFE3_sg6_ as	AAACACGCGCTACCACCTGCAGCAC
TFEB_sg1_ se	CACCGGGTTGCGCATGCAGCTCATG
TFEB_sg1_ as	AAACCATGAGCTGCATGCGCAACCC
TFEB_sg3_ se	CACCGCAGCAGCAACAGCAGCAGCT
TFEB_sg3_ as	AAACAGCTGCTGCTGTTGCTGCTGC
GLIS2_sg1_ se	CACCGGAGTATCACCAAGCTCCGGG
GLIS2_sg1_ as	AAACCCCGGAGCTTGGTGATACTCC
GLIS2_sg2_ se	CACCGAGAGGACGCTGGGTGTGGTC
GLIS2_sg2_ as	AAACGACCACACCCAGCGTCCTCTC
GLIS2_sg3_ se	CACCGAGCTCCCTGTGCAGAGCACG
GLIS2_sg3_ as	AAACCGTGCTCTGCACAGGGAGCTC
GLIS2_sg4_ se	CACCGACACCATCCAAATAGCGCAG
GLIS2_sg4_ as	AAACCTGCGCTATTTGGATGGTGTC
GLIS2_sg5_ se	CACCGAGAGGCACTTGTCCTTGGGA
GLIS2_sg5_ as	AAACTCCCAAGGACAAGTGCCTCTC
GLIS2_sg6_ se	CACCGATGCGGGGTACTGCTGCCAC
GLIS2_sg6_ as	AAACGTGGCAGCAGTACCCCGCATC

The oligonucleotides for cloning sgRNAs into Lenti-CrisprV2 were designed by adding “CACCG” to the start of the sense (se) sequence, and “AAAC” to the start and “C” to the end of the anti-sense (as) sequence of the sgRNA to generate cloning overhangs.

Primers for cloning the blasticidin-resistance cassette into pEF1a-BirA-V5

Primer	Sequence
cloning_blasticidin_1_fwd	CTCCCGGGAGGAGAATCCTGGCCCAAT
cloning_blasticidin_1_rev	CTCTCCAGGAGAATTCTTAGCCCTCCCACA

The primer pair for cloning the blasticidin-resistance cassette into pEF1a-BirA-V5 was designed by adding the cloning overhangs “CTCCCGGG” and “CTCTCCAGGA” to the start of the forward (fwd) primer sequence or to the start of the reverse (rev) primer sequence, respectively.

Primers for cloning p65 gene variants into pTet-on-Puro-HA-miniTurbo

Primer	Sequence
cloning_p65_1_fwd	TCCAGCCTACCGGTAACATGGACGAACTGTTCCCCCTCATCTT
cloning_p65_1_rev	TATCGATGTACAGGAGCTGATCTGACTCAGCAGGGCTG

The primer pair for cloning p65 gene variants into pTet-on-Puro-HA-miniTurbo was designed by adding the cloning overhangs “TCCAGCCTACCGGTAAC” and “TATCGATGTACA” to the start of the forward (fwd) primer sequence or to the start of the reverse (rev) primer sequence, respectively.

Primers for validation by Sanger Sequencing

The validation by Sanger Sequencing was performed through LGC Genomics or Microsynth.

Primer	Sequence
U6-Vector_seq_fwd	GAGATCCAGTTTGGTTAGTACCGGG
U6-Vector_seq_rev	ATGCATGGCGGTAATACGGTTAT
HA-miniTurbo_insert_seq_fwd	CATCCACGCTGTTTTGACC (deposited at LGC Genomics)
HA-miniTurbo_insert_seq_rev	TAAGATCTGGCCTCCGCG (deposited at LGC Genomics)
miniTurbo_fusion_seq_fwd	CATCCACGCTGTTTTGACC
miniTurbo_fusion_seq_rev	CGATTCGATCCAGCAGGTA
SV40-Do	CAGAAGTAGTGAGGAGGC (standard primer list at LGC Genomics)
hU6-fwd	GAGGGCCTATTTCCCATGATT (standard primer list at Microsynth)

Primers for SYBR Green qPCR

Primer	Forward	Reverse
ChIP_ACTB_NCBP1peak	CCGTTCCGAAAGTTGCCTTTT	GCAAAGGCGAGGCTCTGT
ChIP_CDK6gapdhTSS	GCTCTCTGCTCCTCCTGTTC	CTTCAGGCCGTCCCTAGC
ChIP_GUSB_prom_2	CACCGATCTCAGGGGTTCTG	TCTTGGTTGAGGACGAGTGC
ChIP_IL8_prom	AAGAAAACTTTCGTCATACTCCG	TGGCTTTTTATATCATCACCCTAC
ChIP_CXCL3_prom	GAATTTGGGGCAGAAAATGA	GATCGGCGAACCCTTTTTAT
ChIP_CXCL2_prom	GCTGCAGTTCTTGCCCTAAC	GCCAACTGTGGGATGTTCTC
ChIP_CXCL1_prom	AGCCTATCTCCCAGCACCTT	CTGCGCTGAAGATACCACCT
ChIP_NFKBIA_prom	CCAGCCATCATTTCCACTCT	CCTGCACCCTGTAATCCTGT
ChIP_IL6_prom_3	TGGCAAAAAGGAGTCACACA	CCAAGCCTGGGATTATGAAG
ChIP_FOSB_prom	TCATGCAAGTGACCAGATCG	ACCCGCCAGCCTGTATTTAT
ChIP_ZFP36_prom	GTCTTCCCTCCCTTCCTCAC	AAGCTGGAGACTGAGGCTTG
mRNA_ZFP36_Ex1In1_1	GCCATCTACGAGGTGAGTCC	GTTGGAGAAGGGAGGCAAG

ChIP_CCL2_prom	CCCTGCTTCCCTTTCCTACT	TGCGAGCTTCAGTTTGAGAA
ChIP_CCL20_prom	CCTCCTTGACTGGTTCTGGA	GCAAAGAGCAAAAGCAGCTC
HIV-Psi element	GAGAGAGATGGGTGCGAGAG	CCCTCATATCTCCTCCTCCA
WPRE element	CGCTGCTTTAATGCCTTTGT	GAGATCCGACTCGTCTGAGG

2.11 Enzymes and buffers

Enzyme / buffer	Source	Application
FastDigest BstXI	Thermo Scientific™ (FD1024)	DNA restriction
FastDigest XhoI	Thermo Scientific™ (FD0694)	DNA restriction
FastDigest MluI	Thermo Scientific™ (FD0564)	DNA restriction
FastDigest BshTI / Agel	Thermo Scientific™ (FD1464)	DNA restriction
FastDigest Bsp1407I / BsrGI	Thermo Scientific™ (FD0933)	DNA restriction
FastDigest SmaI	Thermo Scientific™ (FD0663)	DNA restriction
FastDigest PfoI	Thermo Scientific™ (FD1754)	DNA restriction
FastDigest Esp3I / BsmBI	Thermo Scientific™ (FD0454)	DNA restriction
10X FastDigest Buffer	Thermo Scientific™	DNA restriction
Phusion™ High-Fidelity DNA Polymerase	Thermo Scientific™ (F-530XL)	DNA extension
5X Phusion HF reaction buffer	Thermo Scientific™ (F-530XL)	DNA extension
T4 DNA Ligase	Thermo Scientific™ (EL0014)	DNA Ligation
10X T4 Ligase buffer	Thermo Scientific™ (EL0014)	DNA Ligation
T4 Polynucleotide Kinase	Thermo Scientific™ (EK0031)	Oligonucleotide phosphorylation
10X T4 PNK buffer A	Thermo Scientific™ (EK0031)	Oligonucleotide phosphorylation
RevertAid Reverse Transcriptase	Thermo Scientific™ (EP0441)	cDNA synthesis
5X Reverse transcription reaction buffer	Thermo Scientific™ (EP0441)	cDNA synthesis
RNase A (10 mg/ml)	Thermo Scientific™ (EN0531)	RNA digestion
Proteinase K (20 mg/ml)	Macherey-Nagel (740506)	Protein digestion

2.12 Antibodies

Primary antibodies

Antibody	Species	Source	Applications and Dilutions
anti β-actin	mouse	Santa Cruz (sc-47778)	1:1000 in 5% milk/TBS-T (WB)
anti tubulin	mouse	Santa Cruz (sc-8035)	1:1000 in 5% milk/TBS-T (WB)
anti CRISPR-Cas9	mouse	Abcam (ab191468)	1:1000 in 3% milk/TBS-T (WB) 2 µg (ChIP)
anti V5-tag	mouse	Santa Cruz (sc-271944)	1:1000 in 5% BSA/TBS-T (WB)
anti HA-tag	mouse	Roche (11583816001)	1:500 in 5% milk/TBS-T (WB)

anti GFP-tag	mouse	Roche (118114460001)	1:1000 in 5% milk/TBS-T (WB)
anti NFκB p65	rabbit	Santa Cruz (sc-372)	1:1000 in 5% milk/TBS-T (WB) 3 µg (ChIP)
anti NFκB p65	mouse	Santa Cruz (sc-8008)	1:1000 in 5% milk/TBS-T (WB) 1:100 (IF)
anti NFκB p65	goat	Bethyl Lab. (A303-945A)	1:1000 (PLA)
anti phospho-NFκB p65 P(Ser536)	rabbit	Cell Signaling (3031)	1:1000 in 5% BSA/TBS-T (WB)
anti NFκB p50	mouse	Santa Cruz (sc-8414)	1:1000 in 5% milk/TBS-T (WB)
anti IκBα	rabbit	Cell Signaling (9242)	1:1000 in 5% BSA/TBS-T
anti phospho-IκBα P(Ser32)	rabbit	Cell Signaling (2859)	1:1000 in 5% BSA/TBS-T, 50 mM NaF, 0.1% Tween-20 (WB)
anti IKKα	rabbit	Santa Cruz (sc-7218)	1:500 in 5% milk/TBS-T (WB)
anti phospho-IKKα/β P(Ser176/180)	rabbit	Cell Signaling (2697)	1:1000 in 5% BSA/TBS-T, 0.1% Tween-20 (WB)
anti TNFAIP3 / A20	rabbit	ProSci Inc. (5131)	1:1000 in 5% milk/TBS-T (WB)
anti Pol II	mouse	Millipore (17-620)	1:5000 in 5% milk/TBS-T (WB)
anti phospho-Pol II P(Ser5)	rabbit	Abcam (ab5131)	1:5000-1:10,000 in 5% milk/TBS-T, 50 mM NaF (WB)
anti Histone H3	rabbit	Abcam (ab1791)	1:2000 in 5% milk/TBS-T (WB)
anti TFE3	rabbit	Sigma-Aldrich (HPA023881)	1:5000 in 5% milk/TBS-T (WB) 1:50 (PLA)
anti TFEB	rabbit	Cell Signaling (4240)	1:1000 in 5% milk/TBS-T (WB) 1:25 (PLA)
anti GLIS2	rabbit	Thermo Fisher Scientific (PA5-40314)	1:500 in 5% milk/TBS-T (WB) 1:25 (PLA)
anti Immunglobulin G (rabbit)	rabbit	Cell Signaling (2729)	2 µl (ChIP)

Secondary antibodies

Antibody	**Species**	**Source**	**Applications and Dilutions**
HRP-conjugated/ anti-rabbit IgG	goat	DakoCytomation (P0448)	Diluted in milk/TBS-T or BSA/TBS-T (WB)
HRP-conjugated/ anti-mouse IgG	goat	DakoCytomation (P0447)	Diluted in milk/TBS-T or BSA/TBS-T (WB)
Dylight488-coupled anti-mouse IgG	donkey	ImmunoReagents (DkxMu-003-D488NHSX)	1:200 (IF) 1:2 pre-dilution, 1:100 dilution

The Streptavidin-HRP reagent (PerkinElmer, #NEL750001EA) was used 1:5000 in 5% BSA/TBS-T to detect biotinylated proteins by Western blot.

2.13 Reagents and materials ready-to-use

Name	Source
DPBS (Dulbecco's Phosphate Buffered Saline)	PAN Biotech (P04-36500)
Trypsin/EDTA (Ethylenediaminetetraacetic acid) solution	PAN Biotech (P10-023100)
DMEM (Dulbecco´s Modified Eagle´s Medium)	PAN Biotech (P04-03550)
FBS Good Forte	PAN Biotech (P40-47500)
Tetracycline-free FBS	PAN Biotech (P30-3602)
Penicillin/Streptomycin	PAN Biotech (P06-07100)
L-Glutamine	PAN Biotech (P04-80100)
Non-essential amino acids (NEAA)	Gibco (11140-035)
Sodium pyruvate	Gibco (11360-039)
Geneticin	Gibco (10131019)
Puromycin	Merck Millipore (540411-100MG)
Blasticidin	Invivogen (ant-bl)
Polybrene (Hexadimethrine bromide)	Sigma-Aldrich (S107689-10G)
Opti-MEM™	Thermo Fisher Scientific (51985-034)
Branched PEI (Polyethylenimine)	Sigma-Aldrich (408727)
Lipofectamine™ LTX and PLUS™ Reagent	Thermo Fisher Scientific (15338100)
HiPerFect Transfection Reagent	Qiagen (301705)
Doxycycline	Sigma-Aldrich (D9891)
Biotin	Sigma-Aldrich (B4501-100MG)
BD Difco™ Dehydrated Culture Media: LB Broth, Miller (Luria-Bertani)	BD (244610)
Standard nutrient agar 1	Merck (1.07881.0500)
Ampicillin sodium salt	BioChemica (A0839,0025)
Kanamycin sulfate	Carl Roth (T832.3)
Leupeptin hemisulfate	Carl Roth (CN33.2)
Microcystin	Enzo Life Sciences (ALX-350-012-M001)
Pepstatin A	Applichem (A2205)
PMSF (Phenylmethanesulfonyl fluoride)	Sigma-Aldrich (P-7626)
Protease inhibitor cocktail tablets	Roche (11873580001)
DTT (Dithiothreitol)	Serva (20710.04)
ROTI®Quant	Carl Roth (K015.1)
BSA (Bovine Serum Albumin)	Serva (11930.04)
ROTI®Load	Carl Roth (K929.3)
ROTIPHORESE®Gel 30 (Acrylamide solution)	Carl Roth (3029.1)
APS (Ammonium peroxodisulfate)	Merck (1.01201.0500)
TEMED (N,N,N',N'-Tetramethyl ethylenediamine)	Sigma Life Science (T9281-25ML)
PageRuler™ Prestained Protein Ladder	Thermo Fisher Scientific (26616)
ROTI®PVDF membrane	Carl Roth (T830.1)
Whatman® gel blotting paper, Grade GB003	Cytiva (10426892)
Ponceau S	Serva (33429)
Milk powder	Sucofin
Coomassie Brilliant Blue R-250	Serva (35051)
Immobilon Western Chemiluminescent HRP Substrate	Merck Millipore (WBKLS0500)

Amersham ECL Western blot Detection Reagent	GE Healthcare (RPN2106)
Fast SYBR™ Green PCR Master Mix	Applied Biosystems (4385612)
TaqMan™ Fast Universal PCR Master Mix 2X	Applied Biosystems (4352042)
Random Hexamer Primer	Thermo Fisher Scientific (S0142)
dNTP mix (Deoxyribonucleotide triphosphate)	Thermo Fisher Scientific (R0192)
ATP (Adenosine triphosphate)	Thermo Fisher Scientific (R0441)
DNA Loading Dye 6X	Thermo Fisher Scientific (R0611)
GeneRuler DNA Ladder Mix	Thermo Fisher Scientific (SM0331)
Ethidium bromide	Carl Roth (2218.2)
Methylene Blue hydrate	Sigma-Aldrich (M-4159)
Paraformaldehyde (4%)	Santa Cruz (sc-281692)
Saponin	Sigma-Aldrich (S4521-10G)
Normal Donkey Serum	Jackson ImmunoResearch (017-000-121)
Fluoromount G	Invitrogen (00-4958-02)
HBSS (Hank′s BSS)	PAN Biotech (P04-32505)
Hoechst 33342	Thermo Fisher Scientific (H3570)
ibiTreat μ-Slide VI 0.4	Ibidi (80606)
Formaldehyde (37%)	Applichem (A0877.0250)
Dynabeads M-280 Streptavidin	Invitrogen (11205D)
Streptavidin Agarose Resin Beads	Thermo Fisher Scientific (20353)
Protein A-Sepharose® CL-4B Beads	GE Healthcare (17-0780-01)
Protein G Sepharose® 4 Fast Flow Beads	GE Healthcare (17-0618-01)

2.14 Kits

Kit	**Source**
ViewRNA^{TM} ISH Cell Assay Kit	Thermo Fisher Scientific (QVC0001)
Duolink® in Situ PLA® Detection Reagents Orange	Sigma-Aldrich (DUO92007)
Duolink® in Situ PLA® Probe Anti-Goat MINUS	Sigma-Aldrich (DUO92006)
Duolink® in Situ PLA® Probe Anti-Rabbit PLUS	Sigma-Aldrich (DUO92002)
NucleoSpin® RNA Kit	Macherey-Nagel (740955.250)
NucleoSpin® Gel and PCR Clean-Up Kit	Macherey-Nagel (740609.50)
Binding Buffer NTB	Macherey-Nagel (740595.150)
NucleoSpin® Plasmid Kit	Macherey-Nagel (740588.250)
NucleoBond® PC500 Kit	Macherey-Nagel (740574.50)
NucleoBond® Xtra Midi Kit	Macherey-Nagel (740410.50)
TaqMan® PreAmp Cells-to-CT^{TM} Kit	Invitrogen**™** (4387299)
Quick-RNA^{TM} Viral Kit	Zymo Research Europe (R1034)
PCR Mycoplasma Test Kit	Applichem (A3744)

2.15 Devices and apparatus

Device	Source
BBD 6220 CO2 Incubator	Thermo Scientific
HERAsafe (sterile workbench)	Thermo Scientific
Water bath	GFL
Water bath Lauda M6	Lauda
Function Line Microbiological Incubator	Heraeus
Multitron Standard	Infors HT
CH-4103 Shaker	Infors HT
Sorvall RC 6+ centrifuge	Thermo Fisher Scientific
Sorvall RC 5C Plus centrifuge	Thermo Fisher Scientific
Table-centrifuge 5415 R, 5417 R, 5424	Eppendorf
TJ-25 centrifuge	Beckman Coulter
IKA mini G centrifuge	IKA
Intellimixer RM-2L	LFT Labortechnik
Varishaker-incubator	Dynatech
Magnetic Stirrer MR 3001	Heidolph
Shaker	Edmund Bühler GmbH
Thermomixer comfort, compact, C	Eppendorf
Vortex Top Mix Stirrers	Heidolph
Vortex mixer	neoLab
Hybridiser HB-1D	Techne
CKX41 microscope	Olympus
DMIRE2 fluorescence microscope	Leica
DMi8 inverse fluorescence microscope	Leica
THUNDER imager (incl. DMi8 inverse fluorescence microscope)	Leica
Elektrophorese Power Supply EPS 600, 601, 3500	Pharmacia Biotech
Power Pack P25	Biometra
Owl P9DS	Owl Separation Systems
PerfectBlue Dual-gel system Twin M	VWR
PerfectBlue ′Semi-Dry′-Blotter, Sedec	VWR Peqlab
ChemiDoc™Touch Imaging System	Bio-Rad
Mupid-exU	Takara
Gel iX Imager UV-Transilluminator	INTAS
7500 Fast Real-Time PCR System	Applied Biosystems
Thermocycler T Professional	Biometra
FI 310	Fischer
MP-3000	Chyo
766 pH meter Calimatic	Knick
NanoDrop ND-1000 Spectrophotometer	Peqlab
SpectraMax Plus 384 Microplate-Reader	Molecular Devices
Bioruptor NextGen with water cooler	Diagenode
Concentrator Plus SpeedVac	Eppendorf
Autoclave T6030	Heraeus
Fisherbrand™ FB70157 Pump	Fisher Scientific

DynaMagTM-2 magnetic stand	Invitrogen
FACSAria™	BD Biosciences
Falcon Round-Bottom Polystyrene Tubes with Cell-Strainer Cap 5 ml for FACS	Fisher Scientific
Neubauer counting chamber	Laboroptik
Syringe filters ROTILABO® PVDF, 0,45 µm	Carl Roth

2.16 Software and webtools

Name	**Version / Weblink**
Adobe Photoshop CS2	Version 9.0
Bio-Rad Image Lab	Version 6.0.1
BlobFinder	Version 3.0 Beta
BD FACSDiva	Version 8.0.2
CHOPCHOP	https://chopchop.cbu.uib.no/ (01-2019 or later)
Citavi	Version 6
Cytoscape	Version 3.9.1
CRISPick	https://portals.broadinstitute.org/gppx/crispick/public (11-2021 or later)
DNASTAR SeqBuilder	Version 11.1.0 (59)
DNASTAR SeqMan Pro	Version 11.1.0 (59) 419
Draw Venn	https://bioinformatics.psb.ugent.be/webtools/Venn/ (09-2020 or later) [148]
GraphPad Prism	Version 9.5.0 (730)
IGV Viewer	Version 2.8.0
ImageJ	Version 1.53k
Inkscape	Version 1.0.2-2
Leica Application suite X (LASX)	Versions 3.7.0.20979 and 3.7.4.23463
MaxQuant	Version 1.6.17.0
Metascape	https://metascape.org/ (09-2020 or later) [149]
Microsoft Excel and Word	Version 2016
NEBioCalculator	http://nebiocalculator.neb.com/#!/ligation (12-2019 or later)
Perseus	Version 1.6.14
Primer3 Plus	https://www.primer3plus.com/ (11-2018 or later)
STRING	https://string-db.org/ (Version 11.0 and newer) [150]

3 Methods

3.1 Methods in Cell Biology

3.1.1 Freezing and thawing of cells

For permanent storage, cells were cryo-conserved in liquid nitrogen. They were pelleted (5 min, 500 × g, RT), suspended in 1 ml freezing medium, and transferred to a cryo-tube. After that, suspended cells were frozen and shortly stored at -80°C until they were preserved in liquid nitrogen for long-term conservation. For re-cultivation, cells were thawed in a water bath at 37°C and then transferred to a cell culture dish of appropriate size. Cells were then cultivated at 37°C and 6% CO_2. When cells reached 80% confluence, they were seeded for subsequent trials with a defined density.

3.1.2 Mycoplasma testing

Mycoplasma are small parasitic bacteria that contaminate eukaryotic cell cultures. This can lead to altered cell line properties and it is therefore part of good laboratory practice to regularly control the cell culture for contamination. For this purpose, 100 µl culture medium of an 80% confluent cell dish was retained, boiled for 5 min at 95°C, and cell debris were pelleted (15 sec, max speed, RT). The supernatant was then transferred to a new reaction tube and stored at -20°C. The PCR Mycoplasma Test Kit was then used according to the manufacturer’s instructions to detect mycoplasma in the prepared cell culture medium.

3.1.3 Splitting of cells

Cells were cultured in culture dishes of different sizes with full DMEM medium at 37°C and 6% CO_2. Throughout cultivation, cells were split regularly by removing the medium and washing them twice with PBS. To detach cells from the culture dish, they were covered in a thin layer of Trypsin-EDTA for 3 min at 37°C. Trypsinization was then stopped by adding full DMEM medium and cells were gently pipetted to obtain a homogenous suspension. Depending on the previous cell density, an appropriate volume of cell suspension was transferred into a new culture dish to maintain the cell culture.

3.1.4 Seeding of cells

Cells were seeded in different densities depending on the cell line, number of cultivation days, and size of the culture dish. The cell concentration was determined using the Neubauer counting chamber and calculated as follows:

$$(\Sigma \text{ of the cell number of all squares}/4) \ast 10^4 = \text{cells/ml}$$

$$\text{desired cell number/measured cell concentration} = \text{required volume}$$

Based on the size of the culture dish, different volumes of full DMEM medium were used (210 µl/48-well, 2 ml/6-well, 4 ml/60 mm dish, 10 ml/100 mm dish, 20 ml/T145 dish, and 45 ml/T175 flask) and supplemented with the required volume of cell suspension. In contrast, Ibidi-slots were filled with 30 µl suspension containing the desired number of cells and pre-incubated for 1 h at 37°C and 6% CO_2 until cells were adherent. After the pre-incubation, each slot was filled up with full DMEM medium to a total volume of 130 µl and cultured until further processing. HeLa cells were cultured in full DMEM medium, however, for the MiniTurboID assay HeLa cells were kept in a tetracycline-free DMEM medium to enable the induction of HA-miniTurbo fusion proteins upon doxycycline treatment. Unless otherwise specified, cells were seeded as follows:

Cell type	Days of culturing	Ibidi-slot	48-well	6-well	60 mm	100 mm	T145	T175
HeLa	1	9×10^3	-	2×10^5	4.4×10^5	-	-	-
	2	-	-	1.7×10^5	3.7×10^5	1×10^6	20×10^5	-
	3	-	3×10^3	-	8×10^4	-	10×10^5	-
	4	-	-	-	-	-	5×10^5	-
HEK293FT	3	-	-	-	-	-	-	1.8×10^7

3.1.5 Harvesting of cells

Cells were harvested on ice by removing the medium from the cells and washing them twice with PBS. Cells were scraped and subsequently suspended in full DMEM medium. The suspension was transferred into a reaction tube and cells were pelleted (5 min, 500 × g, 4°C). After removing the supernatant, cell pellets were either frozen in liquid nitrogen and stored at -80°C or immediately processed.

3.1.6 IL-1α stimulation

To analyze the cell response to IL-1α, cells were seeded and cultured as described above. The cell confluence was then microscopically controlled before IL-1α (10 ng/ml) stimulation was performed for different periods of 30 min, 60 min, 120 min, 180 min, and 240 min. IL-1α-treated cells were always compared to non-treated control cells. After the stimulation, cells were further processed corresponding to the sample preparation steps of the experiment.

3.1.7 Starving cells with HBSS

The starvation-induced cell response was monitored by washing the cells four times with HBSS after they were seeded and cultured as described above. Cells were then incubated in HBSS for different periods of 30 min, 60 min, 120 min, and 240 min. Starved cells were compared to non-treated control cells or cells washed four times with HBSS and supplemented with their own culture medium to exclude that there were effects caused by the washing procedure alone. After starving cells, they were further processed according to the sample preparation steps of the experiment.

3.1.8 Transfection of cells with Polyethyleneimine

For transient transfection of cells with expression vectors, the polyethyleneimine (PEI) technique was used. PEI is a cationic polymer that forms PEI:DNA complexes, which then bind to anionic cell surfaces. They are consequently endocytosed by cells and released into the cytoplasm [151–153]. Transfection was performed at approximately 70% confluence using the following reaction mixture (exemplarily shown for 6-well condition, however, volumes were upscaled for larger dishes):

1 reaction	**Component**
100 µl	Opti-MEM (serum-free medium)
5 µg	Plasmid-DNA
12 µl	Branched PEI (1 mg/ml, pH 7)
added to 2 ml	DMEM (w/o Pen./Strep.)

Pre-warmed Opti-MEM was mixed with Plasmid-DNA and ice-cold branched PEI, vortexed, and incubated for 10 min at RT. After incubation, DMEM (w/o Pen./Strep.) was added to the mixture which was repeatedly vortexed and carefully spread over the cell layer after the culture medium was aspirated. Cells were then incubated overnight (24 h) at 37°C and 6% CO_2 until they were further analyzed.

3.1.9 Transfection of cells with Lipofectamine

Lipofectamine was used to introduce CAPTURE expression vectors into cells, to generate stable dCas9-BirA expressing cell lines (CAPTURE 1.0). Similar to many other transfection reagents, Lipofectamine is a cationic lipid that takes up negatively charged DNA or siRNA by forming liposomes. Positively charged liposomes merge with the cell membrane and release packaged DNA into the cytoplasm through the endocytosis pathway. To transfect cells with Lipofectamine a transfection mixture was prepared as follows (exemplarily shown for 6-well condition, however, volumes were upscaled for larger dishes):

1 reaction	**Component**
300 µl	Opti-MEM (serum-free medium)
6 µl	Lipofectamine
3 µl	Plus Reagent
3 µg	Plasmid-DNA

Lipofectamine was mixed with 150 µl pre-warmed Opti-MEM, while Plasmid-DNA and then Plus Reagent was added to 150 µl Opti-MEM in a separate reaction tube. The mixtures were subsequently united and incubated for 5 min at RT. Following incubation, the transfection mixture was trickled over the cells which were then incubated overnight (24 h) at 37°C and 6% CO_2. Afterwards, stable HeLa cell monoclones were generated as described in section 3.1.11.

3.1.10 Transfection of cells with Hi-PerFect Reagent

RNA interference (RNAi) was used to transiently knock down a set of proteins. RNAi is an endogenous mechanism in eukaryotic cells by which target genes are specifically silenced. This gene silencing is mediated by double-stranded, small interfering RNA (siRNA) molecules. A siRNA mediates mRNA decay by recruiting the Argonaute ribonuclease to its corresponding mRNA, thereby forming an RNA-protein complex also called RNA-induced silencing complex (RISC). This complex successively binds and digests several mRNA molecules and moreover, prevents translation of the target mRNA. The quantity of a specific mRNA and protein is therefore strongly reduced.

Transfection of specific siRNAs was carried out to knock down p65, TFE3, TFEB, or GLIS2 in HeLa cells. Cells were seeded in 60 mm culture dishes and grown overnight. The medium was reduced to 3 ml and a transfection mixture was prepared as follows:

1 reaction	Component
187.5 µl	Opti-MEM (serum-free medium)
15 µl	Hi-PerFect Transfection Reagent
60 µl	siRNA (1 µM, 20 nM final)

The reaction mixture was vortexed and incubated for 10 min at RT, subsequently dripped on the culture dish, and gently mixed. After 6 h of incubation, the transfection mixture was aspirated and replaced by 4 ml fresh full DMEM medium. Cells were then incubated for 48 h until they were further processed.

3.1.11 Generation of stable transfected cell monoclones

To generate HeLa cells stably expressing deactivated Cas9 (dCas9) and BirA, Lipofectamine transfection was performed as previously described (3.1.9). One day after the transfection, cells were split in a 1:10 ratio and cultured for one more day until medium containing the selection markers puromycin (0.75 µg/ml) and blasticidin (7.5 µg/ml) was added. Cells were then selected for 7 days up to the time when untransfected control cells were completely dead. After 7 days, the selection was stopped and cells were grown in full DMEM medium up to confluence. Confluent cells were then seeded on five 100 mm dishes in low density (100 cells/100 mm dish). Monoclones were grown until single colonies became visible. Monoclone colonies were then picked and each one was transferred into a 12-well using sterile Q-tips which were moisturized in the medium before colony picking. Monoclones were further grown and transferred to a 6-well. Confluent 6-well cells were finally transferred to another 6-well for Western blot analysis (3.4.6) and a 60 mm dish for cryo-conservation (3.1.1).

3.1.12 Lentivirus production and harvesting

The lentivirus was used as vector to stably integrate sgRNA (mCherry) and dCas9-CBio (zsGreen1) sequences into cells (CAPTURE 2.0) or to introduce Cas9-sgRNA (Puro) sequences for the generation of stable gene knockouts. The lentiviruses were produced by HEK293FT cells using the second-generation packaging plasmids: pMD2.G encodes the viral envelope protein and psPAX2 encodes the packaging proteins for the viral assembly and formation. Both, packaging and envelope plasmids, were transfected together with the specific transfer plasmid into HEK293FT producer cells. One day before transfection, 1.8 × 10^7 cells were seeded in T175 flasks and grown in 45 ml DMEM (++++) medium overnight (24 h) at 37°C. On the following day, a transduction mixture was prepared for each lentiviral transfer plasmid as follows:

Amount per T175 flask	**Component**
2250 µl	Opti-MEM (serum-free medium)
15.3 µg	pMD2.G (lentiviral envelope plasmid)
23.4 µg	psPAX2 (lentiviral packaging plasmid)
30.6 µg	Lentiviral transfer plasmid

In parallel, a Plus Reagent mixture was prepared and mixed by inverting:

Amount per T175 flask	**Component**
2250 µl	Opti-MEM (serum-free medium)
297 µl	Plus Reagent

Both mixtures were then combined, inverted, and incubated at RT for 5 min. During this time, the Lipofectamine mixture was prepared and inverted to mix:

Amount per T175 flask	**Component**
4500 µl	Opti-MEM (serum-free medium)
270 µl	Lipofectamine

The lentiviral target and Plus Reagent mixture was added to the Lipofectamine mixture, inverted, and incubated at RT for 5 min. In the last step, 9 ml of the resulting mixture was pipetted into each T175 flask and mixed by gently shaking the culture vessel. Cells were then returned to the incubator for 4 h until the medium was replaced with 45 ml pre-warmed DMEM (++++) medium.

48 h post-transfection, the virus-containing supernatant of each T175 flask was collected in a 50 ml tube and the transfection efficiency of producer cells was controlled by fluorescence microscopy. The constitutive GFP expression vector served as a transfection control. The lentiviral supernatant was next cleared of cell debris by centrifugation (5 min, 500 × g, RT), subsequently filtered using 0.45 µm sterile syringe filters, and the lentivirus-containing flow-through was collected in a new 50 ml tube. The lentiviral supernatants were either stored at -80°C or directly used for the transduction as described in the section below (3.1.13).

3.1.13 Lentiviral transduction

To generate stable expressing CAPTURE 2.0 cells or stable gene knockout cells, respectively, parental HeLa cells were transduced with lentiviral vectors carrying different sgRNA (mCherry) and dCas9-CBio (zsGreen1) or combinations of Cas9-sgRNA (Puro). The lentiviral transduction was carried out as follows: 1.8×10^5 cells were seeded in 6-well using full DMEM medium. On the following day, 8 µg/ml polybrene was added to each 6-well and incubated for 10 min at 37°C. As cationic polymer, polybrene increases the transduction efficiency by neutralizing the charge between the virus and cell surface. In the next step, 500-1000 µl of the desired viral stock was supplemented to the well and mixed by gently shaking the culture vessel. Cells were returned to the incubator and transduced overnight (24 h). One day after the transduction, cells were expanded to larger culture vessels as follows: HeLa knockout cells were expanded to 100 mm dishes and cultured for one more day until medium containing the selection marker puromycin (0.75 µg/ml) was added. After selecting the cells for 10-14 days, confluent cells were harvested, analyzed by Western blot (3.4.6), and stored through cryo-conservation (3.1.1). In contrast to that, five confluent 6-wells of CAPTURE 2.0 transduced cells were expanded to one T145 dish and grown for 48 h until they were confluent. The cells were then harvested for FACS to select the top mCherry/zsGreen1 positive cells as described in section 3.1.14.

Analysis of cell culture supernatants after lentiviral transduction

Confirmation that supernatants were free of virus and no longer infectious was required to proceed working under safety level S1 condition. 200 µl culture supernatant of the transduced cells was therefore retained and analyzed in comparison to a dilution series of the viral stock. Both, the supernatant and viral stock, were therefore purified using the Quick-RNA™ Viral Kit. The RNA content was next measured by NanoDrop and an input of 10 ng of each sample was used for cDNA synthesis. The cDNA of the viral stock was next diluted 1:10, $1{:}10^2$, $1{:}10^3$, $1{:}10^4$, and $1{:}10^5$ in nuclease-free H_2O and served as standard reference curve from which the viral titer was estimated upon qPCR analysis. The analysis was conducted using primers against the WPRE or HIV-Psi element which are present in the lentiviral target vectors.

3.1.14 Fluorescence-activated cell sorting

Fluorescence-activated cell sorting (FACS) was carried out to select stable transduced HeLa cells by their sgRNA (mCherry) and dCas9-CBio (zsGreen1) expression. As described above, CAPTURE 2.0 transduced HeLa cells were expanded in a T145 dish and grown for 48 h until they were confluent. On the day of sorting, cells were washed twice with pre-warmed 1X DPBS, trypsinized, and suspended in 10 ml full DMEM medium. Cells were next pelleted (5 min, 300 × g, RT), suspended in 500 µl full DMEM medium, and pipetted through the filter of a FACS-specific 5 ml falcon tube. FACS was performed by a unit of the Department of Medicine V, Internal Medicine, Infectious Diseases and Infection Control of the University Hospital Gießen and Marburg (UKGM) under the direction of Prof.

Dr. med. Susanne Herold, PhD located at the Biomedical Research Center Seltersberg. The cells were sorted per cell line by flow cytometry using the BD FACSAria and the BD FACSDiva 8.0.2 software. As shown exemplarily in Figure 6, the cell size and granularity were visualized in an SSC (sideward scatter, y-axis) / FSC (forward scatter, x-axis) dot plot. Cell doublets were discriminated within dot plots using the parameters FSC-H (Height) and FSC-A (Area). Gated singlets were visualized for mCherry or zsGreen1 fluorescence as histograms using the mCherry (red) or FITC (green) channel. Cells with high fluorescence signals were gated and thereby separated from cells with low fluorescence signals. Following the sorting, cells were centrifuged (5 min, 300 × g, RT) and the supernatants discarded thoroughly to clear cells from the FACS reagent. The sorted cells were suspended in 2 ml fresh full DMEM medium and transferred to a 6-well to be further cultivated for cryo-conservation (3.1.1) and the experimental use.

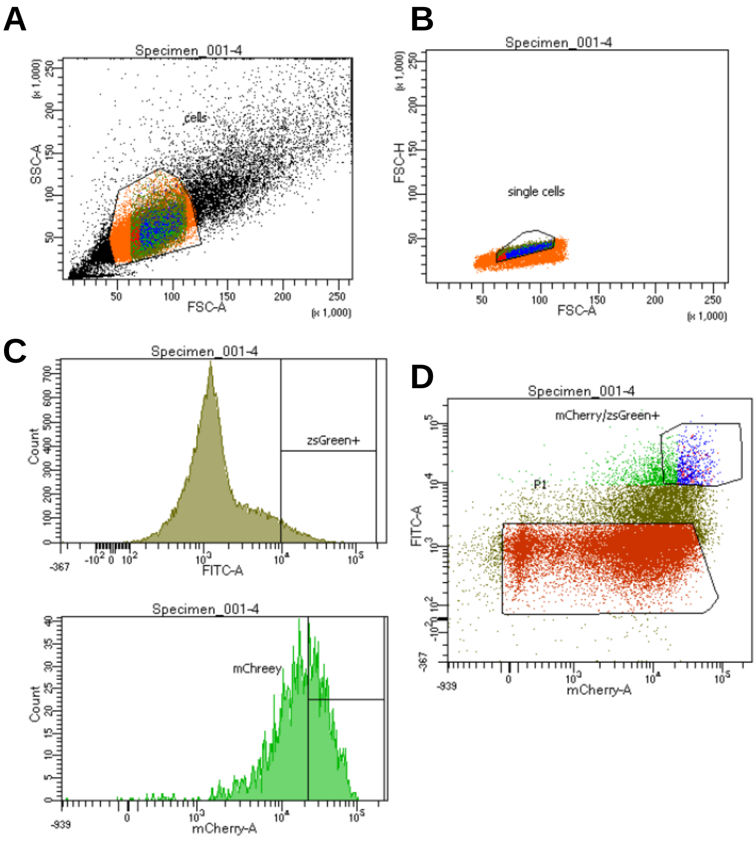

Figure 6: Fluorescence-activated cell sorting of zsGreen1 and mCherry positive CAPTURE 2.0 cells. HeLa cells transduced with dCas9-CBio-zsGreen1 and sgRNA-mCherry plasmids from the CAPTURE 2.0 system were sorted by FACS using the BD FACSAria and the BD FACSDiva 8.0.2 software. (A) The transduced cells were gated according to their cell size and granularity and plotted on a SSC (sideward scatter, y-axis) / FSC (forward scatter, x-axis) dot plot. (B) Cell doublets were discriminated within dot plots by FSC-H (Height) and FSC-A (Area) parameters. (C) Gated singlets were visualized for mCherry or zsGreen1 fluorescence as histograms using the mCherry (red) or FITC (green) channel. (D) The population of top zsGreen1/mCherry positive cells was gated (upper right gate) and separated from negative cells and cells with low fluorescence signals. The diagrams belong to the sorting of HeLa-dCas9-CBio-sg*CXCL3* cells and are presented as examples.

3.2 Methods in Microbiology

3.2.1 Cultivation of bacteria

E. coli mini cultures of 3-5 ml and maxi cultures of 200 ml were prepared by inoculating LB medium without antibiotic, or the specific selection antibiotic ampicillin or kanamycin with bacterial glycerol stocks, or freshly transformed *E. coli* colonies. Bacteria were then cultured for 16-18 h at 37 °C and 160 rpm until further processing as described in sections 3.2.2 and 3.3.9.

3.2.2 Preparation of chemical-competent bacteria

Mini cultures of TOP10 or XL-1 Blue *E. coli* bacteria without antibiotics were prepared according to section 3.2.1. Afterwards, 50-150 ml LB medium without antibiotic was inoculated with a small volume of the mini culture from the day before to an approximate optical density (OD) of 0.05 which was determined by the SpectraMax Plus photometer at 595 nm. Once the bacterial culture reached an OD of 0.3-0.5, the bacteria were pelleted (10 min, 1390 × g, 4°C). The following steps were performed quickly and always on ice. The pellet was suspended in ice-cold TSS buffer which was one-tenth of the original volume and then aliquoted in batches of 200 µl. Competent bacteria were frozen in liquid nitrogen and stored at -80°C.

3.2.3 Transformation of bacteria

<u>Transformation of TOP10 or XL-1 Blue *E. coli*</u>

For transformation of TOP10 or XL-1 Blue *E. coli* bacteria, 2 µg of plasmid DNA or the full ligation mixture was added to 100 µl competent bacteria and incubated on ice for 20 min. After incubation, heat shock was performed for 45 sec at 42°C, and bacteria were immediately placed on ice for 2 min. Then 500 µl of pre-warmed LB medium was added to the suspension and bacteria were recovered while shaking for 1 h at 37°C and 300 rpm. The bacteria were finally spread on an agar plate containing the selection-specific antibiotic ampicillin or kanamycin and grown overnight at 37°C to obtain *E. coli* colonies.

<u>High Efficiency Transformation of NEB® Stable Competent *E. coli*</u>

For high-efficiency transformation of NEB® Stable Competent *E. coli* bacteria, one tube of bacteria was thawed on ice for 10 min. Next, 100 ng of plasmid DNA or 2 µl of the ligation mixture was added and the suspension was carefully mixed. After that, cells were incubated on ice for 30 min until heat shock was performed for 30 sec at 42°C. Bacteria were immediately placed on ice for 5 min, then 950 µl of room temperature NEB 10-beta/Stable Outgrowth Medium was added to the mixture and the tube was shaken horizontally for 1 h at 30°C and 250 rpm. The tube was next inverted and 50-100 µl of cells were spread onto a pre-warmed agar plate containing the selection specific antibiotic ampicillin or kanamycin and grown overnight at 37°C to obtain *E. coli* colonies.

3.2.4 Preparation of bacterial glycerol stocks

Bacteria were permanently stored in cryo-tubes by mixing 500 µl *E. coli* culture with 500 µl of pure glycerol. The bacterial glycerol stock was then frozen in liquid nitrogen and stored at -80°C for the inoculation of new bacterial cultures.

3.3 Methods in Molecular Biology

3.3.1 Design of sgRNAs and important considerations

The sgRNAs were designed for CAPTURE promoter targeting or the generation of stable gene knockouts. For this purpose, the sequence of the target gene and the 1000 bp regions upstream of the transcription start and downstream of the stop codon were extracted from the UCSC genome browser on human GRCh37/hg19 (Feb.2009). The sequence was next transferred to the SeqBuilder application of the DNASTAR navigator to generate a sequence file of the target gene. Within the SeqBuilder file exons marked in upper cases and introns marked in lower cases were additionally labeled with the respective number. For picking promoter targeting CAPTURE sgRNAs, 500-1000 nucleotides upstream from the transcription start site of the gene were selected and transferred to the CHOPCHOP webtool. The tool ranks the best 20 nt sgRNA picks and provides information about the genomic location, target efficiency, and orientation of the sgRNA. In the next step, bed files with the genomic coordinates of the top 3 sgRNAs were uploaded to the IGV genome viewer. The sgRNA binding sites were assessed with respect to ChIP-seq and ATAC-seq data from KB cells treated with IL-1α for 1 h, to ensure that sgRNAs bind to accessible chromatin regions and do not interfere with p65 or RNA-Polymerase II (Pol II) binding sites. According to these additional criteria, the best sgRNA candidate was selected for subsequent cloning into the pSLQ1651 expression vector as described in section 3.3.7. The sgRNAs used for the gene knockouts were picked by selecting about 1000 nucleotides downstream from the transcription start site of the gene. The gene sequence was next transferred to the CRISPick webtool provided by the Broad Institute. The CRISPick tool likewise produces a list of top-ranking 20 nt sgRNAs with similar information as CHOPCHOP provides. From the list, the top 3-6 sgRNAs were chosen and the sequences were marked in the already generated SeqBuilder gene sequence. In the Seqbuilder application, the sgRNAs targeting the gene were virtually tested for efficiency to achieve double-strand breaks. The cut site occurs within the sgRNA binding sequence 3-5 bases off the 5’-3’ end from the PAM sequence (NGG). The sgRNAs that produced the change in the downstream translational sequence, through either a premature stop codon or a frameshift in the amino acid sequence after the cut site, were then selected as the candidate sgRNAs for cloning into the Lenti-CrisprV2 expression vector as described in section 3.3.8.

3.3.2 Design of primers and important considerations

Primers were designed (i) to generate cloning inserts with restriction sites, (ii) validate plasmids by Sanger sequencing or (iii) quantify DNA by SYBR Green-based qPCR. For this purpose, the genomic sequence of interest was extracted from the UCSC genome browser on human GRCh37/hg19 (Feb.2009) and plasmid sequences were downloaded as GenBank files from Addgene. The sequence was next uploaded to the SeqBuilder application of the DNASTAR navigator to generate a sequence file. Within the sequence file, the sequence of interest was selected and transferred to the Primer3 Plus webtool. Based on this sequence, Primer3 Plus generates a list of 18-24 bp primers or primer pairs with melting temperatures between 57°C and 63°C and GC contents of 40-60% that are suitable for PCR amplification or Sanger sequencing. Primer pairs for generating cloning inserts were designed as follows: at the 5’ end of the primer, 3-6 extra bp were added to increase the restriction efficiency, the 5’ to 3’ sequence of the restriction site, and 5’ to 3’ sequence of the forward or reverse primer. Unique restriction sites which were mainly selected from the multiple cloning site were allowed to occur only once within the target plasmid, but not within the insert sequence. The optimal annealing temperature for each primer pair was determined by gradient PCR and the extension time was calculated based on the general rule of 15 sec/1 kb of the PCR product size and individually adjusted for each PCR reaction in section 3.3.3. For generating Sanger sequencing or SYBR qPCR primers, the Primer3 Plus default settings were applied. Primers for Sanger sequencing were placed 50 bp upstream of the sequence to be tested. Primer pairs with a product size of 150-250 bp were designed for SYBR qPCR. In all cases, primers were chosen with a low self-hybridization value of preferably 0.0 or 1.0.

3.3.3 DNA amplification by the polymerase chain reaction

The Phusion™ high-fidelity DNA polymerase was used for insert DNA amplification as it has a low error rate for mutations and is therefore well suited for cloning. Unless otherwise stated, the PCR reaction was composed as follows:

1 reaction	Component
10 µl	5X Phusion HF reaction buffer
2 µl	10 µM forward primer
2 µl	10 µM reverse primer
1 µl	10 mM dNTP
1 µl	1 ng DNA donor/template plasmid
0.5 µl	2 U/µl Phusion polymerase
33.5 µl	Nuclease-free water

The PCR reaction was conducted in the thermocycler using the following temperature profile to generate DNA inserts for cloning sgRNAs into the pSLQ1651-sgRNA(F+E)-sgGal4 vector:

Phases	Temperature [°C]	Time	Cycles
Initial denaturation	98	2 min	1
Denaturation	95	10 sec	30
Annealing	60	15 sec	
Elongation	72	30 sec	
Final extension	72	2 min	1
Pause	4	(hold)	-

The temperature profile below was used with the before determined annealing temperatures and elongation times to generate the DNA inserts for cloning the blasticidin-resistance cassette into BirA-V5-neo (63°C, 8-9 sec) or for cloning p65 gene variants into the HA-miniTurbo vector (69°C, 25 sec).

Phases	Temperature [°C]	Time	Cycles
Initial denaturation	98	30 sec	1
Denaturation	98	10 sec	35
Annealing	x	30 sec	
Elongation	72	x	
Final extension	72	10 min	1
Pause	4	(hold)	-

For the PCR control, 5 µl of the PCR product was supplemented with 1 µl 6X DNA Loading Dye and analyzed for the expected product size by agarose gel electrophoresis as described in detail in section 3.3.4. The residual 45 µl of the PCR product was purified using the NucleoSpin® Gel and PCR Clean-Up Kit from Macherey-Nagel and eluted in 15 µl elution buffer.

3.3.4 Agarose gel electrophoresis with ethidium bromide or methylene blue DNA staining

Agarose gel electrophoresis is a technique that allows the separation of DNA fragments according to their size and charge. In this work, the method was utilized to (i) assess the extent of chromatin fragmentation upon sonication, (ii) verify correct PCR amplification or (iii) extract restriction-digested donor vectors in the cloning procedure. Before running the gel, nucleic acids were mixed 1:6 with 6X DNA Loading Dye. A volume of 8 µl GeneRuler DNA Ladder Mix was run simultaneously on each gel to estimate DNA fragment sizes. The procedure for PCR amplicons and sheared chromatin differed slightly from the procedure for restriction-digested donor vectors. PCR amplicons and sheared chromatin were separated on a 1% or 2% TAE agarose gel with 0.1 µg/ml ethidium bromide. The gel was run for 40 min at 100 V in 1X TAE buffer using the Mupid-exU electrophoresis system. Ethidium bromide-stained nucleic acids were visualized under UV light using the Gel iX Imager UV transilluminator. The restriction-digested donor vectors were likewise supplemented with 6X DNA

Loading Dye, but run on a 1.2% TAE agarose gel w/o ethidium bromide for 1 h at 100 V. This way the digested vector DNA was separated from the digested DNA fragment. Afterwards, DNA was stained with 0.02% methylene blue for 15-30 min and decolorized with ddH_2O until DNA bands were visible. The band corresponding to the expected size of the linearized digested vector was excised from the gel and the DNA was then extracted with the NucleoSpin® Gel and PCR Clean-Up Kit from Macherey-Nagel using 15 µl elution buffer.

3.3.5 Cloning the HA-miniTurbo vector

For generating pTet-on-Puro-HA-miniTurbo(EV), the linker-HA-miniTurbo sequence was synthesized by General Biosystems and provided in donor vector pUC57-BsaI-Free. To obtain the linker-HA-miniTurbo insert, 2 µg of the donor plasmid or 2 µg target plasmid pTet-on-Puro-Myc-BirA(EV) were subjected to a restriction digestion reaction with FastDigest MluI and BshTI/AgeI according to the reaction described in the following section (3.3.6). After enzymatic restriction, the digested linker-HA-miniTurbo insert and target vector was separated from the remaining digestion product on an agarose gel and purified following methylene blue staining (3.3.4). DNA concentrations were measured by the NanoDrop. The digested linker-HA-miniTurbo insert and pTet-on-Puro vector backbone were next ligated in 1:3 amplicon to vector relation in a 20 µl reaction which was set up as described in the following section (3.3.6). The amount of insert DNA (14.46 ng) was calculated using the NEBioCalculator webtool. After the reaction was completed, the full volume of the ligation product was transformed into *E. coli* bacteria (3.2.3). Three *E. coli* clones were picked for mini cultures (3.2.1), plasmids were subsequently isolated (3.3.9), and controlled for the insertion of the linker-HA-miniTurbo sequence by Sanger sequencing. The HA-miniTurbo_insert_seq forward or reverse primers were used (3.3.10).

3.3.6 Cloning the blasticidin-resistance cassette into pEF1a-BirA-V5-neo and p65 gene variants into the HA-miniTurbo vector

The PCR for cloning the blasticidin-resistance cassette into pEF1a-BirA-V5-neo was carried out according to section 3.3.3 using donor vector plenti-dCAS9(D10A, N863A)-VP64_2A_Blast with the forward and reverse primers cloning_blasticidin_1 listed in section 2.10. After PCR amplification the resulting amplicons as well as target vector pEF1a-BirA-V5-neo were enzymatically digested by FastDigest SmaI and PfoI through the 15 µl reaction mixture specified below.

The PCR for cloning p65 gene variants into the HA-miniTurbo(EV) vector was likewise performed as described in section 3.3.3 based on the donor vectors pEF-Puro-hu p65 WT-HA, p65 E/I-HA, and p65 FL/DD-HA together with the forward and reverse primers cloning_p65_1 listed in section 2.10. The resulting PCR amplicons as well as target vector pTet-on-Puro-HA-miniTurbo(EV) were next digested by FastDigest BshTI/AgeI and Bsp1407I/BsrGI by the following 15 µl reaction:

PCR amplicon	Vector	Component
0.2 µg digested PCR amplicon	2 µg digested target vector	DNA
2 µl	2 µl	10X FastDigest Buffer
1 µl	1 µl	FastDigest enzyme 1
1 µl	1 µl	FastDigest enzyme 2
added to 30 µl	added to 20 µl	Nuclease-free water

The reaction was incubated in the thermocycler at 37°C for 15 min. Digested PCR amplicons were purified using the NucleoSpin® Gel and PCR Clean-Up Kit from Macherey-Nagel. The digested target vector was separated from its digestion product on an agarose gel and purified following methylene blue staining as described in section 3.3.4. DNA concentrations were measured by the NanoDrop. The digested PCR amplicon and vector were next ligated in 1:3 amplicon to vector relation. The amount of PCR amplicon for the blasticidin-resistance cassette (10.65 ng) and p65 gene variants (26.24 ng) was calculated using the NEBioCalculator webtool. The 20 µl ligation mixture was set up as follows:

1 reaction	Component
x ng	digested PCR amplicon
50 ng	digested target vector
2 µl	NEB T4 ligase buffer
1 µl	NEB T4 ligase
added to 20 µl	Nuclease-free water

The reaction was incubated for 10 min at RT and the ligase was heat inactivated for 10 min at 65°C. The full volume of the ligation product was subsequently transformed into *E. coli* bacteria as described in section 3.2.3. Three *E. coli* clones were picked for mini cultures (3.2.1), plasmids were subsequently isolated (3.3.9), and checked for the insertion of the sgRNA sequence by Sanger sequencing. The SV40-Do primer was chosen for verification of the blasticidin-resistance cassette whereas the miniTurbo_fusion_seq forward or reverse primers were designed for the p65 gene variants (3.3.10).

3.3.7 Cloning of sgRNAs into the CAPTURE pSLQ1651 vector

The cloning of sgRNA sequences into the pSLQ1651 vector was performed according to the protocol published by Liu et al. (2018) [147]. PCR was conducted according to section 3.3.3 using donor vector pSLQ1651-sgRNA(F+E)-sgGal4, sgRNA-specific forward primers, and the universal reverse primer listed in section 2.10. The resulting PCR amplicon and target vector pSLQ1651-sgRNA(F+E)-sgGal4 were next enzymatically digested by the following 15 µl reaction mixture:

PCR amplicon	Vector	Component
12.5 µl PCR amplicon	1 µg target vector	DNA
1.5 µl	1.5 µl	10X FastDigest Buffer
0.5 µl	0.5 µl	FastDigest BstXI
0.5 µl	0.5 µl	FastDigest XhoI
added to 15 µl	added to 15 µl	Nuclease-free water

The reaction was incubated in the thermocycler at 37°C for 15 min. Digested PCR amplicons were purified using the NucleoSpin® Gel and PCR Clean-Up Kit from Macherey-Nagel. The digested pSLQ1651 vector was separated from its digestion product on an agarose gel and purified following methylene blue staining as described in section 3.3.4. DNA concentrations were measured by the NanoDrop. The digested PCR amplicon and vector were next ligated by the following 10 µl reaction mixture:

1 reaction	Component
100 ng (5 µl)	digested PCR amplicon
200 ng (1 µl)	digested pSLQ1651 vector
1 µl	NEB T4 ligase buffer
1 µl	NEB T4 ligase
added to 10 µl	Nuclease-free water

The reaction was incubated for 10 min at RT. The full volume of the ligation product was next transformed into *E. coli* bacteria (3.2.3). Two *E. coli* clones of each sgRNA plasmid were picked for mini cultures (3.2.1), plasmids were subsequently isolated (3.3.9) and controlled for the insertion of the sgRNA sequence by Sanger sequencing (3.3.10) using the U6-Vector_seq forward or reverse primer.

3.3.8 Cloning of sgRNAs into the Lenti-CrisprV2 vector

For cloning sgRNAs into the Lenti-CrisprV2 vector, the sense and anti-sense strands of the single-stranded oligonucleotides listed in section 2.10 were annealed. One annealing reaction was composed as follows:

1 reaction	Component
1 µl	Each single-stranded oligonucleotide (se + as)
5 µl	T4 PNK buffer A
43 µl	Nuclease-free water

Annealing was performed in the thermocycler using the following temperature profile:

Temperature [°C]	Time [min]
95	4
70	10
37	15

In the second step, the annealed oligonucleotide was phosphorylated in a 10 µl reaction mixture as follows:

1 reaction	Component
2 µl	Double-stranded oligonucleotide
1 µl	T4 PNK buffer A
1 µl	ATP (1 mM)
1 µl	T4 PNK
5 µl	Nuclease-free water

Phosphorylation was conducted in the thermocycler using the following temperature profile:

Temperature [°C]	Time [min]
37	30
70	10

After the reaction was completed, the phosphorylated oligonucleotide was diluted 1:8 in nuclease-free water and supplemented to the following 20 µl reaction mixture for simultaneous restriction and ligation:

1 reaction	Component
100 ng (3µl)	Lenti-CrisprV2 empty vector
2 µl	Phosphorylated ds-oligonucleotide (diluted 1:8)
2 µl	FastDigest buffer
1 µl	ATP (10 mM)
1 µl	FastDigest Esp3l (BsmBI) (10 U/µl)
1 µl	T4 DNA ligase
10 µl	Nuclease-free water

Restriction and ligation were performed in the thermocycler using the following temperature profile:

Temperature [°C]	Time [min]	Cycles
37	5	6
21	5	

Once the reaction was completed, the full volume of ligated plasmid DNA was transformed into NEB® Stable Competent *E. coli* bacteria (3.2.3). Two *E. coli* clones of each sgRNA plasmid were picked for mini cultures (3.2.1), plasmids were subsequently isolated (3.3.9) and controlled for the insertion of the sgRNA sequence by Sanger sequencing (3.3.10). The hU6-fwd primer was selected to verify the correct sgRNA insertion.

3.3.9 DNA extraction

The extraction of plasmid DNA from bacterial mini or maxi cultures was performed using the NucleoSpin® Plasmid Kit for mini preps and the NucleoBond® PC500 Kit or NucleoBond® Xtra Midi Kit for maxi preps according to the manufacturer’s instructions. The eluted plasmid DNA was directly processed or stored at -20°C for longer storage periods.

3.3.10 Sanger sequencing

To verify the cloning of DNA inserts into target plasmids, the purified plasmid DNA was sent alone or as pre-mixture with the specific sequencing primer (2.10) to LGC Genomics or Microsynth according to the instructions provided by the company. The resulting FASTQ files were analyzed with the SeqMan Pro application from the DNASTAR software.

3.3.11 Isolation of RNA

Total RNA was isolated with the use of NucleoSpin® RNA Kit according to the manufacturer's protocol. RNA was eluted in 30-60 µl nuclease-free water and instantly processed or kept at -80°C for longer storage periods.

3.3.12 Measurement of nucleic acid concentrations

The concentration and purity of DNA and RNA were determined by the NanoDrop ND-1000 Spectrophotometer. This is a UV light-based method that detects the absorbance of a nucleic acid or protein sample at a certain wavelength. Nucleic acid concentration was measured in a sample volume of 1.5 µl at a wavelength of 260 nm. In parallel, absorbance was measured at 280 nm resulting in an A_{260}/A_{280} ratio. The absorbance ratio determines the purity of the isolated nucleic acids with respect to protein impurities and should not fall below or exceed a value of 1.9 to 2.2.

3.3.13 Reverse transcription

Reverse transcription was performed to synthesize complementary DNA (cDNA) from total RNA, which was subsequently used for qPCR (3.3.14). The reaction was catalyzed by the enzyme RevertAid reverse transcriptase. A reaction volume of 20 µl was composed as follows:

1 reaction	Component
1 µg	Total RNA
0.5 µl	Random Hexamer Primer
0.5 µl	dNTP (10mM)
0.5 µl	RevertAid reverse transcriptase
4 µl	Reaction buffer for reverse transcription 5X
x µl	Nuclease-free water

Reverse transcription was performed in the thermocycler using the following temperature profile:

Temperature [°C]	Time [min]
25	10
42	60
70	10

3.3.14 Quantitative polymerase chain reaction

The quantitative polymerase chain reaction (qPCR) was used to determine the relative amount of mRNA in a total cell population after reverse transcription (RT-qPCR) or to determine the relative amount of precipitated DNA following ChIP experiments (ChIP-qPCR). The qPCR is a fluorescence-based method that is commonly performed by applying the TaqMan method or by using the fluorescent dye SYBR Green I. RNA samples of this work were mainly analyzed by the TaqMan method and DNA samples were analyzed by the SYBR Green I method.

TaqMan-based qPCR

The TaqMan method includes a TaqMan probe that consists of a gene-specific nucleotide, which carries a fluorophore (FAM) at its 5' end and a quencher at its 3' end. According to the principle of Förster resonance energy transfer (FRET), the quencher weakens the fluorescence by the fluorophore. In addition to the TaqMan probe, a primer pair is used for the amplification of a gene. The TaqMan probe binds the annealing region in between the primer pair. During elongation, Taq polymerase extends the primer and synthesizes each new complementary DNA strand in 5′ to 3′ direction. During synthesis, the enzyme comes across the probe, which is subsequently degraded by the 5′ to 3′ exonuclease activity of the Taq polymerase. Decay of the probe leads to spatial segregation between fluorophore and quencher, whereby the quencher is no longer suppressing the fluorescence emission. Thus, increasing amounts of amplified DNA elevate the number of probes that are released. Correspondingly, the fluorescence signal increases with every cycle and is detected by the PCR device.

SYBR Green I-based qPCR

The SYBR Green I method is likewise based on a specific primer pair to amplify the genomic region of interest. This procedure, however, uses the SYBR Green I fluorescent dye that binds the minor groove of double-stranded DNA. When the SYBR Green I dye binds to DNA, the intensity of the fluorescence increases. The more double-stranded amplicons are produced within each cycle, the more the SYBR Green fluorescence increases. In both methods, the increase in fluorescence signal is measured and finally displayed in an amplification plot showing the fluorescence intensity at a rising cycle number for each sample. To compare samples among each other, a cycle threshold (C_T value) is set, at which the fluorescence signal just differentiates from the background signal, since at this time point amplification of the template is still exponential. The higher the C_T value of a sample, the more RNA or DNA template was present in the initial sample. By that, the C_T value allows indirect conclusions about the initial quantity of an RNA or DNA template in a sample. Thus, this method enables the measurement of expressed mRNA or precipitated DNA and allows the comparison between samples.

In this work, qPCR was applied to determine relative mRNA levels of various genes of interest (GOI). Second, it was used to analyze RNAi efficiencies on the mRNA level after the siRNA-mediated knockdowns of 38 p65/RELA interactors (3.3.15). Third, qPCR measurements were performed to analyze relative amounts of a genomic region of interest (ROI) in precipitated chromatin samples after antibody-based ChIP (3.3.16) or biotin-streptavidin-based CAPTURE-ChIP (3.3.17).

The cDNA from RNA samples served as a template for the TaqMan qPCR reaction. One 10 µl TaqMan qPCR reaction was composed as follows:

1 reaction	**Component**
5 µl	TaqMan® Fast Universal PCR master mix 2X
0.25 µl	TaqMan® Gene Expression Assay 20X
3.75 µl	Nuclease-free water
1 µl	DNA

For the SYBR qPCR reaction, the cDNA from RNA samples or precipitated DNA served as the template. One 10 µl SYBR qPCR reaction was composed as follows or upscaled accordingly:

1 reaction	**Component**
5 µl	FAST SYBR Green PCR master mix
0.25 µl	Forward primer (10 µM)
0.25 µl	Reverse Primer (10 µM)
3.5 µl	Nuclease-free water
1 µl	DNA

The TaqMan qPCR or SYBR qPCR master mix was prepared for each cDNA sample with a specific TaqMan assay or primer pair against the GOI, along with a separate master mix against a housekeeping gene (reference gene). For precipitated DNA, a SYBR qPCR master mix with a primer pair against the ROI was prepared. For each sample, a technical duplicate was measured for the GOI / ROI as well as the reference gene. Measurements were performed under the following temperature profile by using the 7500 Fast Real Time PCR System from Applied Biosystem:

Phases	**Temperature [°C]**	**Time [sec]**	**Cycles**
Initial denaturation	95	20	1
Denaturation	95	3	40
Annealing/elongation	60	30	

Importantly, SYBR Green PCR products were always validated according to their melting curve and showed only one product.

Evaluation of RT-qPCR measurements

C_T values derived from RNA experiments were evaluated using the $2^{-\Delta\Delta C_T}$ method. The normalization process was applied to determine the x-fold expression of a GOI relative to the untreated control. The first step of the method was to normalize the C_T value of a sample to the C_T value of a simultaneously measured reference gene (*GUSB*, *GAPDH*, or *ACTB*). In this way, any variations in the amount of input mRNA used were compensated:

$$\Delta C_T = C_T \text{ GOI} - C_T \text{ reference gene}$$

Next, ΔC_T values were normalized to an experimental control sample (calibrator) as follows:

$$\Delta\Delta C_T = C_T \text{ sample} - C_T \text{ calibrator}$$

Finally, $\Delta\Delta C_T$ values were converted into x-fold mRNA expression of the GOI as follows:

$$\text{x-fold mRNA expression} = 2^{-\Delta\Delta C_T}$$

Evaluation of ChIP-qPCR measurements

C_T values of ChIP and CAPTURE-ChIP experiments were evaluated by normalizing them to the quantity of input DNA of each sample. For this purpose, 1% input DNA of each ChIP sample and 5% of each CAPTURE-ChIP sample, respectively, were retained and analyzed by qPCR. Based on the percentage of input DNA the dilution factor was determined:

$$dilution\ factor = \frac{100\%}{input\ DNA}$$

After that, the amount of DNA was specified as percentage of used input DNA for each individual sample by the following equation:

$$\%\ input = \frac{100\%}{dilution\ factor} \times 2^{-(C_{\mathrm{T}}\ IP\ -\ \mathrm{C_T}\ input)}$$

In an antibody-based ChIP experiment rabbit IgG only and in CAPTURE-ChIP experiments no sgRNA or non-targeting sgGal4 served as controls to assess the background signal of qPCR measurements in each experiment. In the CAPTURE-ChIP, the promoter of housekeeping gene *GAPDH* was analyzed as an additional negative control to exclude off-target binding of dCas9-sgRNA complexes.

3.3.15 RNAi screen using the TaqMan® PreAmp Cells-to-CT™ Kit

To investigate the role of 38 HCI in the expression of prototypical NF-κB target genes, a miniaturized siRNA screen was performed using the TaqMan® PreAmp Cells-to-CT™ Kit. The kit enables to perform gene expression analyses of small numbers of cells without RNA purification. The three-step protocol includes cDNA synthesis directly from cell lysates, an intermediate amplification step (pre-amplification) by a defined pool of TaqMan® Gene-Expression Assays from Applied Biosystems, and real-time PCR measurement. 3×10^3 HeLa cells were therefore seeded in 210 µl full DMEM medium in 48-well and cultured overnight (24 h). Hi-PerFect siRNA transfection (3.1.10) was downscaled accordingly and applied as follows:

1 reaction	Component
12.5 µl	Opti-MEM (serum-free medium)
1 µl	Hi-PerFect transfection reagent
4 µl	siRNA (1 µM; 20 nM final)

38 HCI and *RELA* were targeted by pools of 3-4 gene-specific siRNAs and compared to siLuci, Hi-PerFect only (HP), or untreated control samples. The reaction mixture was vortexed and incubated for 10 min at RT, subsequently dripped on the cells, and gently mixed. After 6 h of incubation, the transfection mixture was aspirated and replaced by 250 µl fresh full DMEM medium. Cells were incubated for 48 h until treatment. One day before the treatment, the medium was changed and adjusted to 210 µl. Cells treated with IL-1α (10 ng/ml) for 1 h or untreated cells were trypsinized and transferred to RNase-free reaction tubes. They were then washed twice with ice-cold PBS and lysed in 12.5 µl Lysis Solution (DNase I was diluted at 1:100).

1 reaction	Component
12.375 µl	Lysis solution
0.125 µl	DNase I

Cells were mixed by vortexing, shortly centrifuged, and incubated at RT for 5 min. The reaction was stopped by adding 1.25 µl Stop Solution. After repeated mixing, samples were incubated for 2 min at RT. The reverse transcription was directly conducted on the lysates by mixing 4.5 µl lysate (or nuclease-free water as a control) with a 5.5 µl RT mixture that was prepared as follows:

1 reaction	Component
5 µl	RT Buffer 2X
0.5 µl	RT Enzyme Mix 20X

The reverse transcription was performed under the following temperature profile:

Temperature [°C]	Time [min]
37	60
95	5
4	∞

For the pre-amplification PCR, TaqMan assays were diluted 1:100 in TE Buffer. Two pools of specific TaqMan assays were used, with pool 1 containing assays for target genes 1-19 and pool 2 containing assays for target genes 20-38. Both pools were additionally supplemented with assays for three prototypical NF-κB target genes *IL8*, *NFKBIA* and *CXCL2* such as two housekeeping genes *GUSB* and *GAPDH*. The pre-amplification PCR mixtures of pool 1 and pool 2 were prepared as follows:

1 reaction	Component
5 µl	TaqMan PreAmp Master Mix 2X
2.5 µl	Pooled TaqMan assay mix (1:100; pool 1/pool 2)

The pre-amplification PCR was prepared by adding a 7.5 µl pre-amplification mixture of pool 1 or pool 2 to 2.5 µl cDNA from the completed RT reaction. Samples with siRNA targets 1-19 were supplemented with the mixture of pool 1 and samples with siRNA targets 20-38 were supplemented with the mixture of pool 2. Controls were supplemented with each of the two pre-amplification mixtures. The reaction was performed under the following temperature profile:

Temperature [°C]	Time	Cycles
95	10 min	1
95	15 sec	15
60	4 min	

For real-time PCR measurements, the pre-amplification product was diluted 1:5 by the addition of 40 µl 1X TE Buffer. The diluted pre-amplification product served as the template for the TaqMan qPCR reaction as described before (3.3.14). Specific TaqMan assays were used for the second time to determine the mRNA levels of NF-κB target genes (*IL8*, *NFKBIA*, *CXCL2*), housekeeping genes (*GUSB*, *GAPDH*) and siRNA target genes (38 targets, *RELA*) across samples.

After determining the expression levels of three prototypical NF-κB target genes (*IL8*, *NFKBIA*, *CXCL2*) by TaqMan qPCR, C_T values were normalized based on *GUSB*. Knockdown effects of 38 HCI and *RELA* were calculated separately for basal and IL-1α-inducible conditions against the luciferase siRNA. Finally, a heatmap of the targeted siRNA screen was generated that visualized the mean $\log_2$ ratios from three biologically independent RNAi screens for basal and IL-1α-inducible conditions. The underlying equations are presented in section 4.3.2.

3.3.16 Chromatin-immunoprecipitation (ChIP)

The chromatin-immunoprecipitation (ChIP) is an antibody-based technique that enables to determine the occupancy of specific proteins at precipitated chromatin regions. In this work, a dCas9-ChIP was performed and compared with the pulldown efficiency of dCas9 obtained with streptavidin-based CAPTURE-ChIP as described in the section below (3.3.17).

Chromatin preparation

Two T145 culture dishes were prepared for each ChIP sample by seeding 20×10^5 HeLa cells (per dish) and culturing them for two days. PEI transfection of the expression vectors was performed on day two to transiently express components of the CAPTURE 1.0 system (3.1.8). On the third day, the medium was reduced to 10 ml and cells were treated with IL-1α (10 ng/ml) for 1 h or kept untreated. Stimulation was stopped and protein:DNA complexes were crosslinked by adding 280 µl 37% formaldehyde (1% final) that was incubated for 10 min at RT. Formaldehyde fixation was quenched by adding 500 µl 2 M glycine that was incubated for 5 min at RT. Cells were next scraped, transferred to reaction tubes, and centrifuged (5 min, 3000 rpm, and 4°C). Supernatants were discarded and cell pellets were washed twice with 2 ml ice-cold 1X PBS with PMSF. Cell pellets were suspended in 2.5 ml lysis buffer with PMSF and Roche and incubated on ice for 10 min. Lysate aliquots of 1 ml were then transferred to TPX tubes and chromatin was sheared to 200-500 bp fragments using the Bioruptor NextGen from Diagenode for 28 cycles at high power for 30 sec on, 30 sec off at 4°C. After sonication, lysates were centrifuged at (15 min, 13,200 rpm, 4°C), then, chromatin supernatants were transferred to new reaction tubes and stored at -80°C until further processing.

Re-crosslinking and agarose gel electrophoresis

To determine the chromatin concentration and fragmentation, 20 µl test chromatin of each sample was supplemented with 100 µl 1X TE and 1 µl RNase A (10 mg/ml) and incubated for at least 30 min at 37°C. After that, 7.5 µl SDS (10%) and 3.8 µl Proteinase K (20 mg/ml) were added and incubated for 2 h at 37°C followed by an overnight re-crosslinking step at 65°C. The chromatin was next purified using the NucleoSpin® Gel and PCR Clean-Up Kit from Macherey-Nagel with the NTB Binding Buffer and eluted in 50 µl elution buffer. Chromatin concentrations were measured by the NanoDrop thereby allowing the adjustment of the amount of input chromatin across all samples. Fragmentation was controlled by agarose gel electrophoresis with ethidium bromide staining (3.3.4).

Immunoprecipitation

In the next step, chromatin was precleared by agarose beads and unspecific rabbit IgG. Bead solutions were prepared for each sample of 30 µl by combining 11.9 µl protein A and 11.9 µl protein G agarose beads with 14.3 µl PBS. Beads were then equilibrated by the addition of 500 µl dilution buffer, inverted, and centrifuged (1 min, 2000 rpm, 4°C). After the supernatant was removed, 88 µg chromatin sample, 900 µl dilution buffer, and 2 µg rabbit IgG were added to the beads and they were precleared under rotation for 2 h at 4°C. Importantly, 10% of the amount of chromatin used (=8.8 µg) was retained as input chromatin. Beads were next centrifuged (1 min, 2000 rpm, 4°C) and precleared chromatin was transferred to a new reaction tube. Chromatin samples were mixed with 2 µg of the antibody and rotated overnight (24 h) at 4°C. In addition, chromatin samples were mixed with 2 µg rabbit IgG for the negative control.

On the next day, new beads were equilibrated with dilution buffer as described above and supplemented with the chromatin-antibody solution. Chromatin-antibody samples were precipitated under rotation for 2 h at 4°C, which was followed by five washing steps. Beads were therefore washed with 900 µl of low salt buffer, high salt buffer, LiCl buffer, and twice with 1X TE buffer. Each buffer was incubated for 5 min while samples were rotating at 4°C. Afterwards, they were centrifuged (1 min, 2000 rpm, 4°C) and supernatants were discarded. Immunoprecipitates (IP) and input chromatin samples were subjected to RNase A and Proteinase K treatment, and re-crosslinking as described above for the test chromatin. On the next day, beads were removed from IP samples by centrifugation (1 min, 2000 rpm, 4°C). The chromatin was then purified using the NucleoSpin® Gel and PCR Clean-Up Kit from Macherey-Nagel with the NTB Binding Buffer and eluted in 50 µl elution buffer/nuclease-free water. SYBR qPCR measurements were conducted on 2 µl of each chromatin sample (3.3.14). Before measurement, 10% of input samples were diluted 1:10 in nuclease-free water.

3.3.17 CAPTURE-ChIP

Chromatin preparation for CAPTURE-ChIP

CAPTURE-ChIP was performed according to Liu et al. (2018) [147] with minor modifications to control the binding specificity and efficiency of transiently and stably expressed sgRNAs in HeLa cells. Two T145 culture dishes were prepared for each CAPTURE-ChIP sample by seeding 20 × 10^5 cells (per dish) and culturing them for two days. PEI transfection of the expression vectors was performed on day two to transiently express components of the CAPTURE 1.0 system (3.1.8). On the third day, the medium was reduced to 10 ml and cells were treated with IL-1α (10 ng/ml) for 1 h or kept untreated. Cells were fixed by adding 280 µl 37% formaldehyde (1% final) and then incubated at RT for 10 min. Formaldehyde fixation was stopped by adding 500 µl 2 M glycine and then incubated at RT for 5 min. Cells were scraped, transferred to reaction tubes and centrifuged (5 min, 400 × g, 4°C). Supernatants were discarded and cell pellets were washed twice with 4 ml ice-cold 1X PBS. Cell pellets were next suspended in 2 ml RIPA 0 nuclear extraction buffer with proteinase inhibitors (PI) and rotated for 30 min at 4°C. Nuclei were subsequently collected through centrifugation (5 min, 2500 × g, 4°C), suspended in 1 ml nuclear lysis buffer with PI, and transferred to TPX tubes. Chromatin was next sheared to 200-500 bp fragments using the Bioruptor NextGen from Diagenode for 36 cycles at high power for 30 sec on, 30 sec off at 4°C. To increase sonication efficiencies, samples were shortly vortexed after 10, 20, and 28 cycles. Following sonication, samples were supplemented with 110 µl 10% Triton X-100 (1% final) and centrifuged (10 min, 16,100 × g, 4°C). Chromatin was transferred to new reaction tubes and stored at -80°C until further processing. Chromatin concentration and fragmentation of each sample were determined based on 20 µl test chromatin as previously described in section 3.3.16.

Streptavidin affinity purification for CAPTURE-ChIP

For each chromatin sample, 30 µl Streptavidin Agarose Resin Bead solution or 20 µl M-280 Dynabead solution (used for test only) was prepared in new reaction tubes. Beads were washed twice with RIPA 0.3 buffer by either centrifugation (3 min, 800 × g, 4°C) or by 2 min separation in the magnetic stand. After supernatant removal, soluble chromatin was added to the beads and rotated overnight (24 h) at 4°C. Unless otherwise stated, 88 µg soluble chromatin was used for each chromatin precipitation. This was the maximum amount of chromatin available for each chromatin precipitation in the very first experiment and has ever since been defined as the standard quantity which was used for CAPTURE-ChIP. Importantly, 5% of the amount of chromatin used for the precipitation (=4.4 µg) was retained as input chromatin.

On the next day, beads were collected (3 min, 800 × g, 4°C) and supernatants were discarded. Beads were washed twice with 1 ml of 2% SDS buffer, high salt wash buffer, LiCl wash buffer, and TE buffer. After the addition of each buffer, beads were gently mixed and centrifuged (3 min, 800 × g, 4°C), and supernatants were aspirated. For the elution, beads were supplemented with 100 µl SDS elution buffer which was also added to input chromatin samples to reach the same volume of 100 µl. Beads and input samples were then incubated overnight (16-18 h) by shaking at 1000 rpm and 65°C.

On the following day, beads were collected (3 min, 800 × g, 4°C), and chromatin eluates were transferred to new reaction tubes. Beads were once more rinsed with 50 µl SDS elution buffer which was subsequently combined with the chromatin eluate from the step before. The same volume of 50 µl SDS elution buffer was added to input samples, before IP and input samples were both subjected to RNase A and Proteinase K treatment. Samples were therefore supplemented with 1 µl RNase A (0.5 µg/ml) and incubated for 30 min at 37°C and 300 rpm, then incubated with 1 µl Proteinase K (20 mg/ml) for 2 h at 37°C and 300 rpm. In the last step, chromatin was purified using the NucleoSpin® Gel and PCR Clean-Up Kit from Macherey-Nagel with the NTB Binding Buffer and eluted in 50 µl elution buffer. 1-2 µl of each chromatin sample was measured by SYBR qPCR (3.3.14).

3.3.18 Microarray analysis

Samples were prepared as described in section 3.3.11, further processed and analyzed in the Institute for lung health (ILH) at the Justus Liebig University Gießen under the direction of Dr. Jochen Wilhelm according to the following protocol: Purified total RNA was amplified and Cy3-labeled using the LIRAK Kit (Agilent) following the kit instructions. Per reaction, 200 ng of total RNA was used. The Cy3-labeled aRNA was hybridized overnight to 8x60K 60mer oligonucleotide spotted microarray slides (Agilent Technologies, design ID 072363). Hybridization and subsequent washing and drying of the slides were performed following the Agilent hybridization protocol. The dried slides were scanned at 2 µm/pixel resolution using the InnoScan is900 (Innopsys, Carbonne, France). Image analysis was performed with Mapix 9.0.0 software, and calculated values for all spots were saved as GenePix results files. Stored data were evaluated using the R software [154] and the limma package [155] from BioConductor [156]. Mean spot signals were background corrected with an offset of 1 using the NormExp procedure on the negative control spots. The logarithms of the background-corrected values were quantile-normalized [155, 157]. The normalized values were then averaged for replicate spots per array. From different probes addressing the same NCBI gene ID, the probe showing the maximum average signal intensity over the samples was used in subsequent analyses. Genes were ranked for differential expression using a moderated t-statistic [155]. Pathway analyses were done using gene set tests on the ranks of the t-values [155]. Pathway annotations were obtained from KEGG [158]. The genes assigned to these annotations, including the signal intensity (E value), differential expression between samples ($\log_2$ fold change, LFC) with the associated significance ($-\log_{10}$ p value) and more, were listed in an Excel file. This Excel spreadsheet was then used for further filtering analyses, based on which Venn diagrams, Violin plots, heatmaps, and protein interaction maps were generated. All of these charts are presented and explained in more detail in the results section 4.6.

3.4 Methods in Protein Biochemistry

3.4.1 “Special” cell lysis

To analyze proteins in whole cell extracts, the harvested cell pellets were mixed with 40-150 µl special lysis buffer, vortexed, and incubated for 15 min on ice, whereby cell membranes were disrupted. Afterwards, the lysate was centrifuged (15 min, 10,000 × g, 4°C) and the protein-containing supernatant was transferred in a new reaction tube. Following lysis, protein concentrations were adjusted between samples according to the Bradford method (3.4.4) and proteins analyzed by Western blot analysis (3.4.6).

3.4.2 Cytosol-nuclear lysis

This lysis protocol was applied to study the cytosolic and nuclear fraction of transcription factors under stimulation conditions. Cells were seeded in T145 culture dishes and cultivated until they were treated. On the following day, cells were treated and harvested. A small portion of cells was kept for the analysis of RNA (3.3.11) or proteins in whole cell extracts (3.4.1). Cell pellets were immediately processed by suspending them in 350 µl buffer A. Suspensions were centrifuged (5 min, 800 × g, 4°C) and supernatants were removed. The remaining pellets were suspended in 400 µl buffer A with NP40 detergent, mixed, and incubated for 10 min on ice. Lysates were subsequently mixed and centrifuged (5 min, 13,000 rpm, 4°C). The cytosolic fraction (C) in the supernatants was transferred to new reaction tubes and stored at 4°C until they were further processed. Nuclear pellets were next suspended in 100 µl buffer B and incubated on ice for 30-60 min. The suspension was mixed several times during incubation. Afterwards, nuclear lysates were centrifuged (5 min, 13,000 rpm, 4°C) and the nuclear fraction (N) in the supernatants was transferred to new reaction tubes. Protein concentrations of the cytosolic and nuclear fraction were determined by the Bradford method (3.4.4). Equal protein amounts of each fraction were analyzed by Western blot (3.4.6).

3.4.3 Fractional lysis

The fractional lysis protocol was applied to differentially analyze the fractions of cytosolic, nuclear, and chromatin-bound proteins under stimulation conditions. Cells were therefore seeded in a T145 culture dish and grown until they reached confluence. After treatment, cells were washed twice and then scraped in 10 ml ice-cold PBS. Cells were pelleted (5 min, 500 × g, 4°C), then suspended and incubated in 300 µl Fractional lysis buffer I for 10 min on ice. The lysate was centrifuged (1 min, 2,300 × g, 4°C) whereupon the supernatant containing the cytosolic fraction (C) was stored in a new reaction tube. The remaining pellet was suspended and incubated in 300 µl Fractional lysis buffer II for 20 min on ice and in the meantime shortly mixed twice. After centrifugation (5 min, 20,400 × g, 4°C), the supernatant with the soluble nuclear fraction (N1) was stored in a new reaction tube. The pellet was next suspended in 300 µl Fractional lysis buffer III and sonicated for 6 cycles at high power for 30 sec on, 30 sec off at 4°C using the Bioruptor NextGen from Diagenode. Afterwards, samples were incubated for 30 min on ice and thoroughly mixed several times. After centrifugation (5 min, 20,400 × g, 4°C), the supernatant with the chromatin-bound nuclear fraction (N2) was stored in a new reaction tube. Protein concentrations of the cytosolic and nuclear fractions were determined by the Bradford method as explained in section (3.4.4). Equal protein amounts of each fraction were finally analyzed by Western blot (3.4.6).

3.4.4 Measurement of protein concentrations using the Bradford-Assay

The Roti-Quant protein quantification assay according to Bradford was used to photometrically determine the amount of protein in lysates. This assay is based on the binding of Coomassie Brilliant Blue G250 dye to basic and aromatic amino acids, whereby the absorption maximum of the dye switches from 470 nm to 595 nm. Since the absorption at 595 nm correlates with the protein concentration of a sample, the latter can easily be determined.

Before the measurement, an appropriate dilution of the lysate was prepared in PBS (between 1:150 and 1:300). After that, 100 µl of the dilution as well as a BSA standard series (0 µg/ml, 5 µg/ml, 10 µg/ml, 15 µg/ml, 20 µg/ml, 25 µg/ml, 30 µg/ml, 35 µg/ml BSA in PBS) was aliquoted in a 96-well plate. Next, 100 µl of a 40% Roti-Quant staining solution (ROTI®Quant diluted in ddH$_2$O) was added to each lysate, shortly mixed on the shaker, and incubated for 5 min at RT. Measurement of the extinction was then performed at 595 nm using the SpectraMax Plus 384 Microplate-Reader. Finally, the unknown protein concentration of a sample was determined based on the BSA standard curve.

3.4.5 Discontinuous SDS-PAGE

The sodium dodecyl sulfate-polyacrylamide gel electrophoresis (SDS-PAGE) enables protein separation depending on the molecular weight. This works through SDS binding to hydrophobic regions of proteins and the associated denaturation. SDS binding also causes the proteins to be coated with a negative charge, which neutralizes the protein's intrinsic charge. The resulting negative charge is proportional to the mass of the protein so that in the electrical field, proteins are moving towards the anode and are separated in a polyacrylamide matrix corresponding to their mass. Typically, larger proteins are migrating slower through the gel pores than smaller ones, and by running a molecular mass standard along with the samples, the size of proteins can be determined.

Polyacrylamide gel pore size is based on the acrylamide concentration. This in turn specifies the separating capability of a gel and varies depending on the proteins that are studied. The protein analyses performed in this work were conducted on separating gels with 8%, 9% or 12.5% acrylamide content and 5% acrylamide stacking gels. The composition of an 8% separating gel and 5% stacking gel is exemplarily demonstrated below:

Separating gel (8%)	**Stacking gel (5%)**	**Solution [ml]**
10.3	-	Separating gel buffer
-	1.26	Stacking gel buffer

5.6	5.6	ddH_2O
2.4	0.9	50% Glycerole
1.35	0.50	2% SDS
7.20	1.68	30% Acrylamide
0.041	0.030	40% APS
0.027	0.020	TEMED

The separating gel and stacking gel were prepared accordingly and samples were loaded into the pockets. Before loading, the total protein amount of each sample was adjusted to 30 µg (sometimes up to 50 µg). By doing that, samples were mixed with loading buffer (ROTI®Load) at a ratio of 4:1 and if required diluted in ddH_2O. After that, lysates were boiled and denatured for 5 min at 95°C. Separation of the proteins was carried out in 1X Laemmli running buffer within an electrophoresis gel chamber at 50 mA per gel and for 2-2.5 h. After the run, gels were used for immunodetection of proteins of interest by Western blot (3.4.6) or silver staining (3.4.9).

3.4.6 Immunodetection of proteins by Western blot

Western blot analysis enables the detection of proteins through the usage of specific antibodies. For this purpose, protein extracts are separated by electrophoresis on an SDS-PAGE and then transferred onto a PVDF membrane. In this work, the semi-dry technique was used in which 2 Whatman paper, 1 polyvinylidene fluoride (PVDF) membrane, the SDS-polyacrylamide gel, and again 2 Whatman paper were stacked in the given order and placed on the anode surface of the transfer chamber. Before stacking, Whatman papers were moisturized in 1X blotting buffer and the PVDF membrane was activated in methanol for 3 min and thereafter equilibrated in 1X blotting buffer. After placing the layers on the anode, the cathode of the transfer chamber was carefully placed on top and the electrophoretic transfer was performed at a constant amperage of 0.8 mA/cm^2 of the PVDF membrane for around 2 h.

Afterwards, the transfer of proteins to the membrane was controlled through Ponceau S staining by incubating the membrane for 3 min with Ponceau S, washing it with water, and subsequent documentation of the staining. In the next step, the staining of the membrane was reversed by several washing steps with TBS-T whereupon the membrane was incubated in 5% milk powder/BSA in TBS-T buffer for 30 min at RT to block unspecific binding sites. After the blocking, the membrane was incubated with a primary antibody solution (diluted in 5% milk powder/BSA in TBS-T buffer) either for 1 h at RT or overnight at 4°C. After the incubation, the primary antibody was removed by washing the membrane four times for 5 min with TBS-T. The membrane was next incubated with an HRP-tagged secondary antibody solution (diluted in 5% milk powder/BSA in TBS-T buffer) for 1 h at RT. After that, four more 5 min TBS-T washing steps were performed to remove excessive secondary antibodies. Finally, proteins were detected through chemiluminescence using the reagents Amersham ECL Western blot Detection Reagent or Immobilon Western Chemiluminescent HRP Substrate according to the manufacturer's information. For detection, the ChemiDoc™ Touch Imaging System was used and the subsequent densitometric relative quantification of chemiluminescence signals was carried out by using the Bio-Rad Image Lab software.

3.4.7 CAPTURE-Proteomics

The CAPTURE-Proteomics protocol previously described by Liu et al. (2018) [147] was used with modifications to isolate protein complexes associated with dCas9-sgRNA targeted inflammatory promoters. The method is based on the *in vivo* expression of dCas9 and customized sgRNAs targeting specific genomic loci. Formaldehyde cross-linking and RNase digestion enable the capture of the locus-associated protein complexes. Following chromatin preparation, the material is subjected to sonication to solubilize and shear the cross-linked chromatin into fragments. High-affinity streptavidin-based purification is performed to separate biotinylated (CAPTURE 1.0) or BioTAP-tagged dCas9 (CAPTURE 2.0) complexes and remove unspecific molecules by extensive washing steps. The isolated locus-specific protein complexes are recovered under denaturing conditions and analyzed by Western blot analysis.

Chromatin preparation for CAPTURE-Proteomics

For CAPTURE-Proteomics, a total of 1 × 10^8 cells was required for each sample. For this purpose, 5 × 10^5 HeLa cells were seeded in T145 dishes (ten dishes per sample) and cultured for four days. Transfection of CAPTURE 1.0 plasmids was performed on the third day of cultivation according to section 3.1.8. On day four, the medium was reduced to 10 ml and cells were treated with IL-1α (10 ng/ml) for 1 h or kept untreated. Cells were fixed by adding 560 µl 37% formaldehyde (2% final) and then incubated at RT for 10 min. Formaldehyde fixation was stopped by adding 1.25 ml 2 M glycine, and then incubated at RT for 5 min. Cells of one sample were scraped, evenly transferred to three 50 ml tubes, and centrifuged (5 min, 400 × g, 4°C). Supernatants were discarded and cell pellets were washed with 2 ml ice-cold 1X DPBS. Cell pellets were next suspended in 1 ml ice-cold 1X PBS and transferred to smaller 2 ml reaction tubes (3 tubes per sample). Following centrifugation (5 min, 400 × g, 4°C), supernatants were removed, and cells were frozen in liquid nitrogen and stored at -80°C until further processing.

Thawed pellets were suspended in 1.33 ml ice-cold cell lysis buffer (4 ml in total) and rotated for 30 min at 4°C. After cell lysis, nuclei were collected through centrifugation (5 min, 2500 × g, 4°C), suspended in 333 µl cell lysis buffer (1 ml in total), and supplemented with 0.7 µl RNase A (0.5 µg/ml). Enzymatic digestion by RNase A was performed for 30 min at 37°C under rotation. Chromatin was then extracted in multiple rounds according to the procedure described in the following: Nuclei were collected (5 min, 2500 × g, 4°C), suspended in 270 µl SDS nuclear lysis buffer (0.81 ml in total) by gentle pipetting and incubated for 10 min at RT. In the next step, 270 µl urea buffer (2.4 ml in total) was added and mixed by inverting the reaction tube. Chromatin was subsequently pelleted (25 min, 16,100 × g, RT) and the supernatant was removed. This procedure was repeated 2-4 times until the supernatant appeared clear.

Chromatin was then washed twice by adding 270 µl SDS nuclear lysis buffer (0.81 ml in total), gentle pipetting, followed by the addition of 800 µl nuclear lysis buffer (2.4 ml in total) and centrifugation (25 min, 16,100 × g, RT) to wash off the urea. Chromatin was subsequently washed twice by adding 270 µl cell lysis buffer (0.81 ml in total), gentle pipetting, followed by the addition of 800 µl cell lysis buffer (2.4 ml in total) and centrifugation (25 min, 16,100 × g, RT) to wash off SDS. The pellet was finally suspended in 270 µl IP binding buffer w/o NaCl (0.81 ml in total) and transferred to a new 1.5 ml sonication-specific reaction tube (3 tubes per sample). Chromatin was sonicated for 28 cycles at high power for 30 sec on, and 30 sec off at 4°C using the Bioruptor NextGen from Diagenode to obtain fragments of 300-1000 bp size. To increase sonication efficiencies, samples were shortly vortexed after 10, 20, and 28 cycles. Sonicated chromatin was centrifuged (5 min, 16,100 × g, 4°C) and the supernatants of one sample were pooled in a new reaction tube. To determine the fragment size, 20 µl test chromatin of each sample was re-crosslinked and analyzed by agarose gel electrophoresis as previously described in section 3.3.4. The pooled chromatin was once more centrifuged (25 min, 16,100 × g, 4°C), transferred to a new reaction tube, and stored at -80°C until further processing.

Streptavidin affinity purification for CAPTURE-Proteomics

Chromatin was thawed and supplemented with 150 mM NaCl. For each chromatin sample, 2X 50 µl Streptavidin Agarose Resin Bead solution was prepared in new reaction tubes. Beads were washed twice with 1 ml IP binding buffer with NaCl and centrifuged (3 min, 800 × g, 4°C). The supernatant was removed from the beads and soluble chromatin was evenly added, which means that 50% of the solution was added to each 50 µl of equilibrated beads. Chromatin and beads were then incubated overnight (24 h) at 4°C under rotation. Importantly, 1% of the chromatin volume used for the precipitation was retained as input for the Western blot analysis. On the next day, beads were collected (3 min, 800 × g, 4°C) and supernatants were discarded. Importantly, 1% of the supernatant was retained for the Western blot analysis. Beads were washed five times with 1 ml IP binding buffer with NaCl by incubating for 10 min at 4°C with rotation followed by centrifugation (3 min, 800 × g, 4°C). The supernatant was completely discarded and beads were suspended in 100 µl IP binding buffer with NaCl. The supernatant was again discarded and beads were boiled in 30 µl RIPA buffer and 10 µl ROTI®Load at 95°C for 20 min to elute dCas9 complexes from the agarose beads. The eluate was stored at -20°C until Western blot analysis as further discussed in section 3.4.6.

3.4.8 MiniTurboID assay

MiniTurboID combines proximity labeling and affinity purification to identify protein interaction candidates of a bait protein in living cells. For establishing the method, several conditions were tested and adjusted accordingly. The final protocol by which the MiniTurboID assay and subsequent mass spectrometric analysis was performed is described below.

For each experimental condition, 5 × 10^5 HeLa cells were seeded in a T145 culture dish and grown for 4 days. On day three, cells were PEI transfected (3.1.8) with 50 µg of pTet-on-Puro expression vectors encoding HA-miniTurbo(EV), p65(wt)-HA-miniTurbo, p65(E/I)-HA-miniTurbo or p65(FL/DD)-HA-miniTurbo. Figure 7 exemplarily shows the vector map of pTet-on-Puro-p65-HA-miniTurbo. Following transfection, constructs were induced with 1 µg/ml doxycycline for 17 h and on the next day supplemented with 50 µM exogenous biotin 10 min prior to IL-1α treatment to ensure availability within the cells from the start of proinflammatory stimulation with 10 ng/ml IL-1α for 1 h. The exact time course from treatment to stimulation to harvesting of the cells is shown schematically in Figure 8.

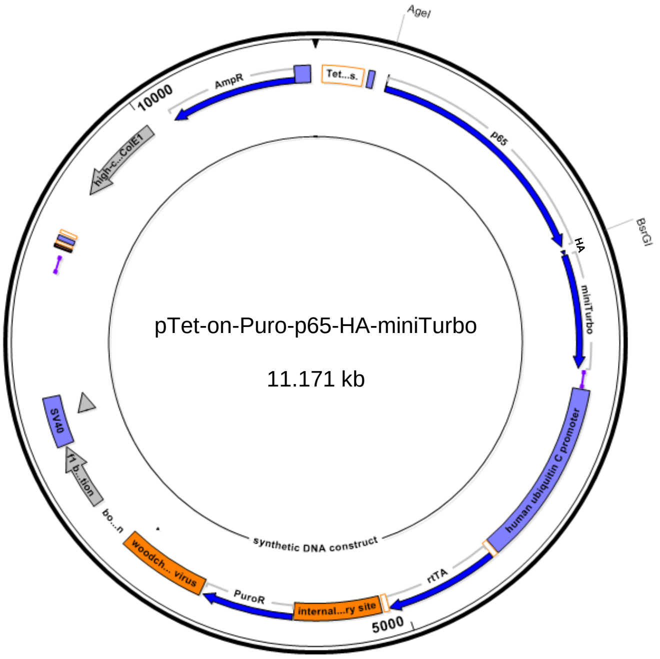

Figure 7: Vector map of pTet-on-Puro-p65-HA-miniTurbo.
The expression plasmid pTet-on-Puro-p65-HA-miniTurbo comprises 11,171 kilobases (kb). The black arrowhead pointing down indicates the first base pair (bp). From position 1: Blue arrows indicate the coding sequences of the p65 gene body, HA-tag, miniTurbo enzyme, reverse tetracycline-controlled transactivator (rtTA), and puromycin-resistance (PuroR) and ampicillin-resistance (AmpR) cassettes. Purple boxes show promoter sequences of human cytomegalovirus (CMV), human ubiquitin C, polyomavirus simian virus 40 (SV40) enhancer and early promoter, *E. coli* lac operon promoter, and bla promoter. White boxes with orange edges indicate regulatory elements, i.e., the tetracycline-responsive element, two Cre-mediated recombination sites, and *E. coli* binding sites for the lac repressor and catabolite activator protein (CAP). Orange boxes mark the internal ribosome entry site (IRES) of the encephalomyocarditis virus (EMCV) and woodchuck hepatitis virus posttranscriptional regulatory element. Pink lines denote polyadenylation signals. Grey arrows denote origins of replication. The two restriction sites AgeI and BsrGI flank the genomic sequence of p65 and allow insertion of any gene of interest (GOI).

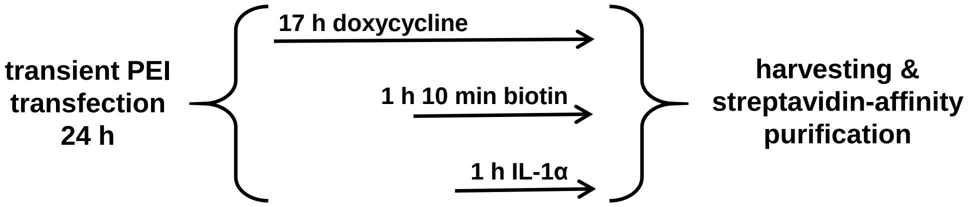

Figure 8: Time course of the MiniTurboID assay.
The schematic illustrates the exact time sequence from treatment to stimulation to collection of cells for the final MiniTurboID experiment: HeLa cells cultured in tetracycline-free DMEM medium were PEI transfected with pTet-on-Puro-HA-miniTurbo expression vectors. 7 h post-transfection, constructs were induced with 1 µg/ml doxycycline for 17 h and on the next day added with 50 µM exogenous biotin 10 min prior to IL-1α treatment. Cells were treated with 10 ng/ml IL-1α for 1 h or left untreated and then harvested for streptavidin-pulldown.

Harvesting and cell lysis

Cells were harvested as described in section 3.1.5, except that they were pelleted for 5 min at 900 × g and 4 °C. Cell pellets were suspended in 475 µl of 50 µM Tris/HCl pH 7.5 and 50 µl of 10% Triton X-100. The cell suspension was then transferred into two 1.5 ml reaction tubes, each containing 262.5 µl. Cells were next mixed with 125 µl room temperature lysis buffer by pipetting and incubated on ice for 10 min. The mixture was next subjected to sonication at high power for 30 sec on, and 30 sec off at 4°C (3-4 cycles) using the Bioruptor NextGen from Diagenode to further disrupt and solubilize the mixture. The sonicated material was centrifuged (15 min, 16,000 × g, 4°C) and supernatants were transferred to new reaction tubes. Importantly, four times the volume of 30 µl containing 1% lysate (7 µl), 1X ROTI®Load (7.5 µl), and water (15.5 µl) was boiled at 95°C for 10 min and retained for subsequent Western blot analyses.

Streptavidin affinity purification for MiniTurboID

For each experimental condition, 60 µl of Streptavidin Agarose Resin Beads were prepared by equilibrating the total volume of beads that was needed for all the conditions. For this purpose, 1 ml lysis buffer was pipetted into a 1.5 ml reaction tube and supplemented with the according amount of agarose beads. After centrifugation (2 min, 1000 × g, RT), the supernatant was discarded and the x-fold volume of 60 µl lysis buffer was added depending on the number of conditions for which the beads were prepared. The equilibrated bead solution was next equally divided among new 1.5 ml reaction tubes and 700 µl of lysate was added. The following overnight incubation (16-18 h) was performed at 4°C under rotation and allowed the non-covalent high-affinity binding between biotinylated proteins and streptavidin beads. In the next step, beads were centrifuged (2 min, 1000 × g, RT) and four times the volume of 30 µl with 1% supernatant (7 µl), 1X ROTI®Load (7.5 µl) and water (15.5 µl) was boiled at 95°C for 10 min and retained for subsequent Western blot analyses to assess the binding efficiency of the biotinylated proteins. Afterwards, eight washing steps were performed to remove non-binding proteins. Unless otherwise stated, washing was performed under the same centrifugation settings used before and supernatants were discarded. Beads were first washed once with 500 µl of washing buffer I and centrifuged at RT. Beads were then washed twice with 500 µl of washing buffer II, twice with washing buffer III, twice with washing buffer IV, and subsequently centrifuged at 4°C. In the end, beads were washed with 1000 µl of washing buffer V and centrifuged at 4°C.

Sample preparation during the establishment of the MiniTurboID Assay

During the establishment of MiniTurboID, the pulldown samples were evaluated by silver staining and Western blot analysis only. For this purpose, 150 µl of 2X ROTI®Load was added to the beads and gently tapped with fingertips. The beads were boiled at 95°C for 10 min and stored at -20°C. The beads were then centrifuged (2 min, 1000 × g, RT) and 25% of the sample was analyzed on SDS-polyacrylamide gels.

Sample preparation for silver gel/Western blot analysis and mass spectrometry (internal)

80% of the sample was used for mass spectrometric analysis (3.4.10) and 20% for silver gel and Western blot analysis. The bead mixture was separated accordingly, centrifuged in new reaction tubes (2 min, 1000 × g, 4°C) and the supernatant discarded. For mass spectrometry, beads were added with 100 µl of washing buffer V (50 mM Tris/HCl pH 7.5) and further analyzed in the Mass Spectrometry Facility of the Department of Chemistry at Philipps University Marburg under the direction of Dr. Uwe Linne. For the silver gel and Western blot, beads were supplemented with 40 µl of 2X ROTI®Load and boiled at 95°C for 10 min. Samples were then stored at -20°C until further processing. Thawed samples were centrifuged (2 min, 1000 × g, RT) and 15% or 5% of the sample was analyzed by silver staining (3.4.9) or streptavidin-HRP-mediated Western blot (3.4.6), respectively.

3.4.9 Silver staining of proteins

Silver staining was applied to detect the proteins pulled down by MiniTurboID (3.4.8). After the electrophoretic separation of proteins, the SDS polyacrylamide gel was incubated in a fixative solution overnight at 4°C on the shaker. The gel was then washed four times with ddH_2O for 10 min and placed in the incubation solution for 30-120 min. After 6 more washing steps with ddH_2O for 10 min, the gel was exposed to a staining solution for 15-60 min. The gel was next washed two times with ddH_2O for 1 min and then staining was initiated by the addition of developer solution. Once the protein staining was sufficiently visible, stop solution was added and incubated until the bubbles vanished. In the last step, staining was documented and, when required, the gel was stored in 1% acetic acid at 4°C in the dark.

3.4.10 Mass spectrometric analysis of MiniTurboID samples

MiniTurboID samples containing bead-bound proteins in washing buffer V (50 mM Tris/HCl pH 7.5) were further processed in the Mass Spectrometry Facility of the Department of Chemistry at Philipps University Marburg under the direction of Dr. Uwe Linne according to the following protocol:

Sample preparation for mass spectrometry (external)

Samples were washed three times with 100 µl 0.1 M ammonium bicarbonate buffer. Sequencing grade modified trypsin (Serva) was then added to the samples and incubated for 45 min at 37°C to digest the proteins on the beads. The supernatant was next collected in fresh reaction tubes and incubated overnight at 37°C. Samples were desalted on Chromabond C18WP spin columns (Macherey-Nagel) to concentrate the peptides. These were then dissolved in 5% acetonitrile and 0.1% formic acid. Samples were next analyzed using the timsTOF mass spectrometer as described below.

Identification of proteins using the timsTOF mass spectrometer

Peptide samples were further processed for mass spectrometric analysis as follows: 200 ng of the peptides in a volume of 2 µl were injected at a constant pressure of 800 bar onto the Aurora C18 RP separation column (25 cm × 75 µm) filled with 1.7 µm beads (IonOpticks) of the nanoElute HPLC system connected to a timsTOF Pro mass spectrometer (Bruker Daltonic). The separation of digested peptides was performed at a column temperature of 50°C, for which the following solutions were used: Water/0.1% formic acid (solvent A) and acetonitrile/0.1% formic acid (solvent B). The flow rate was 400 nl/min and the separation gradients were as follows: Linear increase of B from 2% to 17% in 60 min. Then linear increase of B to 25% in 30 min, followed by linear increase of B to 37% in 10 min. Then B was increased to 95% in 10 min and remained at this level for another 10 min. The data-dependent acquisition mode (DDA PASEF-standard_1.1sec_cycletime, developed by Bruker Daltonics) was used for the mass spectrometric measurement.

3.4.11 Bioinformatic analysis of proteomic data from NF-κB p65 MiniTurboID

The mass spectrometric analysis was performed with 2 biological and 3 technical replicates. The raw data obtained from the analysis (3.4.10) were processed by Dr. Axel Weber or Dr. Uwe Linne using the MaxQuant software with the parameters below. The MaxQuant search tool Andromeda was used to assign protein names and their annotations. The analysis was performed with the parameter "match between runs" to obtain a denser data matrix. The following Uniprot database was used as reference for the annotation of proteins identified in the MiniTurboID pulldown samples:

Organism:
homo sapiens (HeLa cells)

Uniprot ID:
uniprot-reviewed_yes+AND+organism__Homo+sapiens+(Human)+[9606]_ releasedate2019_06

The following parameters were used to run the MaxQuant software:

Parameter	**Value**
Version	1.6.17.0
User name	
Machine name	
Date of writing	11/10/2020 21:52
Include contaminants	True
PSM FDR	0.01
PSM FDR Crosslink	0.01
Protein FDR	0.01
Site FDR	0.01
Use Normalized Ratios For Occupancy	True
Min. peptide Length	7
Min. score for unmodified peptides	0
Min. score for modified peptides	40
Min. delta score for unmodified peptides	0
Min. delta score for modified peptides	6
Min. unique peptides	0
Min. razor peptides	1
Min. peptides	1
Use only unmodified peptides and	True
Modifications included in protein quantification	Oxidation (M);Acetyl (Protein N-term)
Peptides used for protein quantification	Razor
Discard unmodified counterpart peptides	True
Label min. ratio count	2
Use delta score	False
iBAQ	True
iBAQ log fit	True
Match between runs	True
Matching time window [min]	0.7
Match ion mobility window [indices]	0.05
Alignment time window [min]	20
Alignment ion mobility window [indices]	1
Find dependent peptides	False
Fasta file	
Decoy mode	revert
Include contaminants	True
Advanced ratios	True
Fixed andromeda index folder	
Combined folder location	
Second peptides	True
Stabilize large LFQ ratios	True
Separate LFQ in parameter groups	False
Require MS/MS for LFQ comparisons	False
Calculate peak properties	False
Main search max. combinations	200
Advanced site intensities	True
Write msScans table	False
Write msmsScans table	True
Write ms3Scans table	True
Write allPeptides table	True
Write mzRange table	True
Write DIA fragments table	False
Write DIA fragments quant table	-
Write pasefMsmsScans table	True
Write accumulatedPasefMsmsScans table	False
Max. peptide mass [Da]	4600
Min. peptide length for unspecific search	8
Max. peptide length for unspecific search	25
Razor protein FDR	True
Disable MD5	False
Max mods in site table	3
Match unidentified features	False
Epsilon score for mutations	
Evaluate variant peptides separately	True

Variation mode	None
MS/MS tol. (FTMS)	20 ppm
Top MS/MS peaks per Da interval. (FTMS)	12
Da interval. (FTMS)	100
MS/MS deisotoping (FTMS)	True
MS/MS deisotoping tolerance (FTMS)	7
MS/MS deisotoping tolerance unit (FTMS)	ppm
MS/MS higher charges (FTMS)	True
MS/MS water loss (FTMS)	True
MS/MS water loss (FTMS for cross link)	
MS/MS ammonia loss (FTMS)	True
MS/MS ammonia loss (FTMS for cross link)	
MS/MS dependent losses (FTMS)	True
MS/MS recalibration (FTMS)	False
MS/MS tol. (ITMS)	0.5 Da
Top MS/MS peaks per Da interval. (ITMS)	8
Da interval. (ITMS)	100
MS/MS deisotoping (ITMS)	False
MS/MS deisotoping tolerance (ITMS)	0.15
MS/MS deisotoping tolerance unit (ITMS)	Da
MS/MS higher charges (ITMS)	True
MS/MS water loss (ITMS)	True
MS/MS water loss (ITMS for cross link)	
MS/MS ammonia loss (ITMS)	True
MS/MS ammonia loss (ITMS for cross link)	
MS/MS dependent losses (ITMS)	True
MS/MS recalibration (ITMS)	False
MS/MS tol. (TOF)	40 ppm
Top MS/MS peaks per Da interval. (TOF)	10
Da interval. (TOF)	100
MS/MS deisotoping (TOF)	True
MS/MS deisotoping tolerance (TOF)	0.01
MS/MS deisotoping tolerance unit (TOF)	Da
MS/MS higher charges (TOF)	True
MS/MS water loss (TOF)	True
MS/MS water loss (TOF for cross link)	
MS/MS ammonia loss (TOF)	True
MS/MS ammonia loss (TOF for cross link)	
MS/MS dependent losses (TOF)	True
MS/MS recalibration (TOF)	False
MS/MS tol. (Unknown)	20 ppm
Top MS/MS peaks per Da interval. (Unknown)	12
Da interval. (Unknown)	100
MS/MS deisotoping (Unknown)	True
MS/MS deisotoping tolerance (Unknown)	7
MS/MS deisotoping tolerance unit (Unknown)	ppm
MS/MS higher charges (Unknown)	True
MS/MS water loss (Unknown)	True
MS/MS water loss (Unknown for cross link)	
MS/MS ammonia loss (Unknown)	True
MS/MS ammonia loss (Unknown for cross link)	
MS/MS dependent losses (Unknown)	True
MS/MS recalibration (Unknown)	False
Site tables	Oxidation (M)Sites.txt

The output file "proteinGroups.txt" by MaxQuant contains the proteins measured by mass spectrometry with their intensities, and the type of quantification ("by MS/MS", "by matching peptide counts", "LFQ" (label-free quantification)). Also included were data on the number of peptides measured per protein, sequence coverage, molecular weight, protein ID, gene ontology, impurities, and more. The protein group data from the output file were analyzed using the software Perseus. The analytical workflow is described in the section below.

Perseus workflow for the analysis of proteomic data from NF-κB p65 MiniTurboID

After importing the raw data from the MaxQuant output file into Perseus, the two biological and three technical replicates of each experimental condition were categorized as one group (Figure 9). The intensities of the proteins were then log_2-transformed. No data normalization was performed at this stage as MiniTurboID is an enrichment method, so a large variation in distribution between samples is expected. Instead, the lowest occurring intensity value was determined, which was slightly above 9, and all missing values in the matrix were imputed using a value of 9. This was critical since it is common in pulldown experiments for proteins to not be measured in some samples while being enriched in others. Without the imputation step, these proteins would not be included in the subsequent statistical analysis, thereby leading to loss of data. Based on the "imputation matrix," Student's T-tests were performed to compare the different conditions. The test provided the log_2 differences between two groups as log_2 fold change (LFC) and the respective statistical significance of these changes as $-log_{10}$ p value. In this way, it was determined whether the factors were enriched or depleted in certain conditions. The settings used for the test are shown in Figure 9.

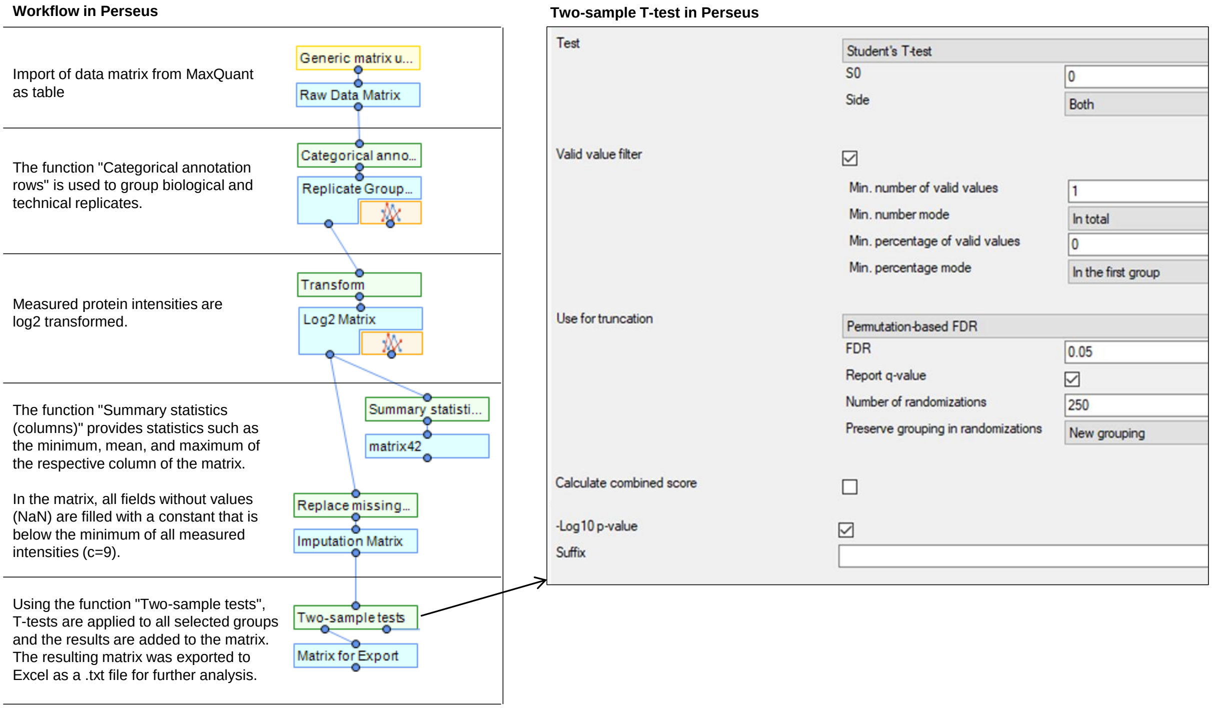
Workflow in Perseus

Import of data matrix from MaxQuant as table

The function "Categorical annotation rows" is used to group biological and technical replicates.

Measured protein intensities are log2 transformed.

The function "Summary statistics (columns)" provides statistics such as the minimum, mean, and maximum of the respective column of the matrix.

In the matrix, all fields without values (NaN) are filled with a constant that is below the minimum of all measured intensities (c=9).

Using the function "Two-sample tests", T-tests are applied to all selected groups and the results are added to the matrix. The resulting matrix was exported to Excel as a .txt file for further analysis.

Two-sample T-test in Perseus

Test: Student's T-test
S0: 0
Side: Both
Valid value filter: ☑
Min. number of valid values: 1
Min. number mode: In total
Min. percentage of valid values: 0
Min. percentage mode: In the first group
Use for truncation: Permutation-based FDR
FDR: 0.05
Report q-value: ☑
Number of randomizations: 250
Preserve grouping in randomizations: New grouping
Calculate combined score: ☐
-Log10 p-value: ☑
Suffix:

Figure 9: The data processing workflow in Perseus.
The schematic on the left shows the different processing steps of proteomic data from NF-κB p65 MiniTurboID experiments in Perseus. The yellow box marks imported data, blue boxes indicate data matrices, and green boxes show executed functions. On the right side, settings for statistical analysis with Student's T-test are shown. (The schematic was created by Jana Juli.)

The matrix resulting from the Student's T-test was imported into an Excel file. This Excel spreadsheet was used for further bioinformatic analyses. The exact subsequent step-wise bioinformatic analysis is shown in detail in Figure 28 and included multiple filtering steps, Venn diagram analyses [148], Metascape pathway analyses [149], and STRING protein interaction analyses [150]. The analysis steps were visualized by Volcano plots, overlaps / Venns, heatmaps, and protein interaction maps. All of these charts are presented and explained in more detail in the results section 4.2.

3.5 Fluorescent staining and microscopy

3.5.1 Immunofluorescence with RNA fluorescence *in situ* hybridization

Immunofluorescence was combined with RNA fluorescence *in situ* hybridization (immuno-FISH) to monitor p65-HA-miniTurbo levels in single cells upon stimulation of the cells with IL-1α. HeLa cells were therefore transfected with HA-miniTurbo(EV) and p65(wt)-HA-miniTurbo plasmids as described in section 3.1.8 and cultured in tetracycline-free medium. After 24 h, cells were washed twice with pre-warmed 1X PBS and detached from the cell culture dish using trypsin. Subsequently, 6000 cells per channel were seeded in Ibidi-slides in 30 µl of tetracycline-free medium. After incubation for 1 h at 37°C, the channel was refilled with 100 µl of medium and the cells were incubated overnight. On the next day, 1 µg/ml doxycycline was added to the cells and incubated for 4 h at 37°C to activate the tetracycline-induced system. For the last hour of incubation, cells were stimulated with IL-1α or left untreated. Afterwards, the medium was removed and the cells were washed twice with 150 µl 1X PBS (Affymetrix) in 5 min and fixed with 100 µl of 4% paraformaldehyde (in PBS) overnight (24 h) at 4°C. Following three washing steps with 150 µl 1X PBS for 3 min, cells were permeabilized with 50 µl detergent solution for 5 min at RT. Cells were washed twice with 150 µl 1X PBS for 3 min and subsequently incubated with 50 µl pre-warmed probe sets diluted 1:100 in probe set diluent QF. For the first step of hybridization, cells were incubated in a humidity chamber for 3 h at 40°C. After three washing steps with 150 µl wash buffer for 3 min, cells were next incubated with 50 µl pre-warmed pre-amplifier diluted 1:30 in amplifier diluent QF. The second step of hybridization was performed in a humidity chamber for 30 min at 40°C. Following three more washing steps with 150 µl wash buffer for 3 min, cells were incubated with 50 µl pre-warmed amplifier diluted 1:30 in amplifier diluent QF. Hybridization was once more carried out in a humidity chamber for 30 min at 40°C. The amplifier solution was removed and cells were washed three times with wash buffer for 3 min. All the following steps were performed in the dark. Cells were incubated with 50 µl pre-warmed label probe mix diluted 1:30 in label probe set diluent QF. The last step of hybridization was conducted in a humidity chamber for 30 min at 40°C. For the immunofluorescence, the buffer was changed by washing cells twice with 150 µl HBSS/0.005% saponin. Cells were next incubated with 100 µl HBSS/0.005% saponin/10% donkey serum for 30 min at RT to block unspecific binding sites. After removing the blocking solution, cells were incubated with 50 µl primary antibody diluted in HBSS/0.005% saponin. Incubation of the primary antibody was performed in a humidity chamber for 1 h at 37°C. Afterwards, cells were washed three times with HBSS/0.005% saponin for 10 min and subsequently incubated with 50 µl secondary antibody diluted in HBSS/0.005% saponin. Incubation of the secondary antibody was likewise performed in a humidity chamber for 1 h at 37°C. Cells were then washed three times with HBSS for 10 min. In the last step, nuclei were stained with 100 µl of 1 µM Hoechst solution diluted in HBSS for

5 min at RT. Hoechst was removed by washing cells twice with 150 µl HBSS within 5 min. Cells were finally mounted in 100 µl fluoromount G and stored in the dark until microscopic documentation (3.5.3). Importantly, to assess the background signal by reagents, the IF/FISH control was included in the study in which no specific probe set or primary antibody was added.

3.5.2 Immunofluorescence with *in situ* proximity ligation assay

Combined immunofluorescence with *in situ* proximity ligation assay (immuno-PLA) was utilized as an independent approach to validate the p65 interactions revealed by MiniTurboID. A total of 9000 cells per channel, of parental or p65-deficient cells, were therefore seeded in Ibidi-slides. On the next day, cells were washed twice with 150 µl 1X PBS for 5 min and fixed with 100 µl of 4% paraformaldehyde (in PBS) for 10 min at RT. Afterwards, 100 µl 0.1 M Tris/HCl pH 7.4 were added and incubated for 10 min at RT. Permeabilization was performed next by adding 100 µl of a 0.005% saponin/0.1% Triton X-100/1X DPBS solution for 10 min at RT. Permeabilized cells were washed twice with 150 µl 1X DPBS for 5 min and incubated overnight (24 h) with 40% glycerol/1X DPBS at RT. On the next day, nuclei were permeabilized by three rounds of freeze and thaw. Ibidi-slides were therefore kept in liquid nitrogen for 1 min and thawed until glycerol cleared up. After nuclear permeabilization, cells were washed twice with 1X DPBS for 5 min and embedded in 100 µl blocking solution which was incubated in a humidity chamber for 30 min at 37°C. The blocking solution was discarded and cells were incubated with 50 µl of the appropriate primary antibody mixture in a humidity chamber for 1 h at 37°C. The primary antibody mixture contained PLA and IF antibodies and was diluted in antibody diluent. Cells were washed three times with 150 µl buffer A for 5 min and then incubated with 50 µl of a secondary antibody mixture in a humidity chamber for 1 h at 37°C. The secondary antibody mixture contained PLA probes which were diluted 1:5 in antibody diluent but also the fluorescence-associated secondary IF antibody. From the time of incubation, all further steps were carried out in the dark. Cells were washed three times with 150 µl buffer A for 5 min and incubated with 50 µl ligase solution in a humidity chamber for 30 min at 37°C. The ligase was therefore diluted 1:60 in ligase solution whose stock solution was diluted 1:5 in nuclease-free water. After that, cells were washed three times with 150 µl buffer A for 2 min and then incubated with 50 µl polymerase solution in a humidity chamber for 100 min at 37°C. The polymerase was therefore diluted 1:80 in amplification solution whose stock solution was diluted 1:5 in nuclease-free water. Cells were first washed three times with 150 µl buffer B for 5 min followed by two HBSS washes for 1 min. Nuclei were then stained with 1 µM Hoechst for 5 min at RT and washed twice with 150 µl HBSS for 5 min. Cells were finally embedded in 50 µl 30% glycerol/HBSS and stored in the dark until microscopic documentation (3.5.3).

3.5.3 Microscopic analysis

Fluorescence imaging of immuno-FISH samples was carried out using the inverse fluorescence microscope DMi8 with filter cubes suited for Hoechst (excitation 405/60 and emission 470/40), DyLight488 (excitation 470/40 and emission 525/50), Cy5 (excitation 620/60 and emission 700/75), and the Leica LASX software (version 3.7.0.20979), whereas for the documentation of immuno-PLA images the THUNDER imager (DMi8) was used with filter cubes for Hoechst (excitation 391/32 and emission 435/30), DyLight488 (excitation 506/21 and emission 539/24), Cy3 (excitation 554/24 and emission 594/32), and the Leica LASX software (version 3.7.4.23463). The Quantification of PPI complexes was performed using the Blobfinder software from the Centre for Image Analysis (Uppsala University, Sweden) and Olink Bioscience. The software configuration was adjusted to HeLa cells with a nucleus size of 100 pixels^2 and cytoplasm size of 100 pixels. For the blob size, the 3 × 3 default setting was applied whereas the blob threshold of 15 was determined by a test image.

4 Results

In the first part of this thesis, two biotin-based pulldown approaches CAPTURE and MiniTurboID were established to define the interactome of known and novel factors that collectively mediate the dynamic spatiotemporal control of inflammatory gene expression. In the second part, some of these novel factors were further investigated to receive a comprehensive understanding of their functions in the IL-1α-NF-κB-driven cellular immune response. The extensive and time-consuming work of method establishment in the first part was performed in collaboration with Jana Juli, the other doctoral candidate funded by the TRR81 project. The subsequent functional analysis of specific factors identified was performed separately.

4.1 Establishment of the CAPTURE system for the investigation of inflammatory promoters in human epithelial cells

4.1.1 Testing the transient CAPTURE 1.0 dCas9-BirA-sgRNA HeLa cell system

The CAPTURE method was published by Liu et al. in 2017 and consists of a three-vector system that allows *in vivo* biotinylation of an N-terminal FB-tagged dCas9 by *E. coli* biotin ligase BirA. Biotinylated dCas9 molecules are directed to a genomic locus of interest through coexpression of customized sgRNAs [138]. The locus-associated dCas9 molecular complex is isolated by high-affinity streptavidin purification and can be analyzed through mass spectrometry or high-throughput sequencing technologies to study locus-specific binding of regulatory proteins, RNA, or DNA elements (Figure 10A). In 2018, Liu et al. published the detailed underlying protocols that were used for CAPTURE-ChIP-seq, CAPTURE-Proteomics, and CAPTURE-3C-seq analyses in a human erythroid cell system [147].

Based on these publications, CAPTURE was to be established in HeLa cells (human epithelial carcinoma cells) to identify IL-1α-dependent protein complexes that associate with promoters of inflammatory genes. These inflammatory promoters were compared to promoters of genes whose expression is driven by the conventional Pol II transcription machinery. To this end, sgRNAs were designed to target the promoters of inflammatory gene *IL8* and a constitutively expressed housekeeping gene *GUSB*. Expression vectors for the target-specific sgRNA, FB-dCas9, and BirA were transiently transfected into HeLa cells (Figure 10B). One-third of the total plasmid DNA was used for each vector. Cells expressing non-targeting sgRNA directed against the binding site of yeast transcription factor Gal4 or BirA only were analyzed as controls. The expression of dCas9 and BirA was detected by Western blot analysis and the transfection efficiency of sgRNAs was microscopically confirmed through mCherry coexpression and estimated to be 52% (Figure 10C).

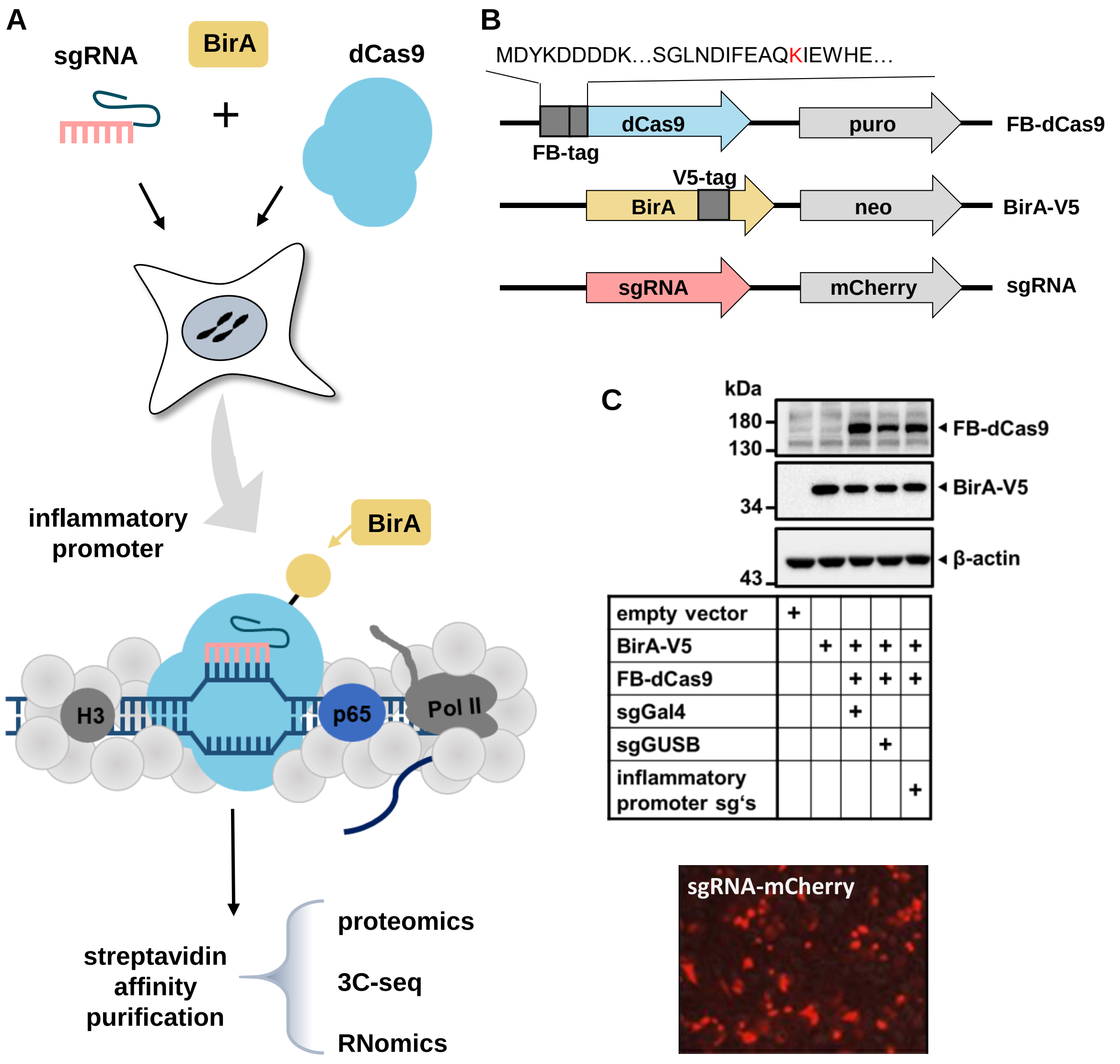

empty vector	+				
BirA-V5		+	+	+	+
FB-dCas9			+	+	+
sgGal4			+		
sgGUSB				+	
inflammatory promoter sg's					+

Figure 10: Principle of the original CAPTURE system and expression of its three components in HeLa cells. (A) Schematic of dCas9-mediated capture of a targeted genomic locus and subsequent analysis of locus-associated proteins, DNA, or RNA. The dCas9 and sgRNA are shown in blue and red colors, respectively, while the biotin modification is indicated by a yellow circle. (B) The three-vector system of CAPTURE 1.0: FLAG and biotin-acceptor-site (FB)-tagged dCas9 with puromycin-resistance cassette, V5-tagged biotin ligase BirA with neomycin-resistance cassette, locus-specific sgRNA with mCherry coexpression. The biotin acceptor lysine (K) is shown in red font. (C) Detection of FB-dCas9 and BirA-V5 expression in HeLa cells by Western blot analysis and confirmation of the sgRNA expression through the detection of mCherry fluorescence. Proteins were detected using the indicated antibodies and β-actin levels were assessed to control equal loading of gels. Shown is the result of one preparative experiment. (The schematic in A & B was adapted from [138] by Lisa Leib; C was performed in cooperation with Jana Juli.)

After verifying the expression of CAPTURE components, ChIP analyses targeting the *IL8 promoter* and *GUSB promoter* were performed to control the specificity and efficiency of the transiently transfected system (Figure 11). For this purpose, transfected HeLa cells were kept untreated, with the only exception of sg*IL8* transfected cells, which were additionally treated with IL-1α. The intention was to improve the pulldown efficiency of this promoter through IL-1α-induced chromatin unwinding allowing better access for dCas9 molecules. The antibody-based dCas9-ChIP was therefore compared to the streptavidin-biotin-based CAPTURE-ChIP using magnetic dynabeads or agarose beads. CAPTURE-ChIP with agarose beads showed that sgRNAs specifically bound to the targeted region of the *IL8 promoter* or *GUSB promoter* and obtained the highest binding intensity with yields up to 3% of input chromatin. Contrary to the assumption that additional treatment with IL-1α increases the pulldown efficiency of the *IL8 promoter*, no significant difference was observed between the untreated and IL-1α-treated condition. As expected, there was no sgRNA binding detectable to the *GAPDH promoter*, indicating no off-target effects of the sg*IL8*. Additionally, there was no unspecific binding observed in the negative controls BirA only and sgGal4. The sgRNA binding intensities were considerably lower when performing CAPTURE-ChIP with magnetic dynabeads compared to agarose beads, but sgRNA binding was almost undetectable in dCas9-ChIP when an antibody was used for the pulldown instead of streptavidin. This result was in line with the comparative ChIP-seq analysis from Liu et al. who previously demonstrated that high-affinity biotin-streptavidin-based CAPTURE-ChIP provided improved sensitivity and specificity compared with antibody-based FLAG- and dCas9-ChIP [138] and thus showed that the CAPTURE approach in the transiently transfected HeLa cell system was successfully established and worked efficiently.

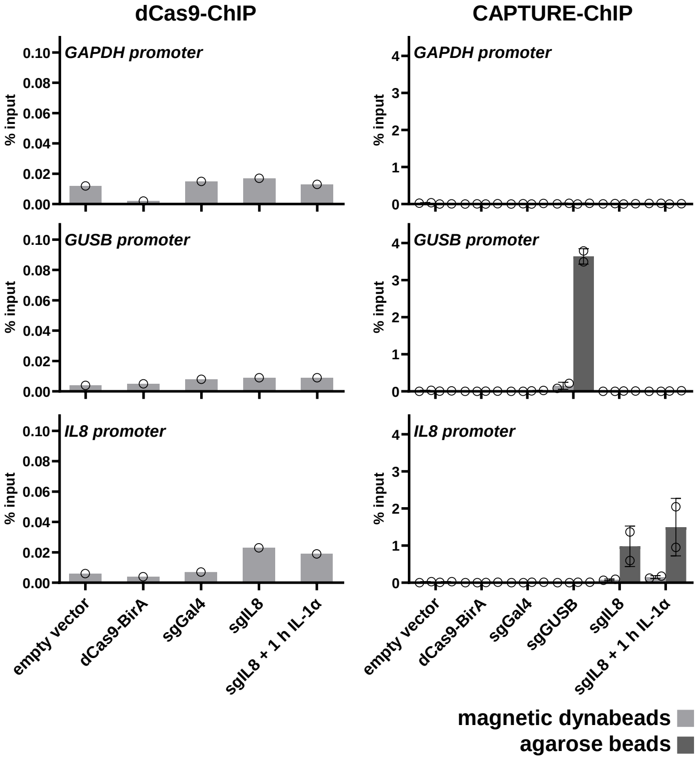

Figure 11: Higher efficiency of streptavidin-based CAPTURE-ChIP compared with antibody-based dCas9-ChIP.

Comparison of pulldown efficiencies between antibody-based dCas9-ChIP and streptavidin-based CAPTURE-ChIP performed with magnetic dynabeads or agarose beads in HeLa cells transiently transfected with dCas9-BirA and locus-specific sgRNAs targeting either the inflammatory *IL8 promoter* or the housekeeping gene *GUSB promoter*. Cells expressing non-targeting sgGal4 or dCas9-BirA only were analyzed as controls. Cells were treated for 1 h with IL-1α (10 ng/ml) or were left untreated. Chromatin precipitation was conducted according to the ChIP or CAPTURE-ChIP protocols using equal amounts (88 µg) of input chromatin. The qPCR analysis of pulldown samples controls sgRNA binding specificities by measuring on-target (*IL8 promoter*, *GUSB promoter*) and off-target (*GAPDH promoter*) enrichments relative to input chromatin. Left bar graphs show the result of one preparative experiment (dCas9-ChIP) and right bar graphs show means of two independent biological replicates ± SD (CAPTURE-ChIP). (The experiments were performed in cooperation with Jana Juli.)

Based on this result, an initial CAPTURE-protein pulldown experiment was performed according to the published protocol with only minor changes. Degradation patterns of large-sized proteins such as dCas9 and Pol II were observed in the Western blot analysis of input samples, indicating that further optimization of the lysis conditions was required before proceeding with protein pulldown experiments. The optimization was particularly important as the success of the pulldown strongly depends on protein integrity and high input quality. At that time, different lysis conditions including buffers and volumes, urea addition, washing steps, and sonication cycles were varied and analyzed. The comparative Western blot analysis showed that the best input quality was obtained with the subcellular fractionation using a fractional lysis protocol (Supplementary Figure 1). The N2 fraction of the fractional lysis, which contains the chromatin-bound nuclear proteins, was selected for the subsequent pulldown attempt.

Western blot analysis of the CAPTURE-protein pulldown that was conducted on N2 lysates displayed the efficient pulldown of dCas9 and confirmed *in vivo* biotinylation by BirA in the dCas9-sg*IL8* pulldown sample. However, the two known and expected binders of the targeted *IL8 promoter*, NF-κB p65 and Pol II, were not specifically enriched when comparing the dCas9-sg*IL8* pulldown sample with the control sample expressing BirA only (Figure 12). One possible reason was that targeting only the two alleles of one inflammatory promoter was not sufficient to enrich expected locus-specific proteins.

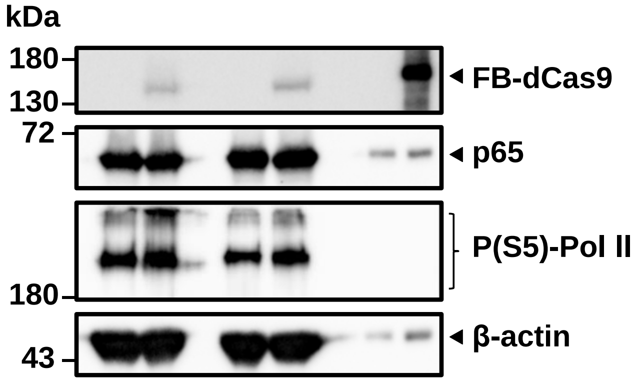

	IN 0.8%			SN 0.8%			PD 100%	
BirA-V5	+	+		+	+		+	+
FB-dCas9		+			+			+
sgIL8		+			+			+
1 h IL-1α		+			+			+

Figure 12: Streptavidin-based pulldown of *in vivo* biotinylated dCas9 targeted to the *IL8 promoter*. CAPTURE-protein pulldown of 1 × 10^8 HeLa cells transiently transfected with CAPTURE 1.0 components FB-dCas9, BirA-V5, and a sgRNA targeting the inflammatory *IL8 promoter*, which were treated for 1 h with IL-1α (10 ng/ml). Cells expressing BirA only were analyzed as a control. Nuclear lysates (input) were generated according to the fractional lysis protocol (3.4.3) and total amounts of lysates were subjected to the streptavidin-based pulldown using 2X 50 µl agarose beads (0.8% input and supernatant was retained for Western blot). The

dCas9 complexes were eluted from agarose beads by the addition of 40 µl elution buffer (30 µl RIPA buffer, 10 µl ROTI®Load). Western blot analysis was conducted on 0.8% input (IN), 0.8% supernatant (SN), and 100% of each pulldown (PD) sample. Proteins were detected using the indicated antibodies. The β-actin levels were assessed to control equal loading of gels. Shown is the Western blot result of one preparative experiment. (The experiment was performed in cooperation with Jana Juli.)

Liu et al. also showed that multiplexed CAPTURE enables targeting several genomic loci at once [159]. Hence, the next step to improve the pulldown efficiencies was to target the promoters of multiple inflammatory genes simultaneously with the expectation that this would increase the specific enrichment of binders (Figure 13A). Further nine promoters of inducible inflammatory genes, which were selected from the top 50 IL-1α-responsive mRNAs (based on RNA-seq data from KB cells), were therefore targeted by sgRNAs in HeLa cells. The subsequent CAPTURE-ChIP analysis confirmed their specific binding when transfected alone or as a pool (Figure 13B). Transfection of the sgRNA pool generally reduced the amount of DNA precipitate of individual promoter target regions. One explanation for this effect was the considerably lower plasmid DNA quantity used for transfection, as in the pool, each sgRNA containing plasmid was reduced to only a tenth of the original amount.

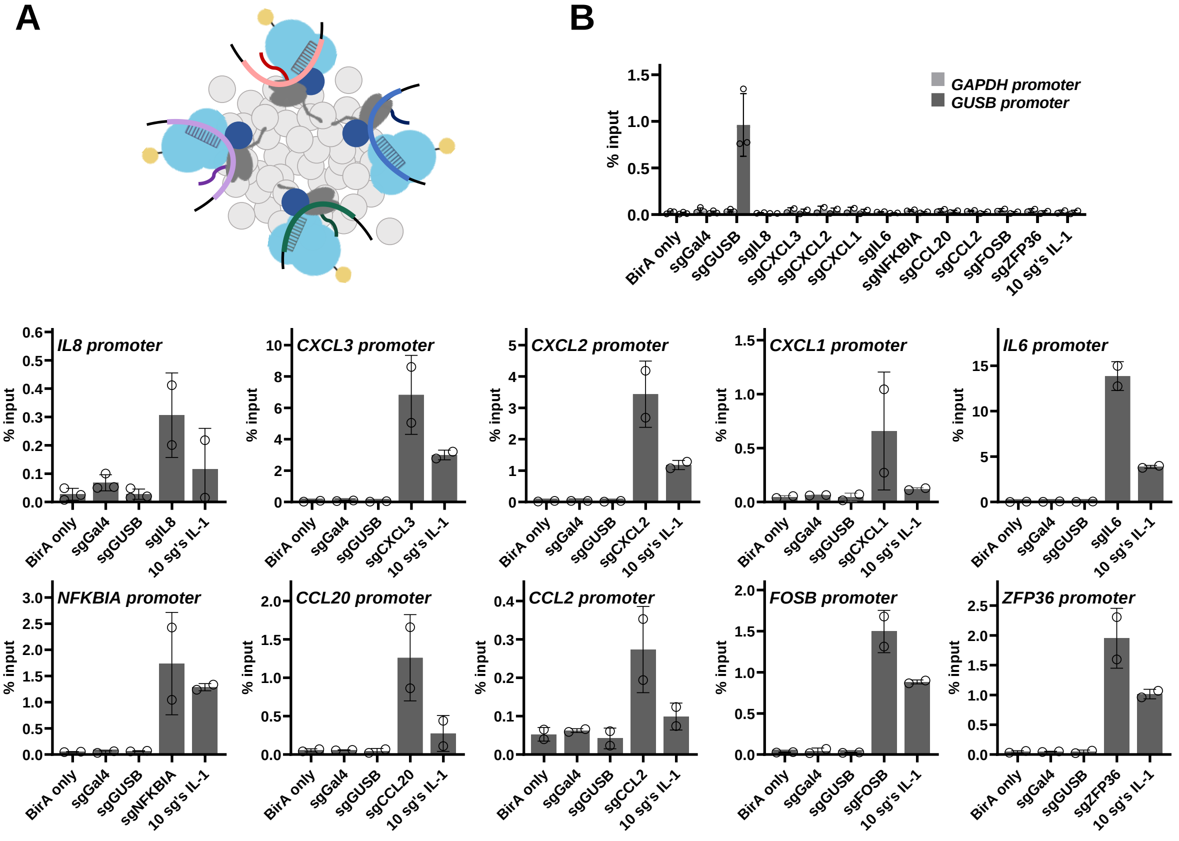

Figure 13: Highly specific pulldown of up to 10 inflammatory promoters by streptavidin-purification. (A) Schematic showing the principle of how targeting multiple inflammatory promoters at once potentially increases the efficiency of the CAPTURE-protein pulldown. (B) qPCR analysis upon CAPTURE-ChIP in HeLa cells transiently transfected with dCas9-BirA and sgRNAs targeting ten promoters of IL-1α-responsive genes (*CXCL 1,2,3,8*; *IL6*; *NFKBIA*; *CCL2,20*; *FOSB*; *ZFP36*), which were transfected alone or as pool (10 sg's IL-1). The bar graphs show the specific binding of all sgRNAs to their target promoters with no off-target binding to the other promoters or the non-inflammatory *GAPDH promoter*. Cells expressing non-targeting sgGal4 or BirA only were analyzed as additional negative controls. Bar graphs in (B) display means of two independent biological replicates ± SD. (The schematic in A was created by Lisa Leib; B was performed in cooperation with Jana Juli.)

Analysis of mRNA expression levels in the same set of samples also showed that binding of sgRNAs to the promoters did not affect IL-1α-inducible expression of the ten target genes, confirming that the selection of sgRNA target sequences was appropriate (Figure 14). However, the Western blot analysis of the streptavidin-pulldown showed that targeting ten promoters of IL-1α-responsive genes at once was still not sufficient to detect and specifically enrich known binders, although, purified dCas9 was again successfully detected (not shown). Since the transient transfection experiments up to this point were not very promising, probably due to the limited transfection efficiency in combination with the low probability of introducing all three expression vectors into the same cell, a stably expressed CAPTURE cell system with a much higher expected pulldown efficiency was established in a next step.

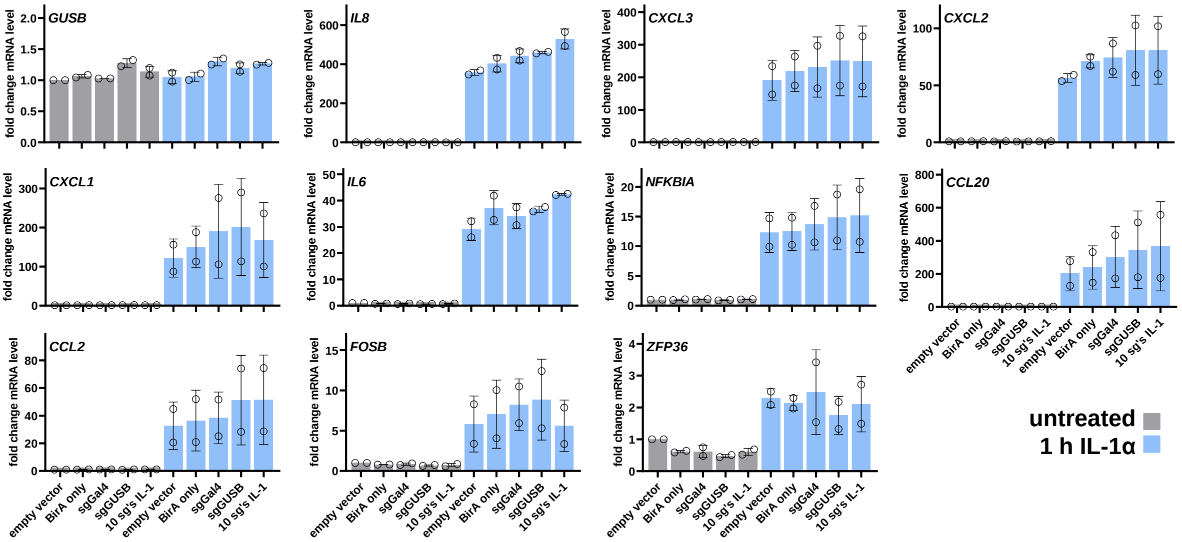

Figure 14: CAPTURE does not interfere with the IL-1α-inducible mRNA expression of targeted inflammatory genes.
RT-qPCR analysis of HeLa cells transiently transfected with dCas9-BirA and sgRNAs targeting the promoters of ten inflammatory genes, termed 10 sg's IL-1 (*CXCL 1,2,3,8*; *IL6*; *NFKBIA*; *CCL2,20*; *FOSB*; *ZFP36*), or the housekeeping gene *GUSB promoter.* Cells were treated with IL-1α (10 ng/ml) for 1 h or kept untreated. Empty vector-transfected cells and cells expressing non-targeting sgGal4 or BirA only were analyzed as controls. Bar graphs display means of two independent biological replicates ± SD. (The experiments were performed in cooperation with Jana Juli.)

4.1.2 Generation of stably transfected CAPTURE 1.0 dCas9-BirA expressing HeLa cell lines

To improve pulldown efficiencies, monoclonal HeLa cell lines expressing FB-dCas9 and BirA-V5 were generated by stable transfection. One of the main challenges in this context was the resistance of HeLa cells towards the neomycin-analog geneticin, which was the antibiotic-selection marker in the pEF1a-BirA-V5-neo expression vector. Therefore, the neomycin-resistance cassette was replaced by a blasticidin-resistance cassette by molecular cloning. This step proved to be essential for generating stable CAPTURE 1.0 HeLa cells.

Parental HeLa cells were thereupon transfected with the according expression vectors for FB-dCas9 and BirA-V5 using lipofectamine. After the transfection, cells were cultured in a medium containing the selection markers puromycin and blasticidin until untransfected control cells were dead. Selected cells were then seeded at low density until single monoclonal colonies became visible, which were picked, expanded, and subsequently tested by Western blot. After several rounds of picking and testing the selected HeLa cells, three potential candidates, clone 1, clone 6, and clone 7, were chosen for further characterization (Figure 15A). Expression patterns of FB-dCas9 and BirA-V5 were maintained for at least three weeks, however, only clone 7 showed a level of FB-dCas9 expression that was comparable to the level in transiently transfected control cells (Figure 15B). The stable expression of dCas9 and BirA in clone 7 furthermore allowed the targeted pulldown of promoter sequences of *GUSB* and *CXCL3* upon sgRNA transfection (Figure 15C) and did, as before, not interfere with the expression of IL-1α-inducible genes (Figure 15D). At this point, Liu et al. published the advanced second-generation of the CAPTURE system, called CAPTURE 2.0. In this publication, they demonstrated the higher efficiency of CAPTURE 2.0 compared with the first-generation system which they from now on referred to as CAPTURE 1.0 [159]. The advanced system used two vectors (instead of three) for all CAPTURE components, an altered biotinylation acceptor sequence, and enabled lentivirus-mediated transduction of the expression vectors and subsequent fluorescence-sorting for each of the CAPTURE components. It was therefore decided to build on the experiences made with CAPTURE 1.0 but switch to CAPTURE 2.0 to generate stable cell lines for large scale purifications.

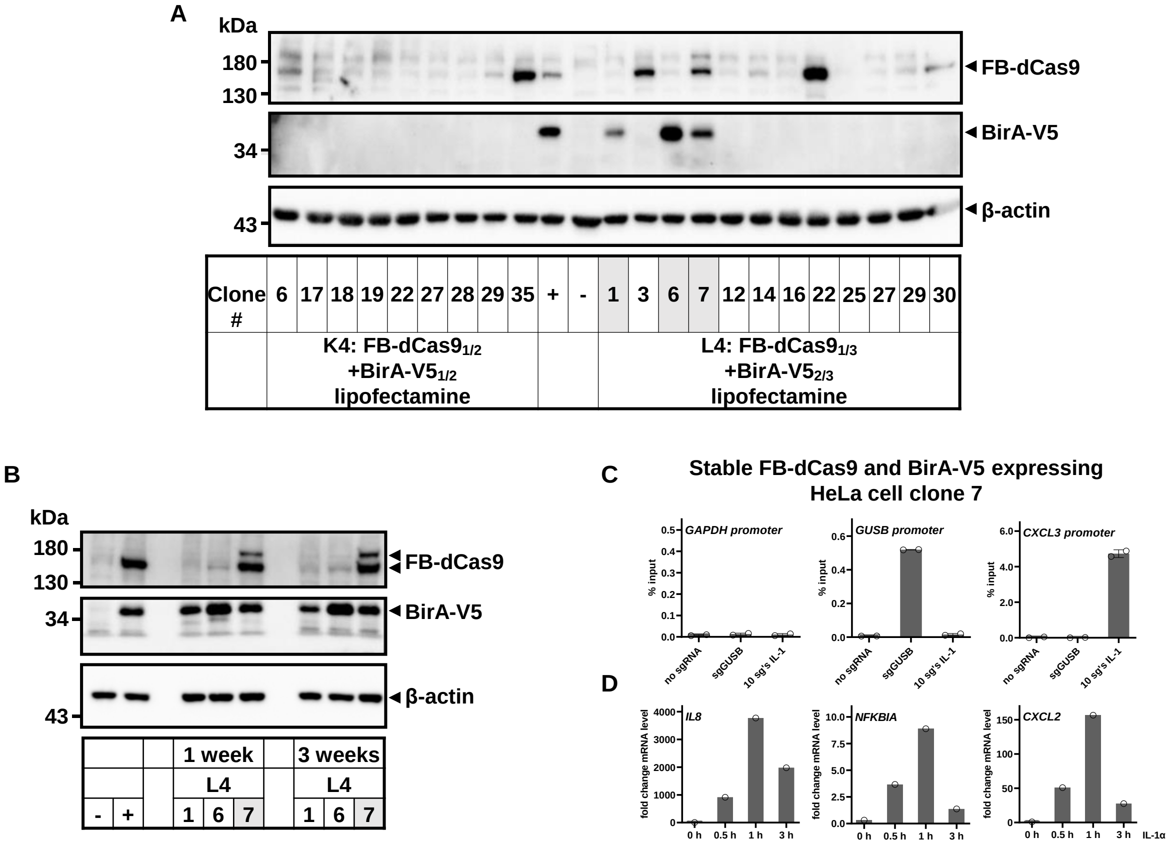

Figure 15: Functional testing of FB-dCas9 and BirA-V5 stable expressing HeLa cell clone 7.
(A) Western blot analysis of HeLa cell clones transfected with FB-dCas9 and BirA-V5 in different ratios (K4, L4) using the lipofectamine transfection reagent and selected with puromycin (0.75 µg/ml) and blasticidin (7.5 µg/ml)

for 7 days. (B) Western blot analysis of the stable expression of dCas9-BirA in HeLa clones 1, 6, and 7 after one and three weeks of culturing in selection medium. In (A) and (B), proteins were detected using the indicated antibodies and β-actin levels were assessed to control equal loading of gels. (C) Demonstration of the functional CAPTURE system in stable FB-dCas9-BirA-V5 expressing HeLa cells (clone 7) by CAPTURE-ChIP-qPCR. The analysis shows locus-specific sgRNA binding at the *GUSB promoter* and *CXCL3 promoter* after transient transfection with sg*GUSB* or 10 sg's IL-1 (*CXCL 1,2,3,8*; *IL6*; *NFKBIA*; *CCL2,20*; *FOSB*; *ZFP36*) compared to control cells that were not transfected (no sgRNA), without unspecific binding of transfected sgRNAs in the off-target promoter region of non-inflammatory gene *GAPDH*. (D) RT-qPCR analysis of clone 7 shows that stable expression of dCas9 and BirA did not hinder the expression of endogenous inducible genes at different time points of stimulation with IL-1α (10 ng/ml). The Western blots in (A) and (B), and bar graphs in (C) show the result of one preparative experiment and bar graphs in (D) show means of two independent biological replicates ± SD. (The experiments were performed in cooperation with Jana Juli.)

4.1.3 Establishing stably transduced CAPTURE 2.0 dCas9-CBio-sgRNA expressing HeLa cells

The CAPTURE vector system was redesigned and published by Liu et al. in 2020 who generated a tricistronic vector system that allows FB-dCas9, BirA, and zsGreen coexpression from only one transcript (CAPTURE 1.1). In a second step, they replaced the FB-tag upstream of dCas9 with an N-terminal or C-terminal BioTAP-tag (CAPTURE 2.0 NBio or CBio). The BioTAP-tag consists of a 69-amino acid sequence that enables *in vivo* biotinylation of dCas9 by endogenous biotin ligases in eukaryotic cells (Figure 16A). Through the direct comparison of these vector systems by CAPTURE-ChIP, Liu et al. showed that each of the systems significantly increased the CAPTURE efficiency relative to CAPTURE 1.0. The highest level of improvement was achieved with the C-terminal biotinylation of dCas9, while the high specificity and on-target enrichment of dCas9-targeted and purified chromatin was retained [159].

A set of stable HeLa cells coexpressing dCas9-CBio and different sgRNAs targeting inflammatory promoters was therefore generated and analyzed. This set of cells was designed to address the question of whether the protein pulldown efficiency increases with the number of targeted loci and comprised cells expressing sgRNA targeting the promoter of the *CXCL3* gene, cells expressing sgRNAs targeting four promoters of the genes which are located in the CXC chemokine locus on chromosome 4 (*CXCL 1,2,3,8*) or sgRNAs targeting ten promoters of IL-1α-responsive genes (*CXCL 1,2,3,8*; *IL6*; *NFKBIA*; *CCL2,20*; *FOSB*; *ZFP36*). The sg*CXCL3* was specifically selected for the single-locus application due to its high CAPTURE efficiency in previous experiments. Cells expressing no sgRNA, non-targeting sgGal4, or sg*GUSB* were generated as controls. Lentiviral transduction was then used to stably integrate these CAPTURE 2.0 components into the HeLa genome. Cells expressing zsGreen (dCas9-CBio) or mCherry (sgRNA) were FACS sorted and cultivated until they were further analyzed. Western blot verified the stable expression of dCas9 and its C-terminal biotinylation by endogenous biotin ligases (Figure 16B). Coexpression of zsGreen was difficult to detect through microscopy, even though it was well-detectable by the previous FACS analysis (see Figure 6). Successful stable expression of the vectors carrying sgRNA, however, was microscopically confirmed through mCherry coexpression and was significantly improved by FACS-sorting to nearly 100%. The mRNA expression analyses of the transduced cells showed that inflammatory gene expression is neither affected by the lentiviral procedure nor by stable coexpression of CAPTURE components of the second-generation (Supplementary Figure 2).

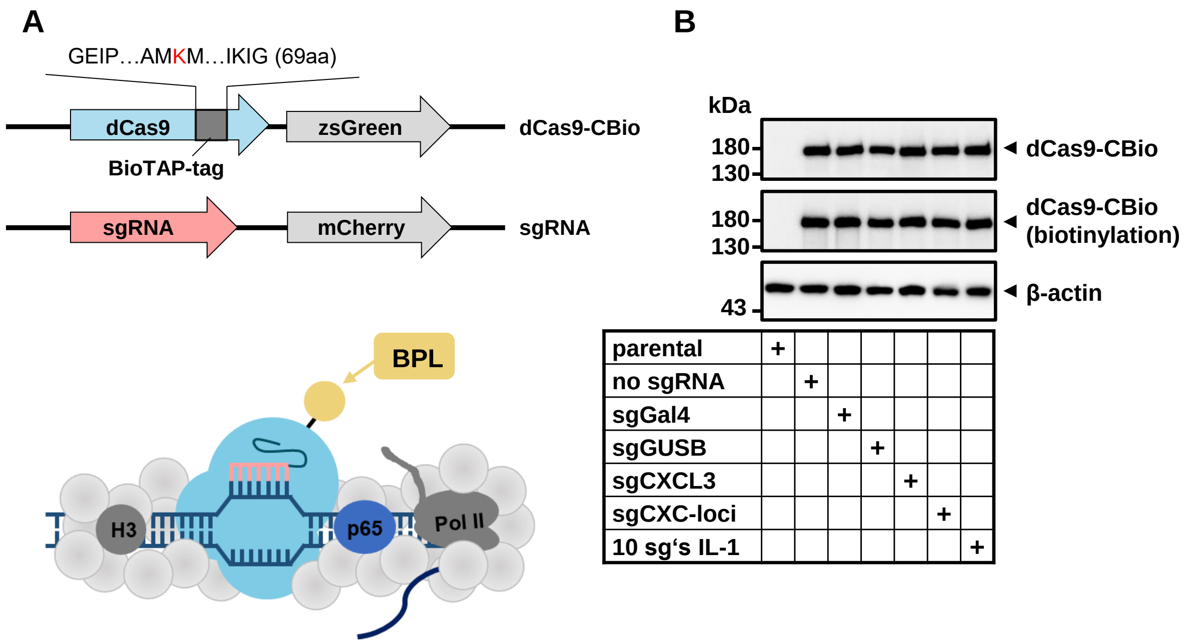

parental	+						
no sgRNA		+					
sgGal4			+				
sgGUSB				+			
sgCXCL3					+		
sgCXC-loci						+	
10 sg‘s IL-1							+

Figure 16: Principle of the advanced CAPTURE 2.0 system and stable expression of dCas9-CBio together with sgRNAs targeting different sets of inflammatory promoters in HeLa cells.
(A) Schematic of the redesigned CAPTURE 2.0 vector system that relies on *in vivo* biotinylation of dCas9 through a C-terminal BioTAP-tag (CBio) that is recognized by endogenous biotin protein ligases (BPL) and coexpression of a target-sgRNA. (B) Western blot analysis confirming the stable expression and biotinylation of dCas9-CBio in HeLa cells which were transduced with lentiviruses containing expression vectors of dCas9-CBio and sgRNAs targeting the *CXCL3 promoter*, promoters of the four genes located in the CXC chemokine cluster on chromosome 4 (*CXCL 1,2,3,8*) or promoters of ten IL-1α-responsive genes, termed 10 sg's IL-1 (*CXCL 1,2,3,8*; *IL6*; *NFKBIA*; *CCL2,20*; *FOSB*; *ZFP36*). Parental cells and cells expressing no sgRNA, non-targeting sgGal4 or sg*GUSB* were generated as controls. Proteins were detected using the indicated antibodies and β-actin levels were assessed to control equal loading of gels. Shown is the result of one preparative experiment. (The schematic in A was adapted from [159] by Lisa Leib; B was performed in cooperation with Jana Juli.)

The CAPTURE-ChIP-qPCR analysis of transduced cells once more illustrated the specific binding of sgRNAs to the targeted promoter regions across the different stable dCas9-CBio-sgRNA expressing cell lines while no off-target enrichment was detectable at the *GAPDH promoter*. The analysis in Figure 17 showed that the pulldown efficiency in stably expressing dCas9-CBio cells (CAPTURE 2.0) was 2.1-17.1-fold higher than in transiently transfected FB-dCas9 cells (CAPTURE 1.0) expressing ten sgRNAs at once. The smallest increase was observed for sg*CXCL3*, which, however, already exhibited one of the highest pulldown efficiencies of 3% input in transiently transfected CAPTURE 1.0 cells, whereas the greatest increase was observed for sg*GUSB*. Accordingly, the extent of the increase in pulldown efficiency was dependent on the sgRNA that was used. This promising result was consistent with the publication from Liu et al. who achieved a 13.6-fold improvement in efficiency using K562 cells [159].

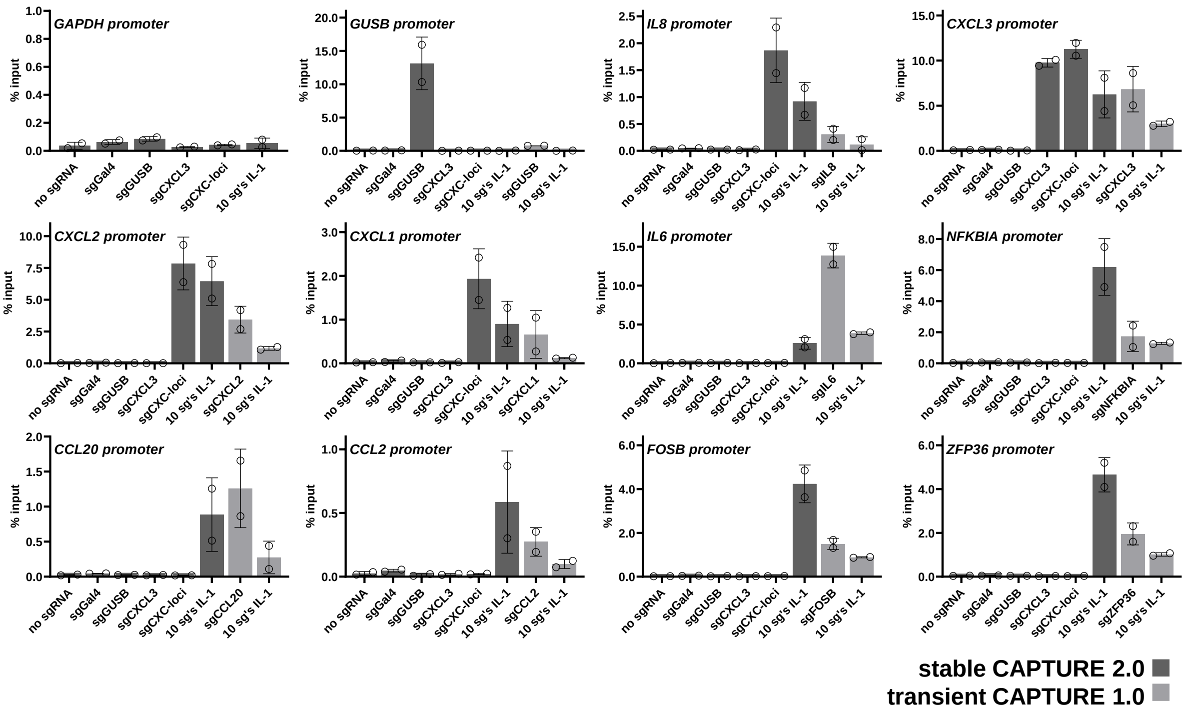

Figure 17: Up to 17-fold increase in pulldown efficiency using the stable CAPTURE 2.0 HeLa cell system. CAPTURE-ChIP-qPCR analysis of stable HeLa cells expressing dCas9-CBio and sgRNAs targeting the promoters of housekeeping gene *GUSB*, *CXCL3*, of four genes located in the CXC chemokine cluster on chromosome 4 (*CXCL 1,2,3,8*) or promoters of ten inflammatory genes, termed 10 sg's IL-1 (*CXCL 1,2,3,8*; *IL6*; *NFKBIA*; *CCL2*,*20*; *FOSB*; *ZFP36*). The bar graphs illustrate the improved CAPTURE efficiency obtained with CAPTURE 2.0 compared to CAPTURE 1.0 samples transiently expressing dCas9-BirA and sgRNAs targeting promoters of ten inflammatory genes at once (10 sg's IL-1). Stable CAPTURE 2.0 cells expressing no sgRNA, non-targeting sgGal4 or sg*GUSB* were analyzed as controls. Bar graphs display means of two independent biological replicates ± SD. (The experiments were performed in cooperation with Jana Juli.)

The improved pulldown efficiency with stable CAPTURE 2.0 cells led to the performance of another CAPTURE-protein pulldown attempt in which dCas9-CBio cells with sgRNAs targeting ten inflammatory promoters at once were compared to no sgRNA expressing control cells. These samples were affinity purified using streptavidin-beads according to the CAPTURE-Proteomics protocol described in this work. However, the CAPTURE-protein pulldown showed that the combination of (i) targeting ten loci at once, (ii) stably expressing CAPTURE components, and (iii) applying the advanced CAPTURE 2.0 vector system was not sufficient to specifically enrich known binders of inflammatory promoters like p65 or histone H3 in HeLa cell extracts under the tested condition (Figure 18).

The challenges and limitations as well as the lack of success of the CAPTURE-protein pulldown using the HeLa cell system at this point prompted the decision to further focus this work on the establishment and implementation of an alternative proximity-dependent interactomics approach, the MiniTurboID method, that allowed to tackle the inflammatory interactome in HeLa cells from a different experimental angle.

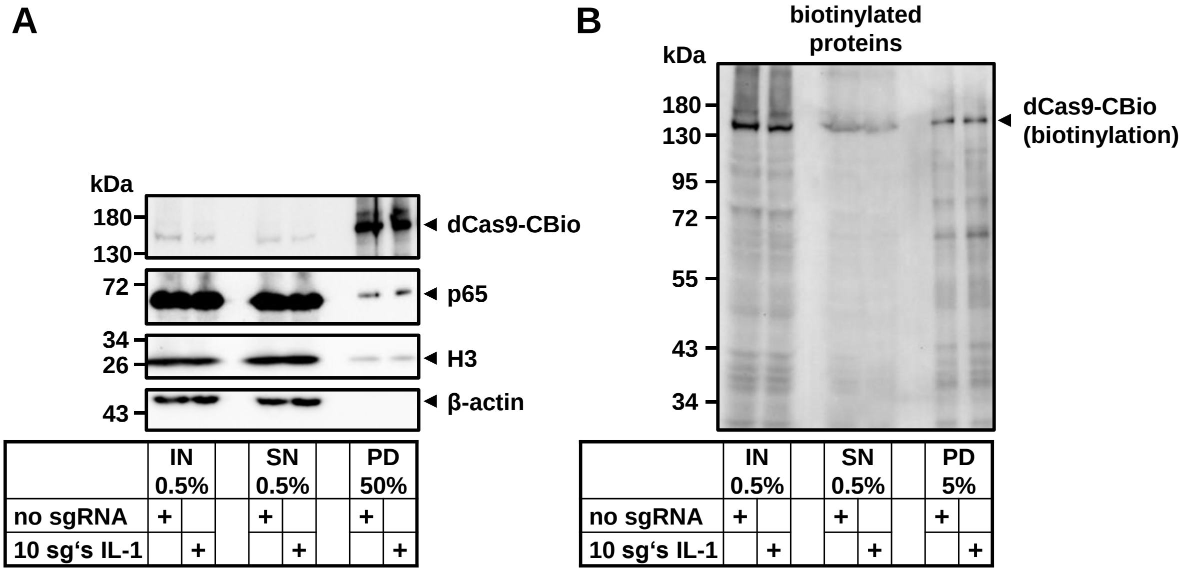

Figure 18: CAPTURE-protein pulldown analysis targeting 10 inflammatory promoters at once using CAPTURE 2.0.

CAPTURE-protein pulldown of 1 × 10^8 stable transduced HeLa cells with CAPTURE 2.0 components dCas9-CBio and sgRNAs targeting promoters of ten inflammatory genes, termed 10 sg's IL-1 (*CXCL 1,2,3,8*; *IL6*; *NFKBIA*; *CCL2,20*; *FOSB*; *ZFP36*). Stable cells expressing dCas9-CBio alone (no sgRNA) were analyzed as control. Nuclear lysates (input) were generated according to the CAPTURE-Proteomics protocol (3.4.7) and total amounts of lysates were subjected to the streptavidin-based pulldown using 2X 50 µl agarose beads (1% input and 1% supernatant was retained for Western blot). The dCas9 complexes were eluted from agarose beads by the addition of 30 µl RIPA buffer and 10 µl ROTI®Load. Western blot analysis was conducted on 0.5% input (IN), 0.5% supernatant (SN) and 50% or 5% of each pulldown (PD) sample. Proteins were detected using the indicated antibodies and β-actin levels were assessed to control equal loading of gels (A). Biotinylation was assessed using streptavidin-horseradish peroxidase conjugates (B). Shown is the Western blot result of one preparative experiment. While dCas9 was successfully enriched in the pulldowns, no difference in the biotinylation pattern compared with the negative control (no sgRNA) was observed. (The experiment was performed in cooperation with Jana Juli.)

Taken together, HeLa cell systems with both transient and stable expression of CAPTURE components from the first- and second-generation were successfully established in this work. The data from CAPTURE-ChIP experiments showed the remarkable sensitivity and specificity of the CAPTURE pulldown mediated by biotin-streptavidin interaction surpassing the antibody-based approach. Furthermore, the results demonstrated the applicability of this method for simultaneous targeting of multiple inflammatory loci at once. The transient and stable HeLa cell system likewise provided reproducible CAPTURE-ChIP results. Notably, the second-generation stable CAPTURE cells provided the highest yield of precipitated target DNA. On the other hand, despite extensive testing of various experimental conditions, the use of CAPTURE for protein identification did not lead to a significant enrichment of locus-specific interactors beyond the background noise. This highlights the technical challenges and limitations of single-locus-based protein pulldowns, in particular, when these innovative techniques are transferred and adapted to other cellular systems.

4.2 MiniTurboID-based proximity labeling of the NF-κB p65 interactome

4.2.1 Principle design of MiniTurboID proximity labeling for mapping the interactomes of wild type and mutant NF-κB p65

In this chapter of the thesis, the inflammatory interactome was approached by placing the experimental focus on the key transcription factor NF-κB p65 that drives inflammatory gene expression. The protein interaction networks of NF-κB p65 and its point mutants that prevent DNA binding or dimerization were therefore examined by the MiniTurboID proximity labeling method using IL-1α-stimulated or unstimulated HeLa cells. The MiniTurboID technique as an unbiased approach allows the mapping of the protein interactome of soluble or insoluble proteins of interest in living cells. As shown schematically in Figure 19, the technique is based on the genetic fusion of a bait protein with a biotin ligase. After the addition of exogenous biotin, the enzyme catalyzes endogenous labeling of proteins within a radius of 10-30 nm [140, 160]. The exact value depends on the length of the linker insertion between the bait protein and enzyme and thus the protein complex under study conditions [161]. Biotin-labeled proteins are subsequently separated through high-affinity biotin-streptavidin purification and analyzed by liquid chromatography with tandem mass spectrometry (LC-MS/MS).

One crucial advantage of this method over the classical, antibody-based affinity-purification was the ability to not only capture constitutive interactions but also transient, low-affinity, and sub-stoichiometric interactions. In contrast to the first generations of proximity labeling techniques, which require 16-18 h of labeling time, newer generations, such as engineered mutants of the *E. coli* biotin ligase BirA, TurboID, and miniTurbo, catalyze labeling in as little as 10 min but with similar labeling radius, size, and specificity of the captured proteome [162]. This was required given that the IL-1α-induced cellular response, including the phosphorylation, release, nuclear migration, and chromatin binding of NF-κB p65, occurs in a small time window of only 1 h. In contrast to TurboID, miniTurbo additionally provided better temporal control of this labeling window due to reduced background labeling before the addition of exogenous biotin. Another benefit was that miniTurbo has a truncated protein size of only 28 kDa. This was important as larger fusion proteins were more likely to interfere with cellular mobility and shuttling of NF-κB p65 between cytoplasm and nucleus. Therefore, improved labeling kinetics, more precise temporal labeling, and small protein size were the key factors for chosing miniTurbo to map the basal and IL-1α-induced NF-κB p65 interactome in HeLa cells.

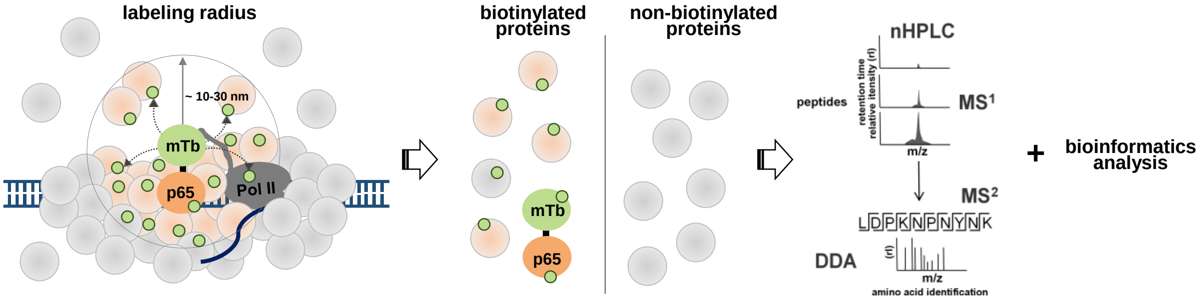

Figure 19: The principle of mapping the NF-κB p65 interactome by MiniTurboID proximity labeling. NF-κB p65 is fused to miniTurbo biotin ligase (mTb), which biotinylates proteins within an approximate radius of 10-30 nm of the transcription factor *in vivo*. In this way, proteins located in the vicinity of p65, whether constitutively or driven by IL-1α, are labeled with biotin. These biotinylated proteins are then extracted from the cells and separated from non-biotinylated proteins by streptavidin-based pulldown. The pulldown material is subjected to mass spectrometry analysis, and in a final step, the resulting data are bioinformatically analyzed. (The schematic was adapted from [161].)

The MiniTurboID mapping was designed to compare the interactomes of wild type p65 and two p65 point mutants. Three point mutations in the N-terminal REL homology domain (RHD), glutamate 39 to isoleucine (E/I), or phenylalanine 213 and leucine 215 to aspartic acid (FL/DD), respectively, were previously shown by co-immunoprecipitation (Co-IP) and electrophoretic mobility shift assay (EMSA) to inhibit DNA binding (E/I) or suppress dimerization (FL/DD) [163]. As shown in Figure 20, the C-terminal fusion of HA-miniTurbo was achieved by introducing the wild type cDNA of p65 and the mutant cDNAs encoding p65(E/I) and p65(FL/DD) into an empty vector containing the HA-miniTurbo expression cassette in the appropriate orientation. Additionally, the single vector system contained a tetracycline-sensitive promoter that allowed control and inducible expression of the construct depending on the availability of a tetracycline. The tetracycline associates with the reverse tetracycline-controlled transactivator (rtTA) which was constitutively coexpressed from the same expression vector (see map on page 70). Upon addition of tetracycline, the tetracycline-rtTA complex activates gene expression of the construct through binding to the tetracycline-responsive element (see map on page 70). In this study, the tetracycline doxycycline was used for the induction of the constructs for its improved pharmacokinetic properties [164].

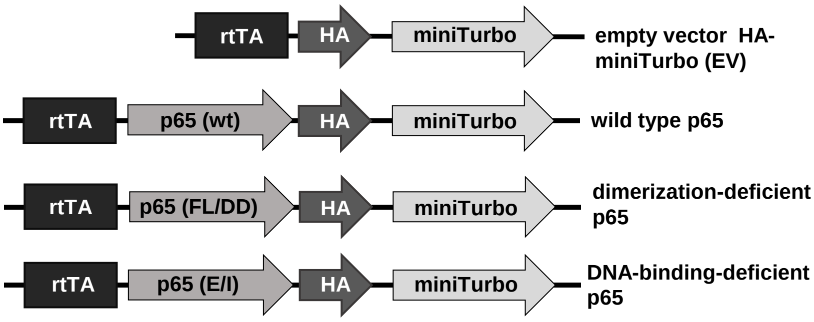

Figure 20: Design of the expression vectors encoding wild type and mutant p65-HA-miniTurbo constructs. The p65-HA-miniTurbo construct was designed as follows (N- to C-terminus): p65 gene, HA-tag, biotin ligase miniTurbo sequence. Glutamate 39 to isoleucine (E/I) or phenylalanine 213 and leucine 215 to aspartic acid (FL/DD) denote point mutations in the N-terminal REL homology domain (RHD) of p65 that have previously been shown to inhibit DNA binding or suppress dimerization, respectively. The constitutively expressed reverse

tetracycline-controlled transactivator (rtTA) activates the expression of the C-terminally tagged fusion protein upon the addition of tetracycline (see map on page 70). (The schematic was created by Prof. M. Kracht.)

4.2.2 Establishing the experimental conditions for the application of MiniTurboID

In the next step of this study, the experimental conditions were defined by using the wild type and empty vector HA-miniTurbo constructs. The doxycycline induction of the constructs was first optimized to find a condition at which the expression of the fusion protein resembled the endogenous expression level of p65. Parental HeLa cells and stable HeLa cells with largely reduced p65 levels (due to CRISPR-Cas9-based InDel mutations) were therefore grown in tetracycline-free DMEM medium and transfected with the expression vectors of p65(wt)-HA-miniTurbo and HA-miniTurbo alone. After 7 h, cells were treated with increasing amounts of 1-1000 ng/ml doxycycline for 17 h to induce the expression of HA-miniTurbo constructs. The expression levels of HA-miniTurbo constructs such as endogenous p65 were then assessed by Western blot analysis in unstimulated cells or cells stimulated with IL-1α for 1 h (Figure 21). The analysis illustrated the doxycycline-dependent expression of p65(wt)-HA-miniTurbo and HA-miniTurbo alone in either cell line using three independent antibodies. While the binding affinity of sc-372 anti-p65 and Roche anti-HA to their specific antigen was low or possibly perturbed by steric differences or through limited accessibility of the mTb-tag, sc-8008 anti-p65 showed the highest binding affinity to the p65 fusion protein and was therefore preferred for all subsequent studies. Another noteworthy observation was that after induction of the p65(wt)-HA-miniTurbo construct, a fragment was detected slightly below 72 kDa. This was likely an incompletely translated by-product, a phenomenon that is often observed with transiently transfected fusion proteins.

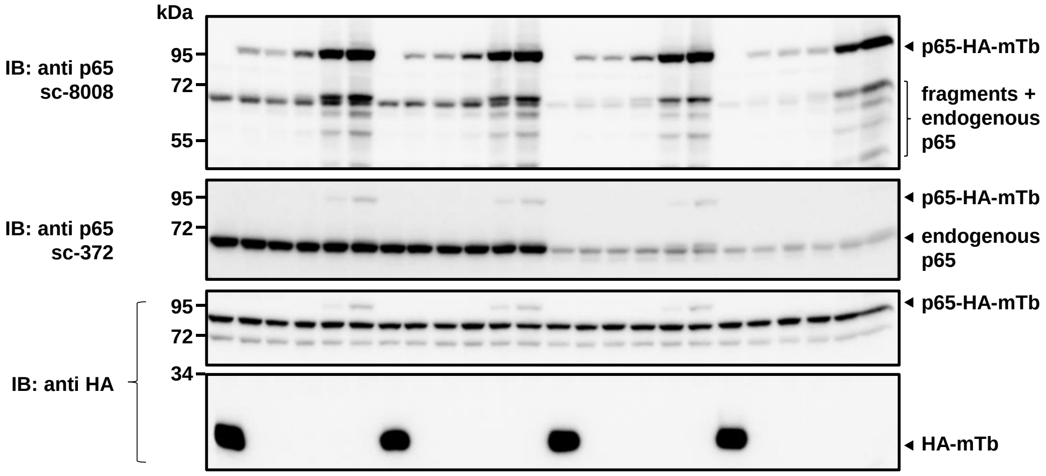

	parental												Δp65											
HA-mTb (EV)	+						+						+						+					
p65(wt)-HA-mTb		+	+	+	+	+		+	+	+	+	+		+	+	+	+	+		+	+	+	+	+
17 h doxycycline [µg/ml]	1	0	0,001	0,01	0,1	1	1	0	0,001	0,01	0,1	1	1	0	0,001	0,01	0,1	1	1	0	0,001	0,01	0,1	1
1 h IL-1α							+	+	+	+	+	+							+	+	+	+	+	+

Figure 21: Dose-dependent regulation of inducible p65-HA-miniTurbo expression and comparison with endogenous p65 expression levels.

Western blot analysis of the expression level of p65(wt)-HA-miniTurbo in parental and p65-deficient HeLa (Δp65) whole cell extracts. Cells were transfected with branched PEI and cultured in tetracycline-free DMEM medium. Then, increasing concentrations of doxycycline ranging from 1-1000 ng/ml were added 7 h post-transfection and cells were further incubated for 17 h to induce the expression of p65(wt)-HA-miniTurbo or HA-miniTurbo (EV) alone. For the last hour of incubation, cells were stimulated with IL-1α (10 ng/ml) or were left unstimulated and were then harvested and analyzed by Western blot. Proteins were detected using the indicated antibodies. Western blot of a single experiment displays a doxycycline-dependent expression of constructs and comparable expression levels of the p65 fusion protein and endogenous p65 at 10 ng/ml doxycycline. (The experiment was performed in cooperation with Jana Juli.)

While the Western blot analysis in Figure 21 showed that the expression levels of p65(wt)-HA-miniTurbo were highest at 1 µg/ml doxycycline, at 10 ng/ml doxycycline they were nearly similar to the endogenous level of p65. Subsequently, it was examined whether the fusion protein also exhibited the same properties as the endogenous protein after induction with 10 ng/ml doxycycline. Western blot analysis of the cytosolic, nuclear, and chromatin-bound proteins was therefore performed in parental and p65-deficient HeLa cells stimulated with IL-1α for 1 h or in unstimulated cells. The differential analysis however revealed that, unlike the endogenous protein, the fusion protein was neither sequestered in the cytosol nor it accumulated in the nucleus upon treatment with IL-1α. Instead, it was found in all three fractions in either cell line (Figure 22A). This showed that a fraction of the fusion protein is constitutively in the nucleus even at low concentrations of doxycycline. The orthogonal IF analysis also confirmed this finding at the single cell level and demonstrated that more p65(wt)-HA-miniTurbo positive cells were obtained at the highest doxycycline concentration of 1 µg/ml (Figure 22B). The improved expression efficiency across all cells was decisive for using 1 µg/ml doxycycline in the following experiments.

Another parameter that was considered related to the use of shorter doxycycline induction times. Both experiments in Figure 22 showed that 4 h of doxycycline treatment was sufficient to induce the expression of p65(wt)-HA-miniTurbo. However, experiments with 16-19 h of doxycycline treatment also showed no signs of toxicity due to the prolonged expression of the fusion protein. Instead, the longer treatment allowed direct performance of the pulldown experiment on the same day, so that treatment with 1 µg/ml doxycycline for 16-19 h was performed in all subsequent experiments.

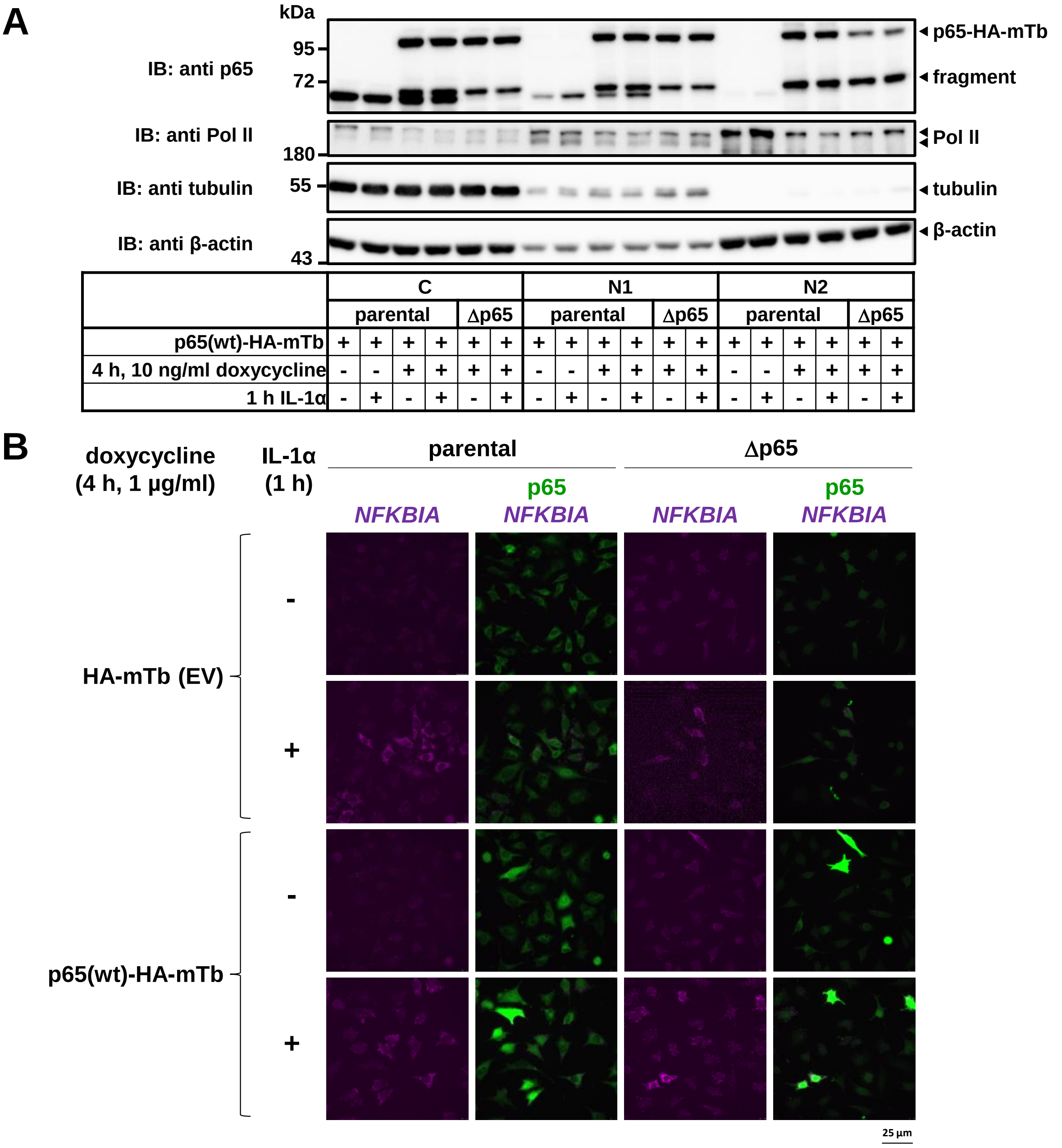

Figure 22: Subcellular localization of p65-HA-miniTurbo fusion proteins after induction with low concentrations of doxycycline.
(A) Western blot analysis of p65(wt)-HA-miniTurbo levels in parental and p65-deficient HeLa cells (Δp65) treated with 10 ng/ml doxycycline 20 h post-transfection and incubated for 4 h to induce the expression of p65(wt)-HA-miniTurbo. For the last hour of incubation, cells were stimulated with IL-1α (10 ng/ml) or left unstimulated, then they were harvested, and fractionated for the comparison of the cytosolic (C), nuclear (N1), and chromatin-bound (N2) proteins by Western blot. The indicated antibodies were used to determine p65 fusion protein levels or tubulin and Pol II levels to validate separation of cytosolic and nuclear fractions. The β-actin levels were assessed to control equal loading of gels. (B) Single-cell immuno-FISH analysis of p65(wt)-HA-miniTurbo and endogenous p65 levels in parental and p65-deficient HeLa cells transfected with HA-miniTurbo plasmids. Expression was induced by treating cells with 1 µg/ml doxycycline for 4 h. In the last hour of incubation, cells were stimulated with IL-1α (10 ng/ml) or were left unstimulated. IL-1α-induced mRNA expression was detected by the type 6 (magenta) specific branched probe set against *NFKBIA* (Affymetrix, #VA6-17971). Both experiments were conducted once. (The experiments were performed in cooperation with Jana Juli.)

In the next step, the biotin labeling condition was optimized by comparing the labeling efficiency of miniTurbo and the conventional BioID enzyme BirA upon different time points of biotin addition to

HeLa cells. In a previous report using various other cell systems [162], miniTurbo biotinylation was demonstrated to be considerably faster than the one of conventional biotin ligases. This was considered as an important point especially in light of the transient nature of IL-1α-NF-κB signaling, which rapidly changes within few hours and these changes were intended to be captured in this work. The expectation was that a short biotin labeling time that precisely matches the IL-1α stimulation time is better suited to ensure efficient biotin labeling and accumulation of inducible interactors, including those associated with NF-κB p65 signaling, translocation, and chromatin binding. The other assumption was that a prolonged biotin labeling time, beginning hours before IL-1α stimulation, does not sufficiently capture the IL-1α dynamics, but rather leads to strong biotin labeling and accumulation of basal p65 interactors only. To determine the labeling efficiency in HeLa cells, HA-miniTurbo or MYC-BirA were expressed and biotin labeling was initiated by the addition of 50 µM biotin. Labeling efficiencies were determined by Western blot analysis after 1 h, 3 h, and 19 h of biotin incubation (Figure 23). The streptavidin-HRP blot showed a strong biotinylation pattern for HA-miniTurbo already after 1 h of biotin labeling, but the intensity still increased with time. Biotinylation of MYC-BirA, in contrast, also increased, but the biotinylation pattern was much weaker at each time point. The test demonstrated that miniTurbo produced a better biotinylation result than BirA after 1 h of biotin addition, which experimentally increased the probability of labeling transient IL-1α-induced proteins.

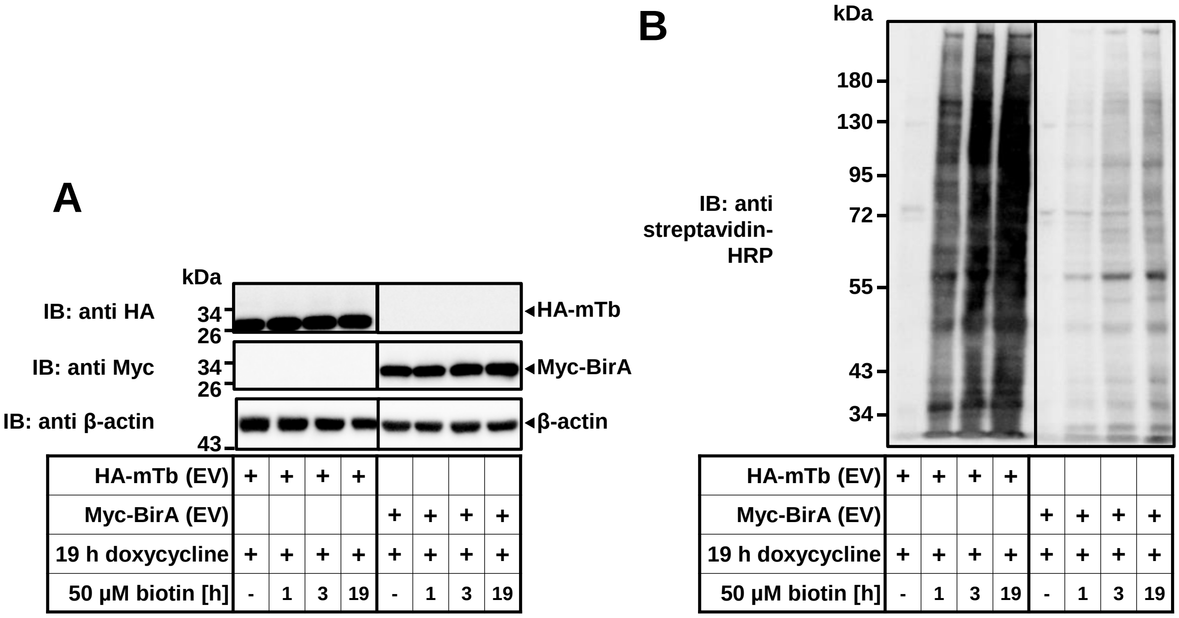

Figure 23: Comparing the biotin labeling efficiencies between miniTurbo and BioID2 in HeLa cells. Biotin labeling by miniTurbo (HA-miniTurbo), a genetically engineered 28 kDa version of *E. coli* BirA (BioID1) was compared to BioID2 (MYC-BirA) derived from *Aquifex aeolicus* after inducing the expression of the biotin ligases with 1 µg/ml doxycycline for 19 h in parental HeLa cells. (A) Expression levels of the enzymes were assessed by Western blot analysis using the indicated tag-antibodies. The β-actin levels were assessed to control equal loading of gels and (B) the biotinylation efficiency was determined through streptavidin-HRP detection after 1 h, 3 h, and 19 h labeling with 50 µM biotin. The single experiment demonstrated improved labeling by miniTurbo after 1 h biotin addition. (The experiment was performed in cooperation with Jana Juli.)

The biotin-labeled proteins were then purified by an initial pulldown experiment to investigate whether IκBα, a known canonical interactor of p65, was present among these proteins. In addition, it was tested whether a higher concentration of 500 µM biotin or a prolonged labeling time of 18 h improved the pulldown result. HeLa cells with deficient p65 levels were therefore transfected with p65(wt)-HA-miniTurbo and HA-miniTurbo alone. After 7 h, the expression of the constructs was induced by treating cells with 1 µg/ml doxycycline for 18 h. One day after transfection, biotin-labeling was induced by 50 µM or 500 µM biotin for 1 h (Figure 24) or 18 h (Supplementary Figure 3). For samples transfected with p65(wt)-HA-miniTurbo, doxycycline or biotin were omitted, providing two additional negative control conditions. Biotinylated proteins in cell lysates were then purified using streptavidin-coated agarose beads and analyzed in comparison to the input by Western blot. Indeed, miniTurbo labeling resulted in the pulldown of IκBα in samples of cells expressing p65(wt)-HA-miniTurbo but not in control samples where doxycycline or biotin had been omitted or samples of cells expressing HA-miniTurbo alone. With 500 µM biotin, neither the amount of IκBα in the pulldown samples (Figure 24A) nor the strength of the biotinylation pattern (Figure 24B) was noticeably increased. Prolonged 18 h labeling in contrast caused an enormous increase of IκBα levels in pulldown samples as well as in the overall biotinylation pattern. However, this most likely occurred through the accumulation of basal p65 binders, such as IκBα, and also through non-specifically biotinylated proteins. For this reason, the approach based on a labeling time that was just covering the IL-1α stimulation time of 1 h was maintained, further assuming that this would preferentially enrich the induced transient interactors. Biotin labeling in subsequent experiments was therefore performed with 50 µM biotin for 1 h.

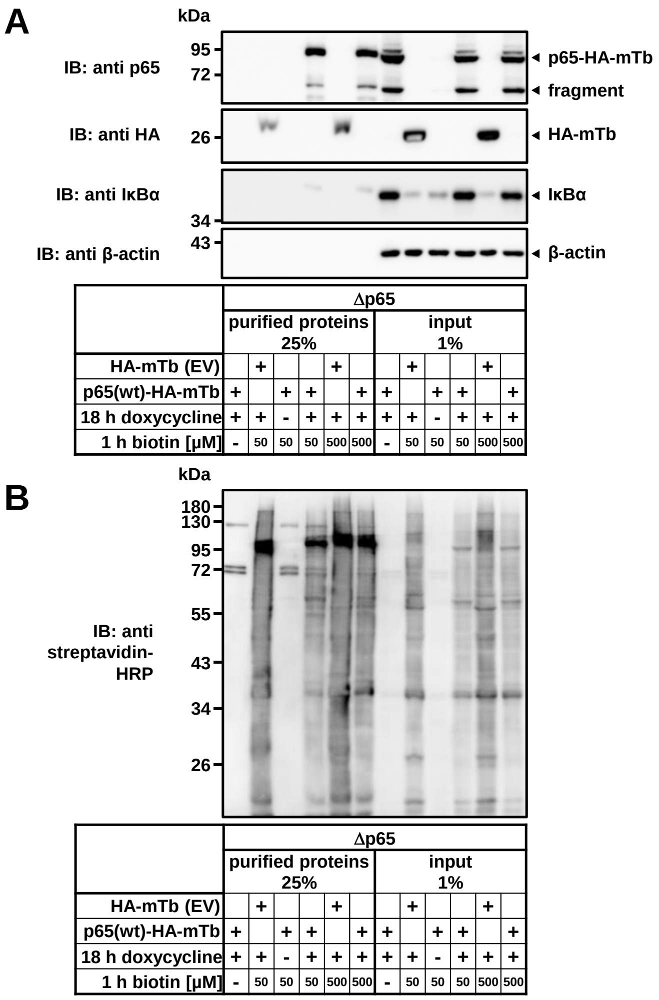

Figure 24: Validation and optimization of biotin-based proximity labeling of NF-κB p65 interactomes. Western blot analysis after streptavidin-based pulldown of biotinylated proteins in p65-deficient HeLa cells (Δp65) treated with 1 µg/ml doxycycline 7 h post-transfection and incubated for 18 h to induce the expression of p65(wt)-HA-miniTurbo or HA-miniTurbo alone. For the last hour of incubation, cells were treated with 50 µM or 500 µM biotin to induce biotin labeling by miniTurbo. In (A), biotinylated proteins were purified by a streptavidin matrix and analyzed in comparison to the input by Western blot using the indicated antibodies. The β-actin levels were assessed to control equal loading of gels. In (B), samples were probed with streptavidin-HRP to assess the overall biotinlyation pattern. Western blots of a single experiment confirm the pulldown of the expected canonical p65 binder IκBα and show that increasing biotin concentrations did not improve the pulldown result. (The experiment was performed in cooperation with Jana Juli.)

After these steps, a further experiment was performed to test whether higher volumes of streptavidin agarose beads further increased the amount of pulldown material or whether the initial volume of 30 µl beads was sufficient to extract the majority of all biotinylated proteins from the lysates. For this purpose, cell extracts from p65-deficient HeLa cells transfected with p65(wt)-HA-miniTurbo and HA-miniTurbo alone were prepared under pre-established conditions and biotinylated proteins were purified using 30 µl, 60 µl, 90 µl, or 120 µl beads. Subsequently, input, supernatant, and purified proteins were analyzed by Western blot. Although there was no major difference in the amount of purified and enriched biotinylated IκBα (Figure 25A), the streptavidin-HRP blot showed that some biotinylated proteins remained in the supernatant when 30 µl beads were used, indicating that this amount of beads was saturated by the large proportion of biotinylated proteins present in the cell extracts (Figure 25B).

This was not the case when using 60 µl beads and for this reason, the 60 µl condition was used for follow-up experiments.

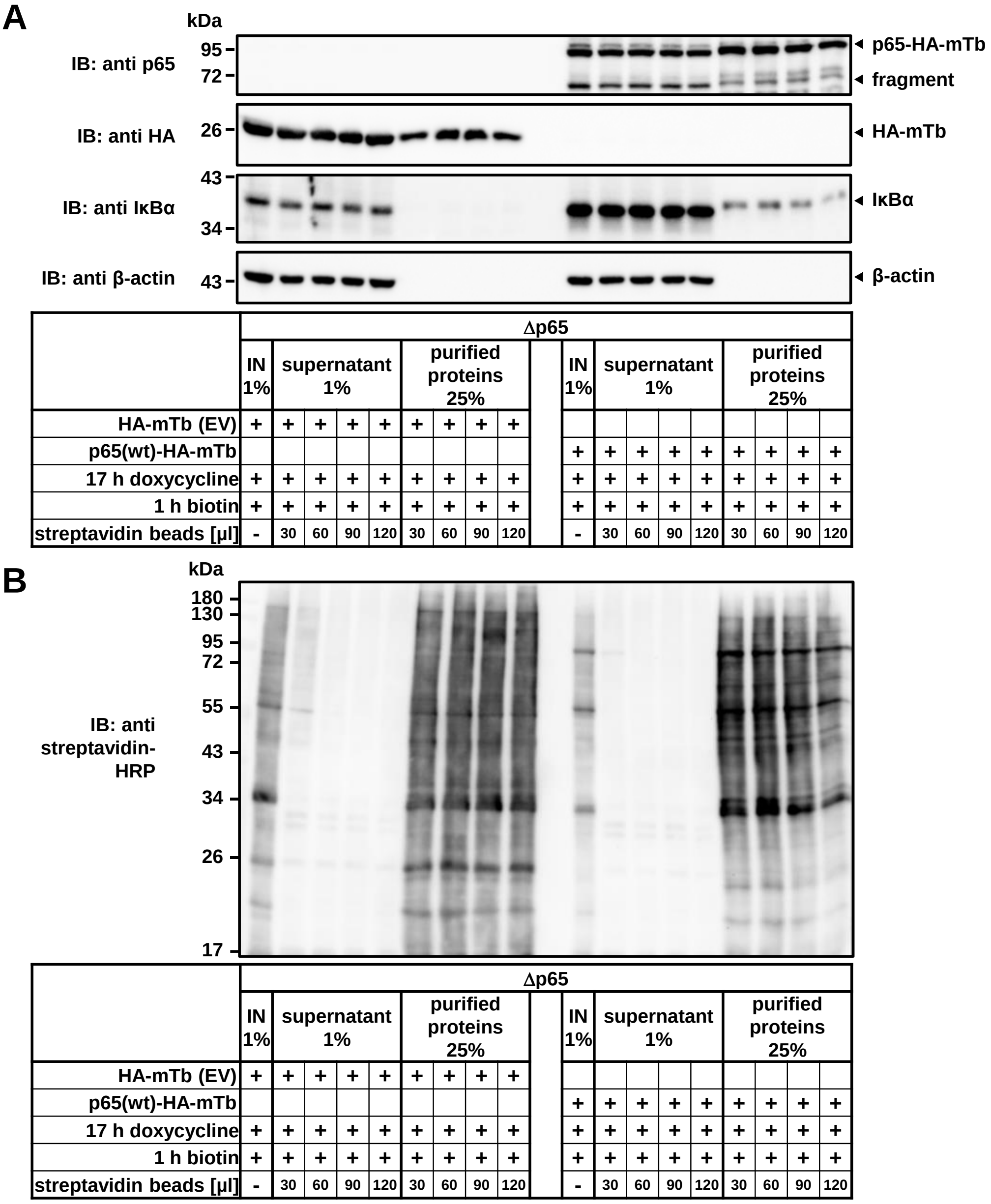

	Δp65																		
	IN 1%	supernatant 1%				purified proteins 25%					IN 1%	supernatant 1%				purified proteins 25%			
HA-mTb (EV)	+	+	+	+	+	+	+	+	+										
p65(wt)-HA-mTb											+	+	+	+	+	+	+	+	+
17 h doxycycline	+	+	+	+	+	+	+	+	+		+	+	+	+	+	+	+	+	+
1 h biotin	+	+	+	+	+	+	+	+	+		+	+	+	+	+	+	+	+	+
streptavidin beads [µl]	-	30	60	90	120	30	60	90	120		-	30	60	90	120	30	60	90	120

	Δp65																		
	IN 1%	supernatant 1%				purified proteins 25%					IN 1%	supernatant 1%				purified proteins 25%			
HA-mTb (EV)	+	+	+	+	+	+	+	+	+										
p65(wt)-HA-mTb											+	+	+	+	+	+	+	+	+
17 h doxycycline	+	+	+	+	+	+	+	+	+		+	+	+	+	+	+	+	+	+
1 h biotin	+	+	+	+	+	+	+	+	+		+	+	+	+	+	+	+	+	+
streptavidin beads [µl]	-	30	60	90	120	30	60	90	120		-	30	60	90	120	30	60	90	120

Figure 25: Optimizing volumes of streptavidin beads for quantitative purification of biotinylated proteins. Western blots comparing the efficacy of 30 µl, 60 µl, 90 µl, or 120 µl streptavidin beads in affinity purification. Cell extracts from p65-deficient HeLa cells (Δp65) transfected with p65(wt)-HA-miniTurbo and HA-miniTurbo alone were prepared under pre-established conditions: Cells were treated with 1 µg/ml doxycycline 7 h post-transfection and incubated for 17 h to induce the expression of the constructs. For the last hour of incubation, cells were treated with 50 µM biotin for 1 h to induce biotin labeling by miniTurbo. Biotinylated proteins were purified from cell extracts by streptavidin agarose matrix and analyzed in comparison to input (IN) and supernatant samples using the indicated antibodies (A) or streptavidin-HRP (B). The β-actin levels were assessed to control equal loading of gels. Western blots from a single experiment demonstrate that 60 µl was the minimum bead volume required to remove all biotinylated proteins from the supernatant. (The experiment was performed in cooperation with Jana Juli.)

4.2.3 Investigating the transcriptional activity of p65-HA-miniTurbo constructs

Next, NF-κB p65 target genes were analyzed to investigate whether the p65 fusion protein was functional, i.e. capable of activating the expression of prototypical inflammatory genes, focussing on p65-deficient HeLa cells that were reconstituted with different p65-HA-miniTurbo constructs. Cells were transfected with p65(wt), p65(E/I), p65(FL/DD), HA-miniTurbo alone, or empty vector and induced by doxycycline for 16 h. Total RNA was isolated from cells that were kept unstimulated or stimulated for 1 h with IL-1α. Subsequent RT-qPCR of two prototypical NF-κB p65 target genes showed that stimulation with IL-1α still resulted in a modest induction of *NFKBIA* and *CXCL2* expression despite depleted p65 levels in the cells. This baseline expression was important to assess the basal and IL-1α-inducible effects of different p65-HA-miniTurbo constructs on gene expression. The analysis revealed gene-specific effects on *NFKBIA* and *CXCL2* expression depending on the construct. *NFKBIA* expression under basal and IL-1α-treated conditions was activated by wild type p65 (Figure 26). Western blot analysis from a similar experiment (see above) showed that this effect was also reflected at the protein level of IκBα (NFKBIA) (Figure 24A & Figure 25A). Transcriptional activation of *NFKBIA* by the wild type construct before and after IL-1α treatment was largely impaired by the p65(E/I) and p65(FL/DD) mutants. Wild type p65 also induced the basal expression of *CXCL2*. A similar but weaker induction was observed for the p65(E/I) mutant, whereas the transcriptional activation of *CXCL2* under basal conditions was completely demolished by the p65(FL/DD) mutant. In contrast to *NFKBIA*, treatment with IL-1α further increased the expression of *CXCL2* after expressing wild type p65 and the p65(E/I) mutant, but not after p65(FL/DD) expression. Using two prototypical NF-κB p65 target genes as examples, this experiment confirmed the constitutive and IL-1α-dependent transcriptional activity of the wild type p65 fusion protein in reconstituted p65-deficient HeLa cells but also demonstrated the limited ability of the p65(FL/DD) fusion protein to induce target gene expression, whereas the p65(E/I) fusion protein still showed some gene-specific transcriptional activity.

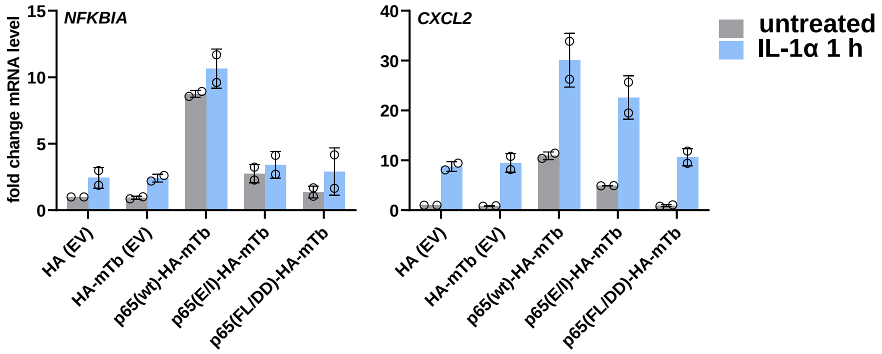

Figure 26: The p65-HA-miniTurbo fusion protein activates inflammatory gene expression.
The transcriptional regulatory function of HA-miniTurbo fusion proteins was examined by RT-qPCR analysis after wild type p65-HA-miniTurbo and its DNA binding (E/I) or dimerization-deficient (FL/DD) analogs were expressed. The analysis was carried out in p65-deficient HeLa cells (Δp65), which were transfected with p65(wt), p65(E/I), p65(FL/DD), and HA-miniTurbo alone or empty vector (as controls) and induced for 16 h with doxycycline. For the last hour of incubation, cells were stimulated with IL-1α (10 ng/ml) or kept unstimulated and subsequently analyzed by RT-qPCR. Bar graphs display the relative mRNA levels of *NFKBIA* and *CXCL2* calculated relative to the unstimulated empty vector control. The analysis shows that expression of p65(wt) induces expression of two prototypical NF-κB p65 target genes under basal and IL-1α-stimulated conditions. While the p65(FL/DD) fusion protein largely impaired the inducible expression of the target genes, the p65(E/I) fusion protein still showed some gene-specific transcriptional activity. Bar graphs show means of two independent biological replicates ± SD. (The experiments were performed in cooperation with Jana Juli.)

4.2.4 Large scale proximity labeling and purification of the NF-κB p65 interactome

The previously established conditions were applied to identify the proximity-labeled interactors of wild type p65 and its point mutants. As before, HeLa cells and cells with reduced p65 levels were therefore reconstituted by transfection with p65(wt)-HA-miniTurbo or the two mutant variants p65(E/I) and p65(FL/DD) or empty vector HA-miniTurbo alone as a control. After transfection, constructs were induced with doxycycline for 17 h, and on the following day, biotin was added 10 min before IL-1α treatment to ensure biotin labeling right at the onset of cytokine stimulation. As additional negative controls, p65(wt)-HA-miniTurbo transfected cells were included in which doxycycline or biotin were omitted. Half of the samples were stimulated for 1 h with IL-1α. Afterwards, the biotin-labeled proteins from the extracts of these cells were purified using streptavidin-coated agarose beads and analyzed by Western blot or mass spectrometry.

Western blot analysis of input samples displayed comparable expression levels of wild type p65 or the two mutant versions in both cell lines (Figure 27A). The expression of the fusion proteins or HA-miniTurbo alone was not influenced by 1 h stimulation with IL-1α. The streptavidin-HRP blot showed a strong pattern of non-specifically biotinylated proteins in pulldown samples of the control condition (empty vector, EV, encoding HA-miniTurbo alone) (Figure 27B), showing the high mobility and intracellular activity of HA-miniTurbo. In contrast, all pulldown samples of p65-HA-miniTurbo constructs exhibited a weaker biotinylation pattern, although, several specific signals were visible which were not found in the HA-miniTurbo control. The streptavidin-HRP blot also showed that *in vivo* labeling of proteins by miniTurbo required the simultaneous addition of doxycycline and biotin to the culture. This was illustrated by the lack of signal when either doxycycline or biotin were omitted. This effect demonstrated the specificity of HA-miniTurbo labeling in HeLa cells under the established labeling conditions. Detection of protein bands by sensitive silver staining showed a similar pattern as the streptavidin-HRP blot and confirmed that there was sufficient protein in the pulldown samples for mass spectrometric identification (Supplementary Figure 4).

In the following analyses, HA-miniTurbo empty vector (EV) and doxycycline-omitted wt(dox) or biotin-omitted wt(bio) samples served as three critical negative controls to define specific p65/RELA interactors by excluding non-specific proteins labeled by (i) HA-miniTurbo alone, (ii) leaky p65-HA-miniTurbo expression outside of the labeling time window, or (iii) naturally occurring intracellular biotinylated proteins and were therefore fundamental in the subsequent bioinformatic evaluation of the mass spectrometric data obtained from the samples.

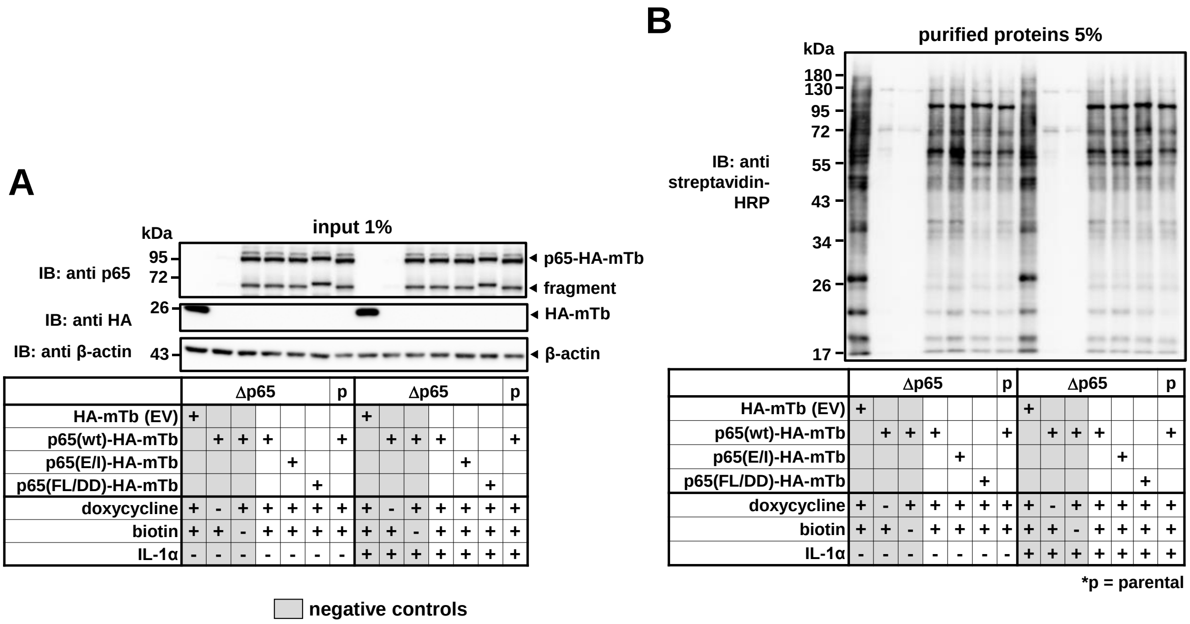

Figure 27: Validation of the large scale MiniTurboID experiment of wild type p65 and p65 DNA binding and dimerization mutants sent for LC-MS/MS analysis.
Western blots of input (A) and purified (B) protein samples from p65-deficient (Δp65) or parental HeLa cells transfected with different HA-miniTurbo constructs encoding p65(wt), p65(E/I), p65(FL/DD), and HA-miniTurbo alone (empty vector, EV) as a negative control. Expression of the constructs was induced 7 h post-transfection with 1 µg/ml doxycycline for 17 h. For the last hour of incubation, biotin labeling by miniTurbo was induced by adding 50 µM biotin 10 min before stimulating half of the cell cultures for 1 h with IL-1α (10 ng/ml). Two additional negative controls were included in which p65(wt) transfected cells were excluded from doxycycline or biotin treatment. Streptavidin-pulldowns were performed with 700 µl of cell extracts using 60 µl agarose beads, and inputs and purified proteins were analyzed by Western blot using construct-specific antibodies or streptavidin-HRP. The β-actin levels were assessed to control equal loading of gels. Presented is a representative replicate from two biological replicates. (The experiments were performed in cooperation with Jana Juli.)

4.2.5 Bioinformatic analysis reveals hundreds of new p65/RELA interactors

Two biological replicates of the pulldown samples defined above were analyzed by mass spectrometry. Liquid chromatography coupled to tandem mass spectrometry (LC-MS/MS) of the purified biotinylated proteins resulted in the identifcation of 3,927 protein IDs across all samples (Figure 28A & B). The raw intensity values corresponding to the IDs were further processed using Perseus. In Perseus, intensity values were $\log_2$-transformed, and missing values were imputed by a value just below the minimum intensity measured throughout all conditions, which allowed the calculation of ratio values and was the basis for statistical comparisons between samples using the Student's T-test (Figure 28B). The comparison between two samples was visualized by Volcano plots, where proteins with a significant p value ≤ 0.05 (corresponding to $-\log_{10}$ p value ≥ 1.3) and an at least fourfold difference (corresponding to LFC ≥ 2) were defined as enriched (Figure 28C). Detailed information on the data processing steps with Perseus can be found on page 73, and the step-by-step bioinformatic workflow is summarized in the legend in Figure 28.

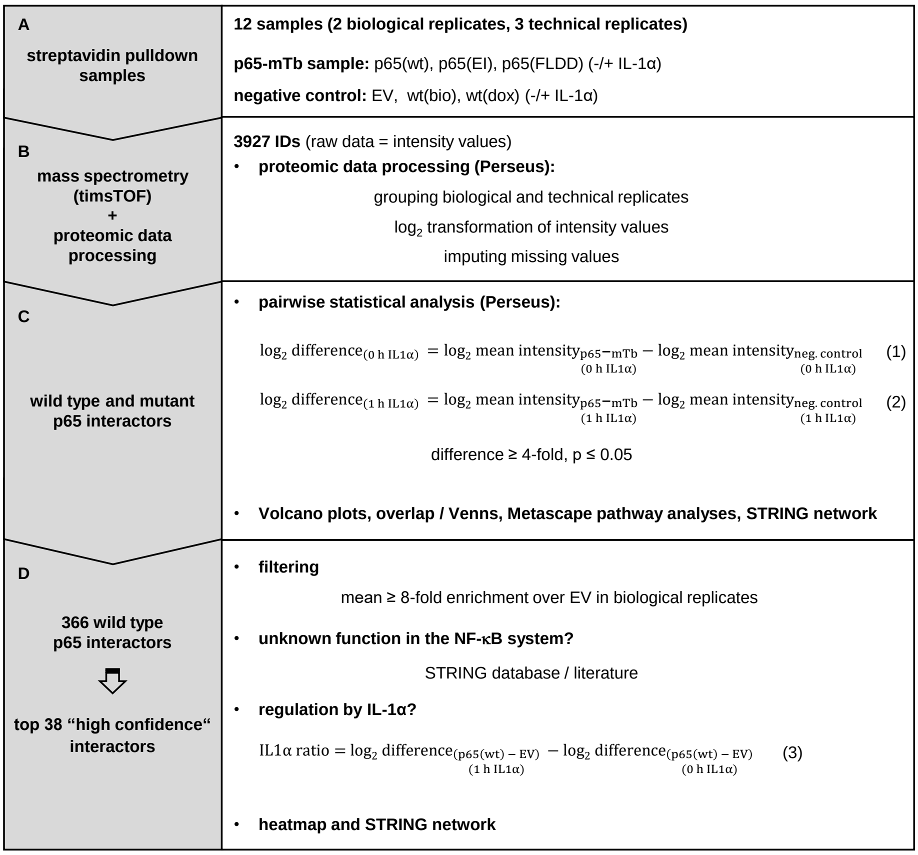

A **streptavidin pulldown samples**	**12 samples (2 biological replicates, 3 technical replicates)** **p65-mTb sample:** p65(wt), p65(EI), p65(FLDD) (-/+ IL-1α) **negative control:** EV, wt(bio), wt(dox) (-/+ IL-1α)
B **mass spectrometry (timsTOF)** **+** **proteomic data processing**	**3927 IDs** (raw data = intensity values) • **proteomic data processing (Perseus):** grouping biological and technical replicates $\log_2$ transformation of intensity values imputing missing values
C **wild type and mutant p65 interactors**	• **pairwise statistical analysis (Perseus):** $\log_2 \text{difference}_{(0\text{ h IL1}\alpha)} = \log_2 \text{mean intensity}_{\underset{(0\text{ h IL1}\alpha)}{\text{p65-mTb}}} - \log_2 \text{mean intensity}_{\underset{(0\text{ h IL1}\alpha)}{\text{neg. control}}}$ (1) $\log_2 \text{difference}_{(1\text{ h IL1}\alpha)} = \log_2 \text{mean intensity}_{\underset{(1\text{ h IL1}\alpha)}{\text{p65-mTb}}} - \log_2 \text{mean intensity}_{\underset{(1\text{ h IL1}\alpha)}{\text{neg. control}}}$ (2) difference ≥ 4-fold, p ≤ 0.05 • **Volcano plots, overlap / Venns, Metascape pathway analyses, STRING network**
D **366 wild type p65 interactors** ⇩ **top 38 "high confidence" interactors**	• **filtering** mean ≥ 8-fold enrichment over EV in biological replicates • **unknown function in the NF-κB system?** STRING database / literature • **regulation by IL-1α?** $\text{IL1}\alpha \text{ ratio} = \log_2 \text{difference}_{\underset{(1\text{ h IL1}\alpha)}{(\text{p65(wt)} - \text{EV})}} - \log_2 \text{difference}_{\underset{(0\text{ h IL1}\alpha)}{(\text{p65(wt)} - \text{EV})}}$ (3) • **heatmap and STRING network**

Figure 28: Step-wise bioinformatic analysis of NF-κB p65 interactome data.
Detailed graphical representation of the NF-κB p65 interactome data analysis. (A) The analysis was based on 12 streptavidin pulldown (MiniTurboID) samples obtained from p65-deficient (Δp65) HeLa cells (see Figure 27 & Supplementary Figure 4). (B) Mass spectrometry of two biological and three technical replicates resulted in a total of 3,927 IDs with corresponding protein intensity values (raw data) across the sample set, which were further processed using Perseus. The three main processing steps included the grouping of the replicates, the $\log_2$ transformation of the intensity values, and the imputation of missing values (for details see page 73). (C) The interactors of wild type p65 (wt) and p65 mutants (E/I, FL/DD) in the presence and absence of IL-1α (six groups) were defined by pairwise statistical analysis (Student's T-test) using Perseus. Pairwise statistics was performed based on the difference between the $\log_2$ mean intensity values of a p65-miniTurbo(mTb) transfected sample (wt, E/I, FL/DD) and a negative control sample (EV, wt(bio), wt(dox)) (equation 1). The same calculation was used for samples treated with IL-1α for 1 h (equation 2). In total, 18 pairwise comparisons were performed between the p65-mTb samples and negative controls in (A). Pairwise comparisons were visualized by Volcano plots. Supplementary Figure 6 exemplarily shows the pairwise comparisons between p65(wt) and the three negative control samples. Figure 29 shows the pairwise comparisons between wild type or mutant p65 (wt, E/I, FL/DD) and the EV control. Enriched proteins with a ≥ 4-fold difference (p value ≤ 0.05) compared to the three negative control samples were defined as interactors of wild type p65 (wt) or mutant p65 (E/I, FL/DD). The six resulting protein groups and their overlaps are shown in Figure 30. Figure 31 and Supplementary Figure 5 display the results of (comparative) Metascape pathway analyses for the six groups or the groups of proteins, which were enriched in p65(wt) and EV samples, respectively. Figure 32 shows a detailed bioinformatic analysis of 366 wild type p65 interactors obtained under basal and IL-1α-treated conditions using Venns [148] / Metascape [149] / STRING [150]. (D) The number of wild type interactors was further restricted by additional filtering steps, which resulted in a list of 38 "high-confidence" p65 interactors (HCI). Filtering steps included the filtering by mean ≥ 8-fold enrichment over the EV control in both biological replicates and the lack of evidence for a function in the NF-κB system (based on the STRING database [150] and literature). The IL-1α ratio was determined to classify inducible and constitutive interactors. This ratio was calculated by the difference between the $\log_2$ differences of the IL-1α-treated p65(wt) and untreated p65(wt) samples with corresponding EV control samples (equation 3). IL-1α ratios of 38 HCI are displayed by a heatmap in Figure 33. Figure 34 shows the STRING interaction network of the HCI.

The MiniTurboID samples were prepared together with Jana Juli (Figure 27 & Supplementary Figure 4). LC-MS/MS mass spectrometry measurements were performed in the Mass Spectrometry Facility of the Department of Chemistry, Philipps University Marburg (headed by Dr. Uwe Linne). Raw data were mapped to the human proteome by Dr. Uwe Linne and Dr. Axel Weber using the MaxQuant framework. The bioinformatic strategy and the entire set of analyses (Figure 29-34, Figure 37, Supplementary Figure 5 & 6) was devised, carried out and visualized by Prof. M. Kracht. Except for the filtering steps and literature search in (D), which were performed by Lisa Leib and Jana Juli. Lisa Leib performed the Metascape pathway analysis in Supplementary Figure 5, created the schematic of the step-wise bioinformatic analysis (Figure 28), and adapted the graphs provided by Prof. M. Kracht. Lisa Leib and Jana Juli extensively discussed, checked, and re-analyzed the data.

The Volcano analyses in Figure 29 of HA-miniTurbo control (EV) and the p65-HA-miniTurbo constructs reflected the strong enrichment of non-specifically biotinylated proteins in the HA-miniTurbo (EV) control sample as observed before by Western blot, but also showed specific labeling and enrichment of hundreds of proteins by the small biotin ligase miniTurbo in the p65 fusion protein samples. Metascape pathway overrepresentation analysis revealed that most of the proteins enriched in the HA-miniTurbo (EV) sample were abundant proteins, which are found in many protein pulldown experiments. These proteins largely belonged to cellular pathways such as cytoskeleton organization or RNA metabolic processes (Supplementary Figure 5). On the other side, p65/RELA was found highly enriched through (auto-) biotinylation across samples expressing the fusion proteins. (Auto-) biotinylation of p65/RELA was largely similar between fusion protein samples showing that not only the expression level but also the biotinylation efficiency of the fusion proteins was greatly comparable. The functionality of the p65-HA-mTb fusion proteins was also evident from the observation that p65/RELA was enriched together with many of its canonical pathway components such as p50 (NFKB1), p52 (NFKB2), IκBα (NFKBIA), and NEMO (IKBKG) across most of the samples, thus demonstrating the high quality and reliability of this MiniTurboID dataset.

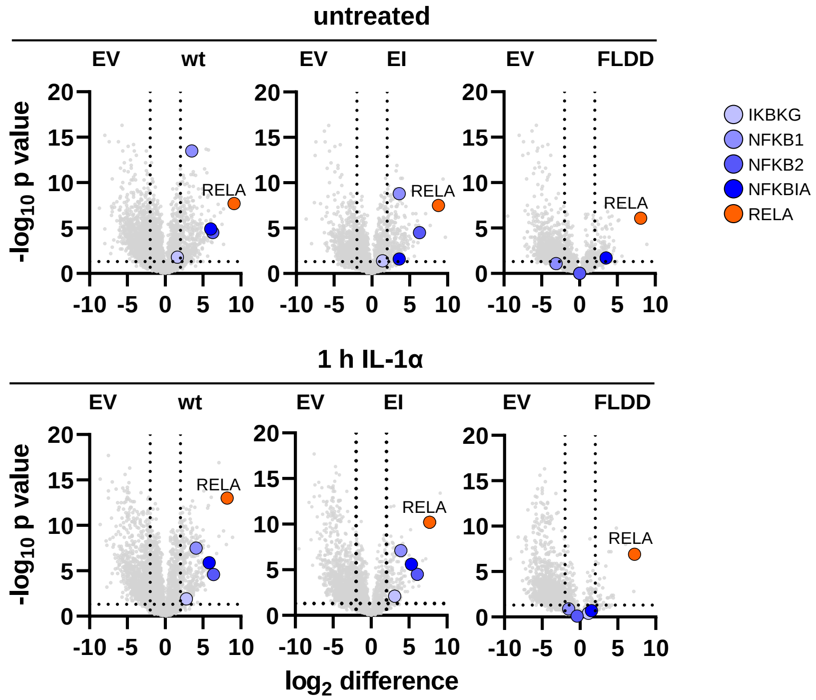

Figure 29: Enrichment of the bait protein p65/RELA-HA-mTb and the core canonical NF-κB pathway components.

The purified biotinylated proteins from the experiment in Figure 27 and a second biological replicate were identified by LC-MS/MS. Volcano comparisons between wild type p65 or the p65 mutants with empty vector control HA-miniTurbo under unstimulated or IL-1α-stimulated condition show the ratios of $\log_2$ mean protein intensity values obtained on the x-axis and their statistical significance as determined by Student's T-tests on the y-axis. Red and blue dots mark the enrichment of the bait p65/RELA proteins as well as the core components of the canonical NF-κB pathway. The analysis is based on two biologically independent experiments and three technical replicates per sample. (See Figure 28 legend for contributions.)

To achieve a better understanding of the composition of the NF-κB p65 interactome, wild type p65 and mutant interactomes were explored in more detail. Interactors of NF-κB p65 were defined as proteins that showed a significant at least fourfold enrichment over the three above-mentioned negative controls. Supplementary Figure 6 shows the enrichment analysis over negative controls based on the example of p65(wt). The Venn diagrams in Figure 30 display the overlap of the enriched protein groups of p65(wt) and the p65(E/I) and p65(FL/DD) mutants. Altogether, the enrichment analysis revealed 279 specific p65/RELA interactors in unstimulated cells and 310 in cells stimulated with IL-1α. Fewer interactors were found with the p65(E/I) mutant, i.e. 251 interactors before and 176 after IL-1α stimulation. Notably, of the 279 specific p65/RELA interactors identified in unstimulated cells, 189 (68%) were associated with both p65(wt) and the p65(E/I) mutant, indicating that the wild type and the DNA binding mutant share some common but also several distinct interactors. Interestingly, a strong decrease in the number of p65/RELA interactors was observed in the p65(FL/DD) mutant, i.e. 95 interactors in unstimulated cells. The significance of this effect is supported by the above-mentioned observation that the expression level and biotin labeling were widely comparable between the fusion protein samples. After stimulation with IL-1α, the number of interactors decreased even further to only 31, demonstrating that single amino acids and cytokine treatment cause a profound remodelling of the NF-κB p65 interactomes. Together, these findings support a model of the p65/RELA interactome that undergoes dynamic changes during IL-1α treatment and to a large extent depends on the capability of the transcription factor to form dimers.

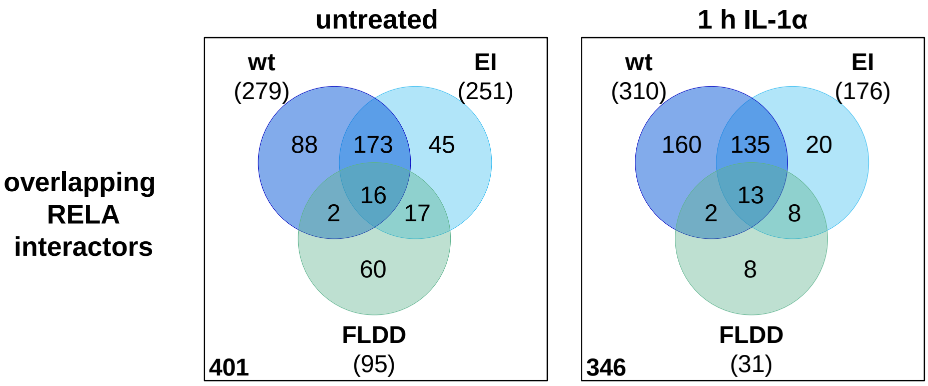

Figure 30: The intersection of the wild type p65 interactome with the interactomes of the p65 mutants reveals different and common binders.
Venn diagrams show the overlap between the identified interactors of wild type p65 and the p65 mutants in the absence or presence of IL-1α. Specific interactors of p65 or the p65 mutants were defined by a significant enrichment (LFC ≥ 2, $-\log_{10} p \geq 1.3$) over three negative controls (see Supplementary Figure 6). The total number of p65/RELA interactors per condition is indicated in parentheses. (See Figure 28 legend for contributions.)

To further investigate whether the changes of the NF-κB p65 interactomes were also reflected at the functional level, a comparative overrepresentation analysis of the top 100 enriched pathways (Figure 31A) was performed for the six protein groups presented in Figure 30. The analysis showed similar characteristics as observed before and revealed that wild type p65 and the p65(E/I) mutant barely differed in the biological function of their interacting proteins, whereas the p65(FL/DD) mutant interactomes were characterized by a large loss of pathway terms. These effects were particularly evident in light of the 15 most enriched pathways (Figure 31B), which showed that the NF-κB p65 interactome was predominantly composed of proteins that were involved in processes like chromatin organization, histone modifications, transcription, NF-κB signaling, or contributed to multiple developmental or differentiation-based mechanism.

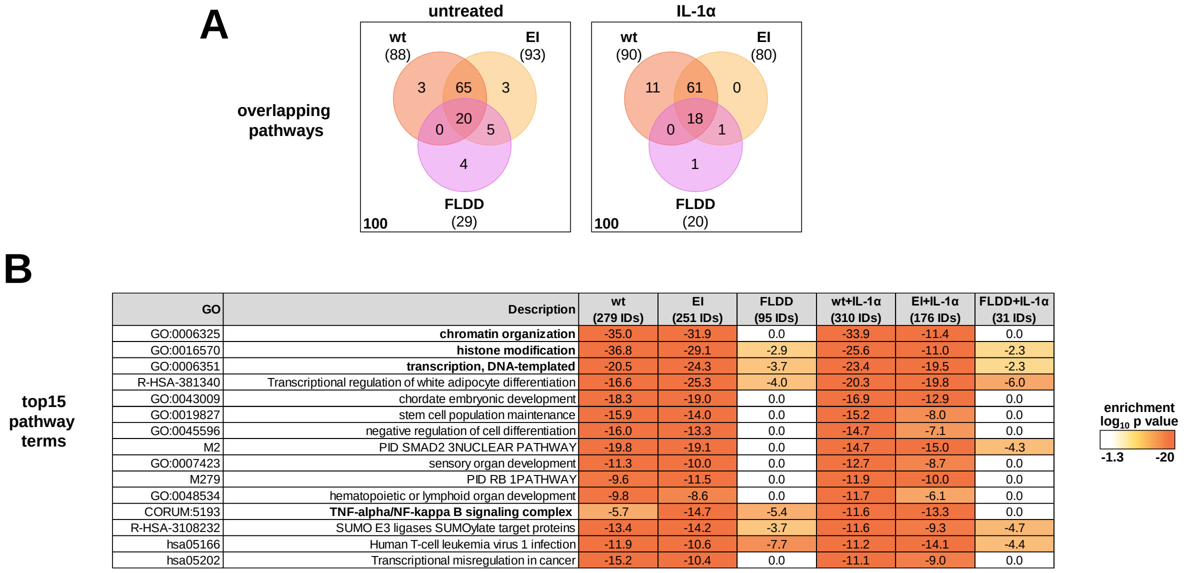

GO	Description	wt (279 IDs)	EI (251 IDs)	FLDD (95 IDs)	wt+IL-1α (310 IDs)	EI+IL-1α (176 IDs)	FLDD+IL-1α (31 IDs)
GO:0006325	**chromatin organization**	-35.0	-31.9	0.0	-33.9	-11.4	0.0
GO:0016570	**histone modification**	-36.8	-29.1	-2.9	-25.6	-11.0	-2.3
GO:0006351	**transcription, DNA-templated**	-20.5	-24.3	-3.7	-23.4	-19.5	-2.3
R-HSA-381340	Transcriptional regulation of white adipocyte differentiation	-16.6	-25.3	-4.0	-20.3	-19.8	-6.0
GO:0043009	chordate embryonic development	-18.3	-19.0	0.0	-16.9	-12.9	0.0
GO:0019827	stem cell population maintenance	-15.9	-14.0	0.0	-15.2	-8.0	0.0
GO:0045596	negative regulation of cell differentiation	-16.0	-13.3	0.0	-14.7	-7.1	0.0
M2	PID SMAD2 3NUCLEAR PATHWAY	-19.8	-19.1	0.0	-14.7	-15.0	-4.3
GO:0007423	sensory organ development	-11.3	-10.0	0.0	-12.7	-8.7	0.0
M279	PID RB 1PATHWAY	-9.6	-11.5	0.0	-11.9	-10.0	0.0
GO:0048534	hematopoietic or lymphoid organ development	-9.8	-8.6	0.0	-11.7	-6.1	0.0
CORUM:5193	**TNF-alpha/NF-kappa B signaling complex**	-5.7	-14.7	-5.4	-11.6	-13.3	0.0
R-HSA-3108232	SUMO E3 ligases SUMOylate target proteins	-13.4	-14.2	-3.7	-11.6	-9.3	-4.7
hsa05166	Human T-cell leukemia virus 1 infection	-11.9	-10.6	-7.7	-11.2	-14.1	-4.4
hsa05202	Transcriptional misregulation in cancer	-15.2	-10.4	0.0	-11.1	-9.0	0.0

Figure 31: The p65/RELA interactors are mostly involved in processes involving chromatin organization and transcription and largely depend on dimerization.
(A) For the six protein groups in Figure 30, a comparative analysis of overrepresented pathways was performed using the Metascape software environment [149]. Venn diagrams display the overlap of the 100 most enriched pathway terms. The numbers in parentheses represent pathway terms exclusively enriched in wild type p65 or one of the p65 mutants. (B) The table shows the top 15 enriched pathway terms associated with the p65/RELA wild type or the p65 mutant interactomes. The total number of p65/RELA interactors for each condition that was subjected to the analysis is indicated in parentheses. Pathway terms in bold indicate an engagement of p65/RELA interactors in various processes at the chromatin. The analysis also shows a loss of pathway terms due to the FL/DD mutation that interferes with dimerization. (See Figure 28 legend for contributions.)

To learn more about the functions and potential connectivities of individual factors, the analysis then focused on the comprehensive characterization of the wild type p65 interactome, for which a total number of 366 interactors was identified in unstimulated and IL-1α-stimulated cells (Figure 32A). By cross-comparing this list of interactors with the entries on direct or functional PPIs deposited in the STRING database, 46 (12.6%) proteins were found with documented experimental evidence for an interaction with p65/RELA (Figure 32B). This portion of the interactome was considered as the known part of the wild type p65 interactome. Among known interactors were numerous transcription factors (e.g., NFATC2, IRF1, ATF2, FOSL1, CEBPD, JUN), histone-modifying enzymes (e.g., EP300, KAT2A), chromatin remodelers (e.g., SMARCC17D1/E1), or nuclear cofactors (e.g., NCOA3, MED15). Most of the factors were strongly enriched in the MiniTurboID data (Figure 32C). Remarkably, 87.4% (320) of the proximity-labeled p65/RELA interactome was novel and had no previously documented interaction with this transcription factor (Figure 32B). The analysis also showed that wild type p65/RELA interactors were preferably involved in the RNA polymerase II-regulated transcription and that nearly half of the identified wild type p65/RELA interactors were nuclear or associated with chromatin, while a smaller fraction was localized in membraneless organelles (Figure 32D).

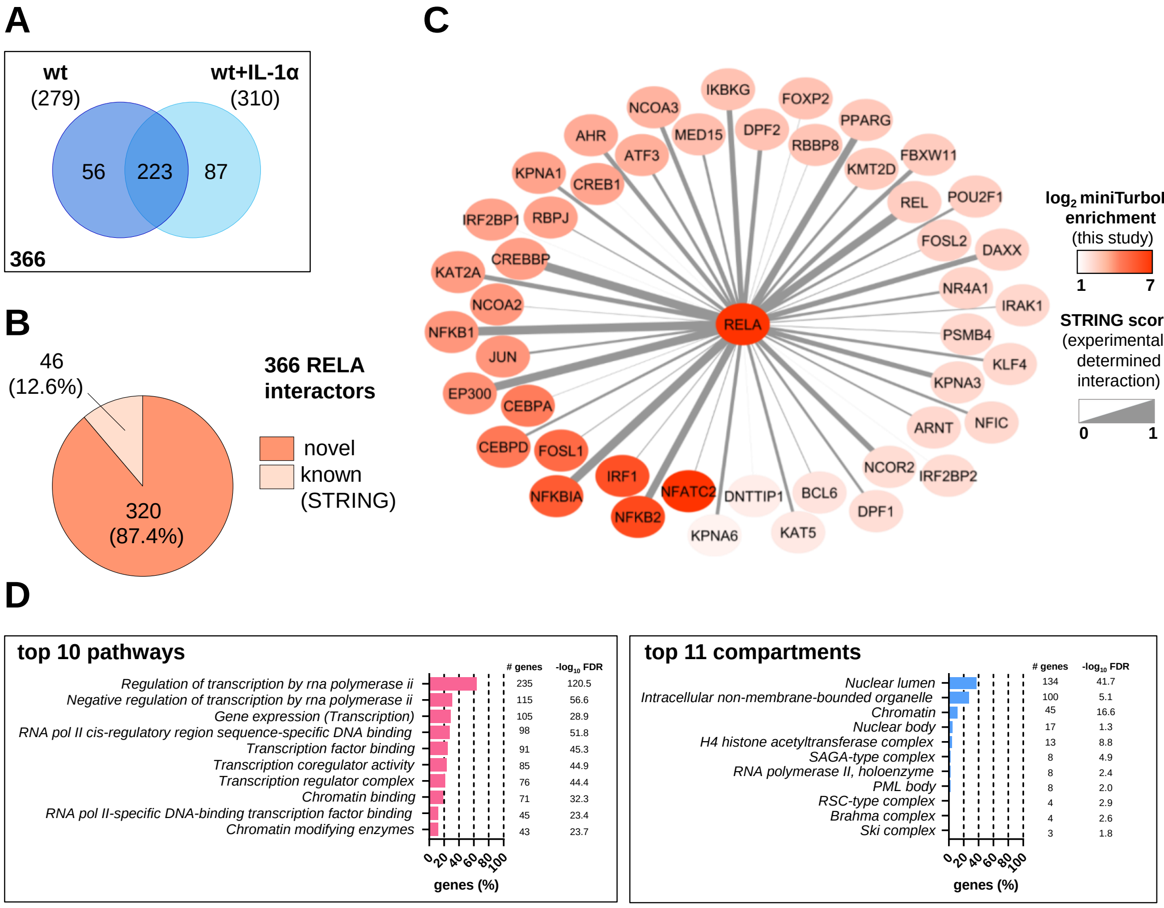

Figure 32: MiniTurboID reveals a large new core of the NF-κB p65 interactome, with about half of the interactors associated with the nucleus or transcriptional functions.
(A) A total number of 366 unique p65/RELA interactors was obtained in the presence or absence of IL-1α from the enrichment analysis over negative controls (see Supplementary Figure 6). The Venn diagram shows the intersection of 223 interactors found under both conditions and the proportions of interactors that exclusively occurred under basal or under IL-1α-stimulated conditions. (B) The pie chart reveals a large novel part of the p65/RELA interactome with 320 (87.4%) interactors having no documented protein interaction entries in the STRING database [150]. (C) Protein interaction network from the 46 known p65/RELA interactors identified by MiniTurboID. The color intensity of nodes in red corresponds to the strength of enrichment by proximity labeling. The width of edges determines the strength of experimental evidence for an interaction deposited in STRING. (D) Top terms resulting from pathway overrepresentation analyses of the 366 p65/RELA interactors conducted based on GO (BP, CC, MF), KEGG, Reactome, STRING clusters, and WikiPathway database entries and subcellular localization. The STRING plugin of Cytoscape was used for the annotations [165]. (See Figure 28 legend for contributions.)

4.2.6 Defining high-confidence NF-κB p65 interactors for functional validation experiments

To select interaction candidates whose functional role in the NF-κB system was to be investigated in the second part of the work, the number of interactors was further refined by applying stringent filtering criteria. This included filtering by (i) high reproducibility within both biological replicates, (ii) an at least eightfold enrichment over the empty vector HA-miniTurbo control in unstimulated or IL-1α-stimulated cells, and (iii) the lack of evidence for a function in the NF-κB system (Figure 28D). This procedure resulted in a list of 38 “high-confidence” p65 interactors (HCI) (Figure 33). The assessment of the IL-1α ratio between stimulated and unstimulated wild type p65 samples moreover allowed conclusions to be drawn as to whether the interaction with p65 was constitutive or inducible. Interestingly, the list contained inducible proteins such as FOXC1 and TBX1, which were more than eightfold enriched upon IL-1α stimulation, and other proteins like NFYC or S100A8/9 that were depleted (Figure 33). However, most of the listed proteins were enriched under either condition and were therefore considered to be constitutive p65 interactors. The combined pathway overrepresentation and PPI analysis of these 38 HCI by STRING also showed once more that the proteins were mostly involved in transcriptional functions, and that they had only few interactions amongst each other and no known functional connection with p65/RELA, except for CEBPD and FOSL1 (Figure 34). These rigorously selected 38 HCI therefore represented a new interaction network of p65/RELA. The proteins were further examined for their functional contribution to inflammatory gene expression in the following chapter.

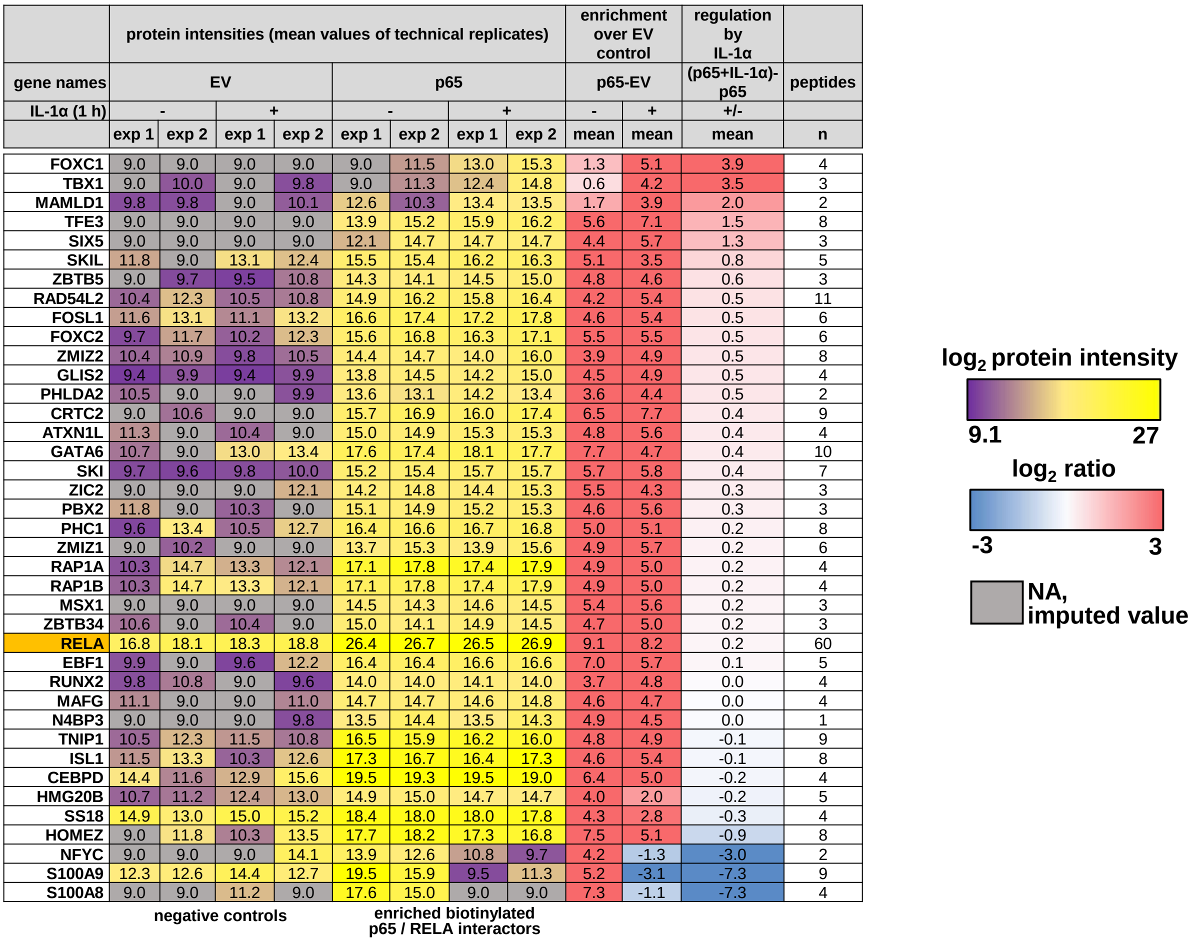

	protein intensities (mean values of technical replicates)								enrichment over EV control		regulation by IL-1α	
gene names	EV				p65				p65-EV		(p65+IL-1α)-p65	peptides
IL-1α (1 h)	-		+		-		+		-	+	+/-	
	exp 1	exp 2	exp 1	exp 2	exp 1	exp 2	exp 1	exp 2	mean	mean	mean	n
FOXC1	9.0	9.0	9.0	9.0	9.0	11.5	13.0	15.3	1.3	5.1	3.9	4
TBX1	9.0	10.0	9.0	9.8	9.0	11.3	12.4	14.8	0.6	4.2	3.5	3
MAMLD1	9.8	9.8	9.0	10.1	12.6	10.3	13.4	13.5	1.7	3.9	2.0	2
TFE3	9.0	9.0	9.0	9.0	13.9	15.2	15.9	16.2	5.6	7.1	1.5	8
SIX5	9.0	9.0	9.0	9.0	12.1	14.7	14.7	14.7	4.4	5.7	1.3	3
SKIL	11.8	9.0	13.1	12.4	15.5	15.4	16.2	16.3	5.1	3.5	0.8	5
ZBTB5	9.0	9.7	9.5	10.8	14.3	14.1	14.5	15.0	4.8	4.6	0.6	3
RAD54L2	10.4	12.3	10.5	10.8	14.9	16.2	15.8	16.4	4.2	5.4	0.5	11
FOSL1	11.6	13.1	11.1	13.2	16.6	17.4	17.2	17.8	4.6	5.4	0.5	6
FOXC2	9.7	11.7	10.2	12.3	15.6	16.8	16.3	17.1	5.5	5.5	0.5	6
ZMIZ2	10.4	10.9	9.8	10.5	14.4	14.7	14.0	16.0	3.9	4.9	0.5	8
GLIS2	9.4	9.9	9.4	9.9	13.8	14.5	14.2	15.0	4.5	4.9	0.5	4
PHLDA2	10.5	9.0	9.0	9.9	13.6	13.1	14.2	13.4	3.6	4.4	0.5	2
CRTC2	9.0	10.6	9.0	9.0	15.7	16.9	16.0	17.4	6.5	7.7	0.4	9
ATXN1L	11.3	9.0	10.4	9.0	15.0	14.9	15.3	15.3	4.8	5.6	0.4	4
GATA6	10.7	9.0	13.0	13.4	17.6	17.4	18.1	17.7	7.7	4.7	0.4	10
SKI	9.7	9.6	9.8	10.0	15.2	15.4	15.7	15.7	5.7	5.8	0.4	7
ZIC2	9.0	9.0	9.0	12.1	14.2	14.8	14.4	15.3	5.5	4.3	0.3	3
PBX2	11.8	9.0	10.3	9.0	15.1	14.9	15.2	15.3	4.6	5.6	0.3	3
PHC1	9.6	13.4	10.5	12.7	16.4	16.6	16.7	16.8	5.0	5.1	0.2	8
ZMIZ1	9.0	10.2	9.0	9.0	13.7	15.3	13.9	15.6	4.9	5.7	0.2	6
RAP1A	10.3	14.7	13.3	12.1	17.1	17.8	17.4	17.9	4.9	5.0	0.2	4
RAP1B	10.3	14.7	13.3	12.1	17.1	17.8	17.4	17.9	4.9	5.0	0.2	4
MSX1	9.0	9.0	9.0	9.0	14.5	14.3	14.6	14.5	5.4	5.6	0.2	3
ZBTB34	10.6	9.0	10.4	9.0	15.0	14.1	14.9	14.5	4.7	5.0	0.2	3
RELA	16.8	18.1	18.3	18.8	26.4	26.7	26.5	26.9	9.1	8.2	0.2	60
EBF1	9.9	9.0	9.6	12.2	16.4	16.4	16.6	16.6	7.0	5.7	0.1	5
RUNX2	9.8	10.8	9.0	9.6	14.0	14.0	14.1	14.0	3.7	4.8	0.0	4
MAFG	11.1	9.0	9.0	11.0	14.7	14.7	14.6	14.8	4.6	4.7	0.0	4
N4BP3	9.0	9.0	9.0	9.8	13.5	14.4	13.5	14.3	4.9	4.5	0.0	1
TNIP1	10.5	12.3	11.5	10.8	16.5	15.9	16.2	16.0	4.8	4.9	-0.1	9
ISL1	11.5	13.3	10.3	12.6	17.3	16.7	16.4	17.3	4.6	5.4	-0.1	8
CEBPD	14.4	11.6	12.9	15.6	19.5	19.3	19.5	19.0	6.4	5.0	-0.2	4
HMG20B	10.7	11.2	12.4	13.0	14.9	15.0	14.7	14.7	4.0	2.0	-0.2	5
SS18	14.9	13.0	15.0	15.2	18.4	18.0	18.0	17.8	4.3	2.8	-0.3	4
HOMEZ	9.0	11.8	10.3	13.5	17.7	18.2	17.3	16.8	7.5	5.1	-0.9	8
NFYC	9.0	9.0	9.0	14.1	13.9	12.6	10.8	9.7	4.2	-1.3	-3.0	2
S100A9	12.3	12.6	14.4	12.7	19.5	15.9	9.5	11.3	5.2	-3.1	-7.3	9
S100A8	9.0	9.0	11.2	9.0	17.6	15.0	9.0	9.0	7.3	-1.1	-7.3	4

Figure 33: Constitutive and IL-1α-inducible high-confidence interactors of p65/RELA.
The heatmap shows the final list of 38 high-confidence p65/RELA interactors selected for functional studies. The table comprises the mean protein intensity values for two biologically independent MiniTurboID experiments (exp 1 and exp 2) based on three technical replicates obtained for the samples of p65(wt)-HA-miniTurbo or HA-miniTurbo (EV) in the absence or presence of IL-1α, the mean enrichment ratio values compared to HA-miniTurbo (EV) control, and the mean IL-1α ratio values. The red color marks enrichment and the blue color marks depletion of proteins in the presence of IL-1α. All proteins were identified by at least two peptides, except for N4BP3. (See Figure 28 legend for contributions.)

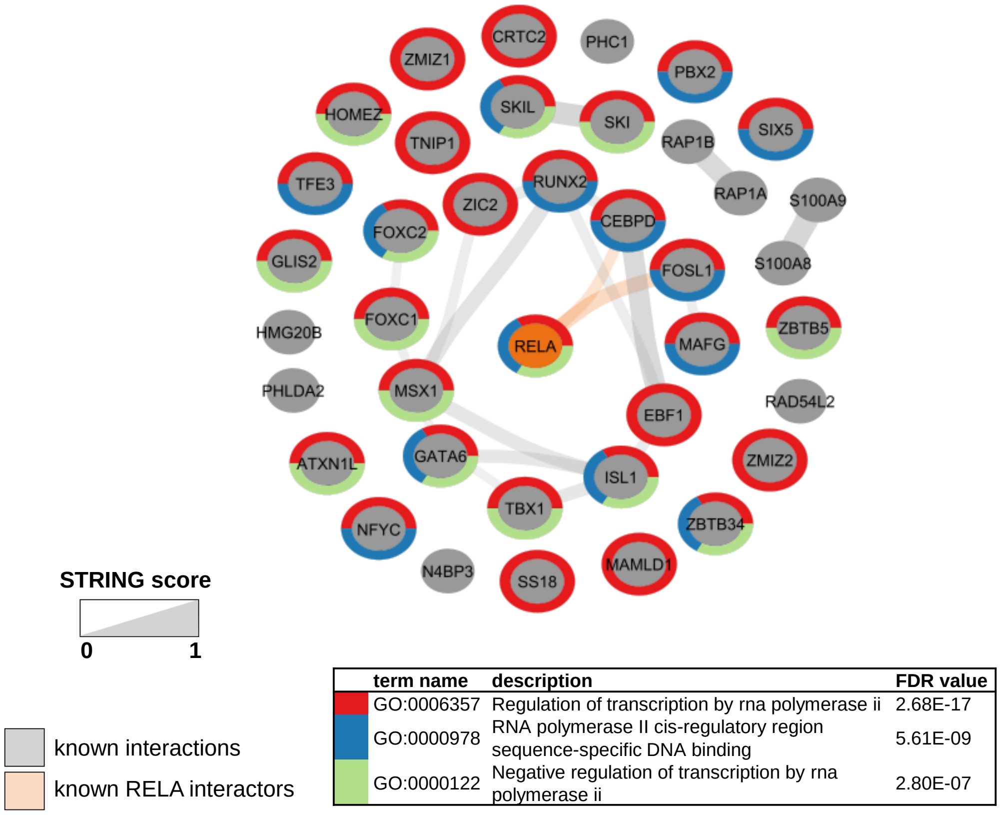

	term name	description	FDR value
🟥	GO:0006357	Regulation of transcription by rna polymerase ii	2.68E-17
🟦	GO:0000978	RNA polymerase II cis-regulatory region sequence-specific DNA binding	5.61E-09
🟩	GO:0000122	Negative regulation of transcription by rna polymerase ii	2.80E-07

Figure 34: High-confidence interactors have only few experimentally verified physical interactions with p65/RELA.
Protein interaction network from the 38 high-confidence p65/RELA interactors identified by MiniTurboID and selected for further studies. The map shows that interactors are largely devoid of known protein interactions based on STRING entries. Grey edges mark known protein interactions deposited in the STRING database. Orange edges mark the only two interactions between the factors (CEBPD and FOSL1) with p65/RELA. The width and transparency of edges correspond to the strength of experimental evidence for a functional STRING interaction. Node borders visualize the top three enriched pathway terms. (See Figure 28 legend for contributions.)

Collectively, the proximity labeling-based dataset of p65/RELA provided new insights into the composition and dynamics of NF-κB p65 protein interaction networks in the context of inflammation. The data demonstrate interactome remodeling depending on DNA binding, dimerization, and IL-1α stimulation, with the strongest effects observed when only two dimerization-related amino acids in the RHD are mutated. This shows that most of the cellular interactions require intact dimerization function whereas the vicinity to DNA is less essential. The data moreover reveal a large new part of the p65/RELA interactome that was previously unknown. Most of these factors are nucleus-associated and involved in transcriptional processes which indicates that these proteins may be cofactors with regulatory functions in the NF-κB-driven gene expression.

4.3 Targeted RNAi screen uncovers functional roles of 38 HCI in the NF-κB p65 gene expression

4.3.1 Experimental design of the RNAi screen

The results from proximity-based interactomic studies do not allow conclusions on the functional roles of the newly discovered binding partners of the bait protein. The 38 HCI were therefore screened for their influence on NF-κB-mediated gene expression using RNA interference (RNAi). As shown in Figure 35, RNAi was carried out in a small-scale setup using the Ambion® TaqMan™ PreAmp Cells-to-CT™ Kit by seeding parental HeLa cells in 48-well plates and transfecting them with siRNA for 48 h. The p65/RELA targeting siRNA was used as a reference siRNA to assess the extent of the effects of other siRNAs (siTarget 1-38) on inflammatory gene expression. On each plate, a set of three negative controls was included comprising untreated cells, cells treated with transfection reagent only (HP), and cells transfected with a non-targeting siRNA directed against the luciferase mRNA that is not expressed in human cells (siLuci). Transfected cells were then kept untreated or stimulated with IL-1α for 1 h followed by harvesting and lysis. Lysates were directly used to synthesize the cDNA, thereby leaving out the adjustment of the amount of RNA input according to the Cells-to-CT™ Kit protocol. The cDNAs of the GOIs were pre-amplified by an additional PCR step using a mixture of specific TaqMan assays. Finally, the same TaqMan assays were separately utilized in qPCR assays to measure C_T values of the according pre-amplification product. The analysis was conducted on three groups of genes: (1) IL-1α-inducible NF-κB target genes; (2) housekeeping genes for normalization; and (3) target genes to control knockdown efficiencies of the HCIs. Measured C_T values of each gene allowed to conclude on the initial quantities of a specific mRNA.

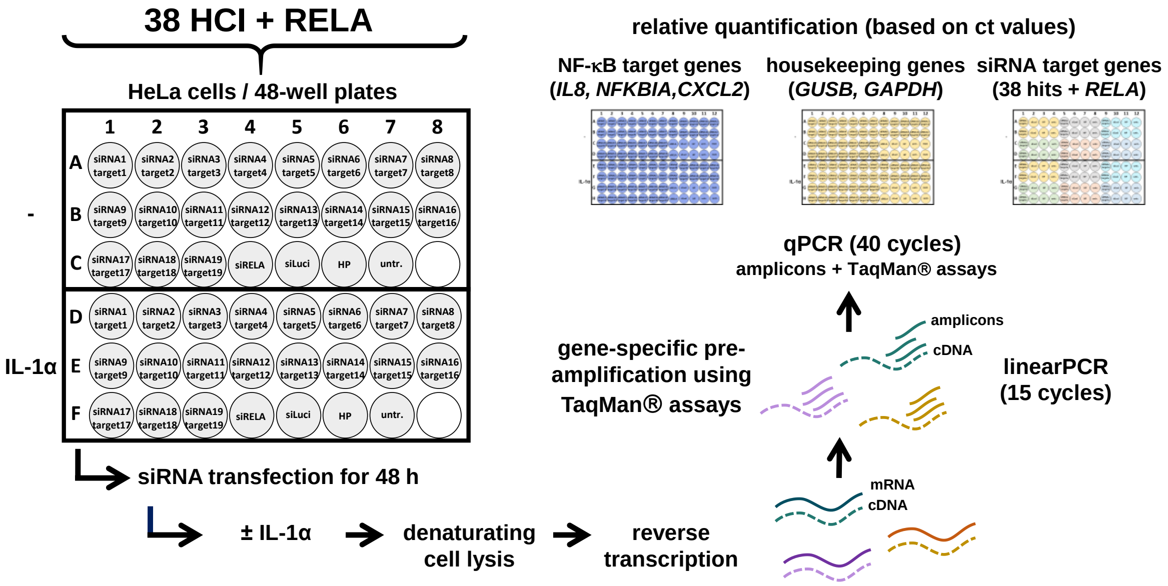

Figure 35: Principle design of the RNAi screen using the TaqMan™ PreAmp Cells-to-CT™ Kit. Schematic workflow illustrating the arrangement of siRNAs and control samples on a 48-well culture plate. HeLa cells were transiently transfected with 20 nM siRNA mixtures for 48 h with HiPerfect reagent. Control samples

included p65/RELA-targeting siRNA, a siRNA targeting luciferase (siLuci), transfection reagent only (HP), and untreated (untr.) cells. After transfection, half of the siRNA and control samples were treated with IL-1α (10 ng/ml) for 1 h. The cDNAs were transcribed in lysates and amplicons for three NF-κB target genes, two housekeeping genes and all 38 HCI of p65/RELA were pre-amplified by linear PCR and finally quantified by qPCR.

The RNAi screen was planned, carried out, and analyzed by Lisa Leib and Jana Juli. Doris Newel helped perform the qPCRs. Lisa Leib and Jana Juli performed the analysis as described in the text and visualized the data by a heatmap. Hierarchical clustering was performed by Prof. M. Kracht (Figure 36). The graph showing the C_T value distribution of housekeeping gene *GUSB* and *GAPDH* (Supplementary Figure 7) and the graphs demonstrating the knockdown efficiencies of 38 HCI and p65/RELA (Supplementary Figure 8) were created by Lisa Leib and Jana Juli. The schematic workflow (Figure 35) was adapted from [166] by Lisa Leib.

4.3.2 Data analysis based on C_T values and hierarchical clustering of expression patterns

Since the Cells-to-CT™ Kit does not allow the adjustment of the amount of input RNA, it was crucial to at first verify the eligibility of the two housekeeping genes for normalization. For this reason, the fluctuation of *GUSB* and *GAPDH* mean C_T values was controlled between untreated and IL-1α-stimulated samples (Supplementary Figure 7); mainly, to exclude a global impact of IL-1α treatment on the expression of one of the two housekeeping genes that might lead to background effects. Mean C_T values and C_T value distributions slightly differed between biological replicates, however, there was no global effect by IL-1α stimulation detectable, neither on *GUSB* mean C_T values nor on *GAPDH* mean C_T values, confirming that both housekeeping genes were suitable for normalization. C_T values of readout genes and target genes were subjected to a multi-step analysis which was conducted using the C_T values of housekeeping gene *GUSB* and *GAPDH* for relative quantification and normalization, respectively. For *GUSB* normalization, the ΔC_T value of each sample was determined by the difference between the C_T value of the GOI (demonstrated by *IL8*) and the C_T value of the housekeeping gene:

$$\Delta C_{T_{\text{siTarget}}} = C_{T_{\text{siTarget}}}^{\text{IL8}} - C_{T_{\text{siTarget}}}^{\text{GUSB}}$$

After normalization, the knockdown effect on *IL8*, *NFKBIA*, and *CXCL2* mRNA expression was determined in comparison to the siLuci control and assessed at the levels of basal mRNA and IL-1α-inducible mRNA expression. To first determine the effect on the basal level, the $\Delta\Delta C_T$ value of each untreated sample was determined by the negative difference between the ΔC_T value of each untreated knockdown sample and the ΔC_T value of untreated siLuci control:

$$\Delta\Delta C_{T\ \underset{(0\text{ h IL1}\alpha)}{\text{siTarget}}} = -\left(\Delta C_{T\ \underset{(0\text{ h IL1}\alpha)}{\text{siTarget}}} - \Delta C_{T\ \underset{(0\text{ h IL1}\alpha)}{\text{siLuci}}}\right)$$

Next, the effect on IL-1α-induced mRNA expression was calculated accordingly by the negative difference between the ΔC_T value of each IL-1α-induced knockdown sample and the ΔC_T value of IL-1α-induced siLuci control:

$$\Delta\Delta C_{T\ \underset{(1\ h\ IL1\alpha)}{\text{siTarget}}} = -\left(\Delta C_{T\ \underset{(1\ h\ IL1\alpha)}{\text{siTarget}}} - \Delta C_{T\ \underset{(1\ h\ IL1\alpha)}{\text{siLuci}}} \right)$$

The mean $\Delta\Delta C_T$ value of three independent screens was finally visualized by a heatmap comprising information about the fold up- or downregulation of the inducible inflammatory IL-1α target genes *IL8*, *NFKBIA* or *CXCL2* on the level of basal or IL-1α-induced mRNA expression corresponding to the gene that was silenced. Hierarchical clustering resulted in six prominent expression patterns that were characterized by either transcriptional upregulation or downregulation in the basal or stimulated state (Figure 36). Three of these clusters (3-6) included genes encoding HCI whose suppression resulted in strong downregulation of IL-1α target genes. Cluster 2, in contrast, contained genes whose suppression strongly influenced the basal expression of *CXCL8* and *CXCL2*. As expected, suppression of p65/RELA had the strongest effect on IL-1α-inducible expression of the three IL-1α target genes tested. However, the analysis also showed that every single HCI had a functional role in the expression of at least one IL-1α target gene under basal or stimulated condition. This highlighted the gene specificity of HCI and suggested that different sets of NF-κB/cofactor complexes coordinate the transcriptional activity at specific inflammatory gene loci.

The assessment of knockdown efficiencies moreover confirmed the successful suppression of HCI (Supplementary Figure 8) and IL-1α stimulation did not influence their expression levels, with the only exception of the mRNAs of *CEBPD*, *FOSL1*, *FOXC2*, and *TNIP1* that were slightly induced by IL-1α (Supplementary Figure 9).

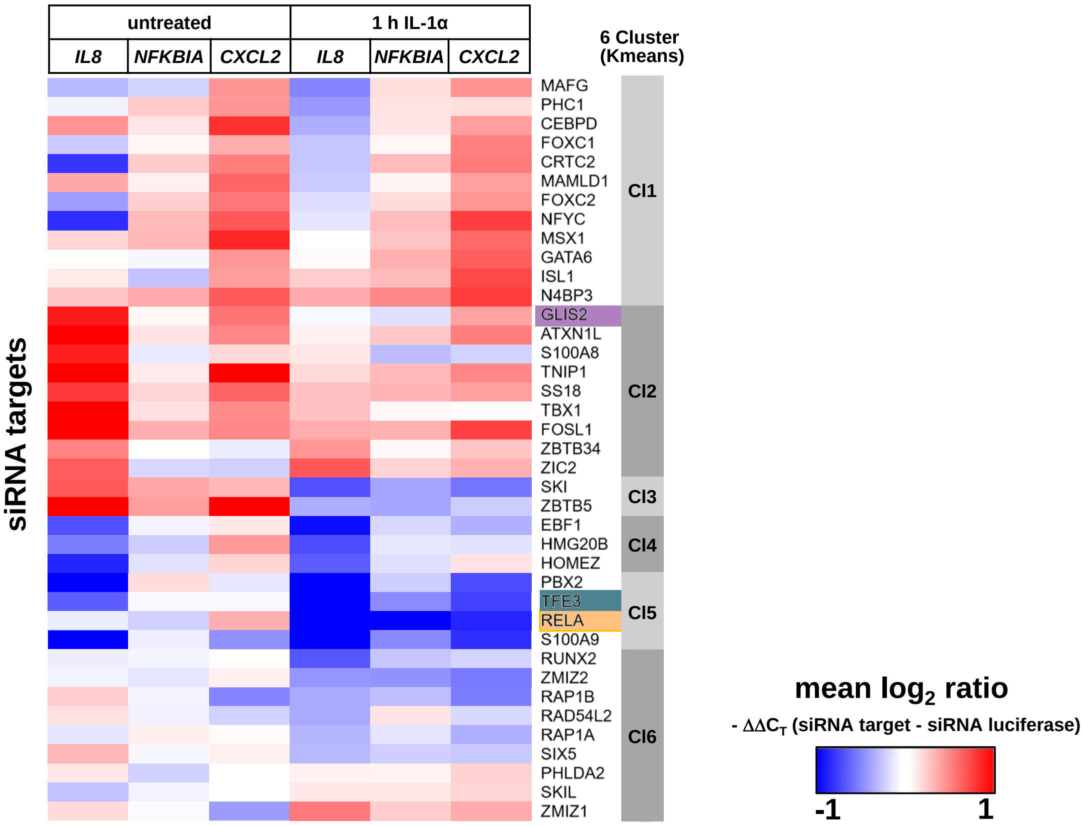

Figure 36: RNAi screen analysis to reveal functions of putative new activators and repressors of NF-κB target genes.
In samples from 38 HCI knockdowns, the mRNA expression levels of three prototypical NF-κB target genes (*IL8*, *NFKBIA*, *CXCL2*) were determined by qPCR and normalized based on *GUSB*. Knockdown effects were calculated separately for basal and IL-1α-inducible conditions against the luciferase siRNA. The heatmap visualizes the mean $\log_2$ ratios from three biologically independent RNAi screens for basal and IL-1α-inducible conditions. Hierarchical clustering of these values revealed six expression patterns (Cluster 1-6) showing transcriptional upregulation (red colored) or downregulation (blue colored). RELA knockdowns in orange were performed in parallel as a reference to assess the extent of knockdown effects. Green and pink colors highlight p65/RELA interactors selected for validation and follow-up analyses, respectively. (See Figure 35 legend for contributions.)

4.3.3 Selecting three candidate interactors for validation and follow-up studies

For the performance of follow-up studies to validate the interaction with p65/RELA and to elucidate the regulatory function of individual factors in the NF-κB system, the focus was placed on the lysosomal transcription factors E3 (TFE3, BHLHE33) and EB (TFEB, BHLHE35), which belong to the MiT/TFE family, as well as GLI-similar 2 (GLIS2, also called Neuronal Krueppel-like protein, NKL), which is a member of the GLI-similar zinc finger family.

TFE3 was selected because its suppression in the RNAi screen caused downregulation of IL-1α-induced genes comparable to the effects of RELA knockdown. TFEB, which is the best-characterized family member of the MiT/TFE protein family was also strongly enriched in the MiniTurboID experiments and was selected to comparatively investigate both closely related proteins.

Zinc finger protein GLIS2 was selected as an example of a poorly characterized protein without any documented link to p65/RELA. All three transcription factors have not yet been studied in the IL-1α-NF-κB system. Proximity labeling-based data furthermore showed co-enrichments of the TFE3/TFEB or GLIS2 protein family relatives such as MITF, GLIS1, and GLIS3, but not TFEC (Figure 37). This reinforced the potential relevance of these proteins/protein families for the NF-κB system and may indicate that other family relatives were also involved in regulatory processes at inflammatory genes through the interaction with p65/RELA.

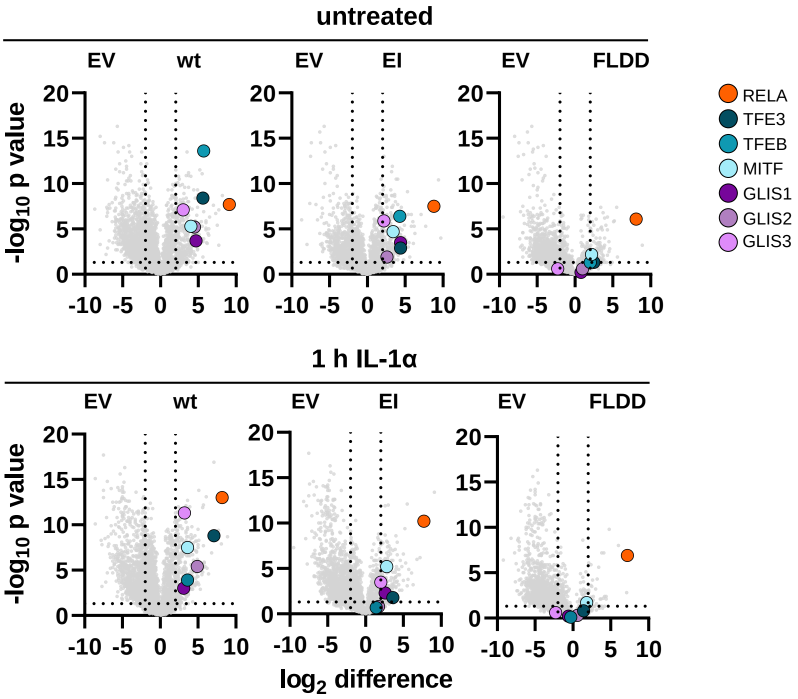

Figure 37: Co-enrichment of TFE3/TFEB and GLIS2 family relatives MITF, GLIS1, and GLIS3 in the proximity-based interactomes of p65/RELA.
Graphs show the enrichment of the selected p65/RELA interactors TFE3/TFEB and GLIS2 in the MiniTurboID dataset and the co-enrichment of members from the same protein family. Members of the MiT/TFE family are colored in green and members of the GLI-similar zinc finger family are colored in pink. RELA as a reference is colored in orange. (The same graphs as in Figure 29, see Figure 28 legend for contributions.)

4.4 Proximity Ligation Assays validate p65 interaction with TFE3/TFEB/GLIS2

Next, the *in situ* proximity ligation assay was utilized as an independent approach to validate the p65 interaction with TFE3/TFEB and GLIS2 as revealed by MiniTurboID. As shown schematically in Figure 38, the method enables the microscopic detection and localization of two interacting proteins in single cells by using two primary antibodies of different species. Secondary antibodies attached with a specific DNA strand, called PLA probes, bind the constant region of the different primary antibodies. The DNA strands together with two other specific DNA oligonucleotides engage in rolling-circle DNA amplification after the addition of synthesis enzymes and substrates. This step only occurs when PLA probes, and therefore the proteins of interest, are in close proximity (<40 nm). Complementary fluorescence-labeled oligonucleotides are next added and bind to several hundredfold amplified DNA circles. This leads to a high concentration of fluorescence and results in a distinct bright spot in cells which marks the PPI complex.

In this work, PLA was combined with immunofluorescence staining by using an antibody from a third-species and Hoechst staining, which allowed the monitoring of PPIs according to their subcellular localization. The immuno-PLA was based on three replicates and compared PLA signals between parental HeLa cells and p65-deficient cells. As also shown in Figure 38, the immuno-PLA comprised three important controls to determine whether the PLA signals were specific or background. PLA signals resulting from unspecific cross-reactions between the specific primary antibody and the reagents were estimated by controls to which only one of the two primary antibodies was added. The general immuno-PLA background signal was estimated by another control to which only the reagents were added but none of the primary antibodies. The third control comprised assay in p65-deficient cells.

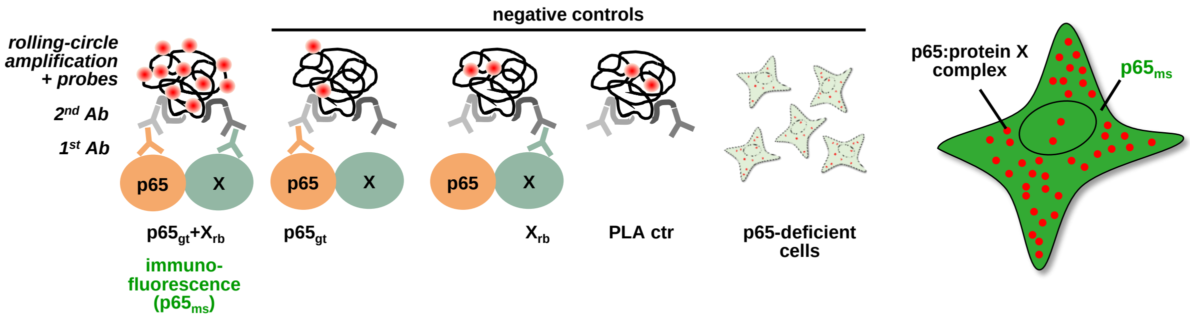

Figure 38: Single cell-based detection of NF-κB p65 protein-protein interactions with new interactors by proximity ligation assay.
Schematic of the PLA used to detect p65 interaction complexes in HeLa cells. The PPI complex is detected by two primary antibodies (1st Ab) of different species recognized by secondary antibodies (2nd Ab) coupled to PLA probes. Only when p65 and the other protein are in close vicinity (<40 nm), rolling circle DNA amplification can be primed based on the PLA probes. Fluorescence-labeled oligonucleotides bind the amplified DNA, and the PPI complex can be detected as fluorescent spot and localized in the cell. Signals per cell can be quantified from microscopic images. Negative controls were included to which only one or neither of the two specific primary antibodies was added to enable evaluation of background signals. The third control comprised assay in p65-deficient cells. Monitoring of endogenous p65 levels was attained by parallel IF staining using a third species antibody. (The schematic was adapted from [167].)

On average, in parental HeLa cells, the p65:TFE3 PLA resulted in 43 signals per cell as compared to HeLa cells with deficient p65 level with only 23 signals (Figure 39A & B). In comparison to that, the number of signals per cell was generally reduced in the analysis of the p65:TFEB PLA which revealed on average 9 signals per cell in parental HeLa and only 6 signals per cell in p65-deficient HeLa. The p65:GLIS2 PLA, on the other hand, resulted in 45 signals per cell in parental HeLa and only 25 signals per cell in p65-deficient HeLa. The overall number of signals in p65-deficient cells was in general significantly reduced. However, in some cells, p65 was still expressed as visualized by immunofluorescence. The reason is that the stable CRISPR-Cas9-based p65/RELA knockdown cells were still pools which contained some cells with non-recombined wild type alleles that survived the puromycin selection procedures. This phenomenon explains the detection of signals above the background noise. This background signal was in the range of 0 to 6 signals per cell across negative controls. The PLA data therefore, provide independent confirmation of the endogenous interaction of

TFE3, TFEB, and GLIS2 with p65/RELA, and thus demonstrate the reliability of the MiniTurboID results.

Regarding the subcellular localization of the interactions, most of them were found in the cytoplasm, while only a minority of 15% to 22% of the interactions occurred in the nucleus (Figure 39C). This was contrary to expectations since all three proteins were transcription factors known to be associated with chromatin. On the other hand, it is well known that the majority of p65/RELA is constrained to the cytoplasm and only a minor fraction is liberated and translocates to the nucleus upon IL-1α stimulation [48]. A similar mechanism of regulation may apply to the new interactions of p65/RELA with TFE3/TFEB and GLIS2.

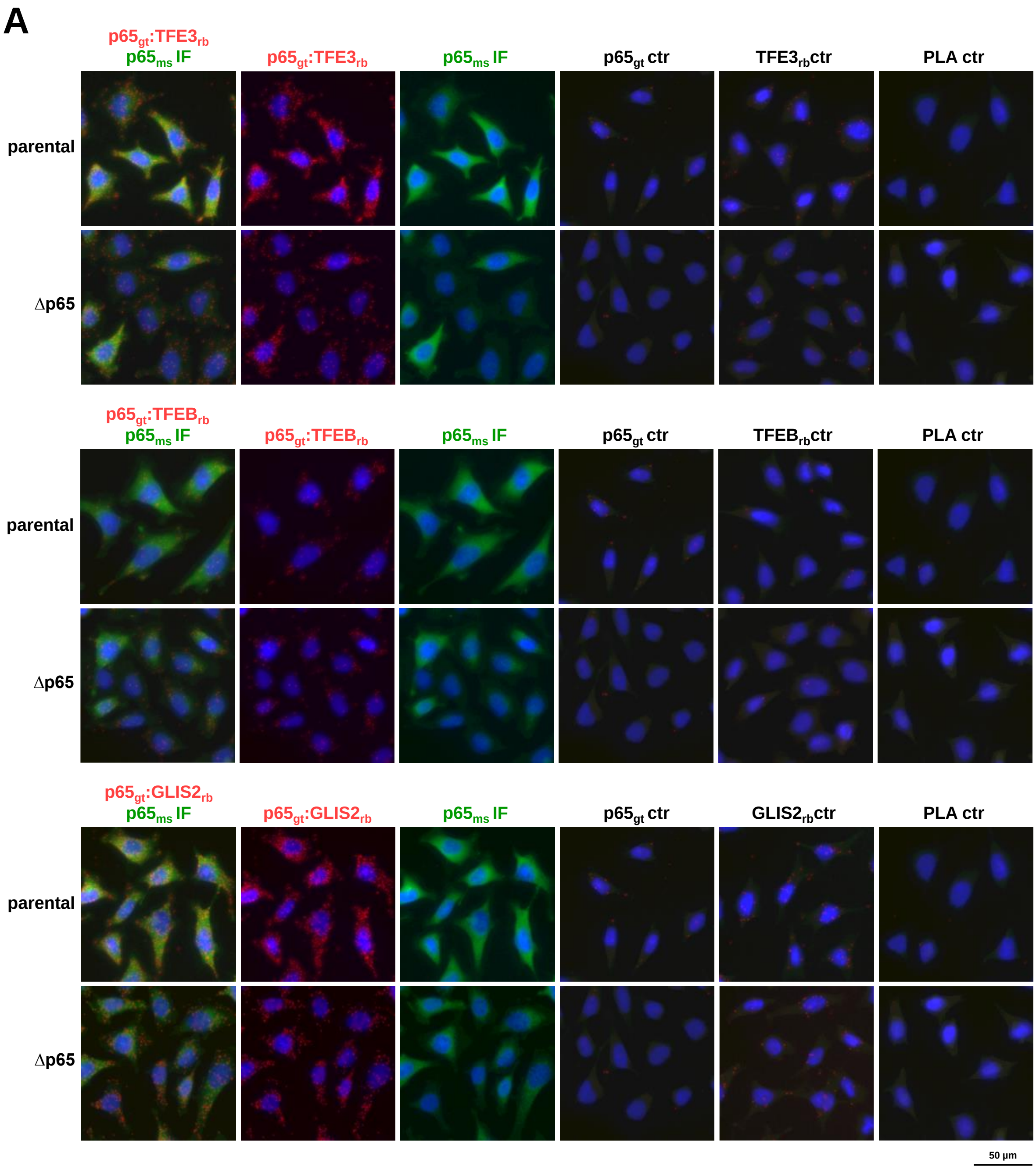
A
p65$_{gt}$:TFE3$_{rb}$
p65$_{ms}$ IF
p65$_{gt}$:TFE3$_{rb}$
p65$_{ms}$ IF
p65$_{gt}$ ctr
TFE3$_{rb}$ctr
PLA ctr
parental
Δp65
p65$_{gt}$:TFEB$_{rb}$
p65$_{ms}$ IF
p65$_{gt}$:TFEB$_{rb}$
p65$_{ms}$ IF
p65$_{gt}$ ctr
TFEB$_{rb}$ctr
PLA ctr
parental
Δp65
p65$_{gt}$:GLIS2$_{rb}$
p65$_{ms}$ IF
p65$_{gt}$:GLIS2$_{rb}$
p65$_{ms}$ IF
p65$_{gt}$ ctr
GLIS2$_{rb}$ctr
PLA ctr
parental
Δp65
50 µm

B

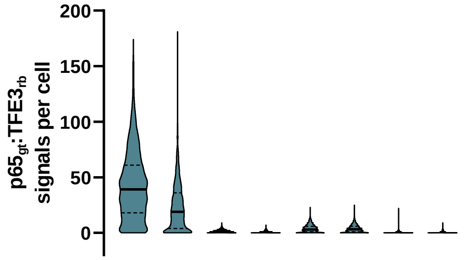

p65$_{gt}$:TFE3$_{rb}$	+	+						
p65$_{gt}$			+	+				
TFE3$_{rb}$					+	+		
PLA ctr							+	+
parental	+		+		+		+	
Δp65		+		+		+		+
	1	2	3	4	5	6	7	8

	p65$_{gt}$:TFE3$_{rb}$				p < 0.0001
	condition		cells	mean PLA spots	
1	p65$_{gt}$:TFE3$_{rb}$	parental	2065	43	
2	p65$_{gt}$:TFE3$_{rb}$	Δp65	2452	23	****
3	p65$_{gt}$	parental	2162	1	****
4	p65$_{gt}$	Δp65	2308	1	****
5	TFE3$_{rb}$	parental	2207	4	****
6	TFE3$_{rb}$	Δp65	2316	4	****
7	PLA ctr	parental	2250	0	****
8	PLA ctr	Δp65	2285	1	****

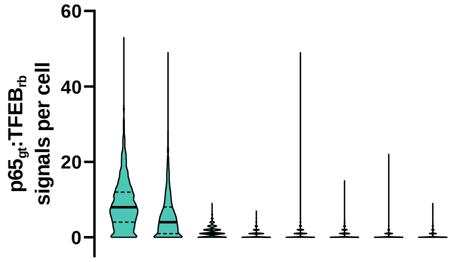

p65$_{gt}$:TFEB$_{rb}$	+	+						
p65$_{gt}$			+	+				
TFEB$_{rb}$					+	+		
PLA ctr							+	+
parental	+		+		+		+	
Δp65		+		+		+		+
	1	2	3	4	5	6	7	8

	p65$_{gt}$:TFEB$_{rb}$				p < 0.0001
	condition		cells	mean PLA spots	
1	p65$_{gt}$:TFEB$_{rb}$	parental	2303	9	
2	p65$_{gt}$:TFEB$_{rb}$	Δp65	2536	6	****
3	p65$_{gt}$	parental	2162	1	****
4	p65$_{gt}$	Δp65	2308	1	****
5	TFEB$_{rb}$	parental	2296	1	****
6	TFEB$_{rb}$	Δp65	2383	1	****
7	PLA ctr	parental	2250	0	****
8	PLA ctr	Δp65	2285	1	****

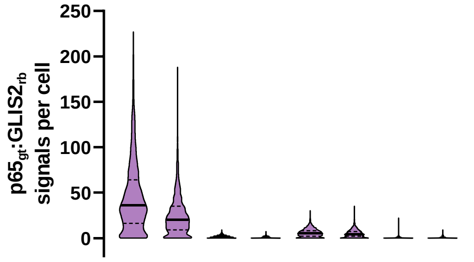

p65$_{gt}$:GLIS2$_{rb}$	+	+						
p65$_{gt}$			+	+				
GLIS2$_{rb}$					+	+		
PLA ctr							+	+
parental	+		+		+		+	
Δp65		+		+		+		+
	1	2	3	4	5	6	7	8

	p65$_{gt}$:GLIS2$_{rb}$				p < 0.0001
	condition		cells	mean PLA spots	
1	p65$_{gt}$:GLIS2$_{rb}$	parental	2338	45	
2	p65$_{gt}$:GLIS2$_{rb}$	Δp65	2601	25	****
3	p65$_{gt}$	parental	2162	1	****
4	p65$_{gt}$	Δp65	2308	1	****
5	GLIS2$_{rb}$	parental	2221	6	****
6	GLIS2$_{rb}$	Δp65	2325	5	****
7	PLA ctr	parental	2250	0	****
8	PLA ctr	Δp65	2285	1	****

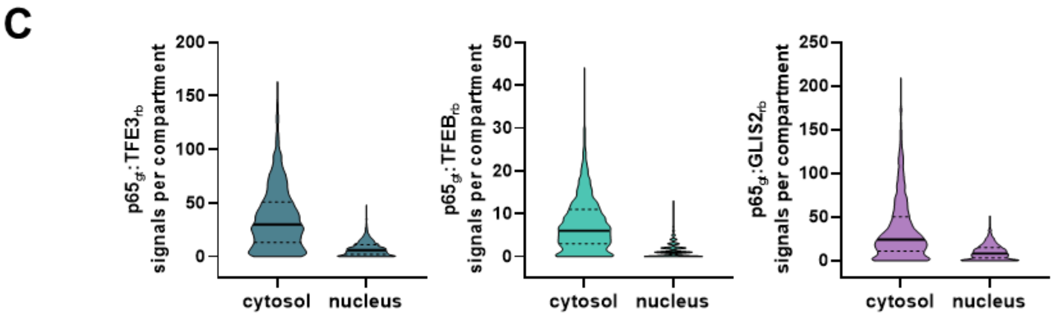

mean PLA spots per compartment				
condition		cells	cytosol	nucleus
p65$_{gt}$:TFE3$_{rb}$	parental	2065	36 (83%)	7 (17%)
p65$_{gt}$:TFEB$_{rb}$	parental	2303	7 (85%)	1 (15%)
p65$_{gt}$:GLIS2$_{rb}$	parental	2338	35 (78%)	10 (22%)

Figure 39: Microscopic validation and quantification of NF-κB p65 interaction complexes.
(A) Parental or p65-deficient (Δp65) HeLa cells were formaldehyde fixated and analyzed by immuno-PLA using PLA antibodies that recognized p65 (A303-945A, goat) and TFE3 (HPA023881, rabbit), TFEB (4240, rabbit), or GLIS2 (PA5-40314, rabbit) together with an IF antibody directed against p65 (sc-8008, mouse) as well. After the immuno-PLA reaction, the nuclei were stained with Hoechst 33342. At the end of the procedure, endogenous p65 levels (in green) were monitored and protein complexes (in red) were visualized as fluorescent spots by microscopic imaging. Merged images from a representative experiment are shown. (B) PLA signals from single cells were quantified using the BlobFinder software. Mean signals per cell were counted for quantification. Violin plots visualize the distribution of PPI complexes (PLA signals) per cell. Data from three independent experiments were pooled. Each table summarizes the total number of analyzed cells per condition, PLA signals per cell, and the significance of the enriched PLA signals compared to negative controls. Asterisks indicate significant changes (****$p < 0.0001$) obtained by the Kruskal-Wallis-Test. (C) The graphs show the distribution of PPI complexes (PLA signals) per cell according to the compartment they were detected in. The table contains the total number of analyzed cells per condition, and the total numbers and percentage of quantified PLA signals detected in the cytosolic or nuclear compartment of the parental cells.

Taken together, the immuno-PLA data validate and complement the data obtained by the MiniTurboID approach by confirming the interaction between p65 and three proteins previously found and provide additional insight into the subcellular localization of this interaction.

4.5 Unidirectional crosstalk between the IL-1α-NF-κB p65 and lysosomal transcription factor system

The transcription factors TFE3 and TFEB change their phosphorylation state to promote the expression of genes involved in lysosome biogenesis and autophagy by associating with CLEAR elements in the regulatory regions of these genes [78, 82, 84, 85]. Lysosomes and autophagosomes play an important role in pathogen defense (besides multiple homeostatic processes), and evidence suggests that some fine-tuning of TLR-mediated inflammatory signal transduction occurs at the endolysosome [60]. The transcription factor NF-κB p65, in contrast, is a master regulator of genes that coordinate the immune response, but its potential role in regulating CLEAR genes in the process of (adaptive) lysosome biogenesis has not yet been studied. It is likewise still unclear to what extent the signaling axes of the two transcription factor systems are linked to each other and whether the transcription factors activate their main target genes in a cooperative manner or independent from each other. These questions were systematically investigated in the following chapter of the doctoral thesis by exposing cells to IL-1α or starvation, respectively, as representative examples for two major triggers of the cellular immune response and lysosome biogenesis.

4.5.1 IL-1α does not trigger nuclear translocation and dephosphorylation of TFE3/TFEB

The first questions to be investigated was whether starvation triggers the migration of p65 into the nucleus or, vice versa, whether TFE3/TFEB migrate to the nucleus in response to IL-1α treatment. HeLa cells were therefore stimulated with either IL-1α or were subjected to starvation for different time spans and control cells were kept untreated. Western blot analysis was then performed to determine the cellular distribution of NF-κB p50/p65 and the lysosomal transcription factors TFE3/TFEB in the cytosolic and nuclear fractions. Stimulation / starvation time points of 0.5 h, 1 h, 2 h, and 4 h were selected, since it has been shown previously in other cell systems and conditions that the transcription factors translocate to the nucleus (e.g., p50/p65 translocation in KB cells treated with IL-1α for 0.5 h and 1 h [48], TFE3 translocation in MEF cells starved for 2 h [90], TFEB translocation in HeLa cells stably overexpressing TFEB starved for 4 h [84]) within these time frames. Western blot analysis of the cytosolic and nuclear fractions are shown in Figure 40A and the quantification of these blots is visualized by the bar graphs in Figure 40B. Tubulin and Pol II antibodies were used to demonstrate the successful subcellular separation as these are typical cytosolic or nuclear proteins, respectively. The data show that neither p65 nor p50 translocated to the nucleus in response to starvation. There was likewise no redistribution of TFE3 and TFEB upon stimulation with IL-1α. Notably, TFE3 and TFEB were equally distributed between nucleus and cytoplasm and their distribution was not changed during IL-1α stimulation. TFE3 and TFEB were detected as multiple bands, whereby the slower migrating forms most likely represent different phosphoforms of the proteins as previously published (reviewed in [168]). In line with the common model of TFE3/TFEB activation [78], these bands collapsed to the faster migrating, dephosphorylated forms upon starvation which was parallel by an increase of the nuclear protein levels and indicated the starvation induced nuclear translocation (Figure 40). None of these effects were observed with IL-1α treatment (Figure 40). Hence, this result showed that both IL-1α and starvation, exclusively induce translocation (and dephosphorylation) of their established target transcription factor targets only. The data further indicated that a functional contribution of TFE3 and TFEB to the IL-1α-NF-κB signal transduction and gene expression pathway would have to occur independent or downstream from the “classical” dephosphorylation-dependent nuclear translocation and could potentially rely on the constitutively nuclear phosphorylated forms of TFE3 and / or TFEB.

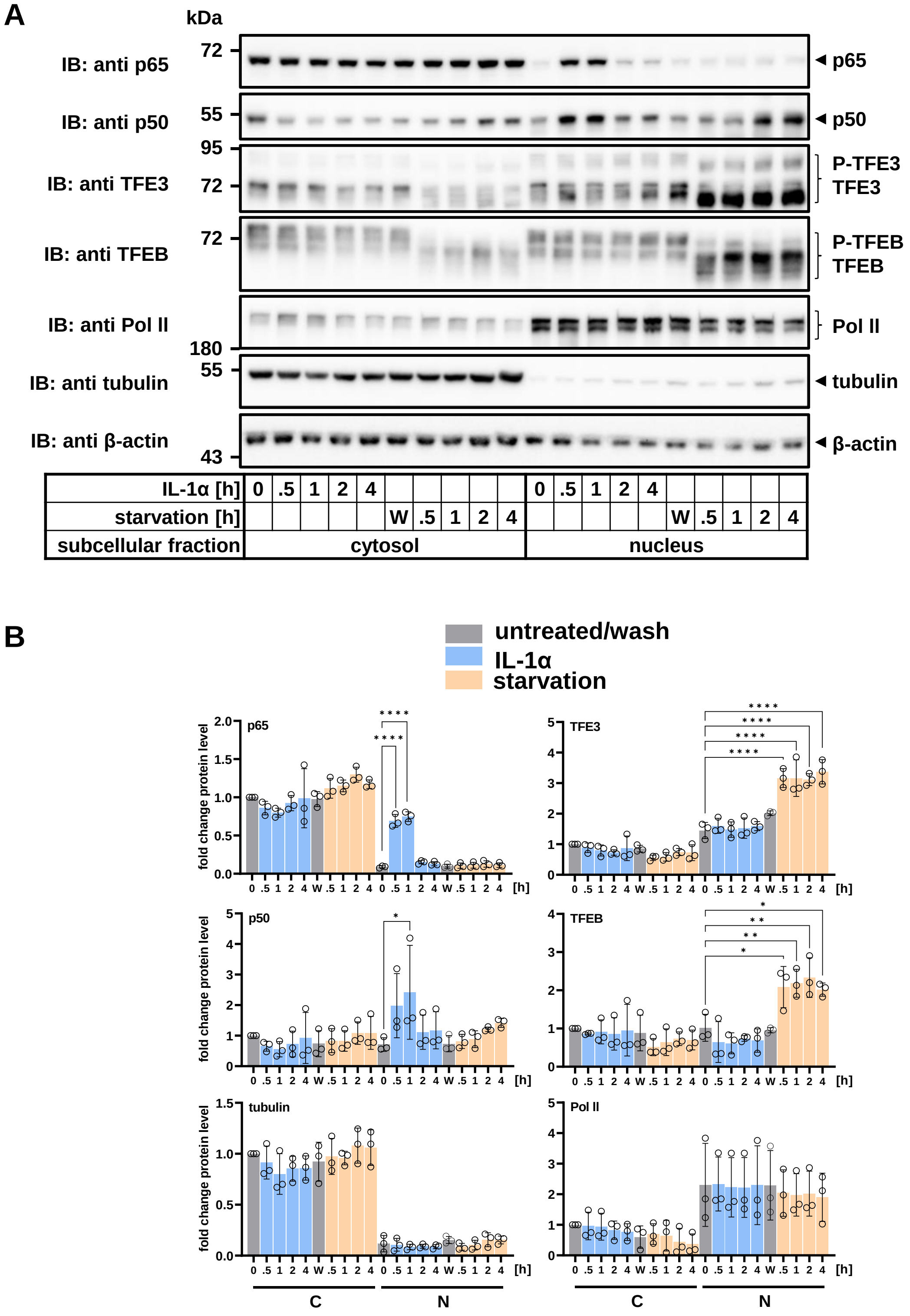

Figure 40: Differential nuclear translocation and dephosphorylation of lysosomal transcription factors TFE3/TFEB or NF-κB subunits p50/p65 upon starvation or IL-1α treatment.
Western blot of the cytosolic (C) and nuclear (N) fractions of HeLa cells exposed to IL-1α or starvation for different periods of 0.5 h, 1 h, 2 h, and 4 h. Cells were treated with IL-1α (10 ng/ml) or left untreated. For starvation, cells were washed four times with HBSS and then incubated in HBSS for the indicated periods, or cells were washed four times and then incubated with complete cell culture medium as an additional control (W/wash). The indicated antibodies were used to determine TFE3/TFEB and NF-κB p50/p65 levels or tubulin and Pol II levels to validate separation of cytosolic and nuclear fractions. The β-actin levels were assessed to control equal loading of gels. While IL-1α induced nuclear translocation of p50/p65 but not TFE3/TFEB, starvation induced nuclear translocation of TFE3/TFEB but not NF-κB subunits. Unlike IL-1α, starvation also caused dephosphorylation of TFE3/TFEB as expected. A representative Western blot experiment is shown in (A). Bar graphs in (B) display the

mean changes in protein level for each condition relative to the cytosolic fraction of the untreated control. The statistical significance of the nuclear translocation was determined by comparing the nuclear fractions under treated conditions (IL-1α or HBSS) with the nuclear fraction of the untreated control. Bar graphs show means of three independent biological replicates ± SD. Asterisks indicate significant changes (*p < 0.05, **p < 0.01, ***p < 0.001, ****p < 0.0001) obtained by one-way ANOVA.

4.5.2 RNAi-mediated knockdowns suggest reciprocal stabilization within NF-κB p65/cofactor complexes

Because there was no reciprocal activation of NF-κB and TFE3/TFEB by IL-1α or starvation at the level of signaling, the next step was to unravel whether suppression of one factor affects the protein levels of the other transcription factors. Given that the function of GLIS2 in the IL-1α-NF-κB or the lysosomal signaling axes was completely unknown, the investigation of a potential role of GLIS2 in these two systems was included in the analyses. RNAi experiments were performed in HeLa cells to suppress the expression levels of p65/RELA, GLIS2, TFE3, TFEB, or both (double knockdown, DK). The siRNA-based knockdowns were carried out according to the screens described in section 4.3, but in an up-scaled format using 60 mm cell culture dishes. Knockdowns were assessed at the RNA level as well as the protein level in HeLa cells stimulated with IL-1α for 1 h and compared with unstimulated control cells. Both, RNA and protein expression were successfully and strongly suppressed (Figure 41A & B). The mean knockdown efficiencies as quantified at the levels of remaining protein were 9% for p65/RELA, 6% for TFE3, 1% for TFEB, and 19% for GLIS2 (Figure 41B). Knockdowns of p65/RELA and TFE3 reduced cell numbers by about 20%, however, the strongest effects were observed with the TFEB knockdown and TFE3/TFEB DK, which reduced cell numbers by more than 50%, indicating that these proteins contribute to the regulation of cell cycle or apoptosis, whereas the knockdown of GLIS2 had only a minor effect on these parameters (Figure 41C). These data demonstrate that p65/RELA and TFE3/TFEB affect general cellular processes (besides their specific effects on inflammatory or stress systems), in line with their broad effects on basal gene expression patterns as shown later on.

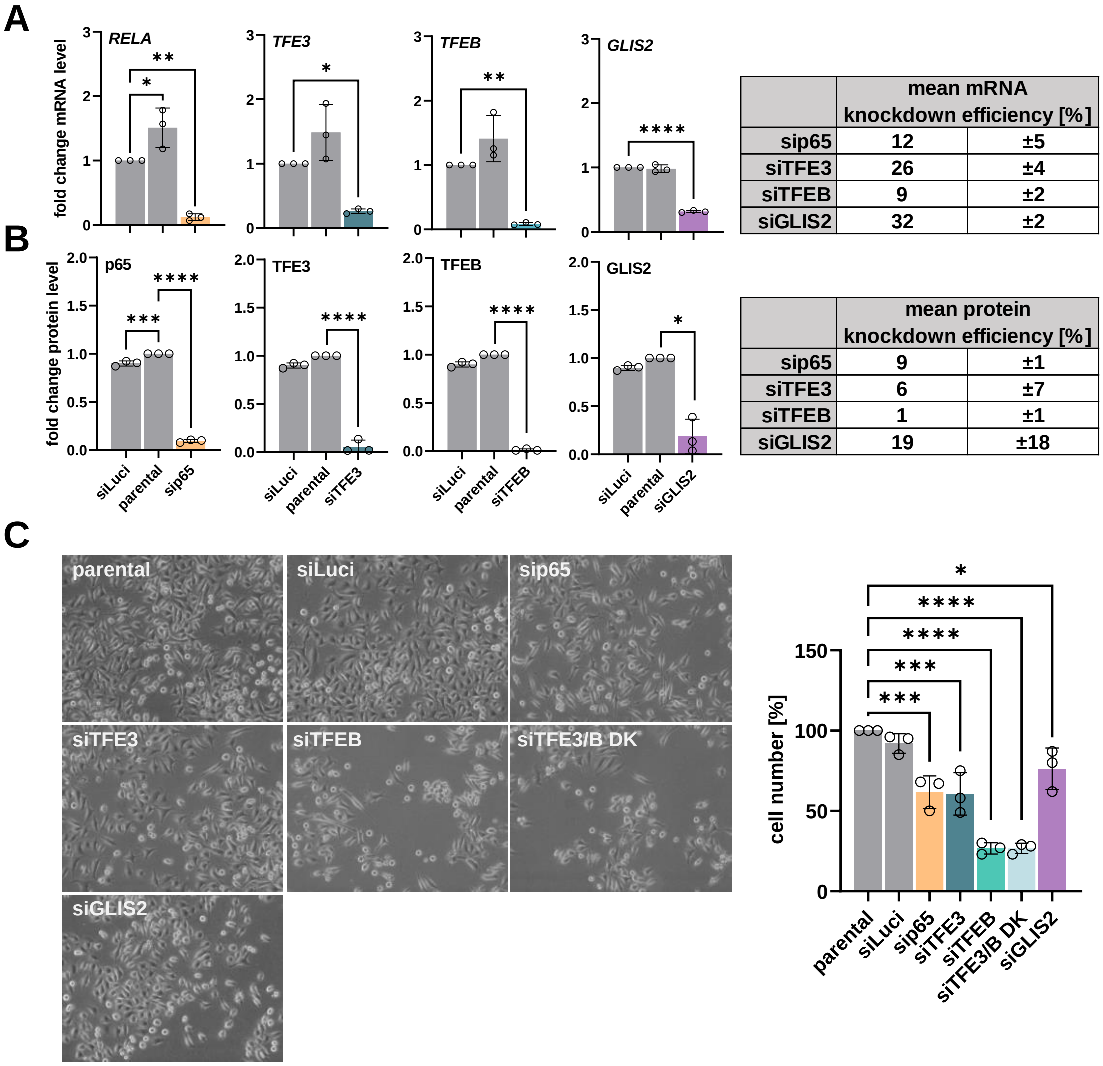

	mean mRNA knockdown efficiency [%]	
sip65	**12**	**±5**
siTFE3	**26**	**±4**
siTFEB	**9**	**±2**
siGLIS2	**32**	**±2**

	mean protein knockdown efficiency [%]	
sip65	**9**	**±1**
siTFE3	**6**	**±7**
siTFEB	**1**	**±1**
siGLIS2	**19**	**±18**

Figure 41: Knockdowns of p65/RELA and its interactors TFE3/TFEB/GLIS2 differentially affect cell proliferation.
HeLa cells were transfected for 48 h with siRNAs directed against p65/RELA, TFE3, TFEB, or both TFE3/TFEB (double knockdown, DK), GLIS2, or luciferase (siLuci, as negative control). As an additional control, one cell culture was left untransfected (parental). The knockdown efficiency was then assessed at the RNA level by RT-qPCR (A) or at the protein level by Western blot analysis (B). Bar graphs show mean changes at the mRNA level (A) or protein level (B) and statistical significance for each condition compared with the siLuci control in (A) or the untransfected control in (B). Tables show the percent knockdown efficiencies corresponding to (A or B). (C) Representative images of cell cultures under the conditions in (A & B). Cell numbers were determined using the Cell Counter plugin of ImageJ based on two images per condition (documented from each experiment). The bar graph shows the mean changes in cell numbers and statistical significance for each condition compared with the untransfected control. For each condition, at least 293 cells were included in the analyses. Bar graphs in (A, B, C) and tables in (A & B) show the means of three independent biological replicates ± SD. Asterisks indicate significant changes (*$p < 0.05$, **$p < 0.01$, ***$p < 0.001$, ****$p < 0.0001$) as determined by one-way ANOVA.

The Western blot in Figure 42A shows the extended analysis from the knockdowns of p65/RELA and its interactors described above, also including samples from cells stimulated with IL-1α for 1 h. The protein levels of all transcription factors were compared and quantified relative to untransfected control cells, as visualized by bar graphs in Figure 42B. Interestingly, this Western blot analysis revealed that suppression of one protein influenced the protein level of at least one other protein. This effect was independent of IL-1α stimulation and was also observed under starvation conditions (Supplementary

Figure 10). Suppression of p65/RELA, for instance, simultaneously reduced the protein levels of TFE3 and TFEB. Suppression of GLIS2 likewise greatly reduced the levels of p65/RELA and TFE3 (Figure 42B). Suppression of TFE3 strongly reduced the level of TFEB, whereas the knockdown of TFEB might have been compensated by enhanced TFE3 expression and increased dephosphorylation (see Figure 42A). One interpretation of these reciprocal regulations of protein levels is that they are indicative for the formation of stable NF-κB/cofactor complexes, whereby in the absence of one component, the other partner protein becomes destabilized or degraded. In addition, the Western blot analysis revealed that protein and phosphorylation levels of IκBα, a key signaling component of the IL-1α-NF-κB pathway, were only slightly reduced upon the suppression of TFE3 and TFEB, whereas IκBα protein and phosphorylation levels were reduced more strongly by the suppression of p65 and GLIS2 (Figure 42B). The reduction in protein and phosphorylation levels as a result of GLIS2 suppression was observed for a variety of proteins and their inducible phosphorylation-sites in the IL-1α-driven canonical NF-κB signaling ((P-)IKKα/β, (P-)IκBα/NFKBIA, (P-)p65/RELA, A20/TNFAIP3) (Supplementary Figure 11). The observed reciprocal regulations of protein levels as well as the broad effect on the IL-1α-NF-κB signaling axis by GLIS2 has not been described previously. However, at this point, it was unclear, if the changes in protein levels resulted from general effects (e.g., caspase-mediated protein breakdown in line with the observed cell numbers) rather than effects specific to the respective p65/RELA protein complex. It was further possible that lower protein levels were a consequence of (indirect) inhibition of transcription or translation, increased protein degradation, or a combination of these effects.

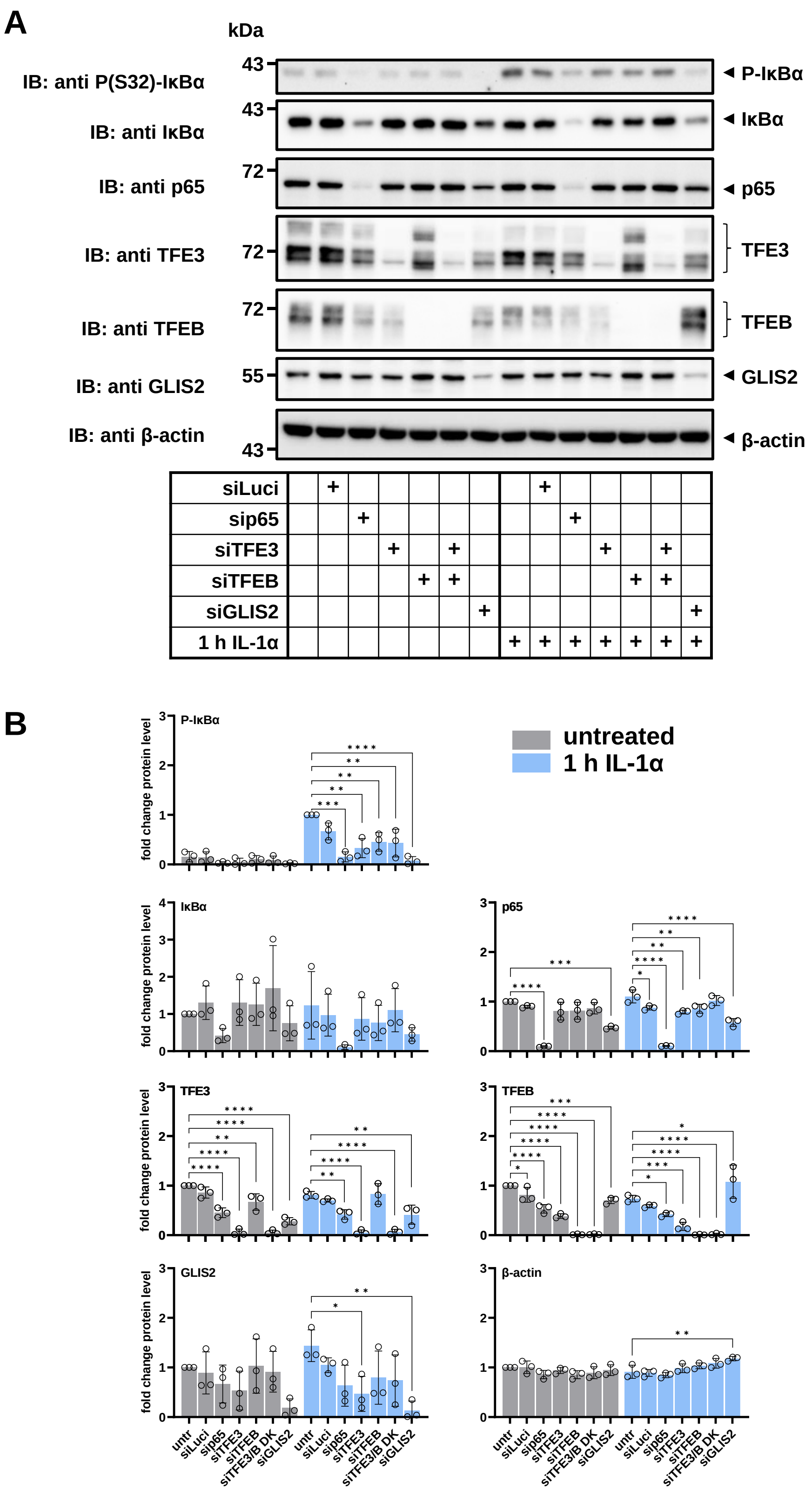

Figure 42: RNAi-mediated knockdown reveals reciprocal regulation of protein levels within NF-κB p65/cofactor complexes.

Western blot analysis from total cell extracts of HeLa cells transiently transfected with siRNAs for 48 h targeting p65/RELA, TFE3, TFEB, or both TFE3/TFEB (double knockdown, DK), GLIS2, or luciferase (siLuci, as negative control). As an additional control, some cell cultures were left untransfected (untr./parental). Cells were stimulated with IL-1α (10 ng/ml) for 1 h or left unstimulated. Western blot was performed using the indicated antibodies and β-actin levels were assessed to control equal loading of gels. The experiment revealed that suppression of one protein affected the protein level of at least one other protein. A representative Western blot experiment is shown in (A). Bar graphs in (B) display the mean changes in protein level for each condition relative to the unstimulated control (untr.). The statistical significance was calculated for each basal sample against the unstimulated control, and for each IL-1α-stimulated sample, the significance was determined relative to the IL-1α-treated control (untr.). Bar graphs show means of three independent biological replicates ± SD. Asterisks indicate significant changes (*p < 0.05, **p < 0.01, ***p < 0.001, ****p < 0.0001) obtained by one-way ANOVA.

4.5.3 RNAi-mediated knockdowns reveal new functions of TFE3/TFEB and GLIS2 in the regulation of inflammatory genes

To assess the potential interplay between NF-κB p65 and TFE3/TFEB at the level of gene regulation, total RNA of the knockdown samples described above was further analyzed to investigate whether p65 is involved in the expression of CLEAR genes and, vice versa, whether TFE3/TFEB influence the expression of prototypical inflammatory genes. Considering that the role of GLIS2 in regulating either CLEAR genes or inflammatory genes had never been described, the potential influence of GLIS2 on these two subsets of genes was studied simultaneously. Six representative CLEAR genes were selected that were shown to be expressed under the control of TFE3/TFEB or had experimental published evidence for promoter recruitment of the lysosomal transcription factors [82, 169]. These genes encode proteins contributing to selective cargo recruitment to the autophagosome (SQSTM1/p62), cargo recruitment to the inner membrane of the autophagosome (MAP1LC3B/LC3B), or are involved in various steps of lysosome biogenesis, such as ion channels (MCOLN1/TRPML1), lysosomal membrane proteins (LAMP1), v-ATPase subunits (ATP6V0D1), or lysosomal hydrolases (HEXA). RT-qPCR analysis of CLEAR genes revealed that the suppression of p65 did not influence the expression of CLEAR gene subsets neither in basal nor under IL-1α (Figure 43A) or starvation conditions (Supplementary Figure 12A). The bar graphs also showed that IL-1α stimulation did not activate the expression of all six CLEAR genes. The data show that the IL-1α-NF-κB signaling axis does not affect the expression of TFE3/TFEB main target genes.

However, unexpectedly and in contrast to the literature [80], the analysis also showed that suppression of TFE3/TFEB, alone or in combination, had only minor effects on the basal expression of the six analyzed CLEAR genes, although several of them reached statistical significance. The greatest effect was observed for TFEB, whose suppression caused almost fourfold upregulation of *MAP1LC3B*, presumably in part due to the counterregulatory enhanced expression of TFE3 or by other compensatory effects that might occur in cells upon suppression of TFEB. The same lack of effect was observed under starvation conditions of up to 4 h that had only little effect on the expression of CLEAR genes (Supplementary Figure 12A), especially when considering the starvation-induced increase of nuclear TFE3/TFEB levels within one hour (see Figure 40). One possible explanation was that inducible CLEAR gene expression follows a rather slow kinetics and accumulative expression pattern and is therefore measurable only many hours after translocation of the transcription factor.

Another interesting finding was that suppression of GLIS2 caused a reproducible upregulation of the *MCOLN1* mRNA which is comparable to the effect observed after the suppression of TFE3. *MCOLN1* is a gene that encodes Transient Receptor Potential Mucolipin 1 (TRPML1) an important ion channel in the lysosomal membrane of mammalian cells that regulates lysosomal Ca^{2+} release in response to different kinds of cellular stresses (e.g., nutrient deprivation [170] or increased levels of reactive oxygen species [171]). The data reveal a novel, hitherto unknown repressory role of GLIS2 in the expression of this gene (Figure 43A & Supplementary Figure 12A).

Next, the mRNA analysis was focused on the impact of the TFE3, TFEB, or GLIS2 knockdown on six prototypical IL-1α-NF-κB-driven inflammatory genes which are mainly involved in negative feedback signaling (NFKBIA/IκBα, TNFAIP3/A20), differentiation of immune cells (CSF2) or chemotaxis (CXCL8/IL-8, CXCL2, CCL2). RT-qPCR showed that suppression of TFE3 or TFEB and both (TFE3/B DK) caused a massive downregulation of the IL-1α-induced expression of all six inflammatory genes to the extent that the inducible expression of *IL8*, *CSF2*, and *CCL2* was almost completely abolished, whereas for *CXCL2*, *TNFAIP3*, and *NFKBIA* some residual expression could be observed (Figure 43B). A similar effect was obtained upon the suppression of GLIS2, which caused significant downregulation of *CSF2*, *CCL2*, and *NFKBIA*. These strong effects on the expression of inflammatory genes were only observed in the IL-1α-induced situation, but not during starvation conditions (Supplementary Figure 12B).

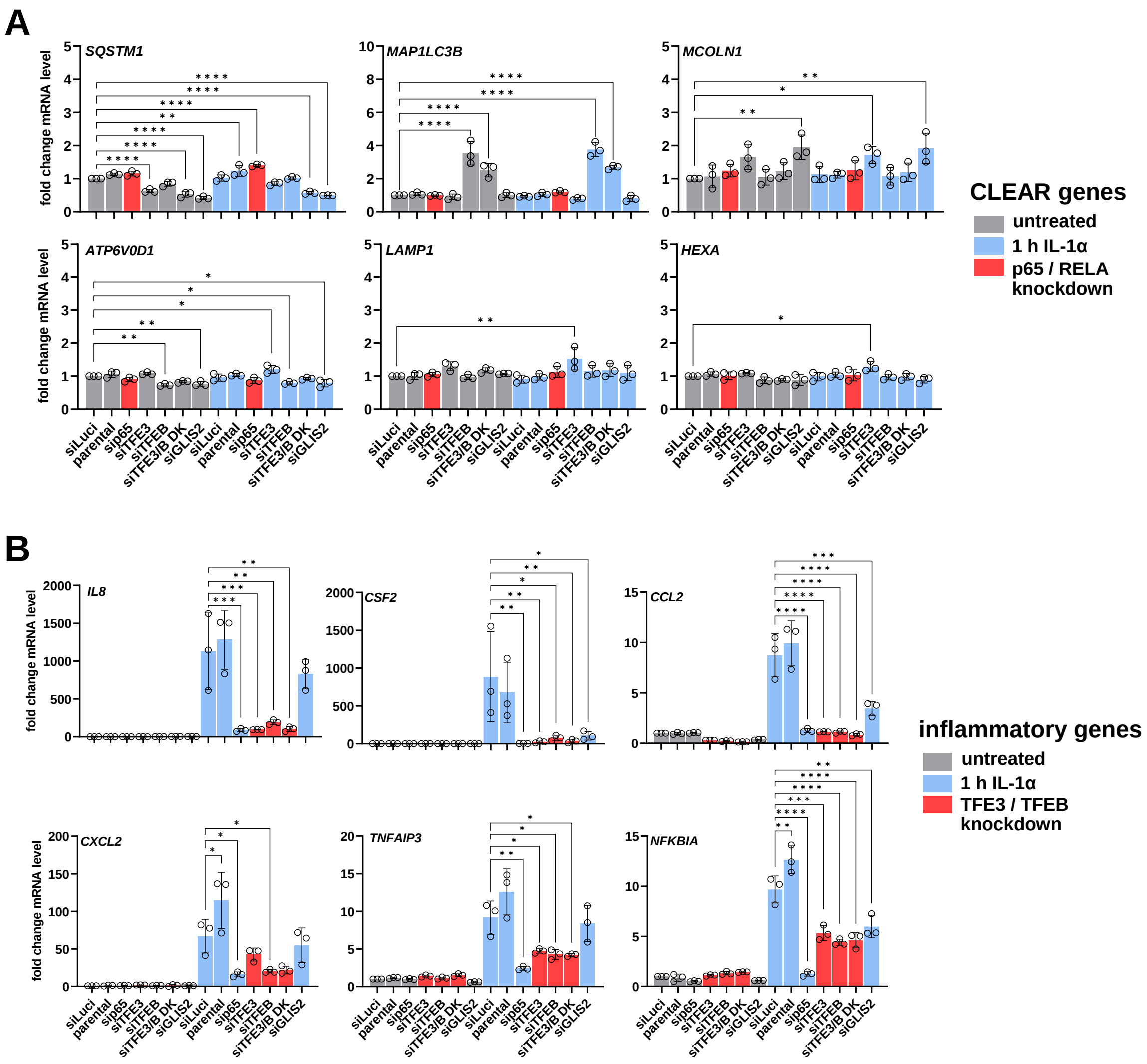

Figure 43: Transient RNAi-mediated suppression of TFE3/TFEB and GLIS2 cause strong downregulation of prototypical inflammatory genes whereas depleting p65/RELA did not affect prototypical CLEAR genes. RT-qPCR analysis of mRNA levels of six CLEAR genes (A) and six inflammatory genes (B) using total RNA from the knockdown samples described in Figure 42. Relative mRNA levels were calculated against the untreated siLuci control. For CLEAR genes, the statistical significance of knockdown effects was determined relative to the untreated siLuci control. For induced inflammatory genes, significance was calculated against the 1 h IL-1α-treated siLuci control. Red colors visualize p65/RELA (A) or TFE3/TFEB (B) knockdown samples. Bar graphs show means of three independent biological replicates ± SD. Asterisks indicate significant changes (*$p < 0.05$, **$p < 0.01$, ***$p < 0.001$, ****$p < 0.0001$) obtained by one-way ANOVA.

In summary, these analyses provided strong evidence for a contribution of lysosomal transcription factors and GLIS2 to cytokine-inducible NF-κB-mediated gene expression, whereas the p65/RELA subunit was not involved in regulation of lysosomal genes, demonstrating unidirectional crosstalk of the NF-κB and lysosomal pathways.

4.5.4 Lysosomal transcription factor function in the IL-1α-driven expression of inflammatory genes is not maintained upon long-term suppression of TFE3 or TFEB

In a further attempt, CRISPR-Cas9-mediated gene editing was used with the initial aim to generate stable TFE3 or TFEB knockout cell lines as a reproducible source for large scale functional experiments. CRISPR gene editing is based on the active endonuclease Cas9, which is targeted to a genomic locus of interest by a specific sgRNA. Cas9 catalyzes a double-strand break within the sgRNA target region, very often followed by InDel mutations during DNA repair. This type of common non-homologous end-joining repair stochastically results in a frame shift mutation and a premature stop codon in the amino acid sequence, which in most cases prevents productive translation of the full-length protein.

CRISPR-mediated gene editing was applied to generate stable gene knockouts of TFE3, TFEB, both (double knockout), GLIS2, and p65/RELA as a reference in HeLa cells. Initially, 3 sgRNAs were newly designed for each of the genes using the CRISPick webtool (Broad Institute). All sgRNAs targeted either the first or the second exons. For preparation of p65/RELA gene knockout cells an already available RELA-sg1 was employed, which was also the sgRNA used for the generation of p65-deficient cells that were utilized for MiniTurboID in the previous parts of this work and which had already been published by our group [49]. The sgRNA sequences were cloned into the LCV2 single-vector system that was suitable for lentiviral use and also provided the sequence of Cas9 as well as a puromycin-resistance cassette. Lentiviral transduction was performed with single sgRNAs or combinations of 2-6 sgRNAs, to increase the chance of a successful gene knockout through the partial deletion of a gene sequence. HeLa cells were also transduced with LCV2 empty vector to exclude cellular changes resulting from the transduction and selection procedures alone. HeLa cells were then selected with puromycin for up to 14 days, harvested, and analyzed by Western blot for the knockout of the targeted transcription factors.

After several attempts, including testing additional sgRNAs targeting exons 3 and 4, knockdown attempts remained unsuccessful for GLIS2 (Supplementary Figure 13A-C), but a set of stable HeLa cells could be generated comprising empty vector transduced cells and cells lacking TFE3, TFEB, both TFE3/TFEB (double knockout), and p65/RELA (Supplementary Figure 13D).

The set of knockout cells was then analyzed for potential disruption of the cellular IL-1α response, similar to the characterization of the effects of siRNA mediated depletions as described above in the previous chapter. The Western blot analysis in Figure 44 showed that empty vector transduced cells showed no abnormalities in the activation of the NF-κB pathway when compared to untransduced cells demonstrating that the lentiviral transduction and selection procedures did not affect signaling (Figure 44). In contrast, the suppression of p65/RELA caused a complete shutdown of the NF-κB downstream signaling, while the IL-1α-induced phosphorylation and activation of IKKα/β remained intact (Figure

44). Notably, long-term suppression of TFE3, TFEB, alone or in combination did not affect the different levels of the IL-1α-induced signal transduction, because the characteristic basal expression of IκBα and IL-1α-mediated phosphorylation and degradation of IκBα, the phosphorylation of p65, and the inducible expression of the inhibitory proteins A20/TNFAIP3 and IκBα/NFKBIA were normal compared with parental and vector control cells.

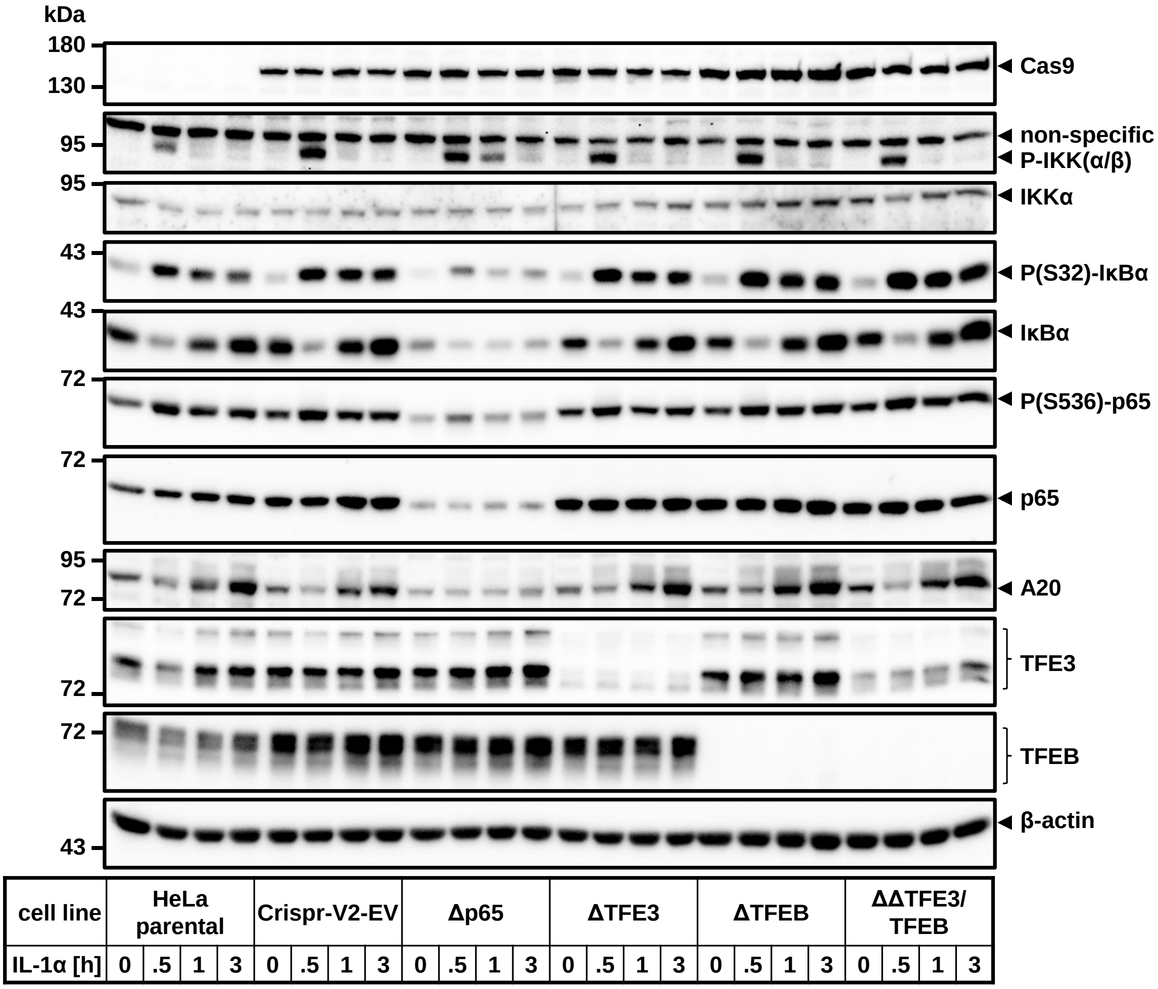

Figure 44: Long-term suppression of lysosomal transcription factors did not affect the IL-1α-driven activation of the NF-κB pathway.
Western blot analysis of components of the canonical NF-κB p65 pathway in stably transduced HeLa knockout cells in comparison to empty vector cells (LCV2) or untransduced (parental) cells. The cells were left unstimulated or stimulated with IL-1α (10 ng/ml) for different times to monitor the different phases of signal transduction using the indicated antibodies. Antibodies against β-actin were used to control for equal loading of gels. Shown is one representative experiment out of two biological replicates.

The analysis of the inflammatory mRNAs in Figure 45 revealed that transduced cells generally exhibited a much higher level of induction as compared to untransduced (parental) cells. The shutdown of the NF-κB downstream signaling as a consequence of the p65/RELA gene knockout moreover caused almost complete disruption of the mRNA expression of the six inflammatory genes. Contrary to that, long-term suppression of TFE3 and TFEB had only minor inhibitory effects on the expression of *CSF2* and *CCL2* and no effects on *IL8*, *CXCL2*, *NFKBIA*, or *TNFAIP3*. Thus, the profound suppressive effects on inflammatory genes observed after transient siRNA-mediated knockdown were not recapitulated in the lentivirally transduced cell lines, despite a similar level of knockdown / knockout efficiency. These data suggested that while p65/RELA is essential, the phenotypes of TFE3/TFEB losses on inflammatory gene expression are context-dependent and can be compensated for by unknown factors. This explanation is plausible, as the acute depletion by siRNAs was associated with reduced cell proliferation and / or viability (see Figure 41C). No attempts were made to identify the putative compensatory factors or mechanisms by genome-wide analyses.

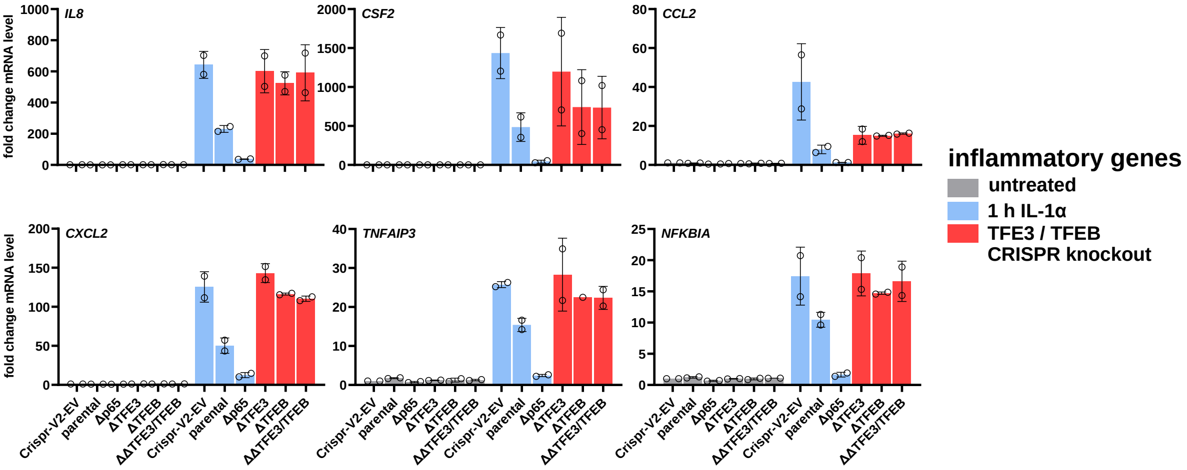

Figure 45: Unlike depletion of p65/RELA, long-term suppression of lysosomal transcription factors is without effect on inflammatory gene expression.
RT-qPCR analysis of mRNA levels of six inflammatory genes from stably transduced HeLa knockout cells in comparison to empty vector (LCV2) transduced and untransduced (parental) control cells. Cells were left untreated or were stimulated with IL-1α (10 ng/ml) for 1 h. Changes in mRNA levels were calculated relative to untreated empty vector control cells and are displayed by bar graphs. The analysis comprises two independent biological replicates. TFE3/TFEB knockout samples are highlighted in red.

Overall, the data show a unidirectional crosstalk between the NF-κB and the lysosomal transcription factor systems. The main evidence for this conclusion is the lack of contribution of p65/RELA to the expression of the lysosomal subset of CLEAR genes, whereas lysosomal transcription factors TFE3 and TFEB were required for full activation of several prototypical inflammatory NF-κB target genes. This pro-inflammatory function of TFE3/TFEB is most likely associated with the constitutive nuclear phosphoforms and therefore independent from the classical starvation-induced activation of TFE3/TFEB, which occurs by dephosphorylation and fast nuclear accumulation of both factors. Moreover, the contribution of TFE3/TFEB to inflammatory gene expression is highly dynamic and, unlike p65/RELA, non-essential in the sense that this phenotype is lost in cells with long-term stable suppression of TFE3/TFEB.

4.6 Transcriptome-wide analysis identifies jointly regulated genetic (sub)networks that strictly depend on TFE3, TFEB, GLIS2, and p65/RELA

In the following, the mRNA expression analysis of the siRNA-knockdown samples was expanded to the transcriptome-wide level by microarray experiments to unveil the functional contribution of the interactors TFE3, TFEB, and GLIS2 to NF-κB p65-dependent gene regulation on a global scale. The first two parts of the analysis focused on constitutively expressed genes and effects on the CLEAR network of genes. The third part was devoted to a comprehensive analysis of IL-1α-responsive genes, focussing on (i) genes that were regulated exclusively by one factor only compared with coregulated genes, (ii) genes that were repressed or activated by p65/RELA and its interactors, and (iii) the functional connectivities of identified gene sets based on their annotated biological functions, as schematically illustrated in Figure 46.

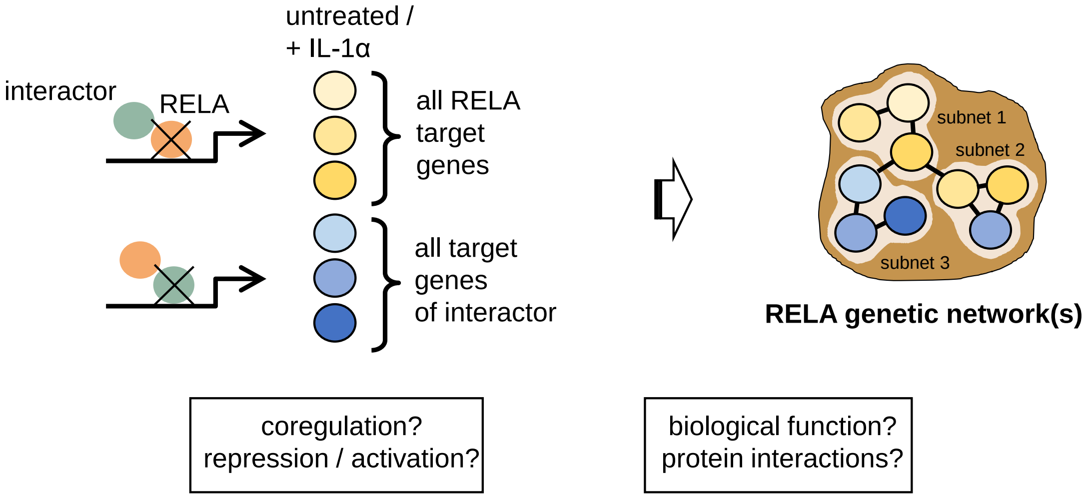

Figure 46: Strategy of the bioinformatic analyses of transcriptomic datasets to examine the knockdown effects of p65/RELA interactors.
Schematic representation of transcriptomic data analysis from the samples in Figure 42 of HeLa cells after siRNA-mediated knockdown of interactors (green circle) compared with p65/RELA (orange circle) in the presence or absence of IL-1α stimulation for 1 h. The goals were to investigate whether (i) specific target genes of individual factors (indicated by yellow or blue circles) were coregulated by p65/RELA, (ii) genes were coregulated into the same direction (i.e. repressed or activated), and (iii) p65/RELA and its interactors jointly regulate functionally connected genetic (sub)networks.

Total RNA samples were prepared and validated by RT-qPCR by Lisa Leib (see Figure 43). The microarray analysis was performed in the genomics core facility of the ILH, Medical Faculty, Justus Liebig University (headed by Dr. Jochen Wilhelm). Raw data were processed by Dr. Jochen Wilhelm who provided spreadsheet tables with normalized mRNA expression values, fold changes of gene expression between pairs of treatments, and the according statistical parameters. Subsequent bioinformatic analyses were devised by Prof. M. Kracht who carried out and visualized the analyses in Figure 47, 51-53. Lisa Leib performed and visualized the analyses in Figure 48-50, 54 & 55 and adapted the schematic representation of the transcriptomic data analysis (Figure 46), which was created by Prof. M. Kracht.

4.6.1 Broad influence of p65/RELA and the interactors on homeostatic gene-regulatory functions

The transcriptome analysis of the knockdown samples in Figure 42 was conducted using microarrays carrying 48,000-probes for annotated and predicted protein-coding human genes and a range of noncoding RNAs. The analysis was performed by Dr. Jochen Wilhelm within the genomics core facility of the ILH, Medical Faculty, Justus Liebig University. He provided spread sheet tables with processed, normalized mRNA expression values, fold changes of gene expression between pairs of treatments and the according statistical parameters. Differentially expressed genes (DEGs) after the suppression of p65/RELA, TFE3, TFEB, TFE3 and TFEB, or GLIS2 were defined by an LFC ≥ 1 with a $-\log_{10}$ p value ≥ 1.3 relative to luciferase siRNA control. Each knockdown affected at least 1000 target genes under basal conditions, an observation that underscores the impact of p65/RELA and each of its interactors on the global scale of gene expression (Figure 47A). As shown by the Venn diagrams of Figure 47A, the majority of basal target genes of each interactor did not overlap with p65/RELA target genes, as only 263 (23%) genes were also affected by GLIS2 knockdown, while only 134 (12%) were affected by both TFE3/TFEB. These groups of genes indicate a joint contribution of p65/RELA and its interactors to some specific subsets of genes involved in homeostatic cell functions. Furthermore, the expression patterns of basally regulated genes were not largely changed by the respective knockdown (Figure 47B).

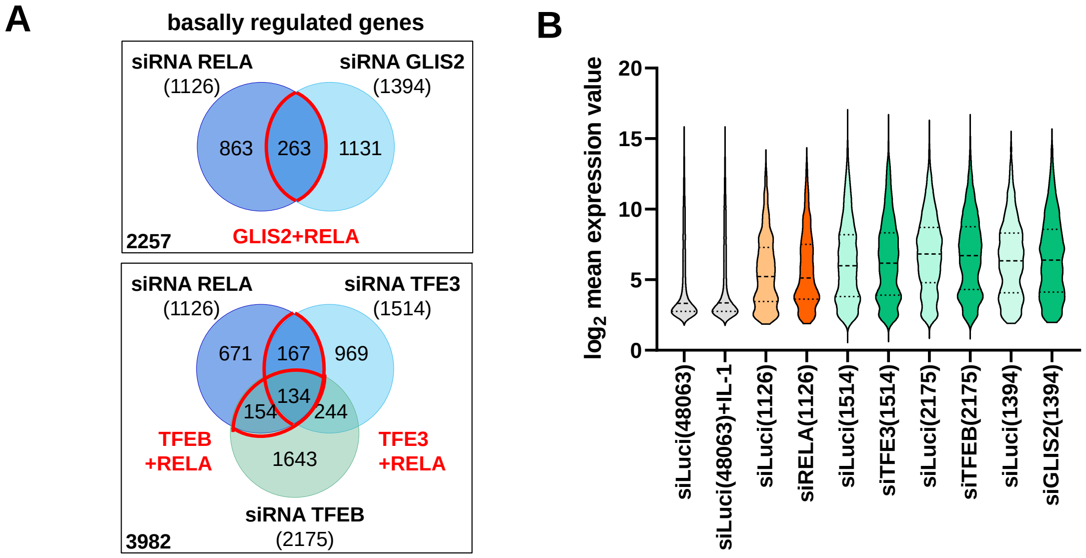

Figure 47: Joint and distinct regulation of subsets of genes in basal conditions by p65/RELA and its interactors.
HeLa cells were transiently transfected with 20 nM siRNA mixtures for 48 h targeting p65/RELA, TFE3, TFEB, and GLIS2, or luciferase. Agilent microarray analyses were performed from total RNA of two independent biological replicates. DEGs were defined by an LFC ≥ 1 with a $-\log_{10}$ p value ≥ 1.3 of each individual knockdown relative to luciferase siRNA control. (A) Venn diagrams demonstrate the overlap of all significantly deregulated DEGs in basal conditions. Genes that were jointly regulated by knockdown of RELA and one of its interactors are marked in red. (B) Violin plots showing the distributions, medians, and interquartile ranges of the normalized expression levels (derived from mean fluorescence intensities of microarray spots) corresponding to the gene subsets as defined in (A). The number of genes is specified in parentheses. These graphs illustrate that the majority of genes that were differentially affected by each individual siRNA target were expressed well above background levels. (See Figure 46 legend for contributions.)

To reveal the biological functions of the specific subsets of basally regulated genes that were affected by each individual knockdown, a comparative pathway analysis was performed, with the most significant DEGs in the knockdowns defined by an LFC ≥ 1 with a $-\log_{10}$ p value ≥ 2 relative to the luciferase siRNA control. The analysis revealed that TFE3 had a strong effect on gene subsets that contribute to the expression and processing of nascent forms of NOTCH precursors, encode histones and histone modifiers, or control the structural composition of chromatin (Figure 48). In contrast, most of the genes affected by TFEB were involved in the regulation of apoptosis and cell death but also contributed to transcriptional regulation, methylation, and histone modification. Some of these pathways might be associated with reduced cell numbers as previously observed in cells after TFEB suppression (see Figure 41). Interestingly, none of the chromatin- or transcription-related genes were found among the genes most strongly affected by GLIS2. GLIS2 primarily affected genes involved in serine/threonine kinase receptor-mediated signaling, such as TGF-β signal transduction, and also genes of the ER lumen or those contributing to protein maturation. The impaired maturation of proteins may also account for the reduced protein levels of canonical NF-κB signaling components observed after GLIS2 suppression (see Supplementary Figure 11). Overall, when comparing pathway annotations of subsets of genes most impacted by suppression of p65/RELA or its individual interactors, there was little overlap suggesting that each transcription factor mainly regulates its own subsets of genes under homeostatic conditions.

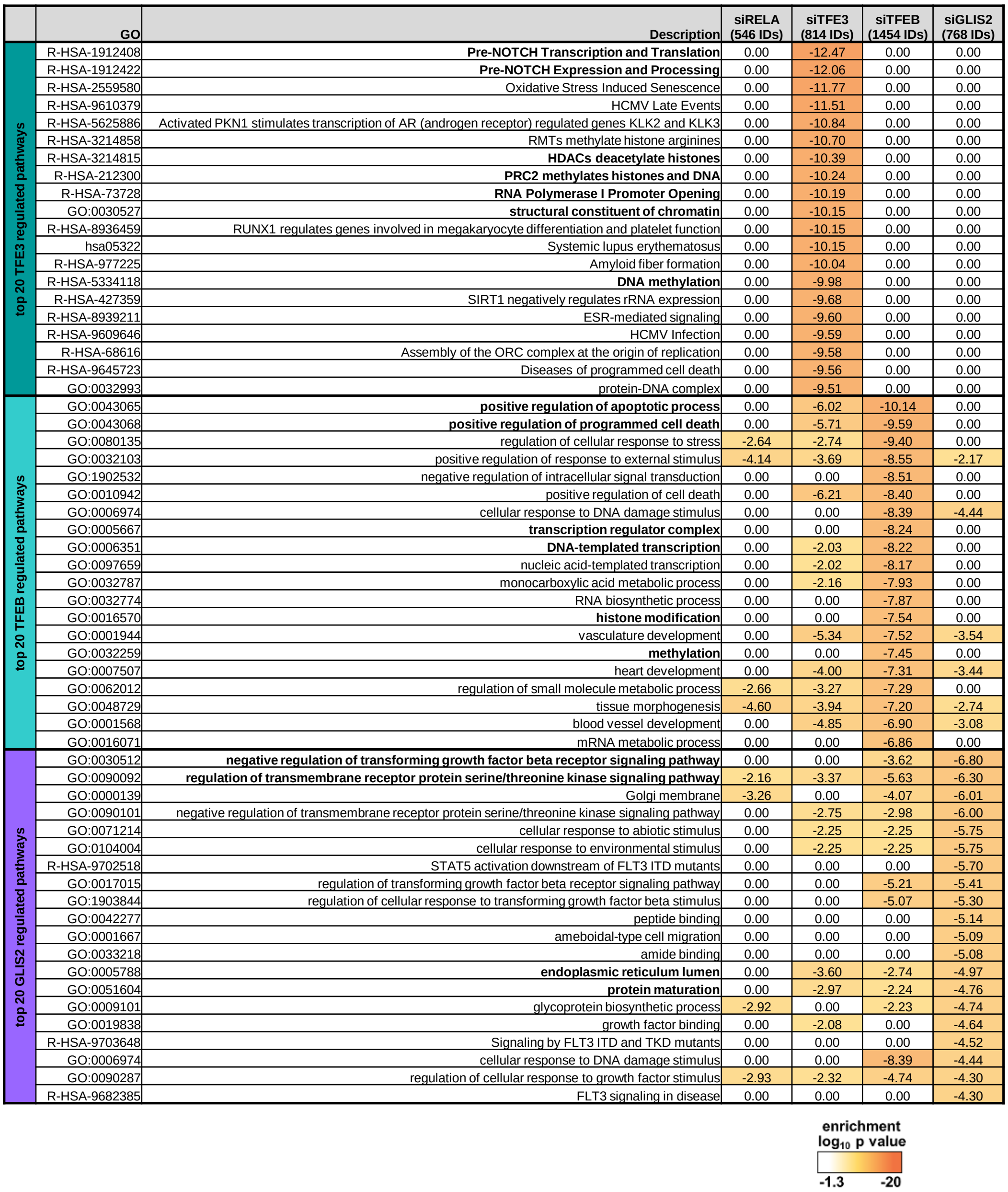

	GO	Description	siRELA (546 IDs)	siTFE3 (814 IDs)	siTFEB (1454 IDs)	siGLIS2 (768 IDs)
top 20 TFE3 regulated pathways	R-HSA-1912408	**Pre-NOTCH Transcription and Translation**	0.00	-12.47	0.00	0.00
	R-HSA-1912422	**Pre-NOTCH Expression and Processing**	0.00	-12.06	0.00	0.00
	R-HSA-2559580	Oxidative Stress Induced Senescence	0.00	-11.77	0.00	0.00
	R-HSA-9610379	HCMV Late Events	0.00	-11.51	0.00	0.00
	R-HSA-5625886	Activated PKN1 stimulates transcription of AR (androgen receptor) regulated genes KLK2 and KLK3	0.00	-10.84	0.00	0.00
	R-HSA-3214858	RMTs methylate histone arginines	0.00	-10.70	0.00	0.00
	R-HSA-3214815	**HDACs deacetylate histones**	0.00	-10.39	0.00	0.00
	R-HSA-212300	**PRC2 methylates histones and DNA**	0.00	-10.24	0.00	0.00
	R-HSA-73728	**RNA Polymerase I Promoter Opening**	0.00	-10.19	0.00	0.00
	GO:0030527	**structural constituent of chromatin**	0.00	-10.15	0.00	0.00
	R-HSA-8936459	RUNX1 regulates genes involved in megakaryocyte differentiation and platelet function	0.00	-10.15	0.00	0.00
	hsa05322	Systemic lupus erythematosus	0.00	-10.15	0.00	0.00
	R-HSA-977225	Amyloid fiber formation	0.00	-10.04	0.00	0.00
	R-HSA-5334118	**DNA methylation**	0.00	-9.98	0.00	0.00
	R-HSA-427359	SIRT1 negatively regulates rRNA expression	0.00	-9.68	0.00	0.00
	R-HSA-8939211	ESR-mediated signaling	0.00	-9.60	0.00	0.00
	R-HSA-9609646	HCMV Infection	0.00	-9.59	0.00	0.00
	R-HSA-68616	Assembly of the ORC complex at the origin of replication	0.00	-9.58	0.00	0.00
	R-HSA-9645723	Diseases of programmed cell death	0.00	-9.56	0.00	0.00
	GO:0032993	protein-DNA complex	0.00	-9.51	0.00	0.00
top 20 TFEB regulated pathways	GO:0043065	**positive regulation of apoptotic process**	0.00	-6.02	-10.14	0.00
	GO:0043068	**positive regulation of programmed cell death**	0.00	-5.71	-9.59	0.00
	GO:0080135	regulation of cellular response to stress	-2.64	-2.74	-9.40	0.00
	GO:0032103	positive regulation of response to external stimulus	-4.14	-3.69	-8.55	-2.17
	GO:1902532	negative regulation of intracellular signal transduction	0.00	0.00	-8.51	0.00
	GO:0010942	positive regulation of cell death	0.00	-6.21	-8.40	0.00
	GO:0006974	cellular response to DNA damage stimulus	0.00	0.00	-8.39	-4.44
	GO:0005667	**transcription regulator complex**	0.00	0.00	-8.24	0.00
	GO:0006351	**DNA-templated transcription**	0.00	-2.03	-8.22	0.00
	GO:0097659	nucleic acid-templated transcription	0.00	-2.02	-8.17	0.00
	GO:0032787	monocarboxylic acid metabolic process	0.00	-2.16	-7.93	0.00
	GO:0032774	RNA biosynthetic process	0.00	0.00	-7.87	0.00
	GO:0016570	**histone modification**	0.00	0.00	-7.54	0.00
	GO:0001944	vasculature development	0.00	-5.34	-7.52	-3.54
	GO:0032259	**methylation**	0.00	0.00	-7.45	0.00
	GO:0007507	heart development	0.00	-4.00	-7.31	-3.44
	GO:0062012	regulation of small molecule metabolic process	-2.66	-3.27	-7.29	0.00
	GO:0048729	tissue morphogenesis	-4.60	-3.94	-7.20	-2.74
	GO:0001568	blood vessel development	0.00	-4.85	-6.90	-3.08
	GO:0016071	mRNA metabolic process	0.00	0.00	-6.86	0.00
top 20 GLIS2 regulated pathways	GO:0030512	**negative regulation of transforming growth factor beta receptor signaling pathway**	0.00	0.00	-3.62	-6.80
	GO:0090092	**regulation of transmembrane receptor protein serine/threonine kinase signaling pathway**	-2.16	-3.37	-5.63	-6.30
	GO:0000139	Golgi membrane	-3.26	0.00	-4.07	-6.01
	GO:0090101	negative regulation of transmembrane receptor protein serine/threonine kinase signaling pathway	0.00	-2.75	-2.98	-6.00
	GO:0071214	cellular response to abiotic stimulus	0.00	-2.25	-2.25	-5.75
	GO:0104004	cellular response to environmental stimulus	0.00	-2.25	-2.25	-5.75
	R-HSA-9702518	STAT5 activation downstream of FLT3 ITD mutants	0.00	0.00	0.00	-5.70
	GO:0017015	regulation of transforming growth factor beta receptor signaling pathway	0.00	0.00	-5.21	-5.41
	GO:1903844	regulation of cellular response to transforming growth factor beta stimulus	0.00	0.00	-5.07	-5.30
	GO:0042277	peptide binding	0.00	0.00	0.00	-5.14
	GO:0001667	ameboidal-type cell migration	0.00	0.00	0.00	-5.09
	GO:0033218	amide binding	0.00	0.00	0.00	-5.08
	GO:0005788	**endoplasmic reticulum lumen**	0.00	-3.60	-2.74	-4.97
	GO:0051604	**protein maturation**	0.00	-2.97	-2.24	-4.76
	GO:0009101	glycoprotein biosynthetic process	-2.92	0.00	-2.23	-4.74
	GO:0019838	growth factor binding	0.00	-2.08	0.00	-4.64
	R-HSA-9703648	Signaling by FLT3 ITD and TKD mutants	0.00	0.00	0.00	-4.52
	GO:0006974	cellular response to DNA damage stimulus	0.00	0.00	-8.39	-4.44
	GO:0090287	regulation of cellular response to growth factor stimulus	-2.93	-2.32	-4.74	-4.30
	R-HSA-9682385	FLT3 signaling in disease	0.00	0.00	0.00	-4.30

Figure 48: Comparative pathway enrichment analysis reveals largely non-overlapping and distinct functions of p65/RELA and its interactors under homeostatic conditions.
Top terms resulting from comparative pathway overrepresentation analyses of four subsets of DEGs affected by siRNA knockdowns conducted based on GO (BP, CC, MF), KEGG, Reactome, Canonical pathways, and transcription factor targets using Metascape [149]. DEGs were defined by an LFC ≥ 1 with a $-\log_{10}$ p value ≥ 2 of each individual knockdown relative to luciferase siRNA control. The table shows the top 20 enriched pathway terms associated with gene subsets affected by the TFE3, TFEB, or GLIS2 knockdown. The total number of DEGs for each condition that were subjected to the analysis is indicated in parentheses. Bold letters mark specific cellular processes to which the interactors contribute under homeostatic conditions and that are mentioned in the text. (See Figure 46 legend for contributions.)

Although a similar analysis aimed at identifying the top 20 shared pathway terms revealed strong overlap in some homeostatic pathways by TFE3 and TFEB, amongst the few pathways jointly regulated by p65/RELA and its interactors under homeostatic conditions were particularly those associated with cancer, cell growth, or the cellular response to external stimuli (Figure 49).

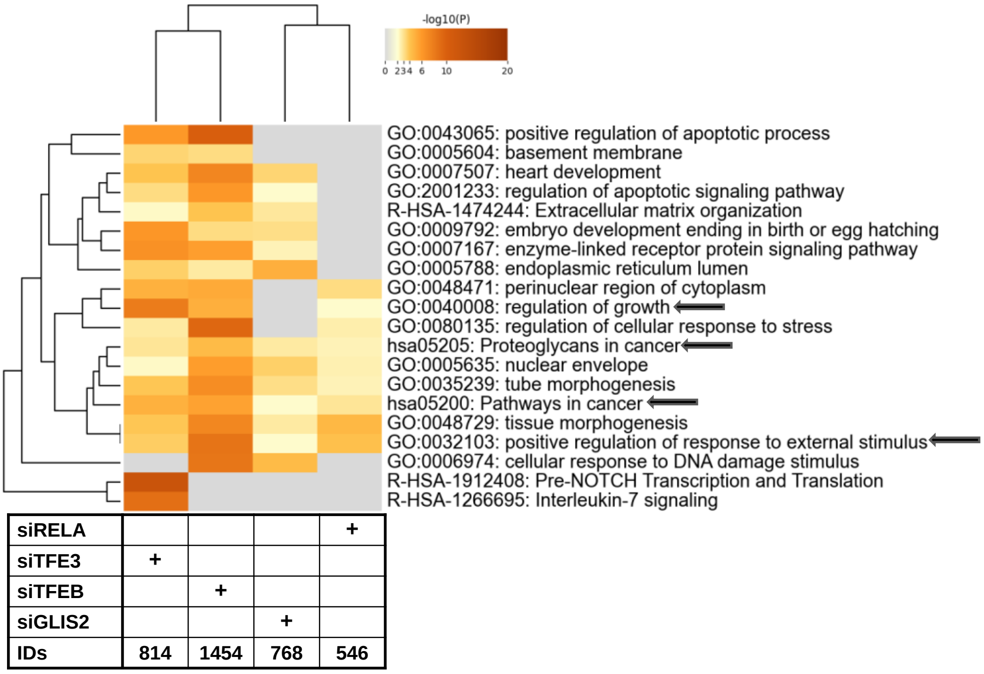

siRELA				+
siTFE3	+			
siTFEB		+		
siGLIS2			+	
IDs	**814**	**1454**	**768**	**546**

Figure 49: Joint contribution of p65/RELA and its interactors in cellular processes associated with cancer. The graph shows the same analysis as in Figure 48 but with a focus on the top 20 pathways that were affected by the four knockdowns simultaneously. Black arrows mark cellular processes to which p65/RELA and the interactors jointly contribute under homeostatic conditions. (See Figure 46 legend for contributions.)

4.6.2 The IL-1α-NF-κB pathway does not regulate the CLEAR network of lysosomal genes

For a more detailed analysis of TFE3 and TFEB concerning their established functions, a list of CLEAR genes was extracted from reference [82] which comprised 73 genes identified as direct targets of the lysosomal transcription factor TFEB and with a known role in lysosomal function [82]. This list was intersected with the transcriptome data of the siRNA knockdown samples. Figure 50 shows the CLEAR genes grouped according to their lysosomal function and the changes of their expression levels upon knockdown of p65/RELA or its interactors as well as in response to 1 h IL-1α treatment. Displayed are the top 3 most strongly up- or downregulated genes that were affected by the knockdown of TFEB in each category of lysosomal function. Additionally, highlighted in green are the CLEAR genes analyzed by RT-qPCR experiments in the previous section (see Figure 43A).

Altogether, the suppression of TFEB had little effect on the basal expression of these genes, with only 6 genes affected by siRNA knockdown by more than 2-fold. Given that CLEAR genes exhibit relatively high basal expression levels (Supplementary Figure 14), high LFCs were generally not expected. However, even small, i.e. 1.5-fold changes, were only observed in 21 cases. The pattern of induction or repression observed by the TFE3/TFEB double knockdown largely resembled the TFEB knockdown alone. Suppression of TFE3 or GLIS2 alone showed hardly any effect on CLEAR gene mRNA levels, except for *MCOLN1*, whose expression was increased by more than 2-fold in GLIS2 knockdown cells, which is in line with previous RT-qPCR analyses (see Figure 43A). As already revealed by RT-qPCR of six representative CLEAR genes (see Figure 43A), there was no obvious regulation of the entire CLEAR gene network by the IL-1α-NF-κB axis (Figure 50).

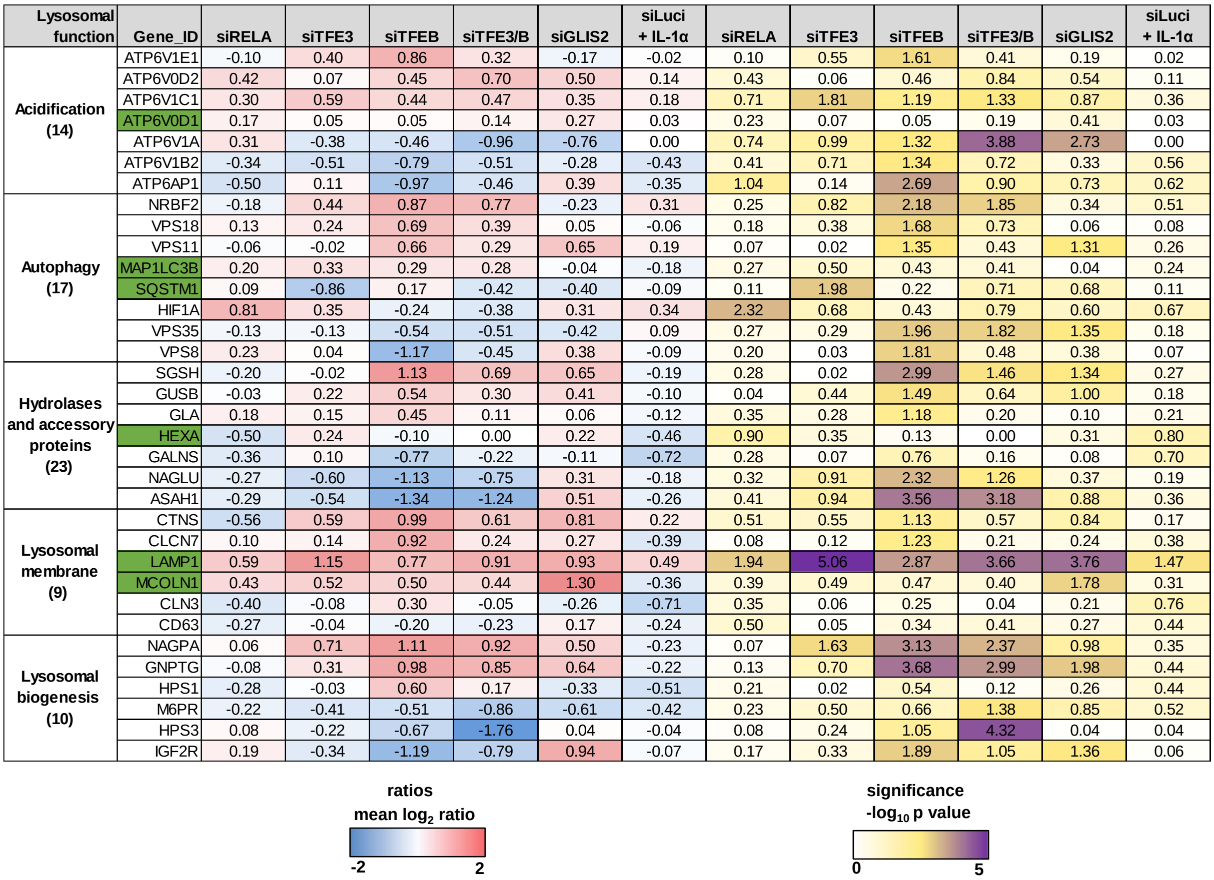

Lysosomal function	Gene_ID	siRELA	siTFE3	siTFEB	siTFE3/B	siGLIS2	siLuci + IL-1α	siRELA	siTFE3	siTFEB	siTFE3/B	siGLIS2	siLuci + IL-1α
Acidification (14)	ATP6V1E1	-0.10	0.40	0.86	0.32	-0.17	-0.02	0.10	0.55	1.61	0.41	0.19	0.02
	ATP6V0D2	0.42	0.07	0.45	0.70	0.50	0.14	0.43	0.06	0.46	0.84	0.54	0.11
	ATP6V1C1	0.30	0.59	0.44	0.47	0.35	0.18	0.71	1.81	1.19	1.33	0.87	0.36
	ATP6V0D1	0.17	0.05	0.05	0.14	0.27	0.03	0.23	0.07	0.05	0.19	0.41	0.03
	ATP6V1A	0.31	-0.38	-0.46	-0.96	-0.76	0.00	0.74	0.99	1.32	3.88	2.73	0.00
	ATP6V1B2	-0.34	-0.51	-0.79	-0.51	-0.28	-0.43	0.41	0.71	1.34	0.72	0.33	0.56
	ATP6AP1	-0.50	0.11	-0.97	-0.46	0.39	-0.35	1.04	0.14	2.69	0.90	0.73	0.62
Autophagy (17)	NRBF2	-0.18	0.44	0.87	0.77	-0.23	0.31	0.25	0.82	2.18	1.85	0.34	0.51
	VPS18	0.13	0.24	0.69	0.39	0.05	-0.06	0.18	0.38	1.68	0.73	0.06	0.08
	VPS11	-0.06	-0.02	0.66	0.29	0.65	0.19	0.07	0.02	1.35	0.43	1.31	0.26
	MAP1LC3B	0.20	0.33	0.29	0.28	-0.04	-0.18	0.27	0.50	0.43	0.41	0.04	0.24
	SQSTM1	0.09	-0.86	0.17	-0.42	-0.40	-0.09	0.11	1.98	0.22	0.71	0.68	0.11
	HIF1A	0.81	0.35	-0.24	-0.38	0.31	0.34	2.32	0.68	0.43	0.79	0.60	0.67
	VPS35	-0.13	-0.13	-0.54	-0.51	-0.42	0.09	0.27	0.29	1.96	1.82	1.35	0.18
	VPS8	0.23	0.04	-1.17	-0.45	0.38	-0.09	0.20	0.03	1.81	0.48	0.38	0.07
Hydrolases and accessory proteins (23)	SGSH	-0.20	-0.02	1.13	0.69	0.65	-0.19	0.28	0.02	2.99	1.46	1.34	0.27
	GUSB	-0.03	0.22	0.54	0.30	0.41	-0.10	0.04	0.44	1.49	0.64	1.00	0.18
	GLA	0.18	0.15	0.45	0.11	0.06	-0.12	0.35	0.28	1.18	0.20	0.10	0.21
	HEXA	-0.50	0.24	-0.10	0.00	0.22	-0.46	0.90	0.35	0.13	0.00	0.31	0.80
	GALNS	-0.36	0.10	-0.77	-0.22	-0.11	-0.72	0.28	0.07	0.76	0.16	0.08	0.70
	NAGLU	-0.27	-0.60	-1.13	-0.75	0.31	-0.18	0.32	0.91	2.32	1.26	0.37	0.19
	ASAH1	-0.29	-0.54	-1.34	-1.24	0.51	-0.26	0.41	0.94	3.56	3.18	0.88	0.36
Lysosomal membrane (9)	CTNS	-0.56	0.59	0.99	0.61	0.81	0.22	0.51	0.55	1.13	0.57	0.84	0.17
	CLCN7	0.10	0.14	0.92	0.24	0.27	-0.39	0.08	0.12	1.23	0.21	0.24	0.38
	LAMP1	0.59	1.15	0.77	0.91	0.93	0.49	1.94	5.06	2.87	3.66	3.76	1.47
	MCOLN1	0.43	0.52	0.50	0.44	1.30	-0.36	0.39	0.49	0.47	0.40	1.78	0.31
	CLN3	-0.40	-0.08	0.30	-0.05	-0.26	-0.71	0.35	0.06	0.25	0.04	0.21	0.76
	CD63	-0.27	-0.04	-0.20	-0.23	0.17	-0.24	0.50	0.05	0.34	0.41	0.27	0.44
Lysosomal biogenesis (10)	NAGPA	0.06	0.71	1.11	0.92	0.50	-0.23	0.07	1.63	3.13	2.37	0.98	0.35
	GNPTG	-0.08	0.31	0.98	0.85	0.64	-0.22	0.13	0.70	3.68	2.99	1.98	0.44
	HPS1	-0.28	-0.03	0.60	0.17	-0.33	-0.51	0.21	0.02	0.54	0.12	0.26	0.44
	M6PR	-0.22	-0.41	-0.51	-0.86	-0.61	-0.42	0.23	0.50	0.66	1.38	0.85	0.52
	HPS3	0.08	-0.22	-0.67	-1.76	0.04	-0.04	0.08	0.24	1.05	4.32	0.04	0.04
	IGF2R	0.19	-0.34	-1.19	-0.79	0.94	-0.07	0.17	0.33	1.89	1.05	1.36	0.06

Figure 50: The IL-1α-NF-κB axis does not affect the CLEAR network of lysosomal genes.
The CLEAR gene network of 73 lysosomal genes as described by Palmieri et al. [82] (plus *MAP1LC3B* according to Pan et al. [169]) was intersected with the transcriptome data of the siRNA knockdown samples. The table summarizes data for five categories of CLEAR genes according to their specific lysosomal functions. The heatmap displays the 3 top up- or downregulated genes that were affected by the knockdown of TFEB plus six CLEAR genes analyzed in the previous section by RT-qPCR (highlighted in green). The effects of the knockdown of p65/RELA and its interactors and 1 h IL-1α treatment were calculated relative to the untreated siLuci control. Mean $\log_2$ ratios and significances of changes were defined by moderated t-statistics [155]. The genes of each group are sorted in descending order according to their dependence on their putative "master" regulator TFEB. (See Figure 46 legend for contributions.)

4.6.3 TFE3, TFEB, and GLIS2 predominantly act as coactivators for the regulation of IL-1α response genes

In the following, it was examined whether the p65/RELA interactors affected the IL-1α-NF-κB response. IL-1α induced the expression of a total number of 617 genes of which a third (168) was under control of p65/RELA (based on a significant twofold up- or downregulation in cells treated with siRNA against targeting RELA). A similar proportion of IL-1α-induced genes was influenced by the individual knockdown of the interactors. About one-half of the 168 IL-1α-induced NF-κB p65 target genes were exclusively regulated by p65/RELA, whereas the other half was coregulated by GLIS2 (83) or TFE3/TFEB (51) as denoted in red in Figure 51A.

The distribution of expression values of the IL-1α response genes showed an increase of the median after cytokine stimulation in line with their overall upregulation (Figure 51B). In contrast, all knockdowns (including p65/RELA) caused a drop in the median expression values of their respective target gene sets, indicating that all four factors largely contribute to induction of gene expression (Figure 51B). This suggested that the interactors function mainly as (co)activators of IL-1α response genes (Figure 51B).

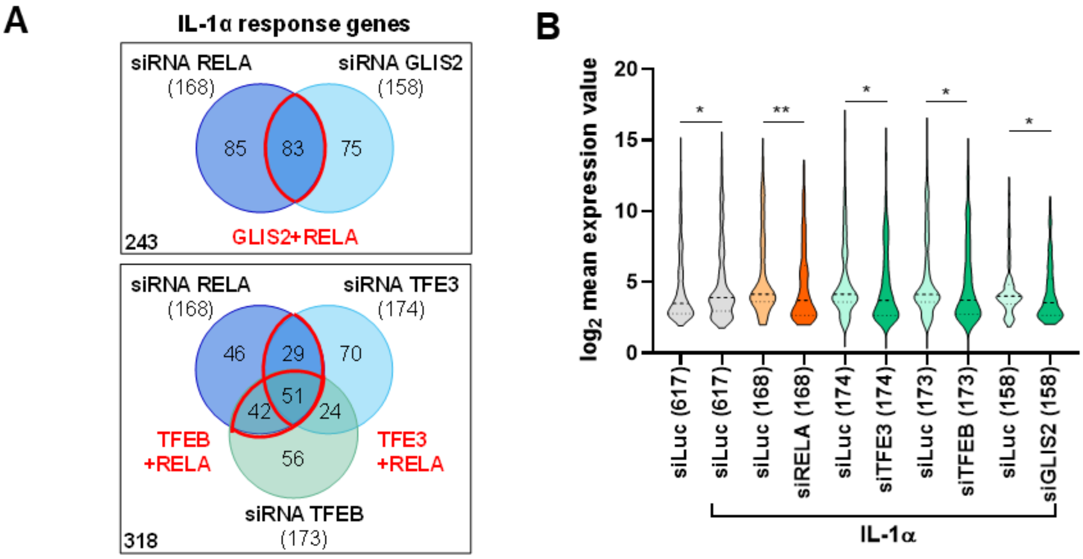

Figure 51: Coactivating roles of p65/RELA, TFE3, TFEB, and GLIS2 in the expression of IL-1α response genes.
(A) Venn diagrams demonstrating the overlap of all DEGs among 617 IL-1α response genes that were affected at least twofold and significantly by siRNA knockdowns. IL-1α response genes were defined by an LFC ≥ 1 with a $-\log_{10}$ p value ≥ 1.3 of the IL-1α-treated siLuci sample relative to the untreated siLuci samples (two independent biological replicates). Groups of genes coregulated by p65/RELA and one of its interactors are marked in red. (B) Violin plots showing the distributions, medians, and interquartile ranges of the normalized expression levels of the IL-1α-induced target gene subsets as defined in (A). The number of genes is specified in parentheses. Asterisks show significant changes as determined by a two-tailed Mann-Whitney test (*$p \leq 0.05$, **$p \leq 0.01$). (See Figure 46 legend for contributions.)

The 83 and 51 IL-1α response genes that were found to be coregulated by GLIS2/RELA or TFE3/TFEB/RELA, respectively, were further examined for their repression and activation patterns at the levels of individual genes. For the TFE3- and TFEB-regulated gene sets, the number of genes was reduced from 51 to 44 when the double TFE3/TFEB knockdown samples were additionally considered. Figure 52 shows the IL-1α-mediated induction, which revealed that 75% of these genes were uniformly and consistently downregulated by all knockdowns, including four genes that were previously identified and validated by RT-qPCR. The remaining 25% of all genes were upregulated by the suppression of lysosomal transcription factors or RELA. The data clearly showed that each knockdown perturbed gene expression into the same direction. This means that if a gene was repressed by p65/RELA knockdown, its expression was also reduced by the knockdown of TFE3/TFEB, alone or in combination, and vice versa (Figure 52).

Combined pathway overrepresentation analysis and STRING interaction analysis of the 44 coregulated IL-1α response genes that were under control of TFE3/TFEB and p65/RELA showed that around half of the encoded proteins map to cytokine pathways or have a known functional interaction to p65/RELA, whereas the other half was not connected to one another (Figure 53). TFE3/TFEB showed a strong PPI according to the literature [78]. Interestingly, the only protein that was functionally connected to both lysosomal transcription factors was folliculin interacting protein 2 (FNIP2), a protein that is originally known to participate in energy- or nutrient-sensing through the mTOR pathway as it functions as GTPase activating protein (GAP) in complex with folliculin (FLCN) [172]. However, none of the other 43 target genes revealed a known interaction with TFE3 or TFEB (Figure 53).

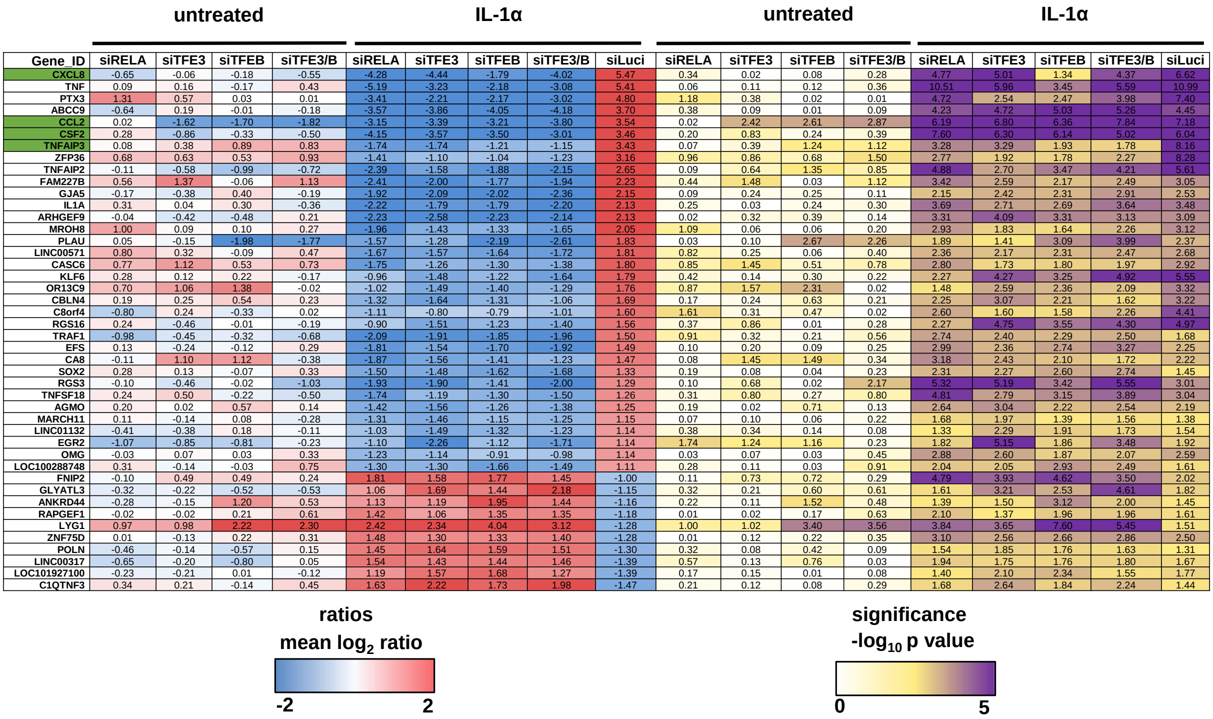

	untreated				IL-1α					untreated				IL-1α				
Gene_ID	siRELA	siTFE3	siTFEB	siTFE3/B	siRELA	siTFE3	siTFEB	siTFE3/B	siLuci	siRELA	siTFE3	siTFEB	siTFE3/B	siRELA	siTFE3	siTFEB	siTFE3/B	siLuci
CXCL8	-0.65	-0.06	-0.18	-0.55	-4.28	-4.44	-1.79	-4.02	5.47	0.34	0.02	0.08	0.28	4.77	5.01	1.34	4.37	6.62
TNF	0.09	0.16	-0.17	0.43	-5.19	-3.23	-2.18	-3.08	5.41	0.06	0.11	0.12	0.36	10.51	5.96	3.45	5.59	10.99
PTX3	1.31	0.57	0.03	0.01	-3.41	-2.21	-2.17	-3.02	4.80	1.18	0.38	0.02	0.01	4.72	2.54	2.47	3.98	7.40
ABCC9	-0.64	0.19	-0.01	-0.18	-3.57	-3.86	-4.05	-4.18	3.70	0.38	0.09	0.01	0.09	4.23	4.72	5.03	5.26	4.45
CCL2	0.02	-1.62	-1.70	-1.82	-3.15	-3.39	-3.21	-3.80	3.54	0.02	2.42	2.61	2.87	6.19	6.80	6.36	7.84	7.18
CSF2	0.28	-0.86	-0.33	-0.50	-4.15	-3.57	-3.50	-3.01	3.46	0.20	0.83	0.24	0.39	7.60	6.30	6.14	5.02	6.04
TNFAIP3	0.08	0.38	0.89	0.83	-1.74	-1.74	-1.21	-1.15	3.43	0.07	0.39	1.24	1.12	3.28	3.29	1.93	1.78	8.16
ZFP36	0.68	0.63	0.53	0.93	-1.41	-1.10	-1.04	-1.23	3.16	0.96	0.86	0.68	1.50	2.77	1.92	1.78	2.27	8.28
TNFAIP2	-0.11	-0.58	-0.99	-0.72	-2.39	-1.58	-1.88	-2.15	2.65	0.09	0.64	1.35	0.85	4.88	2.70	3.47	4.21	5.61
FAM227B	0.56	1.37	-0.06	1.13	-2.41	-2.00	-1.77	-1.94	2.23	0.44	1.48	0.03	1.12	3.42	2.59	2.17	2.49	3.05
GJA5	-0.17	-0.38	0.40	-0.19	-1.92	-2.09	-2.02	-2.36	2.15	0.09	0.24	0.25	0.11	2.15	2.42	2.31	2.91	2.53
IL1A	0.31	0.04	0.30	-0.36	-2.22	-1.79	-1.79	-2.20	2.13	0.25	0.03	0.24	0.30	3.69	2.71	2.69	3.64	3.48
ARHGEF9	-0.04	-0.42	-0.48	0.21	-2.23	-2.58	-2.23	-2.14	2.13	0.02	0.32	0.39	0.14	3.31	4.09	3.31	3.13	3.09
MROH8	1.00	0.09	0.10	0.27	-1.96	-1.43	-1.33	-1.65	2.05	1.09	0.06	0.06	0.20	2.93	1.83	1.64	2.26	3.12
PLAU	0.05	-0.15	-1.98	-1.77	-1.57	-1.28	-2.19	-2.61	1.83	0.03	0.10	2.67	2.26	1.89	1.41	3.09	3.99	2.37
LINC00571	0.80	0.32	-0.09	0.47	-1.67	-1.57	-1.64	-1.72	1.81	0.82	0.25	0.06	0.40	2.36	2.17	2.31	2.47	2.68
CASC6	0.77	1.12	0.53	0.73	-1.75	-1.26	-1.30	-1.38	1.80	0.85	1.45	0.51	0.78	2.80	1.73	1.80	1.97	2.92
KLF6	0.28	0.12	0.22	-0.17	-0.96	-1.48	-1.22	-1.64	1.79	0.42	0.14	0.30	0.22	2.27	4.27	3.25	4.92	5.55
OR13C9	0.70	1.06	1.38	-0.02	-1.02	-1.49	-1.40	-1.29	1.76	0.87	1.57	2.31	0.02	1.48	2.59	2.36	2.09	3.32
CBLN4	0.19	0.25	0.54	0.23	-1.32	-1.64	-1.31	-1.06	1.69	0.17	0.24	0.63	0.21	2.25	3.07	2.21	1.62	3.22
C8orf4	-0.80	0.24	-0.33	0.02	-1.11	-0.80	-0.79	-1.01	1.60	1.61	0.31	0.47	0.02	2.60	1.60	1.58	2.26	4.41
RGS16	0.24	-0.46	-0.01	-0.19	-0.90	-1.51	-1.23	-1.40	1.56	0.37	0.86	0.01	0.28	2.27	4.75	3.55	4.30	4.97
TRAF1	-0.98	-0.45	-0.32	-0.68	-2.09	-1.91	-1.85	-1.96	1.50	0.91	0.32	0.21	0.56	2.74	2.40	2.29	2.50	1.68
EFS	0.13	-0.24	-0.12	0.29	-1.81	-1.54	-1.70	-1.92	1.49	0.10	0.20	0.09	0.25	2.99	2.36	2.74	3.27	2.25
CA8	-0.11	1.10	1.12	-0.38	-1.87	-1.56	-1.41	-1.23	1.47	0.08	1.45	1.49	0.34	3.18	2.43	2.10	1.72	2.22
SOX2	0.28	0.13	-0.07	0.33	-1.50	-1.48	-1.62	-1.68	1.33	0.19	0.08	0.04	0.23	2.31	2.27	2.60	2.74	1.45
RGS3	-0.10	-0.46	-0.02	-1.03	-1.93	-1.90	-1.41	-2.00	1.29	0.10	0.68	0.02	2.17	5.32	5.19	3.42	5.55	3.01
TNFSF18	0.24	0.50	-0.22	-0.50	-1.74	-1.19	-1.30	-1.50	1.26	0.31	0.80	0.27	0.80	4.81	2.79	3.15	3.89	3.04
AGMO	0.20	0.02	0.57	0.14	-1.42	-1.56	-1.26	-1.38	1.25	0.19	0.02	0.71	0.13	2.64	3.04	2.22	2.54	2.19
MARCH11	0.11	-0.14	0.08	-0.28	-1.31	-1.46	-1.15	-1.25	1.15	0.07	0.10	0.06	0.22	1.68	1.97	1.39	1.56	1.38
LINC01132	-0.41	-0.38	0.18	-0.11	-1.03	-1.49	-1.32	-1.23	1.14	0.38	0.34	0.14	0.08	1.33	2.29	1.91	1.73	1.54
EGR2	-1.07	-0.85	-0.81	-0.23	-1.10	-2.26	-1.12	-1.71	1.14	1.74	1.24	1.16	0.23	1.82	5.15	1.86	3.48	1.92
OMG	-0.03	0.07	0.03	0.33	-1.23	-1.14	-0.91	-0.98	1.14	0.03	0.07	0.03	0.45	2.88	2.60	1.87	2.07	2.59
LOC100288748	0.31	-0.14	-0.03	0.75	-1.30	-1.30	-1.66	-1.49	1.11	0.28	0.11	0.03	0.91	2.04	2.05	2.93	2.49	1.61
FNIP2	-0.10	0.49	0.49	0.24	1.81	1.58	1.77	1.45	-1.00	0.11	0.73	0.72	0.29	4.79	3.93	4.62	3.50	2.02
GLYATL3	-0.32	-0.22	-0.52	-0.53	1.06	1.69	1.44	2.18	-1.15	0.32	0.21	0.60	0.61	1.61	3.21	2.53	4.61	1.82
ANKRD44	-0.28	-0.15	1.20	0.53	1.13	1.19	1.95	1.44	-1.16	0.22	0.11	1.52	0.48	1.39	1.50	3.12	2.00	1.45
RAPGEF1	-0.02	-0.02	0.21	0.61	1.42	1.06	1.35	1.35	-1.18	0.01	0.02	0.17	0.63	2.10	1.37	1.96	1.96	1.61
LYG1	0.97	0.98	2.22	2.30	2.42	2.34	4.04	3.12	-1.28	1.00	1.02	3.40	3.56	3.84	3.65	7.60	5.45	1.51
ZNF75D	0.01	-0.13	0.22	0.31	1.48	1.30	1.33	1.40	-1.28	0.01	0.12	0.22	0.35	3.10	2.56	2.66	2.86	2.50
POLN	-0.46	-0.14	-0.57	0.15	1.45	1.64	1.59	1.51	-1.30	0.32	0.08	0.42	0.09	1.54	1.85	1.76	1.63	1.31
LINC00317	-0.65	-0.20	-0.80	0.05	1.54	1.43	1.44	1.46	-1.39	0.57	0.13	0.76	0.03	1.94	1.75	1.76	1.80	1.67
LOC101927100	-0.23	-0.21	0.01	-0.12	1.19	1.57	1.68	1.27	-1.39	0.17	0.15	0.01	0.08	1.40	2.10	2.34	1.55	1.77
C1QTNF3	0.34	0.21	-0.14	0.45	1.63	2.22	1.73	1.98	-1.47	0.21	0.12	0.08	0.29	1.68	2.64	1.84	2.24	1.44

Figure 52: Identifcation of 44 IL-1α response genes that are strictly coregulated by TFE3/TFEB and p65/RELA.

The heatmap shows a list of 44 IL-1α response genes coregulated by TFE3/TFEB and p65/RELA that were affected at least twofold by every individual knockdown or by double knockdown of TFE3/TFEB. Shown are the transcriptome data of siRNA knockdown samples before or after stimulation with IL-1α for 1 h. The relative changes of gene expression in response to IL-1α were calculated based on the siLuci control samples before and after IL-1α treatment. Basal knockdown effects of p65/RELA, TFE3, TFEB, or double knockdown of TFE3/TFEB were calculated against the unstimulated siLuci control. Knockdown effects after treatment with IL-1α were calculated against the IL-1α-stimulated siLuci control. Ratios and significances were determined by moderated t-statistic [155]. Prototypical inflammatory genes that were analyzed by RT-qPCR in the previous section are highlighted in green. (See Figure 46 legend for contributions.)

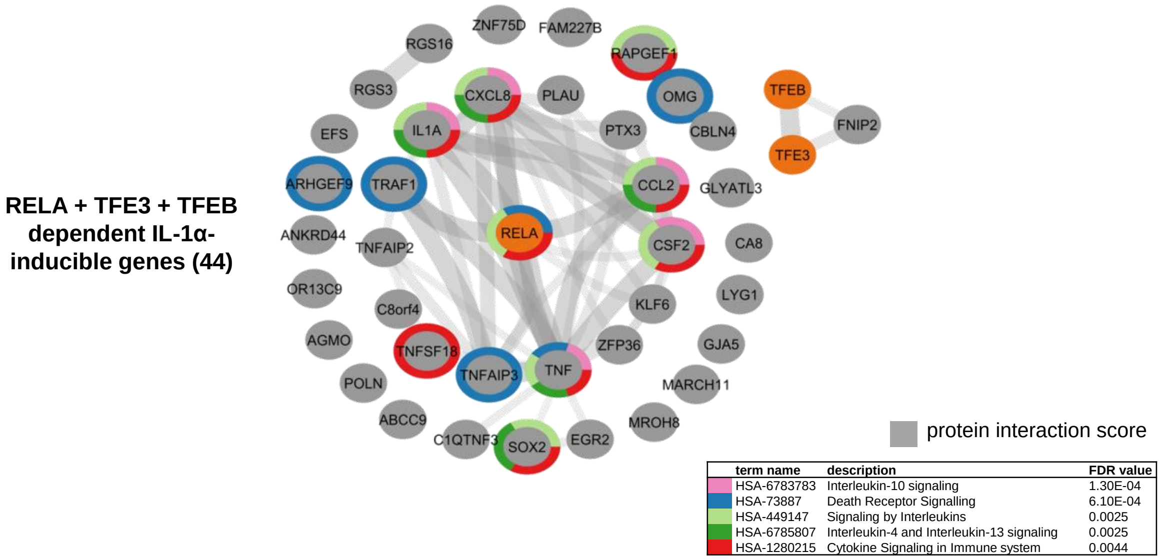

	term name	description	FDR value
🟪	HSA-6783783	Interleukin-10 signaling	1.30E-04
🟦	HSA-73887	Death Receptor Signalling	6.10E-04
🟩	HSA-449147	Signaling by Interleukins	0.0025
🟩	HSA-6785807	Interleukin-4 and Interleukin-13 signaling	0.0025
🟥	HSA-1280215	Cytokine Signaling in Immune system	0.0044

Figure 53: Half of the IL-1α response genes coregulated by TFE3/TFEB and p65/RELA map to cytokine-related pathways, while the other half has no known PPI.
Protein interaction network from 44 IL-1α response genes coregulated by TFE3/TFEB and p65/RELA. The map shows that about half of the proteins are functionally connected based on STRING entries. Grey edges mark known interactions deposited in the STRING database. The width and transparencey of edges correspond to the strength of experimental evidence for a physical or functional PPI as deposited in STRING. Node borders visualize the top five enriched pathway terms. (See Figure 46 legend for contributions.)

A similar observation was made for the 83 GLIS2/RELA coregulated IL-1α response genes, from which two-thirds were repressed by the knockdown of GLIS2 and RELA, whereas one-third were induced (Figure 54). The two genes most repressed by GLIS2 knockdown, *CSF2* and *CCL2*, whose repression was previously detected by RT-qPCR, were also found by microarray (Figure 54). Similar to TFE3/TFEB knockdowns, the majority of genes were deregulated by knockown of GLIS2 or RELA into the same direction, with exceptions of *ICAM1*, *CSF3*, and *CFB*, which were downregulated by the knockdown of RELA but upregulated by GLIS2 knockdown.

The interaction network of the 83 GLIS2/RELA-regulated IL-1α response genes showed that around 20% of the encoded proteins map to cytokine pathways and have a known functional connection to p65/RELA. The analysis also revealed that GLIS2 had a profound influence on a TNF-centered genetic subnetwork. On the other hand, more than 80% of the coregulated proteins were not connected to one another (Figure 55). The network analysis also showed that none of the proteins had any functional interactions with GLIS2. This raised the question by which molecular mechanisms TFE3, TFEB, and GLIS2 regulate the expression of these new genetic subnetworks in the IL-1α-NF-κB pathway.

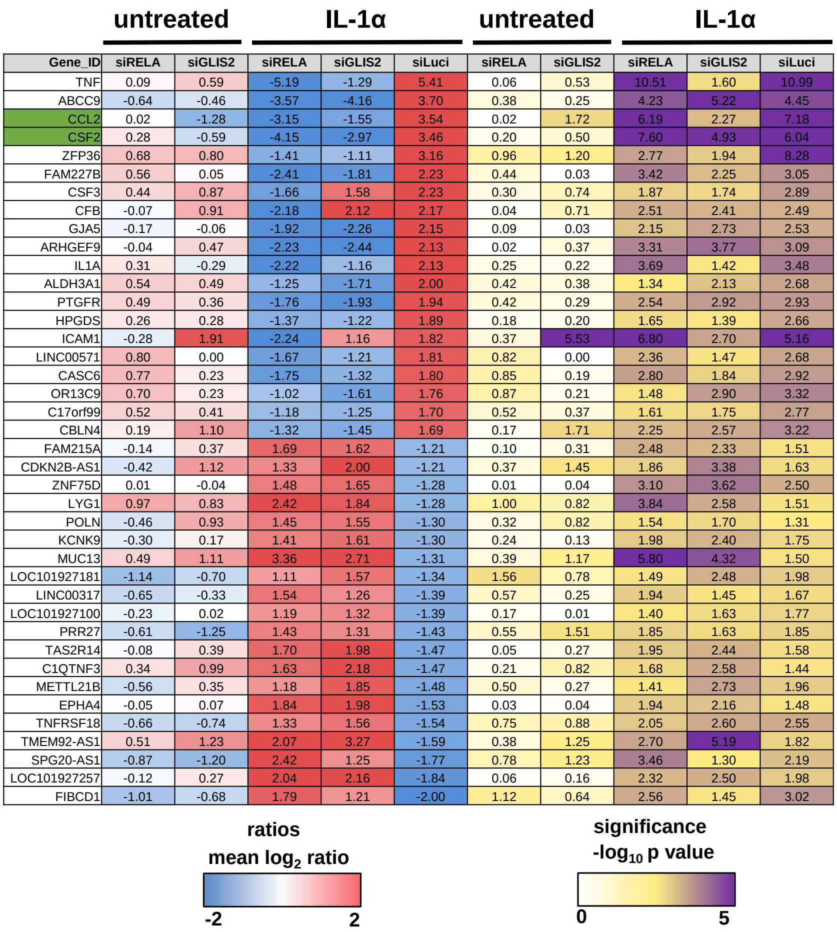

	untreated		IL-1α			untreated		IL-1α		
Gene_ID	siRELA	siGLIS2	siRELA	siGLIS2	siLuci	siRELA	siGLIS2	siRELA	siGLIS2	siLuci
TNF	0.09	0.59	-5.19	-1.29	5.41	0.06	0.53	10.51	1.60	10.99
ABCC9	-0.64	-0.46	-3.57	-4.16	3.70	0.38	0.25	4.23	5.22	4.45
🟩 CCL2	0.02	-1.28	-3.15	-1.55	3.54	0.02	1.72	6.19	2.27	7.18
🟩 CSF2	0.28	-0.59	-4.15	-2.97	3.46	0.20	0.50	7.60	4.93	6.04
ZFP36	0.68	0.80	-1.41	-1.11	3.16	0.96	1.20	2.77	1.94	8.28
FAM227B	0.56	0.05	-2.41	-1.81	2.23	0.44	0.03	3.42	2.25	3.05
CSF3	0.44	0.87	-1.66	1.58	2.23	0.30	0.74	1.87	1.74	2.89
CFB	-0.07	0.91	-2.18	2.12	2.17	0.04	0.71	2.51	2.41	2.49
GJA5	-0.17	-0.06	-1.92	-2.26	2.15	0.09	0.03	2.15	2.73	2.53
ARHGEF9	-0.04	0.47	-2.23	-2.44	2.13	0.02	0.37	3.31	3.77	3.09
IL1A	0.31	-0.29	-2.22	-1.16	2.13	0.25	0.22	3.69	1.42	3.48
ALDH3A1	0.54	0.49	-1.25	-1.71	2.00	0.42	0.38	1.34	2.13	2.68
PTGFR	0.49	0.36	-1.76	-1.93	1.94	0.42	0.29	2.54	2.92	2.93
HPGDS	0.26	0.28	-1.37	-1.22	1.89	0.18	0.20	1.65	1.39	2.66
ICAM1	-0.28	1.91	-2.24	1.16	1.82	0.37	5.53	6.80	2.70	5.16
LINC00571	0.80	0.00	-1.67	-1.21	1.81	0.82	0.00	2.36	1.47	2.68
CASC6	0.77	0.23	-1.75	-1.32	1.80	0.85	0.19	2.80	1.84	2.92
OR13C9	0.70	0.23	-1.02	-1.61	1.76	0.87	0.21	1.48	2.90	3.32
C17orf99	0.52	0.41	-1.18	-1.25	1.70	0.52	0.37	1.61	1.75	2.77
CBLN4	0.19	1.10	-1.32	-1.45	1.69	0.17	1.71	2.25	2.57	3.22
FAM215A	-0.14	0.37	1.69	1.62	-1.21	0.10	0.31	2.48	2.33	1.51
CDKN2B-AS1	-0.42	1.12	1.33	2.00	-1.21	0.37	1.45	1.86	3.38	1.63
ZNF75D	0.01	-0.04	1.48	1.65	-1.28	0.01	0.04	3.10	3.62	2.50
LYG1	0.97	0.83	2.42	1.84	-1.28	1.00	0.82	3.84	2.58	1.51
POLN	-0.46	0.93	1.45	1.55	-1.30	0.32	0.82	1.54	1.70	1.31
KCNK9	-0.30	0.17	1.41	1.61	-1.30	0.24	0.13	1.98	2.40	1.75
MUC13	0.49	1.11	3.36	2.71	-1.31	0.39	1.17	5.80	4.32	1.50
LOC101927181	-1.14	-0.70	1.11	1.57	-1.34	1.56	0.78	1.49	2.48	1.98
LINC00317	-0.65	-0.33	1.54	1.26	-1.39	0.57	0.25	1.94	1.45	1.67
LOC101927100	-0.23	0.02	1.19	1.32	-1.39	0.17	0.01	1.40	1.63	1.77
PRR27	-0.61	-1.25	1.43	1.31	-1.43	0.55	1.51	1.85	1.63	1.85
TAS2R14	-0.08	0.39	1.70	1.98	-1.47	0.05	0.27	1.95	2.44	1.58
C1QTNF3	0.34	0.99	1.63	2.18	-1.47	0.21	0.82	1.68	2.58	1.44
METTL21B	-0.56	0.35	1.18	1.85	-1.48	0.50	0.27	1.41	2.73	1.96
EPHA4	-0.05	0.07	1.84	1.98	-1.53	0.03	0.04	1.94	2.16	1.48
TNFRSF18	-0.66	-0.74	1.33	1.56	-1.54	0.75	0.88	2.05	2.60	2.55
TMEM92-AS1	0.51	1.23	2.07	3.27	-1.59	0.38	1.25	2.70	5.19	1.82
SPG20-AS1	-0.87	-1.20	2.42	1.25	-1.77	0.78	1.23	3.46	1.30	2.19
LOC101927257	-0.12	0.27	2.04	2.16	-1.84	0.06	0.16	2.32	2.50	1.98
FIBCD1	-1.01	-0.68	1.79	1.21	-2.00	1.12	0.64	2.56	1.45	3.02

Figure 54: Identificaton of 83 IL-1α response genes that are coregulated by GLIS2 and p65/RELA mostly into the same direction.
The heatmap shows a list of the 20 top and bottom genes from 83 IL-1α response genes coregulated by GLIS2 and p65/RELA that were affected at least twofold by the individual knockdown. Shown are the transcriptome data of siRNA knockdown samples before or after stimulation with IL-1α for 1 h. The relative changes of gene expression in response to IL-1α were calculated based on the siLuci control samples before and after IL-1α treatment. Basal knockdown effects of p65/RELA and GLIS2 were calculated against the unstimulated siLuci control. Knockdown effects after treatment with IL-1α were calculated against the IL-1α-stimulated siLuci control. Ratios and significances were determined by moderated t-statistic [155]. Prototypical inflammatory genes that were analyzed by RT-qPCR in the previous section are highlighted in green. (See Figure 46 legend for contributions.)

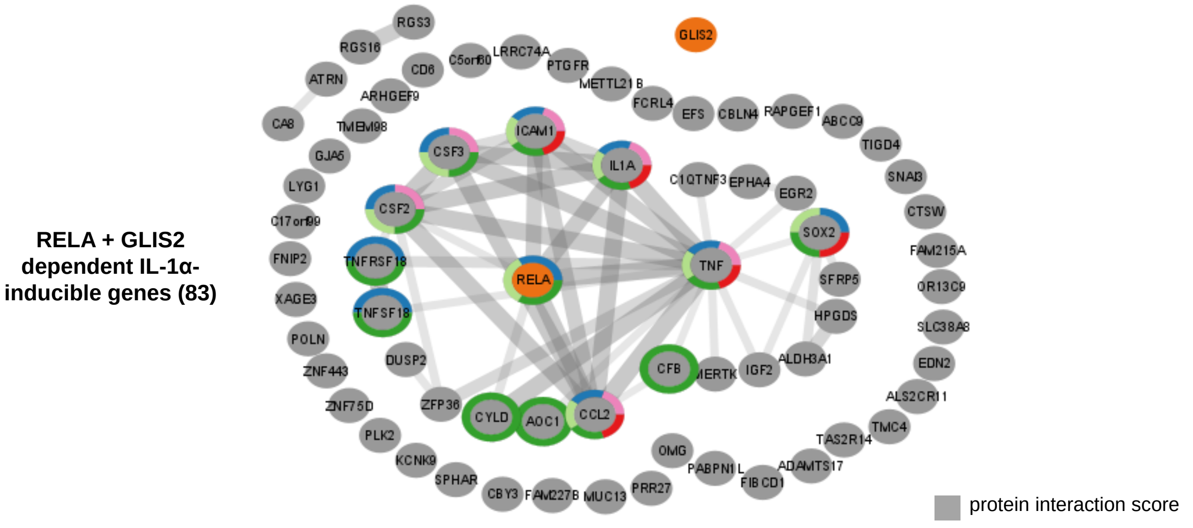

	term name	description	FDR value
🟪	HSA-6783783	Interleukin-10 signaling	6.48E-08
🟦	HSA-1280215	Cytokine Signaling in Immune system	3.80E-06
🟩	HSA-449147	Signaling by Interleukins	2.71E-05
🟩	HSA-168256	Immune System	4.80E-05
🟥	HSA-6785807	Interleukin-4 and Interleukin-13 signaling	9.45E-05

Figure 55: GLIS2 and p65/RELA coregulate genes of the innate immune response, including a TNF-centered genetic subnetwork.
Protein interaction network from 83 IL-1α response genes coregulated by GLIS2 and p65/RELA. The map shows that about a fourth of the proteins are functionally connected based on STRING entries. Grey edges mark known interactions deposited in the STRING database. The width and transparencey of edges correspond to the strength of experimental evidence for a physical or functional connection as deposited in STRING. Node borders visualize the top five enriched pathway terms. (See Figure 46 legend for contributions.)

Overall, the transcriptomic datasets demonstrate the importance of p65/RELA and its interactors for a broad spectrum of genes, with each transcription factor appearing to primarily regulate its own subsets of genes under homeostatic conditions. The data largely suggest that the IL-1α-NF-κB pathway has no role in the regulation of the CLEAR gene network. The lysosomal transcription factors TFE3/TFEB as well as GLIS2, on the other hand, act mostly as (co)activators of new genetic subnetworks relevant for inflammatory cell reactions that are predefined by p65/RELA.

4.7 Genome-wide motif analysis based on p65/RELA ChIP-seq data

4.7.1 Genomic regions defined by p65/RELA ChIP-seq peaks are significantly enriched for TFE3 and GLIS2 binding motifs

To investigate the interaction of p65/RELA and its new interactors also at the chromatin level, motif analysis was performed based on genome-wide p65 ChIP-seq data published by our group [48]. These data were obtained in KB cells, a subclone of HeLa that is highly comparable to the original HeLa cells [49]. Genomic regions of p65 ChIP-seq peaks and their ±500 base pair surrounding were examined for underlying significantly enriched DNA motifs and assigned to their next proximal genes (Figure 56A). The motifs of TFE3, TFEB, GLIS2, and RELA were extracted from the JASPAR database (https://jaspar.genereg.net/) or from the HOmo sapiens COmprehensive MOdel COllection (HOCOMOCO) database (https://hocomoco10.autosome.org/). The overlap analysis distinguished between p65 ChIP-seq peaks with only one motif and those with adjacent motifs of RELA and the RELA interactor as indicated by the scheme in Figure 56B.

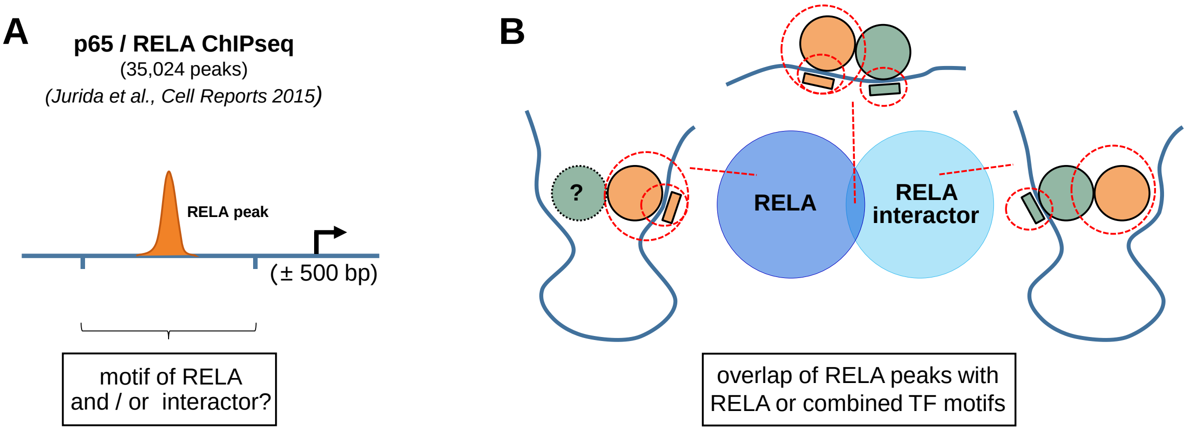

Figure 56: Genome-wide ChIP-seq and motif analysis to identify potential target regions of p65/RELA and its interactors.
Schematic illustrating the strategy of combined p65 ChIP-seq and motif analysis. (A) The p65 ChIP-seq peaks ±500 base pairs upstream/downstream were searched for underlying DNA motifs of RELA or the interactors and documented according to their proximity to genes. Motifs were obtained from the JASPAR database (https://jaspar.genereg.net/) or from the HOCOMOCO database (https://hocomoco10.autosome.org/) and ChIP-seq data were from our group [48]. (B) Venn diagrams show the overlap between regions of p65 ChIP-seq peaks with only one motif and those with adjacent motifs from RELA and the RELA interactor. The diagram also shows the three possible scenarios of interaction between p65/RELA (orange) and the interactor (green) mediated by long-range DNA interaction based on chromatin looping or mutual indirect recruitment of the factors. RELA motifs are denoted in orange, interactor motifs in green, and DNA strands in blue.

The genome-wide ChIP-seq and motif analysis was performed by Dr. Marek Bartkuhn (Biomedical Informatics and Systems Medicine, Science Unit, Justus Liebig University) who provided a spreadsheet table with gene annotations and genomic coordinates to p65 ChIP-seq peak regions and specific motifs, as well as statistical parameters. The subsequent filtering steps were carried out and visualized by Prof. M. Kracht (Figure 57) and Lisa Leib (Figure 58). Lisa Leib adapted the schematic representation of the strategy of the combined genome-wide analysis (Figure 56), which was created by Prof. M. Kracht.

The genome-wide analysis of 35,024 p65 ChIP-seq peaks showed that DNA motifs of TFE3 and GLIS2 were significantly enriched, whereas TFEB motifs were not overrandomly enriched. As to be expected, the analysis also revealed that only a third of all p65/RELA ChIP-seq peaks contained a canonical RELA motif that was recognized by the software. Venn diagrams with the overlap of regions assigned to p65 ChIP-seq peaks containing a RELA motif or a RELA interactor motif showed numerous regions with only one of the two motifs present under p65/RELA peaks. In contrast, composite elements with both motifs and a p65/RELA peak were less frequent. For TFE3, a total of 2521 such genomic regions were identified and 4426 such regions were found for GLIS2 (Figure 57). Identification of these genomic regions provided further supportive evidence for a possible interaction of p65/RELA with its new interactors at chromatin. Since not every p65/RELA peak also contained a motif, the chromatin recruitment could be mediated by long-range DNA interaction based on chromatin looping or by mutual recruitment of the factors as schematically outlined by the three possible scenarios in Figure 56B.

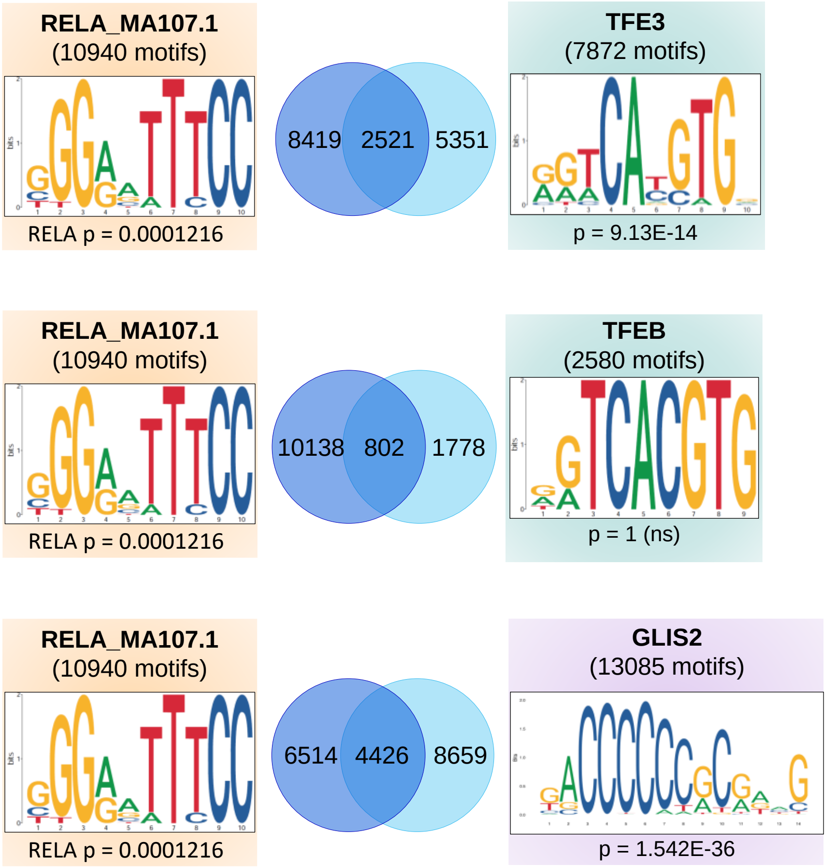

Figure 57: Significant TFE3 and GLIS2 motif enrichment within p65/RELA ChIP-seq peaks.
Venn diagrams display the overlap of chromosomal regions assigned to p65 ChIP-seq peaks containing a RELA motif or a motif for the indicated RELA interactors. Transcription factor binding profiles were obtained from the JASPAR (https://jaspar.genereg.net/) or HOCOMOCO (https://hocomoco10.autosome.org/) databases. The total number of regions identified for each factor is specified in parentheses. P values indicate significant enrichment compared to the frequencies of motifs within the whole genome. (See Figure 56 legend for contributions.)

4.7.2 Novel inflammatory enhancers downstream of the *CSF2* gene locus are likely platform for the corecruitment of p65/RELA and TFE3

To further follow examples of inflammatory loci for direct interaction studies at the chromatin, the analysis focused on the 168 IL-1α-RELA-regulated genes that were identified by microarrays. From this group, all genes that contained adjacent RELA and RELA interactor motifs within p65 ChIP-seq peaks were extracted. For TFE3 and GLIS2, 33 or 44 such genes were identified, respectively, whereas for TFEB, only 11 genes were found (Figure 58). These IL-1α-NF-κB response genes were considered direct targets of p65/RELA and its new interactors. *CSF2*, a gene encoding a cytokine known to primarily control the production and differentiation of granulocyte and macrophage progenitor cells in the bone marrow, was the top-induced gene by IL-1α and its expression was most strongly diminished by knockdowns of RELA and its three interactors (Figure 59A).

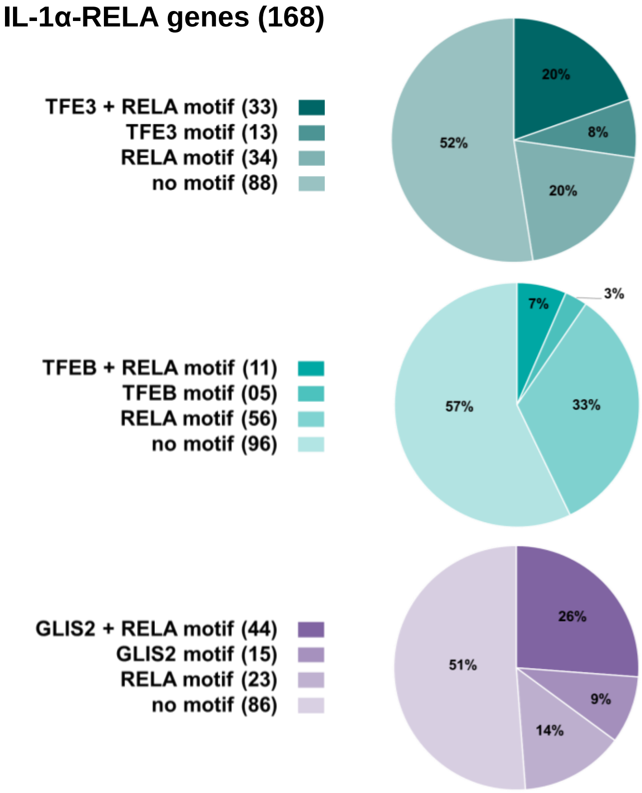

Figure 58: IL-1α-NF-κB response genes that are likely direct targets of p65/RELA and its interactors. Pie charts showing the percentages of IL-1α- and NF-κB-regulated genes assigned to p65 ChIP-seq peaks containing a RELA motif, a motif for the indicated RELA interactors, adjacent RELA and interactor motifs, or no motif. The analysis is based on 168 IL-1α-RELA-regulated genes identified by microarray. The total number of genes identified for each scenario is specified in parentheses. (See Figure 56 legend for contributions.)

Further interesting aspects to this gene emerged from overexpression data in HeLa cells transfected with GFP constructs of p65, TFE3, TFEB, or a constitutive nuclear mutant of TFEB (Δ30TFEB, [88]). The data showed that all fusion proteins were capable to activate the expression of *CSF2* (Figure 59B). While under basal conditions *CSF2* was not or barely expressed, p65/RELA overexpression caused a several thousand-fold induction of its mRNA level. TFE3 and TFEB in comparison also induced the expression of the gene, but the induction was much weaker. It was also interesting that, compared with the wild type, the constitutive nuclear mutant of TFEB (Δ30TFEB) slightly enhanced the activation of *CSF2* expression (Figure 59B). Considering the relatively low expression of TFEB constructs as observed with the GFP antibody (Figure 59C), it can be assumed that the actual magnitude of this induction might be even stronger. This result emphasized the dominant role of p65/RELA in the expression of *CSF2* and indicated that its transcriptional control is enhanced by a supportive function of TFE3/TFEB, which is most likely manifested in the nucleus.

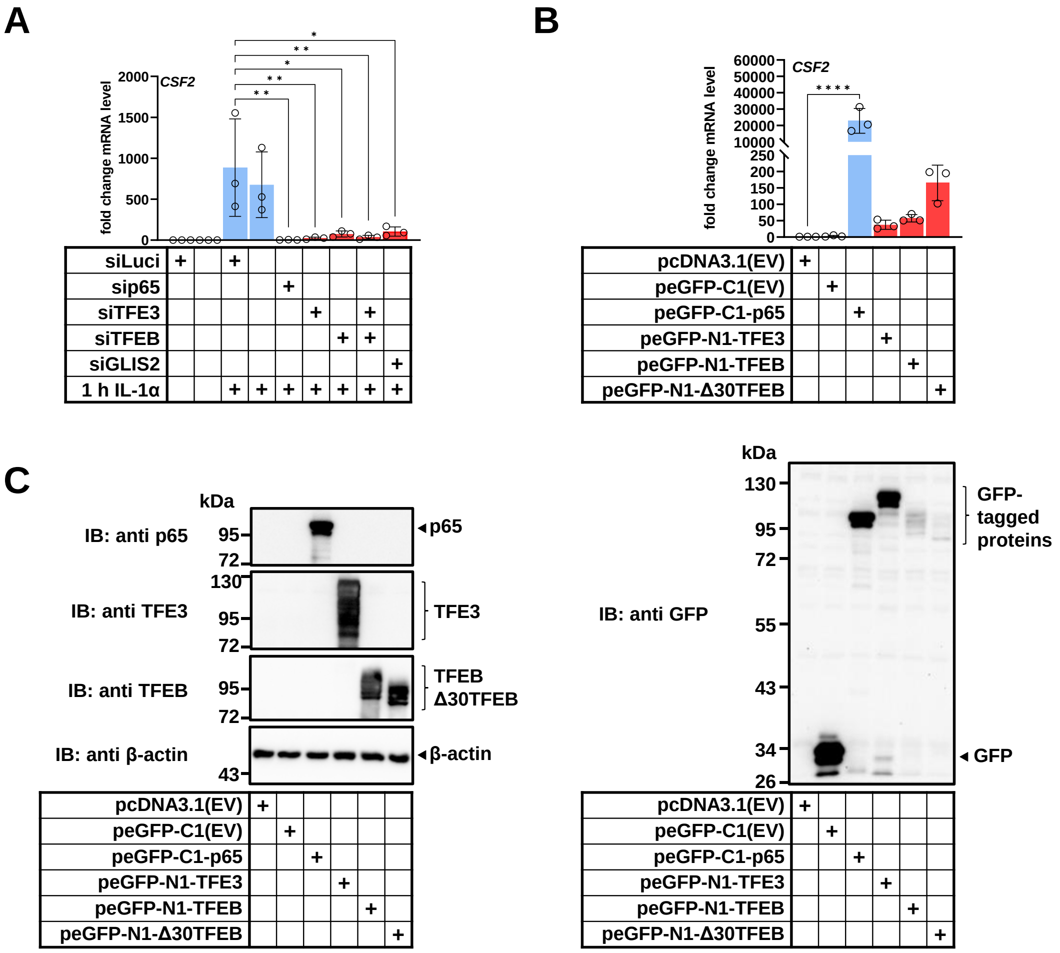

siLuci	+		+						
sip65					+				
siTFE3						+		+	
siTFEB							+	+	
siGLIS2									+
1 h IL-1α			+	+	+	+	+	+	+

pcDNA3.1(EV)	+					
peGFP-C1(EV)		+				
peGFP-C1-p65			+			
peGFP-N1-TFE3				+		
peGFP-N1-TFEB					+	
peGFP-N1-Δ30TFEB						+

pcDNA3.1(EV)	+					
peGFP-C1(EV)		+				
peGFP-C1-p65			+			
peGFP-N1-TFE3				+		
peGFP-N1-TFEB					+	
peGFP-N1-Δ30TFEB						+

pcDNA3.1(EV)	+					
peGFP-C1(EV)		+				
peGFP-C1-p65			+			
peGFP-N1-TFE3				+		
peGFP-N1-TFEB					+	
peGFP-N1-Δ30TFEB						+

Figure 59: Ectopically expressed GFP fusion proteins of p65, TFE3, and TFEB activate *CSF2* gene expression.
The data in (A) were previously shown in Figure 43. The bar graph shows relative *CSF2* mRNA levels after the RNAi-mediated knockdown of p65/RELA, TFE3, TFEB, both TFE3/TFEB (double knockdown, DK), or GLIS2 in HeLa cells treated with IL-1α (10 ng/ml) for 1 h as determined by RT-qPCR. Relative mRNA levels were calculated against the untreated siLuci control. The statistical significance was calculated against the 1 h IL-1α-treated siLuci control. (B) RT-qPCR analysis of *CSF2* gene expression in HeLa cells which were transiently transfected with GFP-tagged p65, TFE3, TFEB, or a constitutive nuclear mutant of TFEB (Δ30TFEB), GFP alone, and empty vector. The mRNA levels were calculated relative to the empty vector control and are displayed by a bar graph. (C) Western blot analysis of the set of samples in (B) shows exemplarily the expression levels of the fusion proteins using the indicated antibodies. The β-actin levels were assessed to control equal loading of gels. Shown is the result of one preparative experiment. Bar graphs in (A & B) display means of three independent biological replicates ± SD. Asterisks indicate significant changes (*p < 0.05, **p < 0.01, ***p < 0.001, ****p < 0.0001) obtained by one-way ANOVA.

In addition to the insights gained from *CSF2* gene expression data, visual exploration of its genomic locus enabled the identification of two novel IL-1α-driven enhancer regions downstream of the gene (Figure 60). These regions were characterized by strong IL-1α-inducible p65/RELA occupancy and increased chromatin accessibility in response to IL-1α paralleled by increased epigenetic modifications typical for active enhancers, namely histone 3 monomethylation at lysine residue 4 (H3K4me1) and acetylation of lysine residue 27 (H3K27ac). Strikingly, the IL-1α-driven enhancers also harbored adjacent RELA and TFE3 motifs within the 1000-bp window of the examined p65 ChIP-seq peak. Thus, the data suggest a corecruitment of TFE3 and p65/RELA to these novel inflammatory enhancer regions at the *CSF2* locus, which most likely mediates the upstream transcriptional control at the *CSF2* promoter by long-range DNA interactions.

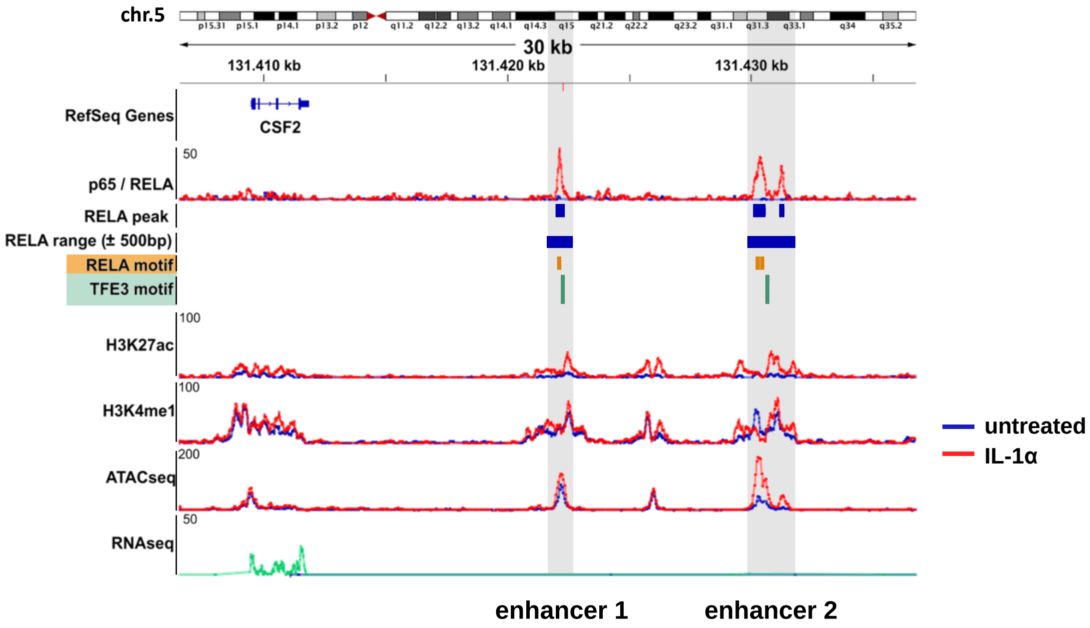

Figure 60: Genomic exploration suggests corecruitment of TFE3 and p65/RELA to novel inflammatory enhancer regions found downstream of the *CSF2* gene.
IGV genome browser view of the genomic locus of the *CSF2* gene on chromosome 5 with data from ChIP-seq, ATAC-seq and RNA-seq experiments from KB cells that were left unstimulated or were stimulated with IL-1α for 1 h [48, 49]. Shown are two active enhancer regions downstream of the *CSF2* gene (highlighted in grey), which are characterized by high levels of H3K4me1 and IL-1α-inducible increases in p65 recruitment, H3K27ac, chromatin accessibility and mRNA expression. The regions encompassing p65 ChIP-seq peaks and the underlying 1000-bp windows used for bioinformatic analyses of motifs are indicated by blue boxes, individual RELA and TFE3 motifs are shown by orange or green boxes, respectively. (The graphic was created by Prof. M. Kracht.)

Taken together, these data provide additional evidence for a supporting role of TFE3/TFEB in the NF-κB p65-dominated control of *CSF2* gene expression in the nucleus. They further reveal novel enhancers in the vicinity of this gene with features that highly qualify the locus for future in-depth mechanistic studies of the interplay between p65 and its new interactors at the chromatin level.

5 Discussion

In this thesis, two unbiased methods, CAPTURE and MiniTurboID, were used to explore the inflammatory protein interactome in the context of chromatin. Subsequent studies focused on the functional relevance of the newly identified interactors in the inflammatory, cytokine-driven cellular response. The research findings as well as challenges and limitations of both approaches are discussed below.

5.1 Challenges and limitations of the isolation of locus-specific protein complexes

Experiments with cells transiently or stably expressing CAPTURE components demonstrated the functionality of the CAPTURE system in HeLa cells when a single promoter or multiple inflammatory promoters were targeted simultaneously, however purifying the specific interactome at a given promoter remained challenging. In general, the study of proteins at a specific chromatin locus involves considerable technical challenges that are difficult to overcome, which is reflected in the small number of publications on this topic [134, 173]. EnChIP, an alternative variant using classical dCas9-IP instead of biotinylation, has proven successful in various cell systems such as human embryonic kidney (HEK) cells [174], myoblasts [175] or neuroblastoma cells [176]. However, the application of enChIP-MS requires a considerable amount of starting cell material, usually 2-3 × 10^8 cells per condition, which is an enormous hurdle [174]. The continued exploration of alternative variants such as CAPTURE for single loci purification highlights the ongoing need for improved systems with increased pulldown efficiency [134]. Nevertheless, since the publication of CAPTURE by Liu et al. in 2017, there have only been three other publications reporting the successful use of CAPTURE-Proteomics [177–179]. In these studies, the CAPTURE technology was used to identify novel regulatory factors at enhancers, promoters, or other upstream regions of genes critical for muscle cell differentiation [177], pre-mRNA processing [178], or maintenance of cellular pluripotency [179]. CAPTURE was applied to myoblasts [177], HEK cells [178], or mouse embryonic stem cells (mESC) [179]. In all studies several novel transcriptional regulators were found. For many of these factors, binding to the targeted chromatin region was confirmed by ChIP experiments [177–179]. Knockdown experiments provided additional insight into the functional significance of the identified factors for muscle cell differentiation [177], U2 snRNA gene expression [178], or the maintenance of mESCs [179]. The enriched factors included proteins of the classical transcription machinery such as Pol II or Mediator components [178] as well as numerous RNA-binding proteins, including RNA processing, splicing, and polyadenylation factors [178, 179]. Of note, in two of these studies, none of the well-characterized transcription factors known to be associated with U2 snRNA genes [178] or pluripotency genes [179] were enriched, whereas in the other study, known factors were not mentioned [177].

In this work, the total amount of p65 and Pol II molecules bound to the dCas9-targeted inflammatory promoters and potentially extractable from cell cultures was increased by using HeLa cells instead of a diploid cell system as they possess up to six copies of a specific gene [180], theoretically allowing larger amounts of locus-specific proteins to be isolated. Additional benefits of HeLa cells include their ease of genetic manipulation [49] and their high sensitivity to IL-1α [48, 49, 167]. One factor that contributed to the nonetheless lack of p65 and Pol II enrichment in the CAPTURE experiments using HeLa may have been that a portion of the cells remains unresponsive to IL-1α [167], so that a substantial number of p65 molecules or components of the transcriptional machinery did not inducibly bind to the targeted inflammatory promoters. This biological aspect is accompanied by several technical limitations associated with the method [134].

The highest pulldown efficiency was achieved by using second-generation stable CAPTURE cells. Maximizing pulldown efficiency by exploiting all technical advances is critical. However, regardless of the method, it is difficult to purify locus-specific transcription factors [134, 173]. This is because standard MS requires at least 600 million molecules for the detection of peptides from complex peptide mixtures [181], which corresponds to approximately 5×10^8 cells required for proteomic identification of a single protein bound at least once to a locus of interest, assuming a purification yield of 100% [134]. Culturing cells at this scale is time consuming and costly, and likely a common reason why protein interactome studies remain unsuccessful after purification of a single locus [134].

Despite extensive testing of various experimental conditions, the use of CAPTURE for protein identification did not result in significant enrichment of locus-specific interactors beyond background noise. The signal-to-noise ratio is defined by the fold enrichment over the non-targeting control [134]. The fold enrichment can be improved experimentally by formaldehyde crosslinking, stringency of washing steps, exclusion of dCas9-sgRNA off-target binding, and finally by ensuring that the target locus is accessible and that there is no competition between binding of dCas9-sgRNA complexes and endogenous locus-binding proteins [134]. Many of these factors were carefully considered in the design and execution of the CAPTURE experiments in this work (see sections 3.3.1 and 4.1) and yet did not result in the enrichment of the expected binding proteins such as p65, Pol II, or H3.

Simultaneous targeting of 10 promoters increased the size of the genomic region targeted by dCas9 but did not result in specific enrichment of the inflammatory transcription factor p65 above background noise. A smaller target sequence, e.g., a single promoter, requires more starting material than a larger target sequence with multiple repetitive elements, e.g., telomeres, because the relative contribution of a single promoter to the genome is much smaller than for telomeres [134]. This, in turn, means that the unaccounted genomic region that may contribute to background noise is much larger for a single promoter than for telomeres [134]. Therefore, one way to proceed with the experiments is to establish principal pulldown conditions by targeting telomeric regions first [138], and then perform the experiments on inflammatory loci using the same strategy. In addition, the scope of inflammatory chromatin targets could be further increased by targeting all 168 genes that were responsive to IL-1α-

NF-κB. This could be done following the example given by Liu et al. who previously generated a sgRNA vector library for a similar purpose [159].

Targeting of inflammatory promoters by dCas9 had no effect on transcription, indicating that all necessary transcriptional complexes remained functional, which, in turn, suggests that p65 and Pol II were bound to the regulatory regions of the targeted genes along with their other cofactors. The binding specificity of a protein to its target site is of high importance and determines whether lower levels of purity can be tolerated in CAPTURE pulldown samples [134]. While p65 binds selectively to κB-motifs [182] and inducibly occupies the inflammatory promoters targeted by dCas9 with high abundance, the binding specificities of H3 and Pol II are much lower, as both proteins bind to numerous other genomic regions as well [48]. Since p65 also binds to gene promoters other than the 10 targeted promoters [48] and can potentially be recruited piggy-back to genomic sites without κB-element, all three proteins can copurify non-specifically in control samples as observed in this work. Mass spectrometric evaluation of such pulldown samples can be useful and theoretically lead to the discovery of a new factor if that factor binds exclusively and in large amounts to the promoters of the targeted inflammatory genes and is not present in control samples [134]. However, mass spectrometric data in which expected binders such as p65, Pol II, and H3 are copurified in control samples are difficult to evaluate bioinformatically. Hence, the biological relevance of such a novel factor needs to be comprehensively validated by other methods [173]. One possible approach is to intersect such a dataset with proteomic data generated under comparable experimental conditions but using different methods, e.g., data from isolated transcription factories [183] or BioID experiments [146]. The intersection of these data can provide insight into the extent to which the components of active RNA polymerase complexes [183] or common interactors of other human transcription factors [146] are involved in transcriptional regulation at the inflammatory target promoters.

The above discussed technical and bioinformatic challenges make it difficult to distinguish between locus-specific proteins and impurities. Nonetheless, it is important to continue this work as it may represent an important advance in understanding the composition and molecular function of a single inflammatory chromatin locus [134]. In addition, the first- and second-generation stable CAPTURE cell systems established in this work can be used for Hi-C [184, 185] or 3C-seq studies [138, 147] to decipher (genome-wide) chromatin interactions at inflammatory promoters or enhancers. Both methods require an initial amplification step, which has the advantage of generating larger amounts of material, facilitating the final step of detection. Liu et al. developed a publicly available C3S pipeline for bioinformatic analysis of these studies [186]. Also, combining CAPTURE with RNA isolation protocols [187] can enable RNA-seq studies to identify known and novel noncoding locus-associated RNAs associated with the regulation of immune gene transcription [50].

5.2 New dimensions of the NF-κB interactome revealed by proximity labeling

The size and composition of the NF-κB p65 interactome

Until the early 2000s, a "pathway-centric" view of the NF-κB system dominated the field. In this context, our research group created a database-driven graphical representation of the IL-1 pathway that included many extensively experimentally validated upstream and downstream NF-κB pathway components and their connections [28]. In recent years, this "pathway-centric" view of the NF-κB system has shifted to a more dynamic NF-κB pathway interactome [188]. Tieri et al. reconstructed the NF-κB pathway interactome based on PPI data from various databases or manually collected data from the literature containing experimental evidence on physical interactions with all five NF-κB members. The resulting NF-κB transcription factor interactome comprised 622 proteins and 6,115 PPIs [188]. However, this computer-curated reconstruction revealed little about individual NF-κB subunits. In addition, there is limited information from large scale proteomic studies of individual subunits. Bouwmeester et al. used an integrated TAP-MS approach and identified 92 p65/RELA and 62 p50/NFKB1 interactors in HEK293 cells [189]. Göös et al. generated proximity labeling data of 109 human transcription factors, including the NF-κB subunit p50/NFKB1, which had only 16 PPIs under constitutive conditions [146]. The Gilmore lab lists 115 factors with a documented interaction to p65/RELA based on different biological systems and conditions (https://www.bu.edu/NF-κB/physiological-mediators/interacting-proteins/). Recently, a first map of the human reference interactome (HuRI) was published in which 17,500 proteins were tested for binary interaction using high-throughput yeast two-hybrid screens (Y2H) [190]. In Y2H, a specific bait and variable prey protein are expressed as fusion proteins in yeast. The interaction between the bait and prey protein at a target promoter activates the expression of a reporter gene, enabling the selective detection of a binary interaction [191, 192]. Nonetheless, Y2H suffers from drawbacks including an elevated incidence of false positive and negative interactions, attributed to factors like testing within inappropriate cellular environments, absence of post-translational modifications, and scenarios where the bait protein alone induces transcription [191]. While classical Y2H is limited to interactions within the nucleus and only tests one interaction at a time [192], BioID allows the detection of multiple dynamic interactions of a single bait protein across cellular compartments [140]. The Y2H-based HuRI interactome comprises 47 interactors for p65/RELA and 27 for p50/NFKB1 (http://www.interactome-atlas.org/) [190]. In comparison with these previous studies, numbers were far exceeded by MiniTurboID proximity labeling in this work, which led to the identification of 366 new p65/RELA interactors under IL-1α and constitutive conditions, implying that the true dimension of the dynamic interactome is much larger than previously reported.

MiniTurboID data from two p65 mutants further revealed that proximity to DNA had less impact on remodeling of the interactome than intact dimerization function, as most cellular interactions were diminished when only two dimerization-specific amino acids were mutated in the RHD. Moreover, these mutants (E/I and FL/DD) showed lower chromatin occupancy in HeLa cells, as revealed by previous

ChIP-seq analyses [163]. Collectively, this suggests that an intact dimerization function leading to the assembly of numerous cofactors is a prerequisite for the ability of p65 to bind DNA. However, since the E/I mutant of p65 was still able to maintain most interactions but shows reduced DNA binding [163], this indicates that information in one specific amino acid residue of the RHD has an overriding importance for DNA binding of p65. Although the RHD plays a crucial role in p65 DNA binding, RT-qPCR data from this work indicate that some gene-specific transcriptional activity persists in the E/I mutant (Figure 26). This prompts the question whether this remaining transcriptional activity, particularly in the context of *CXCL2*, is affected by the interaction between p65 and its newly identified interactors. Therefore, an intriguing next step could involve utilizing p65-GAL4 fusion proteins to assess whether the identified p65 interactors enhance or suppress this transcriptional activity. This assessment could be conducted through a reporter gene assay employing a GAL4-luciferase system, as previously described in a study by our research group examining the cotranscriptional effects of DCP1a [193].

Detailed examination of the wild type interactome showed that most p65 interactors are associated with the nuclear compartment and are involved in transcriptional processes. This is consistent with a Co-IP/MS dataset from a 2007 study by Feldman et al. using agarose beads coated with NF-κB DNA response elements, which were hybridized with nuclear extracts from human trophoblast 8 (HTR8) cells [194]. Among the coprecipitated proteins were 34 factors from four different categories, including DNA-binding proteins and modifying enzymes, RNA-binding proteins and modifying enzymes, nuclear matrix components, and heat shock chaperone proteins, all of which were capable to link the NF-κB complex to the transcriptional machinery and nuclear matrix [194]. The latest developments in mass spectrometric proteomics have significantly enhanced the sensitivity for protein detection [195]. Leveraging this advancement, this study successfully identified 320 previously undiscovered interactors of wild type p65, while also providing additional detailed insights into protein interactions and their functional implications through validation experiments.

Functional validation of the NF-κB p65 interactome

RNAi validation confirmed a functional contribution of 38 HCIs to the expression of prototypical inflammatory genes with a high degree of gene specificity in terms of gene activation or repression and cell state (i.e. basal or cytokine-activated). These findings, obtained by genetic perturbation, suggest that the molecular composition of different clusters of NF-κB/cofactor complexes contains or confers specific information required to fine-tune NF-κB transcriptional activity. The ability to fine-tune transcription has been demonstrated for some RHD- or TAD-associated factors before. These factors were themselves not able to bind κB-sequences but were essential for the regulation of NF-κB binding to DNA [196]. Several cotransfection experiments and EMSA studies illustrated that many of these proteins repress NF-κB p65 binding to κB-DNA sites by physically interacting with p65 [196]. The RHD- and TAD-associated factors include RelA-associated inhibitor (RAI), aryl hydrocarbon receptor

(AhR), β-catenin, cyclin-dependent kinase 9 (Cdk9), protein inhibitor of activated STAT1 (PIAS1), Vibrio parahaemolyticus type III secretion protein (VP1686), and myocardin [196]. In contrast, an opposite effect was demonstrated for ribosomal protein S3 (RPS3), which, as an integral subunit of the NF-κB complex, enhanced the recruitment of p65 to κB-sequences [197]. Notably, many of the proteins involved in the regulation of NF-κB DNA binding have restricted tissue distribution, specific expression profiles, or specific pathophysiological circumstances [196], suggesting that NF-κB/cofactor complexes can vary in their composition depending on cell types and cellular conditions. Thus, the HCI clusters identified in the screen performed in this study, may represent novel groups of integral subunits of NF-κB complexes that repress or enhance NF-κB p65 DNA binding and transcriptional activity in HeLa cells possibly in a cell type-specific and context-dependent manner akin to the examples discussed above.

The proximity-based p65 interactome as a data resource

By defining the basic workflow of NF-κB proximity labeling, from pulldown to bioinformatic analysis, the potential of this approach can now be further exploited for the analysis of other cell types or even tissues, for modifying the experimental setup, e.g. for compartment-specific isolation of interactomes, and also for bioinformatics cross comparisons with other data sets or databases. Intersecting the p65 MiniTurboID dataset of 366 interactors with a catalog of 1,639 human transcription factors [198] or a list of 801 epigenetic regulators from the EpiFactors database [199] can reveal the major subsets of transcription factors and epigenetic writers, readers, erasers, or remodelers that prevalent in NF-κB complexes. In addition, experimental variations to learn more about the dynamics of the p65 interactome could include p65 constructs lacking the NLS [200] or with mutations in target residues for known PTMs [201], inhibitors of NF-κB upstream components (e.g. TAK1 protein kinase inhibitor 5Z-7-oxozeaenol [202]), as well as different time points of IL-1α stimulation. In combination, such MiniTurboID data can further expand knowledge of the quantitative, functional, and subcellular dynamics of the p65 interactome. These options exemplify the versality, analytical power and generic character of the MiniTurboID protocol developed in this thesis and suggests that much more additional information can be obtained by including this approach in multi-level bioinformatic analyses in the future.

5.3 Mechanistic and evolutionary perspectives of the unidirectional crosstalk between the IL-1α-NF-κB p65 and lysosomal transcription factor system

By combining PPI studies and loss-of-function approaches with large scale multi-omics analyses, this work elucidated multiple layers of interaction between the p65 subunit of NF-κB and members of two protein families, the MiT/TFE- and GLI-similar proteins, namely TFE3, TFEB, and GLIS2. The analysis uncovered a unidirectional crosstalk between pathways of the IL-1α-NF-κB and lysosomal transcription factor systems at the level of gene expression and coregulation of multiple genetic (sub)networks enriched in inflammatory cytokines, and further provided first evidence on how this coregulation is mechanistically manifested.

Microarray data and a combined ChIP-seq and motif analysis of HeLa cells stimulated with IL-1α for 1 h showed that TFE3 and TFEB together with p65 jointly regulated 51 immune genes (44 genes when TFE3/TFEB double knockdown is considered) and revealed 33 genes and 11 genes that are likely direct targets of TFE3 and p65 or TFEB and p65. In a comparable 2016 study, Pastore et al. used genomically edited macrophage knockout cell lines and stimulated the cells with LPS for 24 h. At both the protein and mRNA levels, they demonstrated the importance of TFE3 and TFEB in cytokine production and secretion. This was exemplified through the analysis of various cytokines such as CSF2, IL1A, IL1B, IL2, IL27, CSF1, CCL2, and TREM1 using cytokine arrays in RAW cells. Additionally, RT-qPCR revealed a decrease in mRNA expression levels of *Il1b*, *Il6*, *Tnf*, and *Ccl5* after 6 h of LPS stimulation of RAW macrophage knockout cells [92]. Furthermore, microarray data showed significant downregulation of 70 immune genes and upregulation of 20 immune genes in Tfe3/Tfeb knockout BMDMs [92]. A similar proportion of up- and downregulation was observed in this work for 44 IL-1α response genes coregulated by p65/TFE3/TFEB. Of note, the only immune gene that was downregulated in both microarray datasets (Pastore et al. vs. this study) was *TNFAIP3*, suggesting that a general function of TFE3 and TFEB in immune regulation exists across cell types and different organisms, whereas the affected target gene sets seem to differ largely between mice and humans [92]. Moreover, ChIP-seq data in LPS-stimulated RAW macrophage cells showed direct binding of TFE3 to the promoter regions of 84 immune genes with parallel enrichment of TFE3 motifs within the -1500 to -5000 base pair regions from the transcription start site of these genes [92]. Although, gene numbers are not directly comparable because in this work the experimental focus was on the adjacent binding of p65 and TFE3, both genomic datasets reveal subsets of immune genes (84 and 33 genes), which are direct targets of TFE3 (and p65) [92]. Therefore, the combined PPI studies and genome-wide analyses in this work provide additional evidence for a direct interaction with p65 at specific inflammatory gene loci that likely underlies a transcriptional regulatory function of TFE3/TFEB.

Subcellular studies examining the cellular distribution of TFE3 and TFEB come to different mechanistic conclusions about how this function is mediated [92]. Pastore et al. propose a model according to which the gene regulatory role of TFE3 and TFEB upon LPS stimulation is associated with their nuclear accumulation and dephosphorylation, independent of mTORC1 signaling [92]. In contrast, in this work, Western blot analyses of cytosolic and nuclear fractions of IL-1α-stimulated HeLa cells support a model in which TFE3/TFEB exert regulatory control over immune genes in response to IL-1α independent of additional, stimulus-induced nuclear recruitment and without the need for dephosphorylation. Ultimately, this suggests that there may be more than one activation mechanism that shapes the role of TFE3 and TFEB in innate immune gene expression. Integrated data from microscopic analyses, genome-wide chromatin analyses, and reporter assays are required to further understand the subcellular roles of TFE3 and TFEB in the IL-1α-NF-κB system, as elaborated in section 5.4 below.

Of note, the permanent suppression of TFE3/TFEB in CRISPR knockout experiments was largely without effect on gene activation of severel immune genes (*IL8*, *CSF2*, *CCL2*, *CXCL2*, *TNFAIP3*, *NFKBIA*), suggesting that other TF/cofactor complexes compensated this loss in long-term cell cultures. Such compensation may have been mediated by other MiT/TFE family members (e.g. MITF) or by members of the dimeric AP-1 transcription factors consisting of the Fos (c-Fos, FosB, Fra1, and Fra2) and Jun (c-Jun, JunB, and JunD) families [203]. AP-1 members are a group of basic leucine zipper (bZIP) TFs that, like NF-κB members, are involved in inflammatory gene expression and are simultaneously activated by similar stimuli [203]. Our group has previously shown that p65 and AP-1 factors bind to IL-1-inducible enhancers and promoters in a TAK1-dependent manner [48]. In addition, other chromatin studies suggest a mechanism of supported p65-chromatin association that may be promoted in part by additional transcription factors such as AP-1 [163]. This cooperativity between NF-κB and AP-1 members could allow flexibility in the recruitment and quantitative assembly of different TF/cofactor complexes. An interesting way to test for such compensatory events would be to examine the abundance of AP-1 factor motifs and their chromatin occupancy in the promoter regions of previously identified 44 IL-1α-inducible p65/TFE3/TFEB-responsive genes in the knockout cells of this work.

RT-qPCR and microarray analyses of HeLa cells showed that 1 h of IL-1α stimulation, known to rapidly induce NF-κB p50/p65 nuclear translocation [48], did not activate the expression of six CLEAR genes (*SQSTM1*, *MAP1LC3B*, *MCOLN1*, *ATP6V0D1*, *LAMP1*, *HEXA*) or the entire CLEAR gene network, suggesting that the crosstalk between the IL-1α-NF-κB system and the lysosomal system is unidirectional. Nevertheless, based on this result, it cannot be excluded that CLEAR gene expression is affected by sustained IL-1α stimulation or abnormal sustained NF-κB activation, as observed in various human diseases, including autoimmune, inflammatory, and malignant diseases [204]. RNA samples at later time points of IL-1α stimulation, e.g., 24 h or 48 h, could provide further time-resolved insight into the expression of these genes. If it were to be confirmed that sustained cytokine stimulation activates CLEAR genes, it would be interesting to study the expression of CLEAR genes in histological samples from patients or mouse models of chronic inflammatory diseases, such as RA [205] characterized by sustained abnormal activation of the IL-1α-NF-κB pathway.

RT-qPCR and Western blot analyses of HeLa cells showed that 2 h of starvation had minimal effect on the expression of six CLEAR genes, although it triggered rapid dephosphorylation and translocation of the major lysosomal transcription factors TFE3/TFEB. In this context, Pan et al. examined the transcriptional response of lysosomal and autophagy genes after 48 h starvation and showed a moderate upregulation of *MCOLN1* and *LAMP1* transcripts in the retinal pigment epithelial cell line ARPE-19 [169]. Martina et al. also observed a mild upregulation of *MCOLN1* and UPR-related genes after 16 h starvation in the same cell line [90]. The relative changes in CLEAR gene expression in these studies (e.g., approximately 3- to 8-fold) were in a much lower range than the relative changes commonly observed for IL-1α target genes, although TFE3/TFEB were triggered for longer periods [90, 169]. This suggests that short-term starvation is sufficient for rapid accumulation of TFE3/TFEB in the nucleus, whereas long-term starvation and the sustained presence of TFE3/TFEB in the nucleus are required to effectively trigger CLEAR gene expression, which in turn illustrates that the gradual, accumulative pattern of CLEAR gene expression does not allow for an acute, high-amplitude stimulus response as seen with many inflammatory genes [48, 49], regardless of the stimulus.

The unidirectional crosstalk between the lysosomal transcription factors TFE3/TFEB and the IL-1α-NF-κB system, characterized at the levels of PPIs, coregulated genetic networks, and enrichment of TFE3 motifs at inflammatory chromatin loci, provided new insights into the functions of the mammalian innate immune system exerted by TFE3/TFEB from an NF-κB-centric perspective. From an evolutionary standpoint, TFE3/TFEB appear to have NF-κB-independent functions in more primitive innate immunity [114, 206, 207]. The nematode *C. elegans* is a commonly used model organism to study innate immunity, as the worm lacks specialized immune cells and mediates immunity via intestinal epithelial cells [207, 208]. The *C. elegans* genome lacks homologs of NF-κB, including RelA, RelB, or c-Rel, as well as components of TLR signaling, such as the adaptor protein MYD88 [207, 209]. The worm appears to have lost these factors during evolution, as they are present in more primitive metazoans such as the sea anemone *Nematostella vectensis* [210] but also in higher metazoans such as *Drosophila melanogaster* [211], indicating that common ancestor of cnidarians (sea anemones, hydra) and bilaterians (worms, arthropods, vertebrates) possessed these components of innate immunity [207]. Instead, in *C. elegans*, the MiT/TFE ortholog HLH-30 has been shown to regulate approximately 80% of genes expressed during bacterial infection with *S. aureus*, including a variety of immune-related genes and signaling components [114, 206]. The worm still has several other conserved signaling pathways, including p38 MAPK signaling cascades, which are also involved in the mammalian innate immune response [206, 207]. Since the upstream signaling components and events that activate HLH-30 (TFEB/TFE3) during infection and inflammation remain unknown in mammals and lower organisms, but do not appear to require the presence of NF-κB, *C. elegans* may be a suitable model organism to study evolutionarily conserved upstream mechanisms that control HLH-30 (TFE3/TFEB) transcriptional activity in the context of immune gene regulation [207].

5.4 Possible subcellular roles of NF-κB p65 interactors in inflammatory gene expression

Subcellular quantification of PLA images revealed that interactions of p65 with TFE3, TFEB, and GLIS2 were most abundant in the cytosol and appeared to be considerably lower in the nucleus. One explanation is that TFE3, TFEB, and GLIS2 act as cytosolic scaffolding proteins, which transduce or sequester NF-κB pathway signals by constitutively stabilizing and aggregating other pathway components, e.g. TAK1 or IKK kinases, in response to stimulation [38, 212–214]. One example in this regard is that RNAi experiments showed destabilization of p65, TFE3, or TFEB once one component of the NF-κB (scaffold) complex was absent (Figure 42). Scaffolding proteins fine-tune signaling by binding two or more signaling components simultaneously [213]. Scaffolding proteins have also been identified for other important transcription factors, e.g. CNK1 is a scaffold that regulates the function of FoxO transcription factors, which are tumor suppressors in cancer and also migrate from the cytoplasm to the nucleus [215]. In addition, many cytoplasmic scaffold proteins are known to regulate the MAPK signaling pathway, which controls processes such as proliferation, cellular survival, and differentiation [213]. Known MAPK/ERK scaffold proteins include kinase suppressor of RAS (KSR1), MEK binding partner 1 (MP1) and ß-arrestin [213]. JNK-interacting proteins (JIPs) represent another group of scaffold proteins that facilitate signal transduction by aggregating components of a MAPK module, including MLK, MKK7, and JNK [212, 216].

The cytoplasmic interaction between p65 and its interactors TFE3/TFEB may be propagated at lysosomes, as component of a yet unknown sensor mechanism in which two important transcription factors sense cellular stress directly at the lysosome and then collectively transmit this information to the nucleus. A previous study showed that both TFE3 and TFEB interact with mTOR at the cytoplasmic surface of the lysosome [88]. PLA studies in combination with immunofluorescence of LAMP1, a lysosomal marker protein, could be used to demonstrate colocalization of the p65 interaction with TFE3/TFEB at the lysosome and thus reveal a novel link between the lysosomal system and NF-κB. If such colocalizations are confirmed, further investigations could focus on whether triggers of lysosomal signaling, such as starvation, abolish or enhance this lysosome colocalization. To take this one step further, it would be interesting to identify the upstream pathways that influence this putative colocalization. Here, rapamycin, an allosteric inhibitor of mTOR [217], or Torin1, an ATP-competitive mTOR inhibitor [218], as well as the calcineurin inhibitor FK506 [87] can be used to examine whether the observed effect is dependent on mTORC1 or calcineurin upstream signaling.

Although the number of interactions was relatively small, all three proteins (TFE3, TFEB and GLIS2) formed detectable protein complexes with p65 in the nucleus and jointly up- or downregulated IL-1α-induced genetic (sub)networks. Moreover, the DNA binding motifs of TFE3 and GLIS2 were overrandomly enriched within p65 binding ChIP-seq peaks, all together suggesting a nuclear mechanism characterized by the interaction between p65 and its three interactors at chromatin. To date, there are no ChIP-seq data for a chromatin-dependent interaction, e.g. at promoters or enhancers of inflammatory genes, for the three proteins. The above-mentioned ChIP-seq data of TFE3 in the mouse system after treatment with LPS [92], but also after starvation and treatment with tunicamycin [90], an ER stress inducer, are deposited in the public GEO database, as well as a recently published dataset investigating TFE3 occupancy on chromatin in a mouse model of non-alcoholic fatty liver disease (NAFLD) [219]. ChIP-seq datasets are also available for TFEB and GLIS2 in human cell systems. There are two datasets for TFEB from HeLa cells [82] and HEK293 cells [220]. Both are based on stably transfected inducible or non-inducible cell lines expressing FLAG-tagged TFEB. Similarly, there are two datasets for GLIS2 in HEK293 cells stably expressing eGFP-GLIS2 and in HCT116 cells stably expressing FB-GLIS2 [221]. However, some of these experiments are overexpression experiments, mostly from other species or cell systems, and were performed under different experimental conditions. This makes it difficult to compare these data with the p65 ChIP-seq data of our group after IL-1α stimulation [48]. An important next step is therefore to successfully generate ChIP-qPCR or ChIP-seq data from one model system under uniform experimental conditions. In addition, mammalian two-hybrid assays [222] and reporter gene assays [223] for p65 and the three interactors could be used to confirm the transactivating effect of PPIs at promoters of selected inflammatory genes. So far, these assays have not been performed for GLIS2 and TFEB in combination with p65. For TFE3, one *in vitro* transcriptional study from the 90's exists showing that p65 activates HIV-1 promoter DNA in conjunction with three distal enhancer-binding factors, including TFE3 [224].

IL-1α-driven inflammatory gene loci, which are most likely direct targets of p65 and the three interactors, were identified by combining genome-wide motif with p65 ChIP-seq analyses. For TFE3, 33 genes of this type were identified, for TFEB 11 genes and for GLIS2 44 genes. The motif analysis and thus the selection of genes with inflammatory loci was relatively stringent. It is possible that some genes that are direct targets of both factors were left out if the binding motifs of the two proteins are further apart than the ± 500 bp window around the center of the p65 peak, suggesting that these proteins could still interact with each other through chromatin looping. However, since the goal was to find IL-1α-responsive gene loci with high binding probability of p65 and its interactors, the *CSF2* gene induced by the overexpression of p65, TFE3 and TFEB with two new downstream enhancer regions emerged as a promising candidate for further mechanistic studies at chromatin. Conventional ChIP assays but also alternative strategies like CUT&RUN or CUT&Tag assays that require lower cell numbers are gold standard to study protein recruitment to specific chromatin sites [225]. Future experiments utilizing these techniques may provide evidence for the joint recruitment of p65 and the interactors to the predicted binding sites, such as the downstream *CSF2 enhancers*. Based on evidence from the literature, the gene *SQSTM1* emerges as another promising candidate for corecruitment studies. The *SQSTM1* gene encodes the multifunctional protein p62, which is a major cargo receptor for selective autophagy [226] and has been shown to be regulated by TFE3 [227] and TFEB [89]. On the other hand, this protein is known to be transcriptionally regulated by NF-κB [118], modulates NF-κB signaling in a ubiquitin-dependent manner [228], and potentiates constitutive NF-κB activity through IL-1α/p62 feedforward loops [229], indicating that SQSTM1/p62 has dual roles in the IL-1α-NF-κB and lysosome-autophagy systems. Furthermore, extended genome-wide ChIP-seq studies can reveal the real recruitment behavior of p65, TFE3, TFEB, and GLIS2 in terms of the entire inflammatory and CLEAR gene network and will allow correlation of the genomic binding behavior of these factors with the epigenetic states (histone marks), transcription (Pol II occupancy), chromatin accessibility (ATAC-seq), and 3D chromatin interactions (Hi-C or CAPTURE-3C-seq). Such data, generated under the same experimental conditions, and in the absence or presence of p65 or its new interactors, are needed to obtain a comprehensive understanding of the regulation and relevance of specific chromatin loci by p65/TFE3/TFEB or GLIS2 complexes.

Lastly, indirect mechanisms triggered by the interactor can influence the interactor's role in controlling inflammatory genes. In this regard, gene expression data showed that TFE3 and TFEB modulated genes encoding histones and histone modifiers, controlling the structural composition of chromatin, or contributing to transcriptional regulation (Figure 48). GLIS2, on the other hand, affected genes associated with the ER lumen or contributing to protein maturation, suggesting secondary effects of the three interactors on the level of transcription and protein stability, which may also contribute to effects on differential expression patterns (Figure 48). Another possibility is that the interactor regulates a gene involved in feedback or feedforward loops, which in turn limits or sustains transcriptional activity during the course of the stimulus response. A specific example might be that the interactor triggers the production of a factor that subsequently competes for the binding site on target genes, indirectly modulating the gene expression profile of the interactor. These secondary effects are more difficult to predict, but the development and combination of new bioinformatic tools such as the recently published, online tool TFEBexplorer [230] may help predict indirect effects on gene expression in the future. This tool is based on 18 human and 36 mouse gene expression profiles following overexpression, downregulation, or knockdown of TFEB, two human ChIP-seq datasets, and genome-wide predictions of TFEB binding sites in human, mouse, and rat, and thereby provides a rich resource for examining a gene subset or a single gene with respect to its regulation by TFEB [230]. TFEBexplorer also enables the examination of predictive target gene sets. For instance, when examining the top 10 IL-1α-inducible genes downregulated by siRELA in this study (*TNF*, *CXCL8*, *CSF2*, *BIRC3*, *CXCL3*, *ABCC9*, *PTX3*, *CCL2*, *EFNA1*, *NFKBIA*), the database matched 9 genes [230]. It revealed a time-dependent increase in *CCL2* expression following doxycycline-induced TFEB overexpression in HEK293 cells [230]. Moreover, TFEB overexpression in HeLa cells showed a diverse expression profile for 5 genes, and TFEB binding sites were identified in the promoter sequences of 2 genes [230]. Notably, no TFEB ChIP-seq peaks were found across these genes [230]. Hence, this tool can provide initial insights into the regulation of specific gene subsets by TFEB, but it is important to consider that the underlying datasets vary in their experimental setup and cannot be directly applied to other cell systems and conditions.

5.5 Individual and mutual roles in homeostatic cell function link p65 and its interactors to various types of cancer

Comparative analysis of gene subsets deregulated by p65/RELA and its interactors under basal conditions revealed their primary association with cell proliferation and cancer (Figure 49). In addition, each transcription factor controlled distinct networks that included genes involved in the regulation of apoptosis and cell death, as well as those related to Notch signaling and TGF-β signaling (see pathway analyses of Figure 48 & 49). Not surprisingly, abnormal activation of these cellular signaling pathways has been associated with various types of cancer [231, 232].

The Notch receptor-triggered signaling pathway regulates development and plays a role in malignant diseases [233]. Notch signaling involves proteolytic cleavage and release of the intracellular fragment (NICD, Notch intracellular domain), which translocates to the nucleus where it regulates transcription [233]. TFE3 suppression had a strong effect on gene subsets that contribute to the expression and processing of nascent forms of Notch precursors (Pre-NOTCH1-4). These genes included several histones (e.g. H2AC14, H3C4, H4C1), transcription factors (E2F3, ELF3), tumor suppressor protein p53 (TP53), RISC Complex RNA Helicase (MOV10), Trinucleotide Repeat Containing Adaptor 6A (TNRC6A), and O-Fucosylpeptide 3-Beta-N-Acetylglucosaminyltransferase (LFNG). The tumor suppressor protein p53 directly transcriptionally activates microRNA miR-34 expression, which negatively regulates translation of Notch1/2 [234, 235]. MOV10 and TNRC6A are both involved in posttranscriptional gene silencing mediated by RNA interference [236, 237]. Fringe enzymes such as LFNG modify Notch signaling posttranslationally by transferring GlcNAc to O-fucose residues at the EGF repeats in the extracellular domain of the Notch receptor [238, 239]. Hence, the microarray data in this work reveal a novel function of TFE3 in the transcriptional control of Notch signaling, a crosstalk previously described only for MITF, as mice with mutations in the MITF locus have defects in Notch signaling [81] and MITF has been shown to upregulate RBPJK, a master regulator of Notch signaling, via direct binding to the RBPJK promoter [240].

GLIS2 primarily affected the expression of genes involved in serine/threonine kinase receptor-mediated signaling. According to the Metascape database, many of these genes encoded negative regulators (e.g. LDLRAD4, PEG10, LEMD3, PMEPA1, VASN, CD109) of the TGF-β signaling pathway [149], indicating a direct role of GLIS2 in transcriptional control of this pathway. Currently, there is only indirect evidence for a link between GLIS2 and the TGF-β signaling pathway from a recent study [241]. In this study, GLIS2 was identified as a novel biomarker in gastric cancer, as high expression of GLIS2 was associated with poor prognosis [241]. Interestingly, genes of the TGF-β pathway and the cellular tumor antigen p53 pathway were also identified in this study [241], and GLIS2 has been shown to regulate p53 target genes in conjunction with p53 in colorectal cancer [221].

Gene fusions of all three transcription factors occur in various cancers. The CBFA2T3-GLIS2 fusion gene is characteristic for non-Down syndrome acute megakaryoblastic leukaemia (non-DS-AMKL), a subtype of acute myeloid leukaemia (AML) with poor prognosis that occurs particularly in paediatric patients [242]. Several MiT/TFE chromosome translocations and overexpression are found in certain types of cancer, including renal cell carcinoma, melanoma, and sarcoma [63]. Another function of MiT/TFE in cancer progression is based on energy provision due to their transcriptional role in lysosome biogenesis, autophagy, and energy metabolism, which is likely manifested in a broader spectrum of cancers [78]. A recent study focusing on pancreatic ductal adenocarcinoma (PDA) revealed uncontrolled MiT/TFE levels in the nucleus that ensure high levels of autophagy and lysosome-mediated catabolism, which is important for accelerated cell growth in PDA [243]. Similarly, abnormal or constitutive NF-κB activation plays a key role in oncogenesis as it is associated with deregulation of numerous genes involved in processes essential for cancer development and progression, including proliferation, migration, and apoptosis [244]. In addition, several studies link NF-κB activation to Notch signaling pathway and TGF-β signaling. Notch signaling pathway was activated by JNK/NF-κB-regulated GM-CSF expression in LPS-stimulated macrophages [245]. TGF-β has been shown to induce NF-κB activation through TAK1/MEK-dependent AKT activation in osteoclast survival [246]. Thus, the results of this work point to common novel signaling pathways influenced by NF-κB, MiT/TFE transcription factors, and GLIS2, underscoring their shared potential as direct therapeutic targets in human malignancies.

5.6 Insight into new roles of GLIS2 in the IL-1α-NF-κB p65 and lysosomal system

Microarray analysis following the suppression of GLIS2 with siRNA revealed insights into its role in immune gene expression in cooperation with p65. The results demonstrated that GLIS2, together with p65, controls an IL-1α-induced gene network enriched in several cytokines, including the major proinflammatory cytokines IL-1α and TNF. Notably, the analysis also identified a TNF-centric subnetwork jointly regulated by GLIS2 and p65. This subnetwork comprised genes encoding a diverse set of factors, including Hematopoietic prostaglandin D synthase (HPGDS), Zinc finger protein 36 (ZFP36), and Complement factor B (CFB).

HPGDS is a cytosolic enzyme that converts PGH2, a precursor of all prostaglandins and thromboxanes, to prostaglandin (PG) D2 via its glutathione S-transferase function. PGD2, in turn, regulates vasodilation, inhibition of platelet aggregation, and recruitment of immune cells [247]. ZFP36, better known as tristetraprolin (TTP), is a well-studied RNA-binding protein involved in the posttranscriptional control of mRNAs, which includes mRNAs of many pro-inflammatory mediators such as TNF, CXCL1, CXCL2, IL-17, CCL3, and IL-23. TTP binds adenosine and uridine (AU)-rich elements (ARE) in the 3′ untranslated region (3′UTR) of these mRNAs and causes their destabilization and rapid decay [248, 249]. TTP knockout mice develope a systemic inflammatory syndrome characterized by cachexia, erosive arthritis, myeloid hyperplasia, dermatitis, conjunctivitis, and autoimmunity [249, 250]. In a mouse model of LPS-induced acute lung injury (ALI), mice with systemic overexpression of TTP (TTP$^{\Delta ARE}$) were protected from ALI [249, 251], emphasizing the critical role of TTP in inflammation. CFB is a circulating factor in the peripheral blood that can activate the alternative complement pathway, which is another defense mechanism of the innate immune system. The alternative complement pathway is constitutively active due to the spontaneous hydrolysis of complement component 3 (C3) at low concentrations. In the alternative pathway, CFB associates with the hydrolyzed form of C3 and is then cleaved by complement factor D (CFD) into its active subunit Bb, which exerts serine protease activity. This activates the complement system and initiates an amplification loop [252].

Interestingly, microarray data showed that RELA and GLIS2 activated *HPGDS* and *ZFP36*, whereas *CFB* expression was differentially regulated. Suppression of p65 led to downregulation of the *CFB* gene, whereas the absence of GLIS2 led to its upregulation. The data thus suggest an activating function of GLIS2 in cytokine expression, prostaglandin synthesis, and control of mRNA stability, as well as a concomitant repressive function to control the constitutively active alternative complement system. These findings highlight the complex role of GLIS2 in regulating pro-inflammatory and anti-inflammatory innate immune processes. The precise mechanisms by which GLIS2 exerts this dual role remain to be better understood. Further studies need to unravel the underlying mechanisms that allow GLIS2, in conjunction with p65, to repress the expression of certain genes and activate others. In the future, a better understanding of these mechanisms may allow modulation of GLIS2-mediated gene control in a pro-inflammatory or anti-inflammatory direction.

Moreover, the data reveal a novel function of GLIS2 in the lysosomal system as a repressor for the expression of the Ca^{2+} channel MCOLN1 (TRPML1), which is expressed in intracellular endosomes and lysosomes. Interestingly, several recent research papers link abnormal activities of TRPML1, TFE3, TFEB, and lysosomal functions to neurodegenerative diseases. Loss-of-function mutations of human TRPML1 cause MLIV, a childhood neurodegenerative lysosomal storage disease with psychomotor retardation and ophthalmic abnormalities, including corneal opacity, retinal degeneration, and strabismus [75, 253, 254]. TFEB regulates TRPML1 gene expression, and TRPML1 regulates TFEB phosphorylation and subcellular localization via a positive feedback loop [77, 255]. Lysosomal transcription factors play a role in many neurodegenerative diseases, including Parkinson's disease, Alzheimer's disease, and Huntington's disease, as well as amyotrophic lateral sclerosis, Lewy body dementia, and Charcot-Marie-Tooth disease [60]. Although understanding of the function of GLIS2 in the nervous system is still limited, there is evidence suggesting some role exists. Pathophysiological studies in rats using immunofluorescence revealed increased GLIS2 levels in neurons during intracerebral hemorrhage [256]. Furthermore, Glis2 is expressed in the neural tube in mouse, chick, and

Xenopus embryos, and functional data indicate that Glis2 likely influences neuronal differentiation, as the introduction of mouse Glis2 cDNA into the chick neural tube via ovo electroporation was observed to negatively affect neuronal differentiation [257]. Based on these findings, it is interesting to investigate a possible interplay between GLIS2 and the lysosomal transcription factors, not only in the immune system, but also in the context of neurological diseases.

5.7 Limitations

The data in this work are restricted to a single cell system, which allowed standardization and integration of different datasets. HeLa cells possess all key components of the IL-1α-NF-κB signaling pathway [48, 49] and represent the most widely used human cell system [258]. However, the results are not directly transferable to other cell systems and require further investigation. The ectopic expression of p65 in MiniTurboID, although performed in cells lacking p65, may not precisely reflect the tightly controlled endogenous levels of the protein. Additionally, the presence of some constitutive p65 in the nucleus should be considered when interpreting the data. These factors may influence the effects of IL-1α and the stoichiometry of the identified interactors. Proximity labeling provides a snapshot of the interactome but does not capture direct physical interactions. The use of orthogonal approaches to validate the interaction, e.g. by PLA, Co-IP or two-hybrid assays, is therefore important and should be performed in parallel to the functional investigation of further interactors. In addition, the biotin labeling time of 1 h captures accumulating interactions during IL-1α stimulation rather than time-resolved sequential interactions. The choice of a shorter biotinylation time in combination with an IL-1α time series may allow a higher resolution of such sequential interactions. Finally, the bioinformatic analyses required the definition of filtering criteria. In this work, 366 specific p65 interactors were identified using stringent filtering criteria based on negative controls, enrichments, and statistical parameters. However, this means that the number of interactors will change when the criteria are loosened or tightened. The same is true for the number of deregulated genes identified by siRNA knockdown and for the gene set enrichment and protein network analyses of this work, which depend on the underlying databases (Metascape and STRING) and parameters (default parameters) used [149, 150].

6 Conclusions

While the application of two biotin-based pulldown methods has proven difficult in purifying single chromatin loci, MiniTurboID was successfully used to uncover a broad range of novel interactors of NF-κB p65. The interactions appear to be dynamic, with more than 300 interactors identified, and the data show that this interactome is significantly larger compared to data obtained by other methods. The siRNA screen revealed the functional significance of 38 HCIs that mediate gene specificity in IL-1α-NF-κB-driven gene expression. Additional functional and bioinformatic follow-up studies have detailed the role of three novel, previously unknown p65 interactors TFE3, TFEB and GLIS2. The collective data suggest a unidirectional crosstalk between the NF-κB system and the lysosomal transcription factor system and furthermore a transcriptional regulatory function of GLIS2 in the expression of the ion channel MCOLN1, which plays a crucial role in lysosomal Ca^{2+} homeostasis. Transcriptome-wide analyses revealed several genetic (sub)networks that are tightly coregulated by p65 and the three interactors. Analysis of DNA motifs provided initial evidence that this coregulation occurs in genomic regions occupied by p65, although this needs to be confirmed, e.g. by future ChIP studies. As summarized in Figure 61, the workflow established in this work, ranging from MiniTurboID experimental design to mass spectrometric analysis, bioinformatic evaluation and functional follow-up experiments, provides a template for uncovering genetic networks coordinated by "master" transcription factors with strong transactivation domains (TAD) such as p65/RELA.

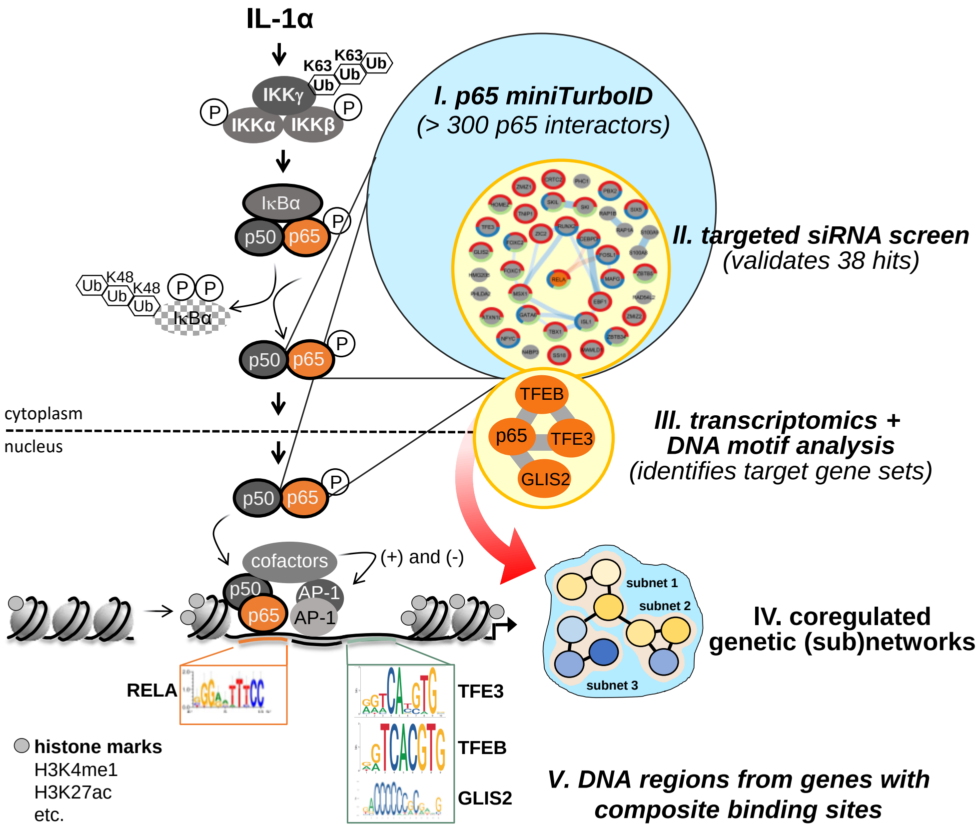

Figure 61: Multi-level interactomic and functional analysis uncovers novel jointly regulated genetic (sub)networks and target DNA regions in p65/RELA-driven inflammation.
The schematic illustrates how MiniTurboID interactome mapping combined with systematic genome- and transcriptome-wide analyses were combined in this work to expand the current knowledge of the IL-1α-NF-κB pathway at multiple levels. This workflow can thus serve as a template for similar “master” transcription factors with strong transactivation domains. The schematic was adapted from [38, 39] by Lisa Leib and Prof. M. Kracht.

7 References

1. Chaplin DD. Overview of the immune response. J Allergy Clin Immunol. 2010;125:S3-23. doi:10.1016/j.jaci.2009.12.980.
2. Bonilla FA, Oettgen HC. Adaptive immunity. J Allergy Clin Immunol. 2010;125:S33-40. doi:10.1016/j.jaci.2009.09.017.
3. Hewitt RJ, Lloyd CM. Regulation of immune responses by the airway epithelial cell landscape. Nat Rev Immunol. 2021;21:347–62. doi:10.1038/s41577-020-00477-9.
4. Mahapatro M, Erkert L, Becker C. Cytokine-Mediated Crosstalk between Immune Cells and Epithelial Cells in the Gut. Cells 2021. doi:10.3390/cells10010111.
5. Chen L, Deng H, Cui H, Fang J, Zuo Z, Deng J, et al. Inflammatory responses and inflammation-associated diseases in organs. Oncotarget. 2017;9:7204–18. doi:10.18632/oncotarget.23208.
6. Takeda K, Akira S. Toll-like receptors. Curr Protoc Immunol. 2015;109:14.12.1-14.12.10. doi:10.1002/0471142735.im1412s109.
7. Hannoodee S, Nasuruddin DN. StatPearls: Acute Inflammatory Response. Treasure Island (FL); 2023.
8. Pahwa R, Goyal A, Jialal I. StatPearls: Chronic Inflammation. Treasure Island (FL); 2023.
9. Hughes CE, Nibbs RJB. A guide to chemokines and their receptors. FEBS J. 2018;285:2944–71. doi:10.1111/febs.14466.
10. Singhal A, Subramanian M. Colony stimulating factors (CSFs): Complex roles in atherosclerosis. Cytokine. 2019;122:154190. doi:10.1016/j.cyto.2017.10.012.
11. Lin F, Young HA. Interferons: Success in anti-viral immunotherapy. Cytokine Growth Factor Rev. 2014;25:369–76. doi:10.1016/j.cytogfr.2014.07.015.
12. Kany S, Vollrath JT, Relja B. Cytokines in Inflammatory Disease. Int J Mol Sci 2019. doi:10.3390/ijms20236008.
13. Kelso A. Cytokines and their receptors: an overview. Ther Drug Monit. 2000;22:40–3. doi:10.1097/00007691-200002000-00008.
14. Zhang J-M, An J. Cytokines, Inflammation and Pain. Int Anesthesiol Clin. 2007;45:27–37. doi:10.1097/AIA.0b013e318034194e.
15. Śledziewski TK, Glińska K. Proinflammatory cytokines in periodontal diseases and certain systemic disorders. Przegl Lek. 2015;72:354–7.
16. Bränn E, Edvinsson Å, Rostedt Punga A, Sundström-Poromaa I, Skalkidou A. Inflammatory and anti-inflammatory markers in plasma: from late pregnancy to early postpartum. Sci Rep. 2019;9:1863. doi:10.1038/s41598-018-38304-w.
17. Han C-K, Lee W-F, Hsu C-J, Huang Y-L, Lin C-Y, Tsai C-H, et al. DPP4 reduces proinflammatory cytokine production in human rheumatoid arthritis synovial fibroblasts. J Cell Physiol. 2021;236:8060–9. doi:10.1002/jcp.30494.

18. Yarur AJ, Jain A, Quintero MA, Czul F, Deshpande AR, Kerman DH, Abreu MT. Inflammatory Cytokine Profile in Crohn's Disease Nonresponders to Optimal Antitumor Necrosis Factor Therapy. J Clin Gastroenterol. 2019;53:210–5. doi:10.1097/MCG.0000000000001002.
19. Moss JW, Ramji DP. Cytokines: roles in atherosclerosis disease progression and potential therapeutic targets. Future Med Chem. 2016;8:1317–30. doi:10.4155/fmc-2016-0072.
20. McInnes IB, Gravallese EM. Immune-mediated inflammatory disease therapeutics: past, present and future. Nat Rev Immunol. 2021;21:680–6. doi:10.1038/s41577-021-00603-1.
21. Abbate A, Toldo S, Marchetti C, Kron J, van Tassell BW, Dinarello CA. Interleukin-1 and the Inflammasome as Therapeutic Targets in Cardiovascular Disease. Circ Res. 2020;126:1260–80. doi:10.1161/CIRCRESAHA.120.315937.
22. Dinarello CA. Overview of the IL-1 family in innate inflammation and acquired immunity. Immunol Rev. 2018;281:8–27. doi:10.1111/imr.12621.
23. Diep S, Maddukuri M, Yamauchi S, Geshow G, Delk NA. Interleukin-1 and Nuclear Factor Kappa B Signaling Promote Breast Cancer Progression and Treatment Resistance. Cells 2022. doi:10.3390/cells11101673.
24. Fields JK, Günther S, Sundberg EJ. Structural Basis of IL-1 Family Cytokine Signaling. Front Immunol. 2019;10:1412. doi:10.3389/fimmu.2019.01412.
25. Boraschi D, Tagliabue A. The interleukin-1 receptor family. Semin Immunol. 2013;25:394–407. doi:10.1016/j.smim.2013.10.023.
26. Ramírez J, Cañete JD. Anakinra for the treatment of rheumatoid arthritis: a safety evaluation. Expert Opin Drug Saf. 2018;17:727–32. doi:10.1080/14740338.2018.1486819.
27. Buckley LF, Abbate A. Interleukin-1 blockade in cardiovascular diseases: a clinical update. Eur Heart J. 2018;39:2063–9. doi:10.1093/eurheartj/ehy128.
28. Weber A, Wasiliew P, Kracht M. Interleukin-1 (IL-1) pathway. Sci Signal. 2010;3:cm1. doi:10.1126/scisignal.3105cm1.
29. Vollmer S, Strickson S, Zhang T, Gray N, Lee KL, Rao VR, Cohen P. The mechanism of activation of IRAK1 and IRAK4 by interleukin-1 and Toll-like receptor agonists. Biochem J. 2017;474:2027–38. doi:10.1042/BCJ20170097.
30. Rodrigues M, Petrova T, Tibbs B, Arthur JSC, Cohen P. TAK1 protein kinase activity is required for TLR signalling and cytokine production in myeloid cells. Biochem J. 2022;479:1891–907. doi:10.1042/BCJ20220314.
31. Israël A. The IKK complex, a central regulator of NF-kappaB activation. Cold Spring Harb Perspect Biol. 2010;2:a000158. doi:10.1101/cshperspect.a000158.
32. Sun S-C. The non-canonical NF-κB pathway in immunity and inflammation. Nat Rev Immunol. 2017;17:545–58. doi:10.1038/nri.2017.52.
33. Liu T, Zhang L, Joo D, Sun S-C. NF-κB signaling in inflammation. Signal Transduct Target Ther. 2017;2:17023-. doi:10.1038/sigtrans.2017.23.

34. Hayden MS, Ghosh S. Shared principles in NF-kappaB signaling. Cell. 2008;132:344–62. doi:10.1016/j.cell.2008.01.020.
35. Zhang Q, Lenardo MJ, Baltimore D. 30 years of NF-κB: a blossoming of relevance to human pathobiology. Cell. 2017;168:37–57. doi:10.1016/j.cell.2016.12.012.
36. Hoffmann A, Natoli G, Ghosh G. Transcriptional regulation via the NF-kappaB signaling module. Oncogene. 2006;25:6706–16. doi:10.1038/sj.onc.1209933.
37. Christian F, Smith EL, Carmody RJ. The Regulation of NF-κB Subunits by Phosphorylation. Cells 2016. doi:10.3390/cells5010012.
38. Meier-Soelch J, Mayr-Buro C, Juli J, Leib L, Linne U, Dreute J, et al. Monitoring the Levels of Cellular NF-κB Activation States. Cancers (Basel) 2021. doi:10.3390/cancers13215351.
39. Mansouri S, Heylmann D, Stiewe T, Kracht M, Savai R. Cancer genome and tumor microenvironment: Reciprocal crosstalk shapes lung cancer plasticity. Elife 2022. doi:10.7554/eLife.79895.
40. Sen R, Baltimore D. Multiple nuclear factors interact with the immunoglobulin enhancer sequences. Cell. 1986;46:705–16. doi:10.1016/0092-8674(86)90346-6.
41. Taniguchi K, Karin M. NF-κB, inflammation, immunity and cancer: coming of age. Nat Rev Immunol. 2018;18:309–24. doi:10.1038/nri.2017.142.
42. Chen L-F, Greene WC. Shaping the nuclear action of NF-kappaB. Nat Rev Mol Cell Biol. 2004;5:392–401. doi:10.1038/nrm1368.
43. Oeckinghaus A, Ghosh S. The NF-kappaB family of transcription factors and its regulation. Cold Spring Harb Perspect Biol. 2009;1:a000034. doi:10.1101/cshperspect.a000034.
44. Perkins ND. Post-translational modifications regulating the activity and function of the nuclear factor kappa B pathway. Oncogene. 2006;25:6717–30. doi:10.1038/sj.onc.1209937.
45. Perkins ND. Integrating cell-signalling pathways with NF-kappaB and IKK function. Nat Rev Mol Cell Biol. 2007;8:49–62. doi:10.1038/nrm2083.
46. Renner F, Schmitz ML. Autoregulatory feedback loops terminating the NF-kappaB response. Trends Biochem Sci. 2009;34:128–35. doi:10.1016/j.tibs.2008.12.003.
47. Tanaka T, Grusby MJ, Kaisho T. PDLIM2-mediated termination of transcription factor NF-kappaB activation by intranuclear sequestration and degradation of the p65 subunit. Nat Immunol. 2007;8:584–91. doi:10.1038/ni1464.
48. Jurida L, Soelch J, Bartkuhn M, Handschick K, Müller H, Newel D, et al. The Activation of IL-1-Induced Enhancers Depends on TAK1 Kinase Activity and NF-κB p65. Cell Rep. 2015;10:726–39. doi:10.1016/j.celrep.2015.01.001.
49. Weiterer S-S, Meier-Soelch J, Georgomanolis T, Mizi A, Beyerlein A, Weiser H, et al. Distinct IL-1α-responsive enhancers promote acute and coordinated changes in chromatin topology in a hierarchical manner. EMBO J. 2020;39:e101533. doi:10.15252/embj.2019101533.

50. Fanucchi S, Fok ET, Dalla E, Shibayama Y, Börner K, Chang EY, et al. Immune genes are primed for robust transcription by proximal long noncoding RNAs located in nuclear compartments. Nat Genet. 2019;51:138–50. doi:10.1038/s41588-018-0298-2.
51. Schmitz ML, Stelzer G, Altmann H, Meisterernst M, Baeuerle PA. Interaction of the COOH-terminal transactivation domain of p65 NF-kappa B with TATA-binding protein, transcription factor IIB, and coactivators. J Biol Chem. 1995;270:7219–26. doi:10.1074/jbc.270.13.7219.
52. Perkins ND, Felzien LK, Betts JC, Leung K, Beach DH, Nabel GJ. Regulation of NF-kappaB by cyclin-dependent kinases associated with the p300 coactivator. Science. 1997;275:523–7. doi:10.1126/science.275.5299.523.
53. AlphaFold Protein Structure Database. Transcription factor p65: AlphaFold structure prediction. https://alphafold.com/entry/Q04206. Accessed 4 Aug 2023.
54. Duve C de, Pressman BC, Gianetto R, Wattiaux R, Appelmans F. Tissue fractionation studies. 6. Intracellular distribution patterns of enzymes in rat-liver tissue*. Biochem J. 1955;60:604–17.
55. Braulke T, Bonifacino JS. Sorting of lysosomal proteins. Biochim Biophys Acta. 2009;1793:605–14. doi:10.1016/j.bbamcr.2008.10.016.
56. Bajaj L, Lotfi P, Pal R, Di Ronza A, Sharma J, Sardiello M. Lysosome biogenesis in health and disease. J Neurochem. 2019;148:573–89. doi:10.1111/jnc.14564.
57. Chapel A, Kieffer-Jaquinod S, Sagné C, Verdon Q, Ivaldi C, Mellal M, et al. An extended proteome map of the lysosomal membrane reveals novel potential transporters. Mol Cell Proteomics. 2013;12:1572–88. doi:10.1074/mcp.M112.021980.
58. Bagshaw RD, Mahuran DJ, Callahan JW. A proteomic analysis of lysosomal integral membrane proteins reveals the diverse composition of the organelle. Mol Cell Proteomics. 2005;4:133–43. doi:10.1074/mcp.M400128-MCP200.
59. Yang C, Wang X. Lysosome biogenesis: Regulation and functions. J Cell Biol 2021. doi:10.1083/jcb.202102001.
60. Ballabio A, Bonifacino JS. Lysosomes as dynamic regulators of cell and organismal homeostasis. Nat Rev Mol Cell Biol. 2020;21:101–18. doi:10.1038/s41580-019-0185-4.
61. Settembre C, Fraldi A, Medina DL, Ballabio A. Signals from the lysosome: a control centre for cellular clearance and energy metabolism. Nat Rev Mol Cell Biol. 2013;14:283–96. doi:10.1038/nrm3565.
62. Ballabio A. The awesome lysosome. EMBO Mol Med. 2016;8:73–6. doi:10.15252/emmm.201505966.
63. Perera RM, Di Malta C, Ballabio A. MiT/TFE Family of Transcription Factors, Lysosomes, and Cancer. Annu Rev Cancer Biol. 2019;3:203–22. doi:10.1146/annurev-cancerbio-030518-055835.
64. Mony VK, Benjamin S, O'Rourke EJ. A lysosome-centered view of nutrient homeostasis. Autophagy. 2016;12:619–31. doi:10.1080/15548627.2016.1147671.

65. Efeyan A, Comb WC, Sabatini DM. Nutrient-sensing mechanisms and pathways. Nature. 2015;517:302–10. doi:10.1038/nature14190.
66. Hosokawa N, Hara T, Kaizuka T, Kishi C, Takamura A, Miura Y, et al. Nutrient-dependent mTORC1 association with the ULK1-Atg13-FIP200 complex required for autophagy. Mol Biol Cell. 2009;20:1981–91. doi:10.1091/mbc.e08-12-1248.
67. Sancak Y, Bar-Peled L, Zoncu R, Markhard AL, Nada S, Sabatini DM. Ragulator-Rag complex targets mTORC1 to the lysosomal surface and is necessary for its activation by amino acids. Cell. 2010;141:290–303. doi:10.1016/j.cell.2010.02.024.
68. Bar-Peled L, Schweitzer LD, Zoncu R, Sabatini DM. Ragulator is a GEF for the rag GTPases that signal amino acid levels to mTORC1. Cell. 2012;150:1196–208. doi:10.1016/j.cell.2012.07.032.
69. Tsun Z-Y, Bar-Peled L, Chantranupong L, Zoncu R, Wang T, Kim C, et al. The folliculin tumor suppressor is a GAP for the RagC/D GTPases that signal amino acid levels to mTORC1. Mol Cell. 2013;52:495–505. doi:10.1016/j.molcel.2013.09.016.
70. Anandapadamanaban M, Masson GR, Perisic O, Berndt A, Kaufman J, Johnson CM, et al. Architecture of human Rag GTPase heterodimers and their complex with mTORC1. Science. 2019;366:203–10. doi:10.1126/science.aax3939.
71. Petit CS, Roczniak-Ferguson A, Ferguson SM. Recruitment of folliculin to lysosomes supports the amino acid-dependent activation of Rag GTPases. J Cell Biol. 2013;202:1107–22. doi:10.1083/jcb.201307084.
72. Luzio JP, Pryor PR, Bright NA. Lysosomes: fusion and function. Nat Rev Mol Cell Biol. 2007;8:622–32. doi:10.1038/nrm2217.
73. Lloyd-Evans E, Waller-Evans H. Lysosomal Ca2+ Homeostasis and Signaling in Health and Disease. Cold Spring Harb Perspect Biol 2020. doi:10.1101/cshperspect.a035311.
74. Raffaello A, Mammucari C, Gherardi G, Rizzuto R. Calcium at the Center of Cell Signaling: Interplay between Endoplasmic Reticulum, Mitochondria, and Lysosomes. Trends Biochem Sci. 2016;41:1035–49. doi:10.1016/j.tibs.2016.09.001.
75. Bargal R, Avidan N, Ben-Asher E, Olender Z, Zeigler M, Frumkin A, et al. Identification of the gene causing mucolipidosis type IV. Nat Genet. 2000;26:118–23. doi:10.1038/79095.
76. Li R-J, Xu J, Fu C, Zhang J, Zheng YG, Jia H, Liu JO. Regulation of mTORC1 by lysosomal calcium and calmodulin. Elife 2016. doi:10.7554/eLife.19360.
77. Medina DL, Di Paola S, Peluso I, Armani A, Stefani D de, Venditti R, et al. Lysosomal calcium signaling regulates autophagy via calcineurin and TFEB. Nat Cell Biol. 2015;17:288–99. doi:10.1038/ncb3114.
78. Raben N, Puertollano R. TFEB AND TFE3, LINKING LYSOSOMES TO CELLULAR ADAPTATION TO STRESS. Annu Rev Cell Dev Biol. 2016;32:255–78. doi:10.1146/annurev-cellbio-111315-125407.

79. Helip-Wooley A, Thoene JG. Sucrose-induced vacuolation results in increased expression of cholesterol biosynthesis and lysosomal genes. Exp Cell Res. 2004;292:89–100. doi:10.1016/j.yexcr.2003.09.003.
80. Sardiello M, Palmieri M, Di Ronza A, Medina DL, Valenza M, Gennarino VA, et al. A gene network regulating lysosomal biogenesis and function. Science. 2009;325:473–7. doi:10.1126/science.1174447.
81. Nabar NR, Kehrl JH. The Transcription Factor EB Links Cellular Stress to the Immune Response. Yale J Biol Med. 2017;90:301–15.
82. Palmieri M, Impey S, Kang H, Di Ronza A, Pelz C, Sardiello M, Ballabio A. Characterization of the CLEAR network reveals an integrated control of cellular clearance pathways. Hum Mol Genet. 2011;20:3852–66. doi:10.1093/hmg/ddr306.
83. Glick D, Barth S, Macleod KF. Autophagy: cellular and molecular mechanisms. J Pathol. 2010;221:3–12. doi:10.1002/path.2697.
84. Settembre C, Di Malta C, Polito VA, Garcia Arencibia M, Vetrini F, Erdin S, et al. TFEB links autophagy to lysosomal biogenesis. Science. 2011;332:1429–33. doi:10.1126/science.1204592.
85. Martina JA, Diab HI, Lishu L, Jeong-A L, Patange S, Raben N, Puertollano R. The nutrient-responsive transcription factor TFE3 promotes autophagy, lysosomal biogenesis, and clearance of cellular debris. Sci Signal. 2014;7:ra9. doi:10.1126/scisignal.2004754.
86. Martina JA, Puertollano R. Rag GTPases mediate amino acid-dependent recruitment of TFEB and MITF to lysosomes. J Cell Biol. 2013;200:475–91. doi:10.1083/jcb.201209135.
87. Martina JA, Chen Y, Gucek M, Puertollano R. MTORC1 functions as a transcriptional regulator of autophagy by preventing nuclear transport of TFEB. Autophagy. 2012;8:903–14. doi:10.4161/auto.19653.
88. Roczniak-Ferguson A, Petit CS, Froehlich F, Qian S, Ky J, Angarola B, et al. The transcription factor TFEB links mTORC1 signaling to transcriptional control of lysosome homeostasis. Sci Signal. 2012;5:ra42. doi:10.1126/scisignal.2002790.
89. Settembre C, Zoncu R, Medina DL, Vetrini F, Erdin S, Erdin S, et al. A lysosome-to-nucleus signalling mechanism senses and regulates the lysosome via mTOR and TFEB. EMBO J. 2012;31:1095–108. doi:10.1038/emboj.2012.32.
90. Martina JA, Diab HI, Brady OA, Puertollano R. TFEB and TFE3 are novel components of the integrated stress response. EMBO J. 2016;35:479–95. doi:10.15252/embj.201593428.
91. Nezich CL, Wang C, Fogel AI, Youle RJ. MiT/TFE transcription factors are activated during mitophagy downstream of Parkin and Atg5. J Cell Biol. 2015;210:435–50. doi:10.1083/jcb.201501002.
92. Pastore N, Brady OA, Diab HI, Martina JA, Sun L, Huynh T, et al. TFEB and TFE3 cooperate in the regulation of the innate immune response in activated macrophages. Autophagy. 2016;12:1240–58. doi:10.1080/15548627.2016.1179405.

93. Li Y, Xu M, Ding X, Yan C, Song Z, Chen L, et al. Protein kinase C controls lysosome biogenesis independently of mTORC1. Nat Cell Biol. 2016;18:1065–77. doi:10.1038/ncb3407.
94. Hemesath TJ, Steingrímsson E, McGill G, Hansen MJ, Vaught J, Hodgkinson CA, et al. microphthalmia, a critical factor in melanocyte development, defines a discrete transcription factor family. Genes Dev. 1994;8:2770–80. doi:10.1101/gad.8.22.2770.
95. Hodgkinson CA, Moore KJ, Nakayama A, Steingrímsson E, Copeland NG, Jenkins NA, Arnheiter H. Mutations at the mouse microphthalmia locus are associated with defects in a gene encoding a novel basic-helix-loop-helix-zipper protein. Cell. 1993;74:395–404. doi:10.1016/0092-8674(93)90429-T.
96. Kim S, Song H-S, Yu J, Kim Y-M. MiT Family Transcriptional Factors in Immune Cell Functions. Mol Cells. 2021;44:342–55. doi:10.14348/molcells.2021.0067.
97. Hartman ML, Czyz M. MITF in melanoma: mechanisms behind its expression and activity. Cell Mol Life Sci. 2015;72:1249–60. doi:10.1007/s00018-014-1791-0.
98. Goding CR, Arnheiter H. MITF-the first 25 years. Genes Dev. 2019;33:983–1007. doi:10.1101/gad.324657.119.
99. Aksan I, Goding CR. Targeting the microphthalmia basic helix-loop-helix-leucine zipper transcription factor to a subset of E-box elements in vitro and in vivo. Mol Cell Biol. 1998;18:6930–8. doi:10.1128/MCB.18.12.6930.
100. Zhao GQ, Zhao Q, Zhou X, Mattei MG, Crombrugghe B de. TFEC, a basic helix-loop-helix protein, forms heterodimers with TFE3 and inhibits TFE3-dependent transcription activation. Mol Cell Biol. 1993;13:4505–12. doi:10.1128/mcb.13.8.4505-4512.1993.
101. Huan C, Kelly ML, Steele R, Shapira I, Gottesman SRS, Roman CAJ. Transcription factors TFE3 and TFEB are critical for CD40 ligand expression and thymus-dependent humoral immunity. Nat Immunol. 2006;7:1082–91. doi:10.1038/ni1378.
102. Pastore N, Vainshtein A, Klisch TJ, Armani A, Huynh T, Herz NJ, et al. TFE3 regulates whole-body energy metabolism in cooperation with TFEB. EMBO Mol Med. 2017;9:605–21. doi:10.15252/emmm.201607204.
103. Steingrímsson E, Tessarollo L, Reid SW, Jenkins NA, Copeland NG. The bHLH-Zip transcription factor Tfeb is essential for placental vascularization. Development. 1998;125:4607–16. doi:10.1242/dev.125.23.4607.
104. Steingrímsson E, Tessarollo L, Pathak B, Hou L, Arnheiter H, Copeland NG, Jenkins NA. Mitf and Tfe3, two members of the Mitf-Tfe family of bHLH-Zip transcription factors, have important but functionally redundant roles in osteoclast development. Proc Natl Acad Sci U S A. 2002;99:4477–82. doi:10.1073/pnas.072071099.
105. Betschinger J, Nichols J, Dietmann S, Corrin PD, Paddison PJ, Smith A. Exit from Pluripotency Is Gated by Intracellular Redistribution of the bHLH Transcription Factor Tfe3. Cell. 2013;153:335–47. doi:10.1016/j.cell.2013.03.012.

106. Yagil Z, Hadad Erlich T, Ofir-Birin Y, Tshori S, Kay G, Yekhtin Z, et al. Transcription factor E3, a major regulator of mast cell-mediated allergic response. J Allergy Clin Immunol. 2012;129:1357-1366.e5. doi:10.1016/j.jaci.2011.11.051.
107. Irazoqui JE. Key Roles of MiT Transcription Factors in Innate Immunity and Inflammation. Trends Immunol. 2020;41:157–71. doi:10.1016/j.it.2019.12.003.
108. Shi C-S, Kehrl JH. TRAF6 and A20 regulate lysine 63-linked ubiquitination of Beclin-1 to control TLR4-induced autophagy. Sci Signal. 2010;3:ra42. doi:10.1126/scisignal.2000751.
109. Shi C-S, Shenderov K, Huang N-N, Kabat J, Abu-Asab M, Fitzgerald KA, et al. Activation of autophagy by inflammatory signals limits IL-1β production by targeting ubiquitinated inflammasomes for destruction. Nat Immunol. 2012;13:255–63. doi:10.1038/ni.2215.
110. Jiang S, Dupont N, Castillo EF, Deretic V. Secretory versus Degradative Autophagy: Unconventional Secretion of Inflammatory Mediators. J Innate Immun. 2013;5:471–9. doi:10.1159/000346707.
111. Cui B, Lin H, Yu J, Yu J, Hu Z. Autophagy and the Immune Response. Adv Exp Med Biol. 2019;1206:595–634. doi:10.1007/978-981-15-0602-4_27.
112. Levine B, Mizushima N, Virgin HW. Autophagy in immunity and inflammation. Nature. 2011;469:323–35. doi:10.1038/nature09782.
113. Deretic V, Saitoh T, Akira S. Autophagy in infection, inflammation and immunity. Nat Rev Immunol. 2013;13:722–37. doi:10.1038/nri3532.
114. Visvikis O, Ihuegbu N, Labed SA, Luhachack LG, Alves A-MF, Wollenberg AC, et al. Innate host defense requires TFEB-mediated transcription of cytoprotective and antimicrobial genes. Immunity. 2014;40:896–909. doi:10.1016/j.immuni.2014.05.002.
115. Vural A, Al-Khodor S, Cheung GYC, Shi C-S, Srinivasan L, McQuiston TJ, et al. Activator of G-Protein Signaling 3-Induced Lysosomal Biogenesis Limits Macrophage Intracellular Bacterial Infection. J Immunol. 2016;196:846–56. doi:10.4049/jimmunol.1501595.
116. Hasan M, Koch J, Rakheja D, Pattnaik AK, Brugarolas J, Dozmorov I, et al. Trex1 regulates lysosomal biogenesis and interferon-independent activation of antiviral genes. Nat Immunol. 2013;14:61–71. doi:10.1038/ni.2475.
117. Brady OA, Martina JA, Puertollano R. Emerging roles for TFEB in the immune response and inflammation. Autophagy. 2018;14:181–9. doi:10.1080/15548627.2017.1313943.
118. Füllgrabe J, Klionsky DJ, Joseph B. The return of the nucleus: transcriptional and epigenetic control of autophagy. Nat Rev Mol Cell Biol. 2014;15:65–74. doi:10.1038/nrm3716.
119. Jetten AM. GLIS1-3 transcription factors: critical roles in the regulation of multiple physiological processes and diseases. Cell Mol Life Sci. 2018;75:3473–94. doi:10.1007/s00018-018-2841-9.
120. Dimitri P. The role of GLIS3 in thyroid disease as part of a multisystem disorder. Best Pract Res Clin Endocrinol Metab. 2017;31:175–82. doi:10.1016/j.beem.2017.04.007.

121. TAKAHASHI K, SAKURAI N, EMURA N, HASHIZUME T, SAWAI K. Effects of downregulating GLIS1 transcript on preimplantation development and gene expression of bovine embryos. J Reprod Dev. 2015;61:369–74. doi:10.1262/jrd.2015-029.
122. Lee S-Y, Noh HB, Kim H-T, Lee K-I, Hwang D-Y. Glis family proteins are differentially implicated in the cellular reprogramming of human somatic cells. Oncotarget. 2017;8:77041–9. doi:10.18632/oncotarget.20334.
123. Zhang F, Nakanishi G, Kurebayashi S, Yoshino K, Perantoni A, Kim Y-S, Jetten AM. Characterization of Glis2, a novel gene encoding a Gli-related, Krüppel-like transcription factor with transactivation and repressor functions. Roles in kidney development and neurogenesis. J Biol Chem. 2002;277:10139–49. doi:10.1074/jbc.M108062200.
124. Kim Y-S, Kang HS, Herbert R, Beak JY, Collins JB, Grissom SF, Jetten AM. Kruppel-like zinc finger protein Glis2 is essential for the maintenance of normal renal functions. Mol Cell Biol. 2008;28:2358–67. doi:10.1128/MCB.01722-07.
125. Kim Y-S, Lewandoski M, Perantoni AO, Kurebayashi S, Nakanishi G, Jetten AM. Identification of Glis1, a novel Gli-related, Kruppel-like zinc finger protein containing transactivation and repressor functions. J Biol Chem. 2002;277:30901–13. doi:10.1074/jbc.M203563200.
126. Kim Y-S, Nakanishi G, Lewandoski M, Jetten AM. GLIS3, a novel member of the GLIS subfamily of Krüppel-like zinc finger proteins with repressor and activation functions. Nucleic Acids Res. 2003;31:5513–25. doi:10.1093/nar/gkg776.
127. Kim S-C, Kim Y-S, Jetten AM. Krüppel-like zinc finger protein Gli-similar 2 (Glis2) represses transcription through interaction with C-terminal binding protein 1 (CtBP1). Nucleic Acids Res. 2005;33:6805–15. doi:10.1093/nar/gki985.
128. Li B, Rauhauser AA, Dai J, Sakthivel R, Igarashi P, Jetten AM, Attanasio M. Increased hedgehog signaling in postnatal kidney results in aberrant activation of nephron developmental programs. Hum Mol Genet. 2011;20:4155–66. doi:10.1093/hmg/ddr339.
129. Koyabu Y, Nakata K, Mizugishi K, Aruga J, Mikoshiba K. Physical and functional interactions between Zic and Gli proteins. J Biol Chem. 2001;276:6889–92. doi:10.1074/jbc.C000773200.
130. Kourtidis A, Ngok SP, Anastasiadis PZ. p120 catenin: an essential regulator of cadherin stability, adhesion-induced signaling, and cancer progression. Prog Mol Biol Transl Sci. 2013;116:409–32. doi:10.1016/B978-0-12-394311-8.00018-2.
131. Attanasio M, Uhlenhaut NH, Sousa VH, O'Toole JF, Otto E, Anlag K, et al. Loss of GLIS2 causes nephronophthisis in humans and mice by increased apoptosis and fibrosis. Nat Genet. 2007;39:1018–24. doi:10.1038/ng2072.
132. Dolgalev G, Poverennaya E. Applications of CRISPR-Cas Technologies to Proteomics. Genes (Basel) 2021. doi:10.3390/genes12111790.
133. Trinkle-Mulcahy L. Recent advances in proximity-based labeling methods for interactome mapping. F1000Res 2019. doi:10.12688/f1000research.16903.1.

134. Gauchier M, van Mierlo G, Vermeulen M, Déjardin J. Purification and enrichment of specific chromatin loci. Nat Methods. 2020;17:380–9. doi:10.1038/s41592-020-0765-4.
135. Fujita T, Fujii H. Efficient isolation of specific genomic regions and identification of associated proteins by engineered DNA-binding molecule-mediated chromatin immunoprecipitation (enChIP) using CRISPR. Biochem Biophys Res Commun. 2013;439:132–6. doi:10.1016/j.bbrc.2013.08.013.
136. Waldrip ZJ, Byrum SD, Storey AJ, Gao J, Byrd AK, Mackintosh SG, et al. A CRISPR-based approach for proteomic analysis of a single genomic locus. Epigenetics. 2014;9:1207–11. doi:10.4161/epi.29919.
137. Tsui C, Inouye C, Levy M, Lu A, Florens L, Washburn MP, Tjian R. dCas9-targeted locus-specific protein isolation method identifies histone gene regulators. Proc Natl Acad Sci U S A. 2018;115:E2734-E2741. doi:10.1073/pnas.1718844115.
138. Liu X, Zhang Y, Chen Y, Li M, Zhou F, Li K, et al. In Situ Capture of Chromatin Interactions by Biotinylated dCas9. Cell. 2017;170:1028-1043.e19. doi:10.1016/j.cell.2017.08.003.
139. Ummethum H, Hamperl S. Proximity Labeling Techniques to Study Chromatin. Front Genet. 2020;11:450. doi:10.3389/fgene.2020.00450.
140. Roux KJ, Kim D in, Raida M, Burke B. A promiscuous biotin ligase fusion protein identifies proximal and interacting proteins in mammalian cells. J Cell Biol. 2012;196:801–10. doi:10.1083/jcb.201112098.
141. Schmidtmann E, Anton T, Rombaut P, Herzog F, Leonhardt H. Determination of local chromatin composition by CasID. Nucleus. 2016;7:476–84. doi:10.1080/19491034.2016.1239000.
142. Gao XD, Tu L-C, Mir A, Rodriguez T, Ding Y, Leszyk J, et al. C-BERST: defining subnuclear proteomic landscapes at genomic elements with dCas9-APEX2. Nat Methods. 2018;15:433–6. doi:10.1038/s41592-018-0006-2.
143. Gao XD, Rodríguez TC, Sontheimer EJ. Adapting dCas9-APEX2 for subnuclear proteomic profiling. Methods Enzymol. 2019;616:365–83. doi:10.1016/bs.mie.2018.10.030.
144. Myers SA, Wright J, Peckner R, Kalish BT, Zhang F, Carr SA. Discovery of proteins associated with a predefined genomic locus via dCas9-APEX-mediated proximity labeling. Nat Methods. 2018;15:437–9. doi:10.1038/s41592-018-0007-1.
145. Qiu W, Xu Z, Zhang M, Zhang D, Fan H, Li T, et al. Determination of local chromatin interactions using a combined CRISPR and peroxidase APEX2 system. Nucleic Acids Res. 2019;47:e52. doi:10.1093/nar/gkz134.
146. Göös H, Kinnunen M, Salokas K, Tan Z, Liu X, Yadav L, et al. Human transcription factor protein interaction networks. Nat Commun. 2022;13:766. doi:10.1038/s41467-022-28341-5.
147. Liu X, Zhang Y, Chen Y, Li M, Shao Z, Zhang MQ, Xu J. CAPTURE: In Situ Analysis of Chromatin Composition of Endogenous Genomic Loci by Biotinylated dCas9. Curr Protoc Mol Biol. 2018;123:e64. doi:10.1002/cpmb.64.

148. Draw Venn: web tool. https://bioinformatics.psb.ugent.be/webtools/Venn/.

149. Zhou Y, Zhou B, Pache L, Chang M, Khodabakhshi AH, Tanaseichuk O, et al. Metascape provides a biologist-oriented resource for the analysis of systems-level datasets. Nat Commun. 2019;10:1523. doi:10.1038/s41467-019-09234-6.

150. Szklarczyk D, Gable AL, Lyon D, Junge A, Wyder S, Huerta-Cepas J, et al. STRING v11: protein-protein association networks with increased coverage, supporting functional discovery in genome-wide experimental datasets. Nucleic Acids Res. 2019;47:D607-D613. doi:10.1093/nar/gky1131.

151. Boussif O, Lezoualc'h F, Zanta MA, Mergny MD, Scherman D, Demeneix B, Behr JP. A versatile vector for gene and oligonucleotide transfer into cells in culture and in vivo: polyethylenimine. Proc Natl Acad Sci U S A. 1995;92:7297–301. doi:10.1073/pnas.92.16.7297.

152. Sonawane ND, Szoka FC, Verkman AS. Chloride accumulation and swelling in endosomes enhances DNA transfer by polyamine-DNA polyplexes. J Biol Chem. 2003;278:44826–31. doi:10.1074/jbc.M308643200.

153. Longo PA, Kavran JM, Kim M-S, Leahy DJ. Transient mammalian cell transfection with polyethylenimine (PEI). Methods Enzymol. 2013;529:227–40. doi:10.1016/B978-0-12-418687-3.00018-5.

154. R Core Team (2018) R. A Language and Environment for Statistical Computing: R Foundation for Statistical Computing, Vienna.

155. Ritchie ME, Phipson B, Di Wu, Hu Y, Law CW, Shi W, Smyth GK. limma powers differential expression analyses for RNA-sequencing and microarray studies. Nucleic Acids Res. 2015;43:e47. doi:10.1093/nar/gkv007.

156. Gentleman RC, Carey VJ, Bates DM, Bolstad B, Dettling M, Dudoit S, et al. Bioconductor: open software development for computational biology and bioinformatics. Genome Biol. 2004;5:R80. doi:10.1186/gb-2004-5-10-r80.

157. Silver JD, Ritchie ME, Smyth GK. Microarray background correction: maximum likelihood estimation for the normal–exponential convolution. Biostatistics. 2008;10:352–63. doi:10.1093/biostatistics/kxn042.

158. Kanehisa M, Sato Y, Kawashima M, Furumichi M, Tanabe M. KEGG as a reference resource for gene and protein annotation. Nucleic Acids Res. 2016;44:D457-62. doi:10.1093/nar/gkv1070.

159. Liu X, Chen Y, Zhang Y, Liu Y, Liu N, Botten GA, et al. Multiplexed capture of spatial configuration and temporal dynamics of locus-specific 3D chromatin by biotinylated dCas9. Genome Biol. 2020;21:59. doi:10.1186/s13059-020-01973-w.

160. Kim D in, Birendra KC, Zhu W, Motamedchaboki K, Doye V, Roux KJ. Probing nuclear pore complex architecture with proximity-dependent biotinylation. Proc Natl Acad Sci U S A. 2014;111:E2453-61. doi:10.1073/pnas.1406459111.

161. Varnaitė R, MacNeill SA. Meet the neighbors: Mapping local protein interactomes by proximity-dependent labeling with BioID. Proteomics. 2016;16:2503–18. doi:10.1002/pmic.201600123.
162. Branon TC, Bosch JA, Sanchez AD, Udeshi ND, Svinkina T, Carr SA, et al. Efficient proximity labeling in living cells and organisms with TurboID. Nat Biotechnol. 2018;36:880–7. doi:10.1038/nbt.4201.
163. Riedlinger T, Liefke R, Meier-Soelch J, Jurida L, Nist A, Stiewe T, et al. NF-κB p65 dimerization and DNA-binding is important for inflammatory gene expression. FASEB J. 2019;33:4188–202. doi:10.1096/fj.201801638R.
164. Maaland MG, Papich MG, Turnidge J, Guardabassi L. Pharmacodynamics of doxycycline and tetracycline against Staphylococcus pseudintermedius: proposal of canine-specific breakpoints for doxycycline. J Clin Microbiol. 2013;51:3547–54. doi:10.1128/JCM.01498-13.
165. Shannon P, Markiel A, Ozier O, Baliga NS, Wang JT, Ramage D, et al. Cytoscape: a software environment for integrated models of biomolecular interaction networks. Genome Res. 2003;13:2498–504. doi:10.1101/gr.1239303.
166. Meier-Soelch J, Jurida L, Weber A, Newel D, Kim J, Braun T, et al. RNAi-Based Identification of Gene-Specific Nuclear Cofactor Networks Regulating Interleukin-1 Target Genes. Front Immunol. 2018;9:775. doi:10.3389/fimmu.2018.00775.
167. Mayr-Buro C, Schlereth E, Beuerlein K, Tenekeci U, Meier-Soelch J, Schmitz ML, Kracht M. Single-Cell Analysis of Multiple Steps of Dynamic NF-κB Regulation in Interleukin-1α-Triggered Tumor Cells Using Proximity Ligation Assays. Cancers (Basel) 2019. doi:10.3390/cancers11081199.
168. Puertollano R, Ferguson SM, Brugarolas J, Ballabio A. The complex relationship between TFEB transcription factor phosphorylation and subcellular localization. EMBO J 2018. doi:10.15252/embj.201798804.
169. Pan H-Y, Alamri AH, Valapala M. Nutrient deprivation and lysosomal stress induce activation of TFEB in retinal pigment epithelial cells. Cell Mol Biol Lett 2019. doi:10.1186/s11658-019-0159-8.
170. Sun X, Yang Y, Zhong XZ, Cao Q, Zhu X-H, Zhu X, Dong X-P. A negative feedback regulation of MTORC1 activity by the lysosomal Ca2+ channel MCOLN1 (mucolipin 1) using a CALM (calmodulin)-dependent mechanism. Autophagy. 2018;14:38–52. doi:10.1080/15548627.2017.1389822.
171. Zhang X, Cheng X, Yu L, Yang J, Calvo R, Patnaik S, et al. MCOLN1 is a ROS sensor in lysosomes that regulates autophagy. Nat Commun. 2016;7:12109. doi:10.1038/ncomms12109.
172. Shen K, Rogala KB, Chou H-T, Huang RK, Yu Z, Sabatini DM. Cryo-EM Structure of the Human FLCN-FNIP2-Rag-Ragulator Complex. Cell. 2019;179:1319-1329.e8. doi:10.1016/j.cell.2019.10.036.

173. Vermeulen M, Déjardin J. Locus-specific chromatin isolation. Nat Rev Mol Cell Biol. 2020;21:249–50. doi:10.1038/s41580-020-0217-0.

174. Alkhayer R, Ponath V, Frech M, Adhikary T, Graumann J, Neubauer A, Strandmann EP von. KLF4-mediated upregulation of the NKG2D ligand MICA in acute myeloid leukemia: a novel therapeutic target identified by enChIP. Cell Commun Signal. 2023;21:94. doi:10.1186/s12964-023-01118-z.

175. Campbell AE, Shadle SC, Jagannathan S, Lim J-W, Resnick R, Tawil R, et al. NuRD and CAF-1-mediated silencing of the D4Z4 array is modulated by DUX4-induced MBD3L proteins. Elife 2018. doi:10.7554/eLife.31023.

176. Hamidian A, Vaapil M, Stedingk K von, Fujita T, Persson CU, Eriksson P, et al. Promoter-associated proteins of EPAS1 identified by enChIP-MS - A putative role of HDX as a negative regulator. Biochem Biophys Res Commun. 2018;499:291–8. doi:10.1016/j.bbrc.2018.03.150.

177. Zhang J, Hua C, Zhang Y, Wei P, Tu Y, Wei T. KAP1-associated transcriptional inhibitory complex regulates C2C12 myoblasts differentiation and mitochondrial biogenesis via miR-133a repression. Cell Death Dis. 2020;11:732. doi:10.1038/s41419-020-02937-5.

178. Guiro J, Fagbemi M, Tellier M, Zaborowska J, Barker S, Fournier M, Murphy S. CAPTURE of the Human U2 snRNA Genes Expands the Repertoire of Associated Factors. Biomolecules 2022. doi:10.3390/biom12050704.

179. Burramsetty AK, Nishimura K, Kishimoto T, Hamzah M, Kuno A, Fukuda A, Hisatake K. Locus-Specific Isolation of the Nanog Chromatin Identifies Regulators Relevant to Pluripotency of Mouse Embryonic Stem Cells and Reprogramming of Somatic Cells. Int J Mol Sci 2022. doi:10.3390/ijms232315242.

180. Liu Y, Mi Y, Mueller T, Kreibich S, Williams EG, van Drogen A, et al. Multi-omic measurements of heterogeneity in HeLa cells across laboratories. Nat Biotechnol. 2019;37:314–22. doi:10.1038/s41587-019-0037-y.

181. Timp W, Timp G. Beyond mass spectrometry, the next step in proteomics. Sci Adv. 2020;6:eaax8978. doi:10.1126/sciadv.aax8978.

182. Kunsch C, Ruben SM, Rosen CA. Selection of optimal kappa B/Rel DNA-binding motifs: interaction of both subunits of NF-kappa B with DNA is required for transcriptional activation. Mol Cell Biol. 1992;12:4412–21.

183. Melnik S, Deng B, Papantonis A, Baboo S, Carr IM, Cook PR. The proteomes of transcription factories containing RNA polymerases I, II or III. Nat Methods. 2011;8:963–8. doi:10.1038/nmeth.1705.

184. Lieberman-Aiden E, van Berkum NL, Williams L, Imakaev M, Ragoczy T, Telling A, et al. Comprehensive mapping of long-range interactions reveals folding principles of the human genome. Science. 2009;326:289–93. doi:10.1126/science.1181369.

185. Belaghzal H, Dekker J, Gibcus JH. Hi-C 2.0: An optimized Hi-C procedure for high-resolution genome-wide mapping of chromosome conformation. Methods. 2017;123:56–65. doi:10.1016/j.ymeth.2017.04.004.

186. Chen Y, Wang Y, Liu X, Xu J, Zhang MQ. Model-based analysis of chromatin interactions from dCas9-Based CAPTURE-3C-seq. PLoS One. 2020;15:e0236666. doi:10.1371/journal.pone.0236666.

187. Mondal T, Subhash S, Kanduri C. Chromatin RNA Immunoprecipitation (ChRIP). Methods Mol Biol. 2018;1689:65–76. doi:10.1007/978-1-4939-7380-4_6.

188. Tieri P, Termanini A, Bellavista E, Salvioli S, Capri M, Franceschi C. Charting the NF-κB Pathway Interactome Map. PLoS One 2012. doi:10.1371/journal.pone.0032678.

189. Bouwmeester T, Bauch A, Ruffner H, Angrand P-O, Bergamini G, Croughton K, et al. A physical and functional map of the human TNF-alpha/NF-kappa B signal transduction pathway. Nat Cell Biol. 2004;6:97–105. doi:10.1038/ncb1086.

190. Luck K, Kim D-K, Lambourne L, Spirohn K, Begg BE, Bian W, et al. A reference map of the human binary protein interactome. Nature. 2020;580:402–8. doi:10.1038/s41586-020-2188-x.

191. Roux KJ, Kim D in, Burke B, May DG. BioID: A Screen for Protein-Protein Interactions. Curr Protoc Protein Sci. 2018;91:19.23.1-19.23.15. doi:10.1002/cpps.51.

192. van Criekinge W, Beyaert R. Yeast Two-Hybrid: State of the Art. Biol Proced Online. 1999;2:1–38. doi:10.1251/bpo16.

193. Rzeczkowski K, Beuerlein K, Müller H, Dittrich-Breiholz O, Schneider H, Kettner-Buhrow D, et al. c-Jun N-terminal kinase phosphorylates DCP1a to control formation of P bodies. J Cell Biol. 2011;194:581–96. doi:10.1083/jcb.201006089.

194. Feldman I, Feldman GM, Mobarak C, Dunkelberg JC, Leslie KK. Identification of proteins within the nuclear factor-kappa B transcriptional complex including estrogen receptor-alpha. Am J Obstet Gynecol. 2007;196:394.e1-11; discussion 394.e11-3. doi:10.1016/j.ajog.2006.12.033.

195. Meier F, Park MA, Mann M. Trapped Ion Mobility Spectrometry and Parallel Accumulation–Serial Fragmentation in Proteomics. Mol Cell Proteomics 2021. doi:10.1016/j.mcpro.2021.100138.

196. Wan F, Lenardo MJ. Specification of DNA binding activity of NF-kappaB proteins. Cold Spring Harb Perspect Biol. 2009;1:a000067. doi:10.1101/cshperspect.a000067.

197. Wan F, Anderson DE, Barnitz RA, Snow A, Bidere N, Zheng L, et al. Ribosomal protein S3: a KH domain subunit in NF-kappaB complexes that mediates selective gene regulation. Cell. 2007;131:927–39. doi:10.1016/j.cell.2007.10.009.

198. Lambert SA, Jolma A, Campitelli LF, Das PK, Yin Y, Albu M, et al. The Human Transcription Factors. Cell. 2018;172:650–65. doi:10.1016/j.cell.2018.01.029.

199. Marakulina D, Vorontsov IE, Kulakovskiy IV, Lennartsson A, Drabløs F, Medvedeva YA. EpiFactors 2022: expansion and enhancement of a curated database of human epigenetic factors and complexes. Nucleic Acids Res. 2023;51:D564-D570. doi:10.1093/nar/gkac989.
200. Florio TJ, Lokareddy RK, Yeggoni DP, Sankhala RS, Ott CA, Gillilan RE, Cingolani G. Differential recognition of canonical NF-κB dimers by Importin α3. Nat Commun. 2022;13:1207. doi:10.1038/s41467-022-28846-z.
201. Huang B, Yang X-D, Lamb A, Chen L-F. Posttranslational modifications of NF-κB: another layer of regulation for NF-κB signaling pathway. Cell Signal. 2010;22:1282–90. doi:10.1016/j.cellsig.2010.03.017.
202. Wu J, Powell F, Larsen NA, Lai Z, Byth KF, Read J, et al. Mechanism and in vitro pharmacology of TAK1 inhibition by (5Z)-7-Oxozeaenol. ACS Chem Biol. 2013;8:643–50. doi:10.1021/cb3005897.
203. Fujioka S, Niu J, Schmidt C, Sclabas GM, Peng B, Uwagawa T, et al. NF-kappaB and AP-1 connection: mechanism of NF-kappaB-dependent regulation of AP-1 activity. Mol Cell Biol. 2004;24:7806–19. doi:10.1128/MCB.24.17.7806-7819.2004.
204. Park MH, Hong JT. Roles of NF-κB in Cancer and Inflammatory Diseases and Their Therapeutic Approaches. Cells 2016. doi:10.3390/cells5020015.
205. Schinnerling K, Rosas C, Soto L, Thomas R, Aguillón JC. Humanized Mouse Models of Rheumatoid Arthritis for Studies on Immunopathogenesis and Preclinical Testing of Cell-Based Therapies. Front Immunol. 2019;10:203. doi:10.3389/fimmu.2019.00203.
206. Tiller GR, Garsin DA. Of Worms and Men: HLH-30 and TFEB Regulate Tolerance to Infection. Immunity. 2014;40:857–8. doi:10.1016/j.immuni.2014.06.002.
207. Pukkila-Worley R, Ausubel FM. Immune defense mechanisms in the Caenorhabditis elegans intestinal epithelium. Curr Opin Immunol. 2012;24:3–9. doi:10.1016/j.coi.2011.10.004.
208. Ermolaeva MA, Schumacher B. Insights from the worm: the C. elegans model for innate immunity. Semin Immunol. 2014;26:303–9. doi:10.1016/j.smim.2014.04.005.
209. Brena D, Bertran J, Porta-de-la-Riva M, Guillén Y, Cornes E, Kukhtar D, et al. Ancestral function of Inhibitors-of-kappaB regulates Caenorhabditis elegans development. Sci Rep. 2020;10:16153. doi:10.1038/s41598-020-73146-5.
210. Wolenski FS, Garbati MR, Lubinski TJ, Traylor-Knowles N, Dresselhaus E, Stefanik DJ, et al. Characterization of the core elements of the NF-κB signaling pathway of the sea anemone Nematostella vectensis. Mol Cell Biol. 2011;31:1076–87. doi:10.1128/MCB.00927-10.
211. Cammarata-Mouchtouris A, Acker A, Goto A, Di Chen, Matt N, Leclerc V. Dynamic Regulation of NF-κB Response in Innate Immunity: The Case of the IMD Pathway in Drosophila. Biomedicines 2022. doi:10.3390/biomedicines10092304.
212. Mugabo Y, Lim GE. Scaffold Proteins: From Coordinating Signaling Pathways to Metabolic Regulation. Endocrinology. 2018;159:3615–30. doi:10.1210/en.2018-00705.

213. Meister M, Tomasovic A, Banning A, Tikkanen R. Mitogen-Activated Protein (MAP) Kinase Scaffolding Proteins: A Recount. Int J Mol Sci. 2013;14:4854–84. doi:10.3390/ijms14034854.
214. Good MC, Zalatan JG, Lim WA. Scaffold proteins: hubs for controlling the flow of cellular information. Science. 2011;332:680–6. doi:10.1126/science.1198701.
215. Fritz RD, Radziwill G. CNK1 and other scaffolds for Akt/FoxO signaling. Biochim Biophys Acta. 2011;1813:1971–7. doi:10.1016/j.bbamcr.2011.02.008.
216. Yasuda J, Whitmarsh AJ, Cavanagh J, Sharma M, Davis RJ. The JIP group of mitogen-activated protein kinase scaffold proteins. Mol Cell Biol. 1999;19:7245–54. doi:10.1128/mcb.19.10.7245.
217. Benjamin D, Colombi M, Moroni C, Hall MN. Rapamycin passes the torch: a new generation of mTOR inhibitors. Nat Rev Drug Discov. 2011;10:868–80. doi:10.1038/nrd3531.
218. Thoreen CC, Kang SA, Chang JW, Liu Q, Zhang J, Gao Y, et al. An ATP-competitive mammalian target of rapamycin inhibitor reveals rapamycin-resistant functions of mTORC1. J Biol Chem. 2009;284:8023–32. doi:10.1074/jbc.M900301200.
219. Gosis BS, Wada S, Thorsheim C, Li K, Jung S, Rhoades JH, et al. Inhibition of nonalcoholic fatty liver disease in mice by selective inhibition of mTORC1. Science. 2022;376:eabf8271. doi:10.1126/science.abf8271.
220. Gambardella G, Staiano L, Moretti MN, Cegli R de, Fagnocchi L, Di Tullio G, et al. GADD34 is a modulator of autophagy during starvation. Sci Adv 2020. doi:10.1126/sciadv.abb0205.
221. Yao J, Lei P-J, Li Q-L, Chen J, Tang S-B, Xiao Q, et al. GLIS2 promotes colorectal cancer through repressing enhancer activation. Oncogenesis 2020. doi:10.1038/s41389-020-0240-1.
222. He R, Li X. Mammalian two-hybrid assay for detecting protein-protein interactions in vivo. Methods Mol Biol. 2008;439:327–37. doi:10.1007/978-1-59745-188-8_22.
223. Brasier AR, Ron D. Luciferase reporter gene assay in mammalian cells. Methods Enzymol. 1992;216:386–97. doi:10.1016/0076-6879(92)16036-J.
224. Pazin MJ, Sheridan PL, Cannon K, Cao Z, Keck JG, Kadonaga JT, Jones KA. NF-kappa B-mediated chromatin reconfiguration and transcriptional activation of the HIV-1 enhancer in vitro. Genes Dev. 1996;10:37–49. doi:10.1101/gad.10.1.37.
225. Akdogan-Ozdilek B, Duval KL, Meng FW, Murphy PJ, Goll MG. Identification of chromatin states during zebrafish gastrulation using CUT&RUN and CUT&Tag. Dev Dyn. 2022;251:729–42. doi:10.1002/dvdy.430.
226. Xu C, Li T, Lei J, Zhang Y, Zhou J, Hu B. The Autophagy Cargo Receptor SQSTM1 Inhibits Infectious Bursal Disease Virus Infection through Selective Autophagic Degradation of Double-Stranded Viral RNA. Viruses 2021. doi:10.3390/v13122494.
227. Lu H, Zhu C, Ruan Y, Fan L, Wei K, Yang Z, Chen Q. TFE3 Regulates the Function of the Autophagy-Lysosome Pathway to Drive the Invasion and Metastasis of Papillary Thyroid Carcinoma. Anal Cell Pathol (Amst). 2021;2021:3081491. doi:10.1155/2021/3081491.

228. Schwob A, Teruel E, Dubuisson L, Lormières F, Verlhac P, Abudu YP, et al. SQSTM-1/p62 potentiates HTLV-1 Tax-mediated NF-κB activation through its ubiquitin binding function. Sci Rep. 2019;9:16014. doi:10.1038/s41598-019-52408-x.
229. Ling J, Kang Y, Zhao R, Xia Q, Lee D-F, Chang Z, et al. KrasG12D-induced IKK2/β/NF-κB activation by IL-1α and p62 feedforward loops is required for development of pancreatic ductal adenocarcinoma. Cancer Cell. 2012;21:105–20. doi:10.1016/j.ccr.2011.12.006.
230. Cegli R de, Carrella D, Siciliano D, Gambardella G, Napolitano G, Di Malta C, et al. TFEBexplorer: An integrated tool to study genes regulated by the stress-responsive Transcription Factor EB. Autophagy Reports. 2022;1:295–305. doi:10.1080/27694127.2022.2097822.
231. Zhou B, Lin W, Long Y, Yang Y, Zhang H, Wu K, Chu Q. Notch signaling pathway: architecture, disease, and therapeutics. Signal Transduct Target Ther 2022. doi:10.1038/s41392-022-00934-y.
232. Bierie B, Moses HL. TGF-beta and cancer. Cytokine Growth Factor Rev. 2006;17:29–40. doi:10.1016/j.cytogfr.2005.09.006.
233. Bray SJ. Notch signalling: a simple pathway becomes complex. Nat Rev Mol Cell Biol. 2006;7:678–89. doi:10.1038/nrm2009.
234. Chang T-C, Wentzel EA, Kent OA, Ramachandran K, Mullendore M, Lee KH, et al. Transactivation of miR-34a by p53 broadly influences gene expression and promotes apoptosis. Mol Cell. 2007;26:745–52. doi:10.1016/j.molcel.2007.05.010.
235. Ji Q, Hao X, Zhang M, Tang W, Yang M, Li L, et al. MicroRNA miR-34 Inhibits Human Pancreatic Cancer Tumor-Initiating Cells. PLoS One 2009. doi:10.1371/journal.pone.0006816.
236. Liu Z, Johnson ST, Zhang Z, Corey DR. Expression of TNRC6 (GW182) Proteins Is Not Necessary for Gene Silencing by Fully Complementary RNA Duplexes. Nucleic Acid Ther. 2019;29:323–34. doi:10.1089/nat.2019.0815.
237. Nawaz A, Shilikbay T, Skariah G, Ceman S. Unwinding the roles of RNA helicase MOV10. Wiley Interdiscip Rev RNA. 2022;13:e1682. doi:10.1002/wrna.1682.
238. Kakuda S, Haltiwanger RS. Deciphering the Fringe-Mediated Notch Code: Identification of Activating and Inhibiting Sites Allowing Discrimination between Ligands. Dev Cell. 2017;40:193–201. doi:10.1016/j.devcel.2016.12.013.
239. Brückner K, Perez L, Clausen H, Cohen S. Glycosyltransferase activity of Fringe modulates Notch-Delta interactions. Nature. 2000;406:411–5. doi:10.1038/35019075.
240. Golan T, Levy C. Negative Regulatory Loop between Microphthalmia-Associated Transcription Factor (MITF) and Notch Signaling. Int J Mol Sci 2019. doi:10.3390/ijms20030576.
241. Yuan J, Tan L, Yin Z, Tao K, Wang G, Shi W, Gao J. GLIS2 redundancy causes chemoresistance and poor prognosis of gastric cancer based on co-expression network analysis. Oncol Rep. 2019;41:191–201. doi:10.3892/or.2018.6794.
242. Masetti R, Bertuccio SN, Pession A, Locatelli F. CBFA2T3-GLIS2-positive acute myeloid leukaemia. A peculiar paediatric entity. Br J Haematol. 2018;184:337–47. doi:10.1111/bjh.15725.

243. Perera RM, Stoykova S, Nicolay BN, Ross KN, Fitamant J, Boukhali M, et al. Transcriptional control of autophagy-lysosome function drives pancreatic cancer metabolism. Nature. 2015;524:361–5. doi:10.1038/nature14587.
244. Dolcet X, Llobet D, Pallares J, Matias-Guiu X. NF-kB in development and progression of human cancer. Virchows Arch. 2005;446:475–82. doi:10.1007/s00428-005-1264-9.
245. Chen GQ, Wang QM, Yu M, Cheng YD, Zhang ZC, Wang WS, et al. Notch signaling is involved in regulation of LPS-induced macrophage apoptosis through JNK/NF-kB signaling pathway. J Biol Regul Homeost Agents 2020. doi:10.23812/19-283-A.
246. Gingery A, Bradley EW, Pederson L, Ruan M, Horwood NJ, Oursler MJ. TGF-beta coordinately activates TAK1/MEK/AKT/NFkB and SMAD pathways to promote osteoclast survival. Exp Cell Res. 2008;314:2725–38. doi:10.1016/j.yexcr.2008.06.006.
247. Kanaoka Y, Urade Y. Hematopoietic prostaglandin D synthase. Prostaglandins Leukot Essent Fatty Acids. 2003;69:163–7. doi:10.1016/s0952-3278(03)00077-2.
248. Brooks SA, Blackshear PJ. Tristetraprolin (TTP): interactions with mRNA and proteins, and current thoughts on mechanisms of action. Biochim Biophys Acta. 2013;1829:666–79. doi:10.1016/j.bbagrm.2013.02.003.
249. Choudhary I, Vo T, Bathula CS, Lamichhane R, Lewis BW, Looper J, et al. Tristetraprolin Overexpression in Non-hematopoietic Cells Protects Against Acute Lung Injury in Mice. Front Immunol 2020. doi:10.3389/fimmu.2020.02164.
250. Taylor GA, Carballo E, Lee DM, Lai WS, Thompson MJ, Patel DD, et al. A pathogenetic role for TNF alpha in the syndrome of cachexia, arthritis, and autoimmunity resulting from tristetraprolin (TTP) deficiency. Immunity. 1996;4:445–54. doi:10.1016/S1074-7613(00)80411-2.
251. Patial S, Curtis AD, Lai WS, Stumpo DJ, Hill GD, Flake GP, et al. Enhanced stability of tristetraprolin mRNA protects mice against immune-mediated inflammatory pathologies. Proc Natl Acad Sci U S A. 2016;113:1865–70. doi:10.1073/pnas.1519906113.
252. Armento A, Ueffing M, Clark SJ. The complement system in age-related macular degeneration. Cell Mol Life Sci. 2021;78:4487–505. doi:10.1007/s00018-021-03796-9.
253. Cheng X, Shen D, Samie M, Xu H. Mucolipins: Intracellular TRPML1-3 Channels. FEBS Lett. 2010;584:2013–21. doi:10.1016/j.febslet.2009.12.056.
254. Bassi MT, Manzoni M, Monti E, Pizzo MT, Ballabio A, Borsani G. Cloning of the gene encoding a novel integral membrane protein, mucolipidin-and identification of the two major founder mutations causing mucolipidosis type IV. Am J Hum Genet. 2000;67:1110–20. doi:10.1016/S0002-9297(07)62941-3.
255. Medina DL, Fraldi A, Bouche V, Annunziata F, Mansueto G, Spampanato C, et al. Transcriptional activation of lysosomal exocytosis promotes cellular clearance. Dev Cell. 2011;21:421–30. doi:10.1016/j.devcel.2011.07.016.

256. Ke K, Song Y, Shen J, Niu M, Zhang H, Yuan D, et al. Up-regulation of Glis2 involves in neuronal apoptosis after intracerebral hemorrhage in adult rats. Cell Mol Neurobiol. 2015;35:345–54. doi:10.1007/s10571-014-0130-1.

257. Hosking CR, Ulloa F, Hogan C, Ferber EC, Figueroa A, Gevaert K, et al. The Transcriptional Repressor Glis2 Is a Novel Binding Partner for p120 Catenin. Mol Biol Cell. 2007;18:1918–27. doi:10.1091/mbc.E06-10-0941.

258. Adey A, Burton JN, Kitzman JO, Hiatt JB, Lewis AP, Martin BK, et al. The haplotype-resolved genome and epigenome of the aneuploid HeLa cancer cell line. Nature. 2013;500:207–11. doi:10.1038/nature12064.

8 Supplement

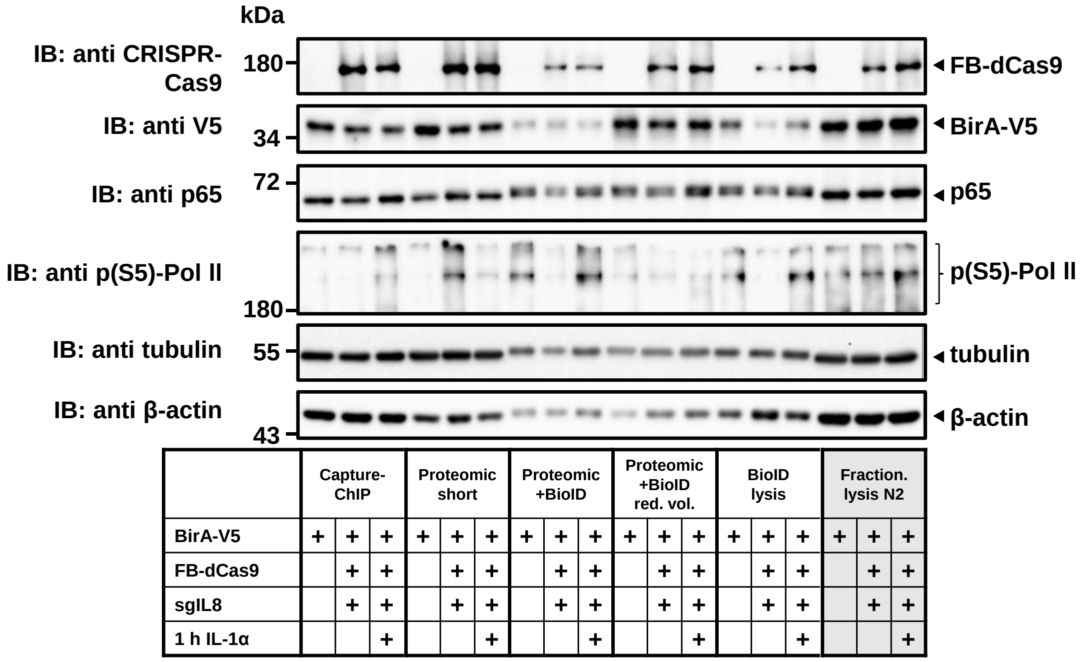

Supplementary Figure 1: Comparing six different lysis conditions for the CAPTURE-Proteomics protocol. Western blot analysis of lysates prepared with six different lysis protocols. HeLa cells transfected with BirA only or dCas9-BirA-sg*IL8* were stimulated with IL-1α (10 ng/ml) for 1 h or left unstimulated. Lysis conditions were compared using different buffers and volumes, urea addition, washing steps, and sonication cycles. The highest input quality was achieved with the N2 fraction of the fractional lysis protocol (highlighted in grey), which was used for the streptavidin-pulldown experiment in Figure 12. Shown is the Western blot result of one experiment. (The experiment was performed in cooperation with Jana Juli.)

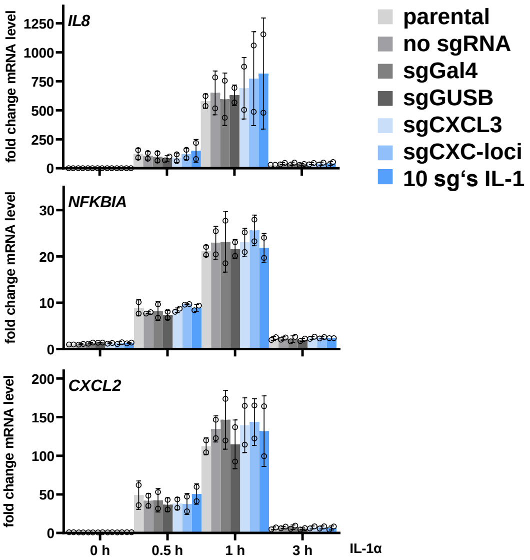

Supplementary Figure 2: Stable expression of CAPTURE 2.0 components does not interfere with the IL-1α-inducible expression of targeted inflammatory genes.
RT-qPCR analysis of a set of stable transduced CAPTURE 2.0 HeLa cells coexpressing dCas9-CBio and different sgRNAs targeting inflammatory promoters, which were stimulated with IL-1α (10 ng/ml) for 0.5 h, 1 h, 3 h, or left unstimulated. The effect of the lentiviral procedure or stable coexpression of CAPTURE components of the second-generation was assessed by normalization relative to untreated parental HeLa cells. The experiment shows

that none of the factors affected the expression level of the quantified inflammatory mRNAs. Displayed is the mean ± SD from two independet experiments. (The experiments were performed in cooperation with Jana Juli.)

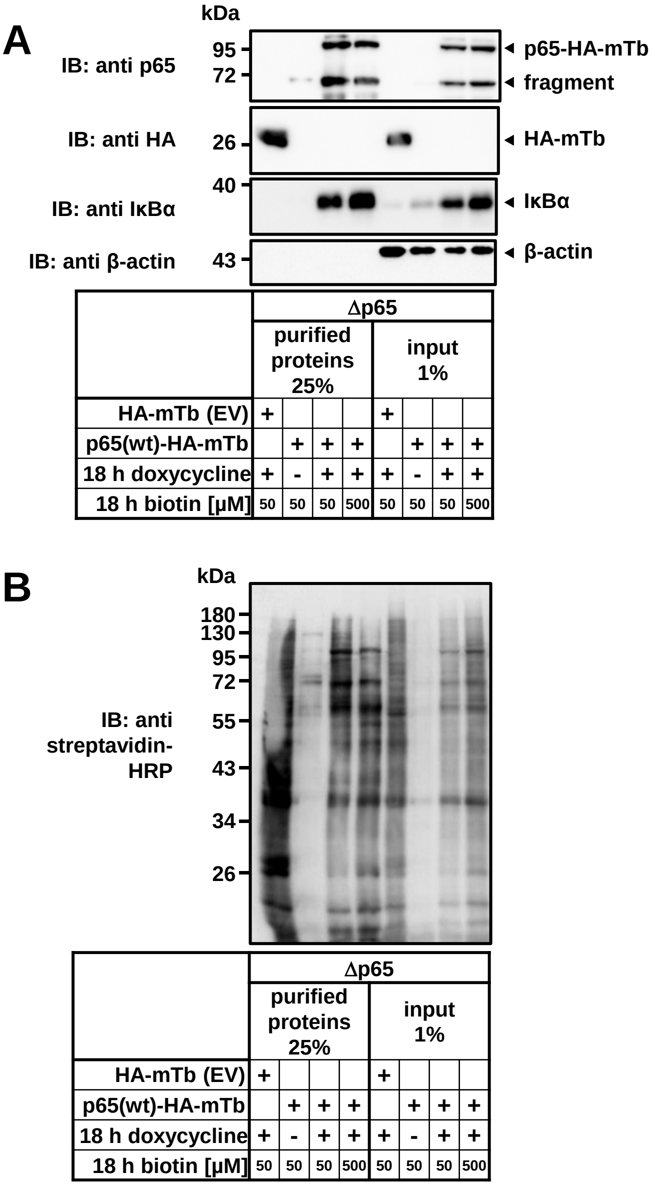

A

	Δp65							
	purified proteins 25%				input 1%			
HA-mTb (EV)	+				+			
p65(wt)-HA-mTb		+	+	+		+	+	+
18 h doxycycline	+	-	+	+	+	-	+	+
18 h biotin [µM]	50	50	50	500	50	50	50	500

B

	Δp65							
	purified proteins 25%				input 1%			
HA-mTb (EV)	+				+			
p65(wt)-HA-mTb		+	+	+		+	+	+
18 h doxycycline	+	-	+	+	+	-	+	+
18 h biotin [µM]	50	50	50	500	50	50	50	500

Supplementary Figure 3: Extended biotin labeling time of 18 h increases the pulldown material.
Western blot analysis after streptavidin affinity purification of biotinylated proteins in p65-deficient HeLa cells (Δp65) treated with 1 µg/ml doxycycline 7 h after transfection and incubated for 18 h to induce expression of p65(wt)-HA-miniTurbo or HA-miniTurbo alone. Cells were then treated with 50 µM or 500 µM biotin for 18 h to induce labeling by miniTurbo and the biotinylated proteins were purified from cell extracts by a streptavidin pulldown and analyzed in comparison to the input using indicated antibodies (A) or streptavidin-HRP (B). The β-actin levels were assessed to control equal loading of gels. Western blots from a single experiment show that prolonged 18 h biotin labeling increases pulldown of biotinylated proteins, but predominantly through the accumulation of basal p65 binders such as IκBα and most likely also through non-specifically biotinylated proteins. (The experiment was performed in cooperation with Jana Juli.)

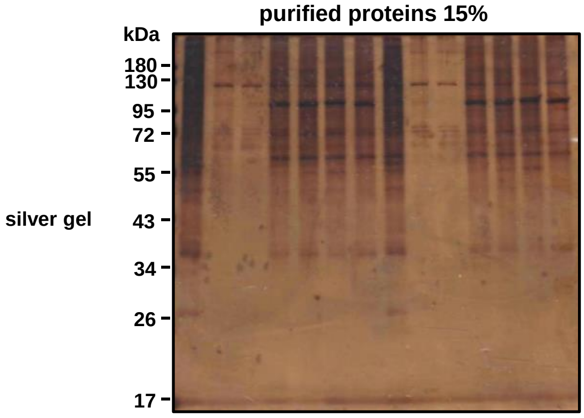

	Δp65						p	Δp65						p
HA-mTb (EV)	+							+						
p65(wt)-HA-mTb		+	+	+			+		+	+	+			+
p65(E/I)-HA-mTb					+							+		
p65(FL/DD)-HA-mTb						+							+	
doxycycline	+	-	+	+	+	+	+	+	-	+	+	+	+	+
biotin	+	+	-	+	+	+	+	+	+	-	+	+	+	+
IL-1α	-	-	-	-	-	-	-	+	+	+	+	+	+	+

***p = parental**

Supplementary Figure 4: Silver staining of purified proteins after the MiniTurboID pulldown.
Silver gel from the same samples as in Figure 27B derived from p65-deficient HeLa cells (Δp65) or parental HeLa cells transfected with different HA-miniTurbo constructs of p65(wt), p65(E/I), p65(FL/DD), or HA-miniTurbo (EV), whose expression was induced 7 h after transfection with 1 µg/ml doxycycline for 17 h. Biotin labeling by miniTurbo was induced by adding 50 µM biotin 10 min before stimulating cells with 10 ng/ml IL-1α for the last hour of incubation or cells were left untreated. Streptavidin-pulldown was performed with cell extracts using 60 µl agarose beads and purified proteins were detected after SDS-PAGE by silver staining. Shown is a representative replicate from two biological replicates. (The experiments were performed in cooperation with Jana Juli.)

top20 pathway terms

	GO	Description	EV (1017 IDs)	p65 (wt) (327 IDs)
HA-mTb (EV)	GO:0045296	cadherin binding	-44.84	0.00
	R-HSA-9012999	RHO GTPase cycle	-39.04	0.00
	R-HSA-9716542	Signaling by Rho GTPases, Miro GTPases and RHOBTB3	-38.07	0.00
	GO:0050839	cell adhesion molecule binding	-37.62	0.00
	R-HSA-194315	Signaling by Rho GTPases	-37.47	0.00
	R-HSA-199991	Membrane Trafficking	-36.38	0.00
	R-HSA-5653656	Vesicle-mediated transport	-34.91	0.00
	GO:0034660	ncRNA metabolic process	-28.24	0.00
	GO:0003779	actin binding	-26.90	0.00
	GO:0048471	perinuclear region of cytoplasm	-25.86	0.00
	GO:0048193	Golgi vesicle transport	-25.30	0.00
	GO:0030029	actin filament-based process	-24.34	0.00
	GO:0051640	organelle localization	-24.34	0.00
	GO:0061024	membrane organization	-24.27	0.00
	GO:0030055	cell-substrate junction	-23.24	0.00
	GO:0030036	actin cytoskeleton organization	-23.19	0.00
	GO:0005925	focal adhesion	-23.07	0.00
	GO:0019904	protein domain specific binding	-22.79	-4.13
	GO:0010256	endomembrane system organization	-21.52	0.00
	GO:0051493	regulation of cytoskeleton organization	-20.96	0.00
p65(wt)-HA-mTb	GO:0005667	transcription regulator complex	0.00	-65.33
	GO:0001228	DNA-binding transcription activator activity, RNA polymerase II-specific	0.00	-51.15
	GO:0001216	DNA-binding transcription activator activity	0.00	-50.91
	GO:0008134	transcription factor binding	0.00	-49.13
	GO:0140297	DNA-binding transcription factor binding	0.00	-48.04
	GO:0003682	chromatin binding	0.00	-43.09
	GO:0006351	DNA-templated transcription	0.00	-42.12
	GO:0097659	nucleic acid-templated transcription	0.00	-42.04
	GO:0032774	RNA biosynthetic process	0.00	-41.57
	GO:0003712	transcription coregulator activity	0.00	-37.20
	GO:0016570	histone modification	0.00	-36.87
	R-HSA-4839726	Chromatin organization	0.00	-34.90
	R-HSA-3247509	Chromatin modifying enzymes	0.00	-34.90
	GO:0006325	chromatin organization	0.00	-34.21
	GO:0003713	transcription coactivator activity	-2.93	-33.10
	GO:0061629	RNA polymerase II-specific DNA-binding transcription factor binding	0.00	-33.01
	GO:0090575	RNA polymerase II transcription regulator complex	0.00	-31.04
	GO:0006338	chromatin remodeling	0.00	-30.32
	GO:0006282	regulation of DNA repair	0.00	-29.84
	GO:0070603	SWI/SNF superfamily-type complex	0.00	-29.76

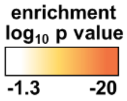

Supplementary Figure 5: Enriched proteins in the HA-miniTurbo (EV) control belong to pathways of abundant cellular proteins or potential contaminants.

The table displays the top 20 enriched pathway terms associated with the proteins enriched in the samples of p65(wt)-HA-miniTurbo or the empty vector control HA-miniTurbo alone. Comparison of overrepresented pathways was performed based on GO (BP, CC, MF), KEGG, Reactome, PANTHER, WikiPathways, Canonical pathways, and transcription factor targets using Metascape [149]. Proteins enriched in the control sample were defined by LFC ≤ -2 and in the p65(wt) sample by LFC ≥ 2 based on the p65(wt) sample compared to the empty vector control ($-\log_{10}$ p value ≥ 1.3). Numbers in parentheses denote proteins that were enriched in each sample and subjected to the analysis. (See Figure 28 legend for contributions.)

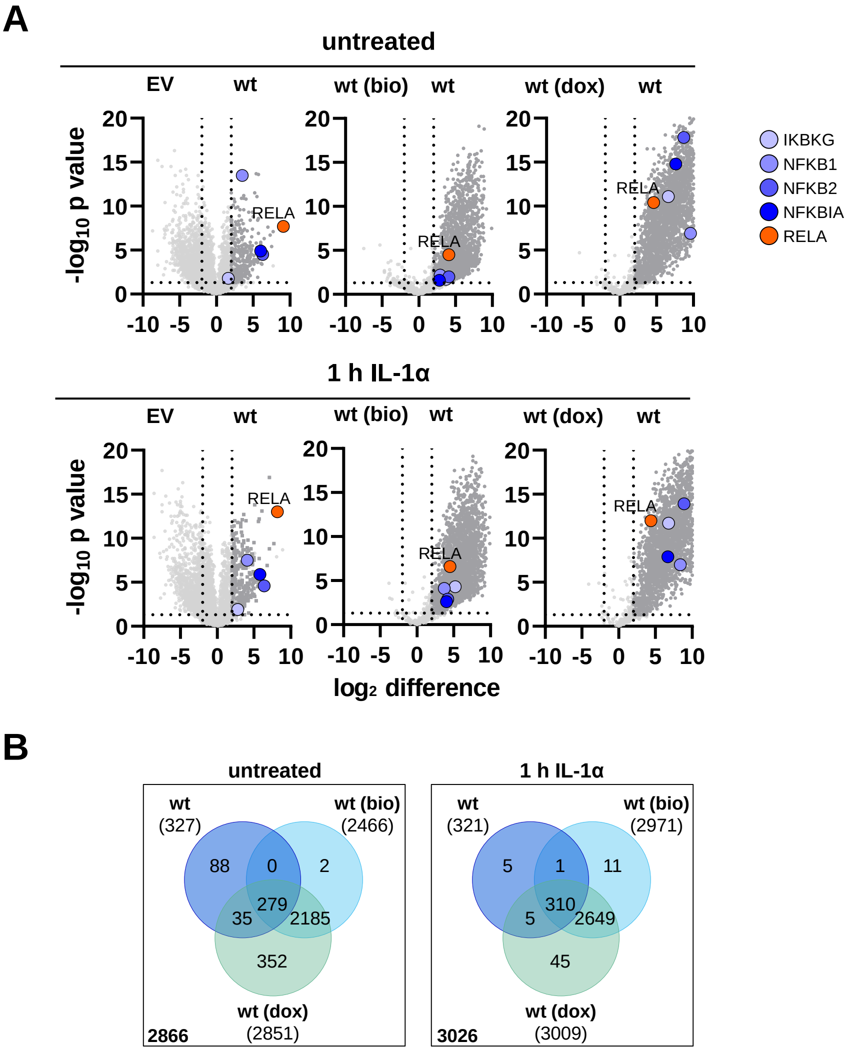

Supplementary Figure 6: Identification of specifically enriched proteins that bind to wild type p65/RELA. (A) Volcano comparisons between wild type p65 and negative controls HA-miniTurbo (EV) or cells exposed to doxycycline or biotin only under unstimulated or IL-1α-stimulated conditions. The plots show the ratios of $\log_2$ mean protein intensity values with their statistical significance determined by Student's T-test. Dark grey dots mark proteins significantly enriched with an LFC ≥ 2 and $-\log_{10}$ p value ≥ 1.3 in wild type p65 samples compared to the three negative control samples. (B) Venn diagrams show the overlap of the enriched proteins from the three negative controls. Proteins enriched across all three negative controls (279 in unstimulated cells, 310 in IL-1α-stimulated cells) were defined as specific interactors of p65/RELA wild type. The analysis was based on two biological experiments and three technical replicates per sample. (See Figure 28 legend for contributions.)

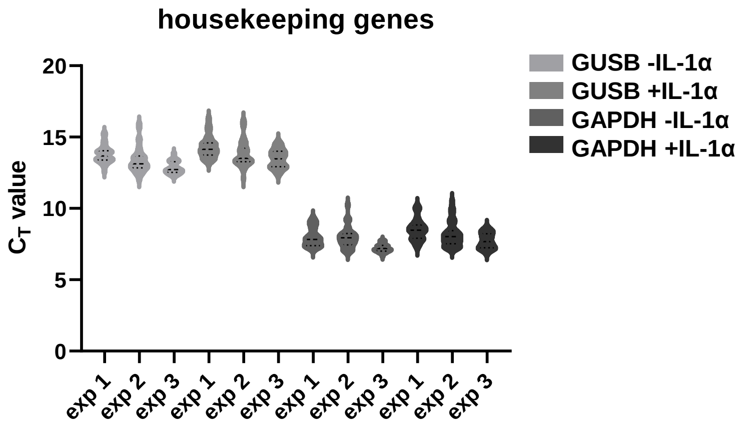

Supplementary Figure 7: C_T value distribution of *GUSB* and *GAPDH* across samples of the RNAi screen. The Violin plot illustrates the C_T value distribution of housekeeping genes *GUSB* and *GAPDH* across all samples of the RNAi screen according to experiment 1-3 (see section 4.3). Major fluctuations in the mean C_T values between the experiments or between the IL-1α-stimulated or unstimulated condition were thereby excluded. This control was fundamental for further use of the two housekeeping genes for normalization. (See Figure 35 legend for contributions.)

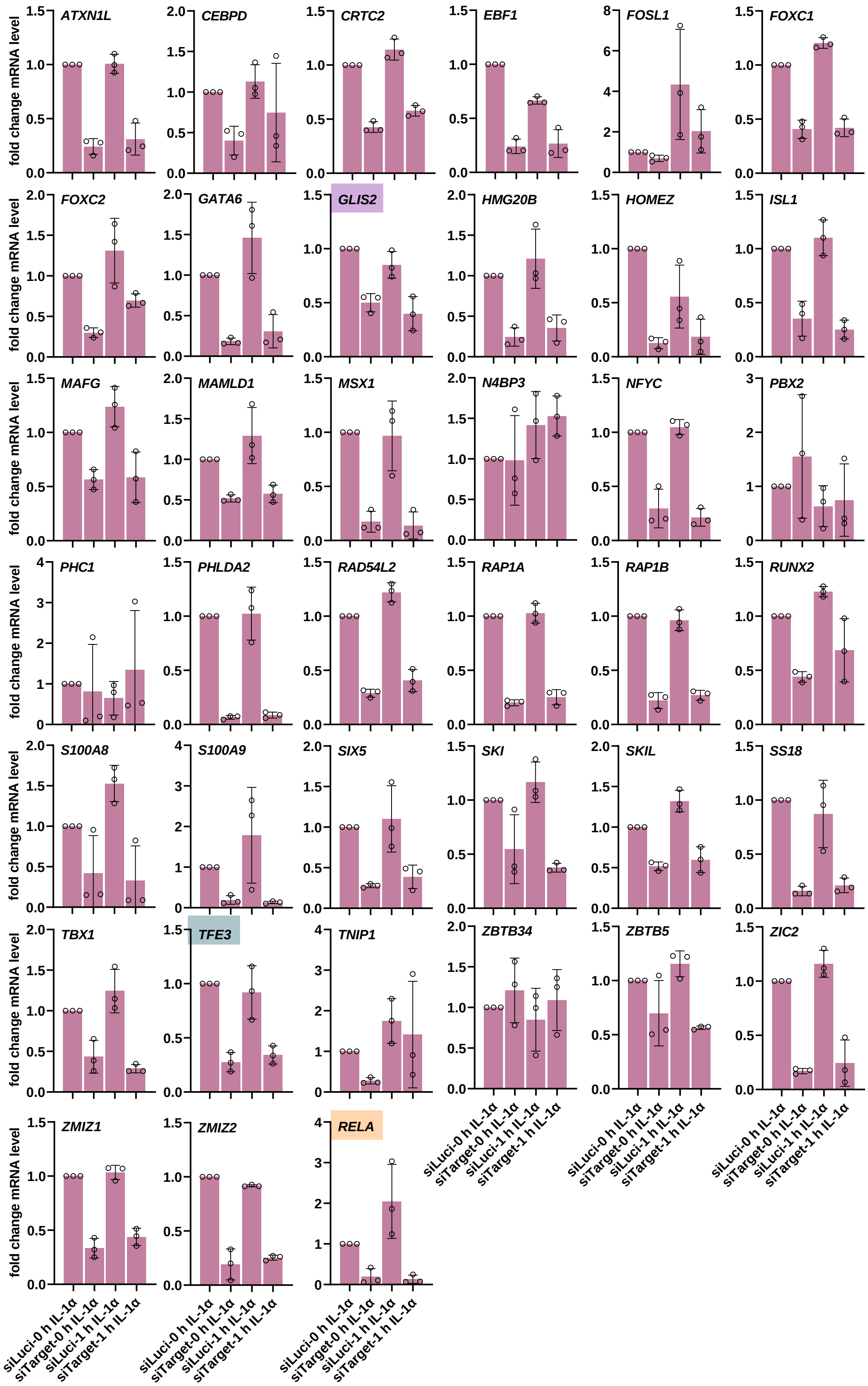

Supplementary Figure 8: Knockdown efficiencies of 38 HCI and p65/RELA in the RNAi screen.
Bar graphs showing the knockdowns of 38 HCI and p65/RELA in unstimulated and IL-1α-stimulated samples of the RNAi screen described in section 4.3. The mRNAs were quantified by qPCR and normalized to *GUSB*. Effects through knockdowns and IL-1α treatment were normalized against the luciferase siRNA control. The RNA analysis is based on three independent replicates. (See Figure 35 legend for contributions.)

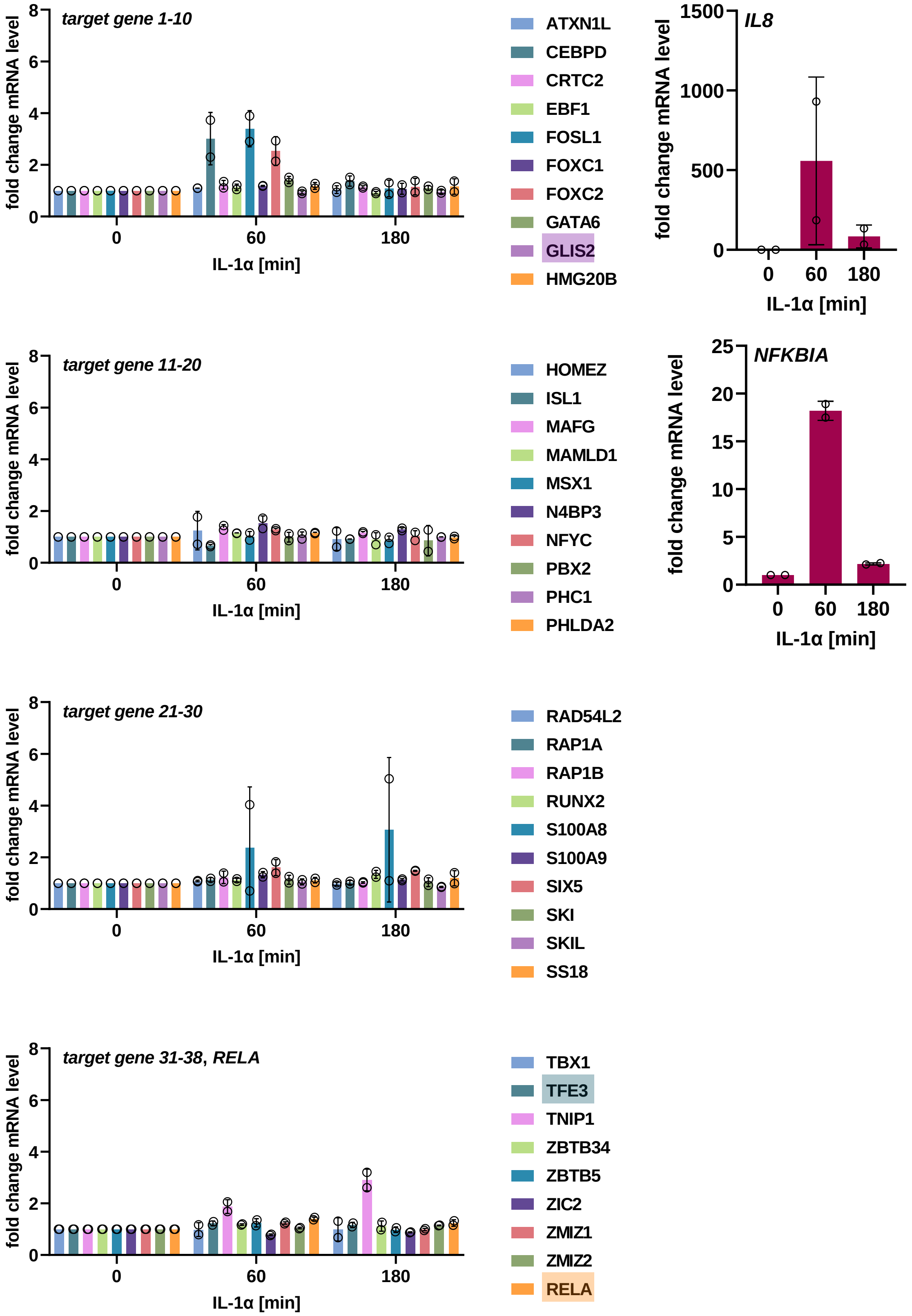

Supplementary Figure 9: The mRNA expression of 38 HCI and p65/RELA upon stimulation with IL-1α. RT-qPCR analysis of mRNA levels from 38 HCI and *RELA* in HeLa cells following stimulation with IL-1α for 0 min, 60 min, or 180 min. None of the genes targeted in the siRNA screen in section 4.3 were induced by treatment with IL-1α, except for *CEBPD*, *FOSL1*, *FOXC2*, and *TNIP1*, whose induction was by far not as strong as observed for the IL-1α response genes *IL8* and *NFKBIA*. (The experiments were planned and analyzed together with Jana Juli and performed by Doris Newel.)

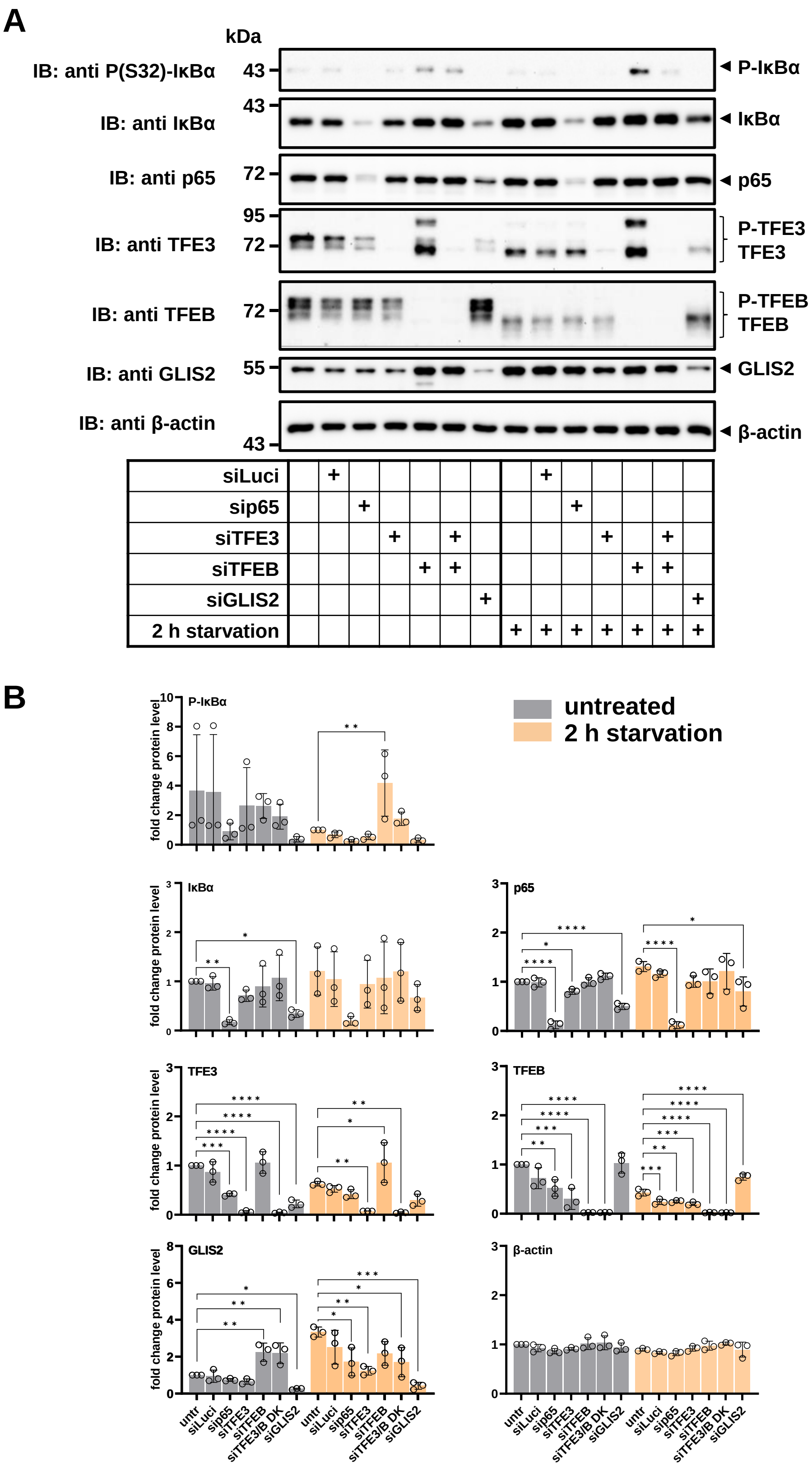

siLuci		+							+					
sip65			+							+				
siTFE3				+		+					+		+	
siTFEB					+	+						+	+	
siGLIS2							+							+
2 h starvation								+	+	+	+	+	+	+

Supplementary Figure 10: The siRNA-mediated knockdown of p65/RELA, TFE3, TFEB, and GLIS2 under starvation.

Western blot analysis from total cell extracts of HeLa cells transiently transfected with siRNAs for 48 h targeting p65/RELA, TFE3, TFEB, or both TFE3/TFEB (double knockdown, DK), GLIS2, or luciferase (siLuci, as negative control). As an additional control, some cell cultures were left untransfected (untr.). Cells were either left untreated or starved by washing cells four times with HBSS followed by incubation in HBSS for 2 h. Western blot was performed using the indicated antibodies and β-actin levels were assessed to control equal loading of gels. A representative Western blot experiment is shown in (A). Bar graphs in (B) display the mean changes in protein level for each condition relative to the unstimulated control (untr.). The statistical significance was calculated for each basal sample against the unstimulated control (untr.), and for each HBSS-treated sample, the significance was determined relative to the 2 h HBSS-starved control (untr.). Bar graphs show means of three independent biological replicates ± SD. Asterisks indicate significant changes (*p < 0.05, **p < 0.01, ***p < 0.001, ****p < 0.0001) obtained by one-way ANOVA.

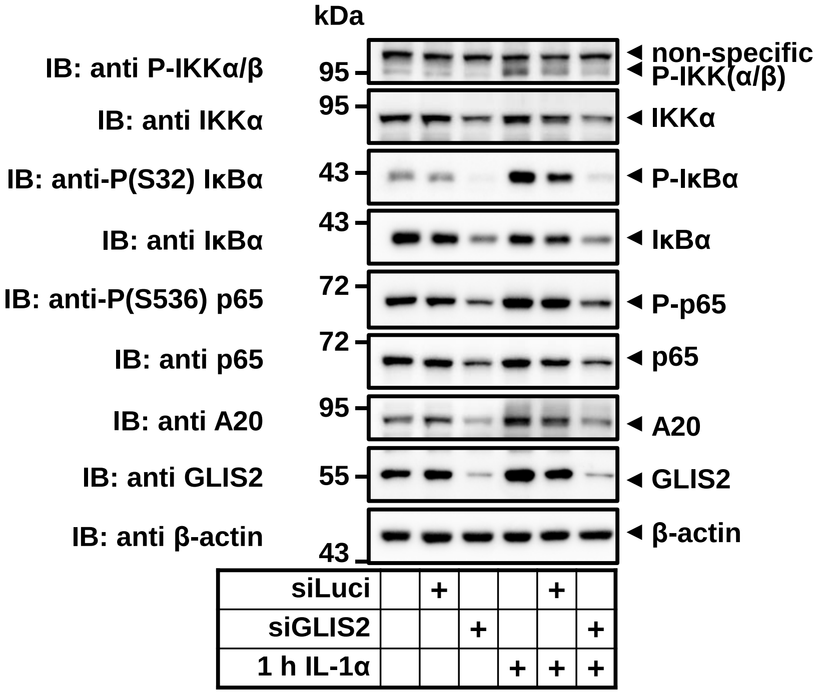

Supplementary Figure 11: GLIS2 suppression causes broad reduction of protein levels across signaling components of the canonical NF-κB pathway.
Western blot analysis from total cell extracts of HeLa cells transiently transfected with siRNAs for 48 h targeting GLIS2 or luciferase, and untransfected cells that were stimulated with IL-1α (10 ng/ml) for 1 h or left unstimulated. Western blot was performed using the indicated antibodies for detection of proteins of the canonical NF-κB pathway and GLIS2. The β-actin levels were assessed to control equal loading of gels. Shown is one representative experiment.

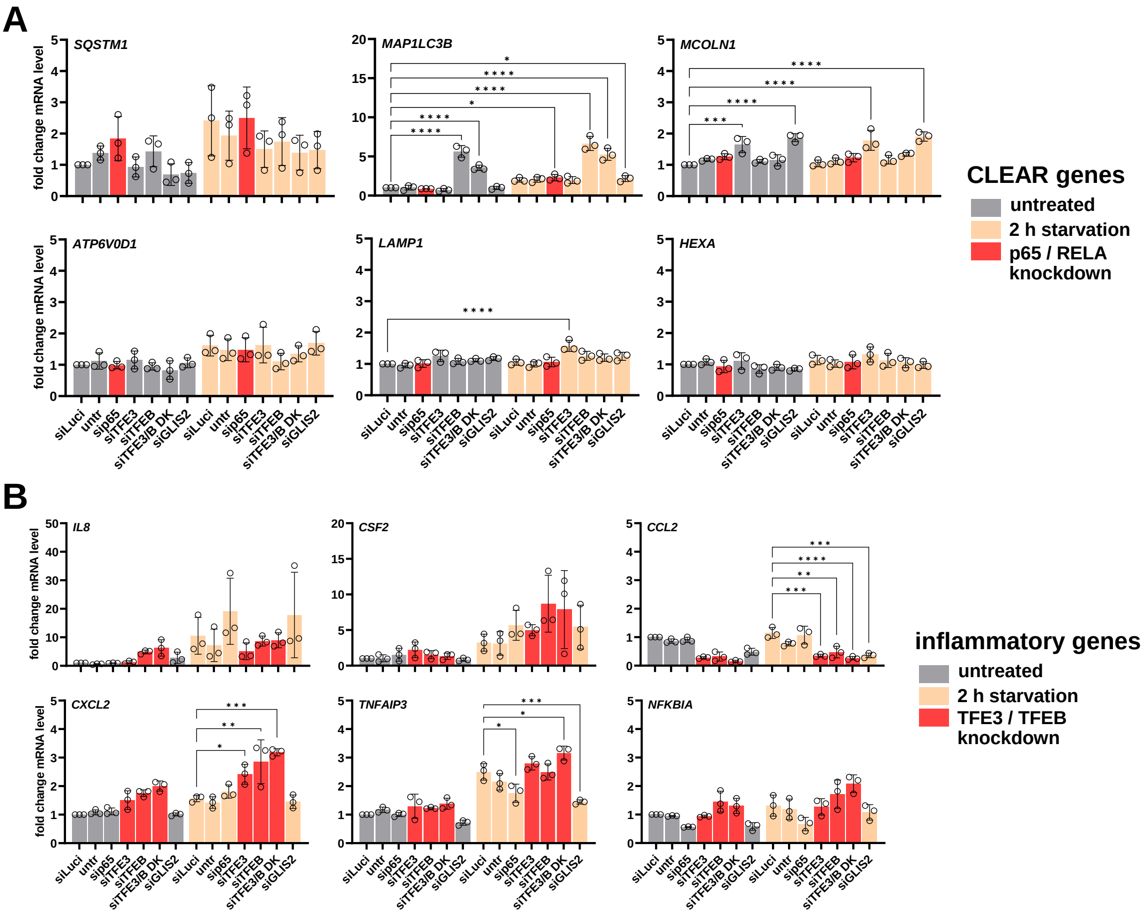

Supplementary Figure 12: Expression of CLEAR and inflammatory subsets of genes upon starvation. RT-qPCR analysis of mRNA levels of six CLEAR genes (A) and six inflammatory genes (B) using total RNA from the knockdown samples described in Supplementary Figure 10. Relative mRNA levels were calculated against the untreated siLuci control. For CLEAR genes, the statistical significance of knockdown effects was determined relative to the untreated siLuci control. For induced inflammatory genes, significance was calculated against the 2 h HBSS-starved siLuci control. Red colors visualize p65/RELA (A) or TFE3/TFEB (B) knockdown samples. Bar graphs show means of three independent biological replicates ± SD. Asterisks indicate significant changes (*p < 0.05, **p < 0.01, ***p < 0.001, ****p < 0.0001) obtained by one-way ANOVA.

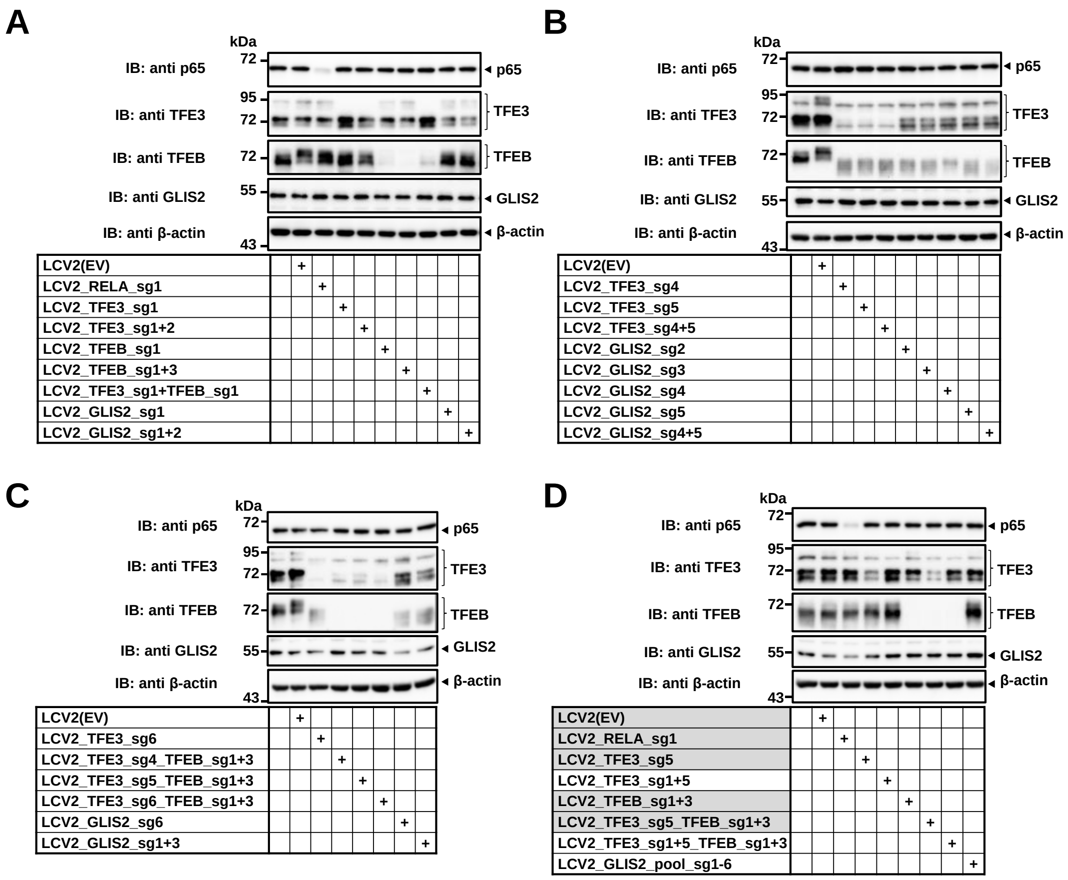

Supplementary Figure 13: Testing of sgRNAs for generating stable CRISPR gene knockout cells.
CRISPR-mediated gene editing was applied to generate stable gene knockouts of TFE3, TFEB, both (double knockout), GLIS2 and p65/RELA in HeLa cells. First, 3 sgRNAs (1-3) were designed for each of the genes targeting a region within the first or second exon. Later, additional 3 sgRNAs (4-6) were designed targeting exon 3 or 4. For the p65/RELA gene knockout, the published sgRNA (RELA-sg1) from our group was used. Lentiviral transduction was then performed with single sgRNAs or combinations of 2-6 sgRNAs using the LCV2 vector system. Control cells were transduced with LCV2 empty vector (EV). 48 h post-transduction, cells were selected with puromycin (0.75 µg/ml) for up to 14 days and analyzed for gene knockouts by Western blot using the indicated antibodies. The β-actin levels were assessed to control equal loading of gels. (A-C) Testing of sgRNAs and assessement of their performace in gene knockout generation relative to empty vector transduced and untransduced (parental) cells. (D) Final experiment generating a set of HeLa knockout cells for TFE3, TFEB, the double knockout, RELA, and the empty vector with the best performing sgRNAs transduced all at the same time to ensure the highest possible comparability of the cells. Knockout cells with the corresponding sgRNAs used for the analyses in Figure 44 & Figure 45 are highlighted in grey.

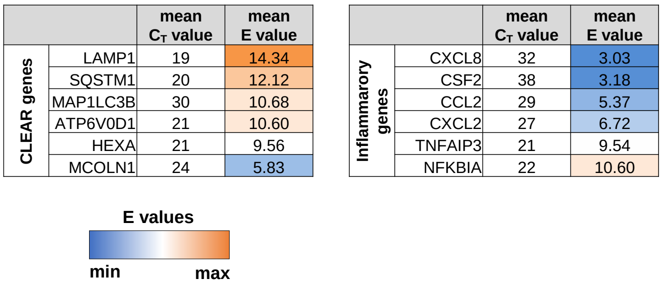

		mean C_T value	mean E value
CLEAR genes	LAMP1	19	14.34
	SQSTM1	20	12.12
	MAP1LC3B	30	10.68
	ATP6V0D1	21	10.60
	HEXA	21	9.56
	MCOLN1	24	5.83

		mean C_T value	mean E value
Inflammarory genes	CXCL8	32	3.03
	CSF2	38	3.18
	CCL2	29	5.37
	CXCL2	27	6.72
	TNFAIP3	21	9.54
	NFKBIA	22	10.60

Supplementary Figure 14: Comparison between the basal mean C_T values and E values between CLEAR genes and inflammatory genes.
Lists of six CLEAR genes and six inflammatory genes with their respective mean C_T values from RT-qPCR analyses of untreated HeLa cells from three independent experiments and expression values (E values) derived from transcriptome data of siLuci transfected unstimulated HeLa cells from two independent experiments.

9 Figures

10 Supplementary figures

List of figures involved external contributions:

Figure	Contributions
Figure 9	The schematic was created by Jana Juli.
Figure 10	The schematic in A & B was adapted from [138] by Lisa Leib; C was performed in cooperation with Jana Juli.
Figure 11, 12	The experiments were performed in cooperation with Jana Juli.
Figure 13	The schematic in A was created by Lisa Leib; B was performed in cooperation with Jana Juli.
Figure 14, 15	The experiments were performed in cooperation with Jana Juli.
Figure 16	The schematic in A was adapted from [159] by Lisa Leib; B was performed in cooperation with Jana Juli.
Figure 17, 18	The experiments were performed in cooperation with Jana Juli.
Figure 20	The schematic was created by Prof. M. Kracht.
Figure 21-26	The experiments were performed in cooperation with Jana Juli.
Suppl. Figure 1-4	The experiments were performed in cooperation with Jana Juli.
Figure 27-34, **Figure 37,** **Suppl. Figure 5 & 6**	The MiniTurboID samples were prepared together with Jana Juli (Figure 27 & Supplementary Figure 4). LC-MS/MS mass spectrometry measurements were performed in the Mass Spectrometry Facility of the Department of Chemistry, Philipps University Marburg (headed by Dr. Uwe Linne). Raw data were mapped to the human proteome by Dr. Uwe Linne and Dr. Axel Weber using the MaxQuant framework. The bioinformatic strategy and the entire set of analyses (Figure 29-34, Figure 37, Supplementary Figure 5 & 6) was devised, carried out and visualized by Prof. M. Kracht. Except for the filtering steps and literature search in (D), which was performed by Lisa Leib and Jana Juli. Lisa Leib performed the Metascape pathway analysis in Supplementary Figure 5, created the schematic of the step-wise bioinformatic analysis (Figure 28), and adapted the graphs provided by Prof. M. Kracht. Lisa Leib and Jana Juli extensively discussed, checked, and re-analyzed the data.
Figure 36 **Suppl. Figure 7 & 8**	The RNAi screen was planned, carried out, and analyzed by Lisa Leib and Jana Juli. Doris Newel helped perform the qPCR. Lisa Leib and Jana Juli performed the analysis as described in the text and visualized the data by a heatmap. Hierarchical clustering was performed by Prof. M. Kracht (Figure 36). The graph showing the C_T value distribution of housekeeping gene *GUSB* and *GAPDH* (Supplementary Figure 7) as well as the graphs demonstrating the knockdown efficiencies of 38 HCI and p65/RELA (Supplementary Figure 8) were created by Lisa Leib and Jana Juli. The schematic workflow (Figure 35) was adapted from [166] by Lisa Leib.
Suppl. Figure 9	The experiments were planned and analyzed together with Jana Juli and performed by Doris Newel.

Figure 46-55	Total RNA samples were prepared and validated by RT-qPCR by Lisa Leib (see Figure 43). The microarray analysis was performed in the genomics core facility of the ILH, Medical Faculty, Justus Liebig University (headed by Dr. Jochen Wilhelm). Raw data were processed by Dr. Jochen Wilhelm who provided spreadsheet tables with normalized mRNA expression values, fold changes of gene expression between pairs of treatments, and the according statistical parameters. Subsequent bioinformatic analyses were devised by Prof. M. Kracht who carried out and visualized the analyses in Figure 47, 51-53. Lisa Leib performed and visualized the analyses in Figure 48-50, 54 & 55 and adapted the schematic representation of the transcriptomic data analysis (Figure 46), which was created by Prof. M. Kracht.
Figure 56-58	The genome-wide ChIP-seq and motif analysis was performed by Dr. Marek Bartkuhn (Biomedical Informatics and Systems Medicine, Science Unit, Justus Liebig University) who provided a spreadsheet table with gene annotations and genomic coordinates to p65 ChIP-seq peak regions and specific motifs, as well as statistical parameters. The subsequent filtering steps were carried out and visualized by Prof. M. Kracht (Figure 57) and Lisa Leib (Figure 58). Lisa Leib adapted the schematic representation of the strategy of the combined genome-wide analysis (Figure 56) created by Prof. M. Kracht.
Figure 60	The graphic was created by Prof. M. Kracht.
Figure 61	The schematic was adapted from [38, 39] by Lisa Leib and Prof. M. Kracht.

11 Declaration

I declare that I have completed this dissertation single-handedly without the unauthorized help of a second party and only with the assistance acknowledged therein. I have appropriately acknowledged and cited all text passages that are derived verbatim from or are based on the content of published work of others, and all information relating to verbal communications. I consent to the use of an anti-plagiarism software to check my thesis. I have abided by the principles of good scientific conduct laid down in the charter of the Justus Liebig University Gießen "Satzung der Justus-Liebig-Universität Gießen zur Sicherung guter wissenschaftlicher Praxis" in carrying out the investigations described in the dissertation.

_________________________	_________________________
Location / Date	Signature